Influence of anisotropy induced effects on the collective spin excitations in skyrmion hosting system Cu_2OSeO_3

Jan Pascal Sahliger

Abstract

In the framework of this thesis the effects, induced by the underlying cubic crystal structure and its resulting anisotropies, on the collective spin excitations in the chiral magnet Cu_2OSeO_3 are investigated. The analysis comprises results obtained from numerical calculations and microwave spectroscopy experiments.

First, the resonance modes of the helical/conical, tilted conical, field polarized, skyrmion lattice and elongated skyrmion lattice phases are calculated numerically in presence of the cubic magnetocrystalline anisotropy. In this regard the field dependence of the resonance frequencies and the time evolution of the spatial distribution of the dynamic magnetization are presented. These results reveal mode hybridizations with higher order modes in the tilted conical and skyrmion lattice phase, respectively. The calculated microwave spectra are finally compared to the experimental ones, provided by collaborators from our group. A good agreement between these is evident.

In the second part, the mode interactions between the skyrmion lattice resonances are studied in more detail. It could be shown that the cubic magnetocrystalline anisotropy mediates a selection rule based on the symmetry and polarization of the interacting modes. In order to characterize the hybridization strength, the minimum frequency gap between the interacting resonance branches is extracted from the calculated microwave spectra for two different sample shapes. The obtained gap size as a function of cubic magnetocrystalline anisotropy strength K increases linearly and does not depend on the sample shape. These results are finally compared to experimental data, provided by collaborators from different groups. In the experiments a linear dependence on the temperature is observed, the gap size is, however, larger by a factor of around 2-3. In order to account for this difference, the energy functional is complemented by the exchange anisotropy. It was found that the gap size increases as a function of exchange anisotropy constant C in the case of $C > 0$ and decreases first and subsequently increases again in the case of $C < 0$.

The last part comprises angle and temperature resolved microwave spectroscopy experiments on a cuboid and a spherical sample. The quantities to be measured are the resonances in the field polarized phase and the critical

I

transition field H_{c2}. The measurements reveal a dominant twofold and a fourfold symmetry for the resonances and a fourfold symmetry for the second quantity, H_{c2}. While the fourfold symmetry originates mainly from the cubic magnetocrystalline anisotropy, the twofold symmetry is attributed to the dipolar interactions. These are taken into account by considering the formation of standing spin waves, instead of a uniform excitation of the magnetization dynamics. By fitting the analytically derived equations to the experimental data, a continuous decrease of K as a function of temperature is extracted. The comparison of the extracted K values obtained on one hand from the resonances in the field polarized phase and on the other hand from H_{c2} reveals a finite difference. This suggests that an additional fourfold symmetry contribution, such as the exchange anisotropy, is missing in the energy functional. The exchange anisotropy constant, which is obtained from subsequent analysis, agrees well with the one assumed in the preceding numerical treatment in order to compensate the difference in the hybridization gap size. It can be concluded that both the cubic magnetocrystalline and the exchange anisotropy are the main contributions to the mode-mode interactions.

Zusammenfassung

Im Rahmen dieser Arbeit werden die durch die zugrundeliegende kubische Kristallstruktur und die daraus resultierenden Anisotropien induzierten Effekte auf die kollektiven Spinanregungen in dem chiralen Magneten Cu_2OSeO_3 untersucht. Die Analyse umfasst Ergebnisse aus numerischen Berechnungen und Mikrowellen Spektroskopie Experimenten. Zunächst werden die Resonanzmoden der helikalen/konischen, gekippt konischen, feldpolarisierten, Skyrmion-Gitter und elongierten Skyrmion-Gitter Phasen in Gegenwart der kubischen magnetokristallinen Anisotropie numerisch berechnet.

In diesem Zusammenhang werden die Feldabhängigkeit der Resonanzfrequenzen und die zeitliche Entwicklung der räumlichen Verteilung der dynamischen Magnetisierung dargestellt. Diese Ergebnisse offenbaren Modenhybridisierungen mit Moden höherer Ordnung in der gekippt konischen und der Skyrmion-Gitter Phase. Die berechneten Mikrowellenspektren werden schließlich mit den experimentellen Spektren verglichen, die von Mitarbeitern unserer Gruppe bereitgestellt wurden. Es zeigt sich eine gute Übereinstimmung zwischen diesen.

Im zweiten Teil werden die Moden-Wechselwirkungen zwischen den Skyrmion-Gitterresonanzen genauer untersucht. Es konnte gezeigt werden, dass die kubische magnetokristalline Anisotropie eine auf der Symmetrie und Polarisation der wechselwirkenden Moden basierende Auswahlregel vermittelt. Zur Charakterisierung der Hybridisierungsstärke wird die minimale Frequenzlücke zwischen den wechselwirkenden Resonanzzweigen aus den berechneten Mikrowellenspektren für zwei verschiedene Probenformen entnommen. Die erhaltene Lückengröße als Funktion der Stärke der kubischen magnetokristallinen Anisotropie K nimmt linear zu und ist unabhängig von der Probenform. Diese Ergebnisse werden schließlich mit experimentellen Daten verglichen, die von Mitarbeitern verschiedener Gruppen zur Verfügung gestellt wurden. In den Experimenten wird eine lineare Abhängigkeit von der Temperatur beobachtet, die Frequenzlücke ist jedoch um einen Faktor von etwa 2-3 größer. Um diesen Unterschied zu erklären, wird das Energie Funktional durch die Austauschanisotropie ergänzt. Es wurde festgestellt, dass die Lückengröße als Funktion der Austauschanisotropiekonstante C im Fall von $C > 0$ zunimmt und im Fall von $C < 0$ zunächst abnimmt und

dann wieder zunimmt.

Der letzte Teil umfasst winkel- und temperaturaufgelöste Mikrowellen Spektroskopie Experimente an einer quaderförmigen und einer kugelförmigen Probe. Die zu messenden Größen sind die Resonanzen in der feldpolarisierten Phase und das kritische Übergangsfeld H_{c2}. Die Messungen zeigen eine dominante zwei- und vierfache Symmetrie für die Resonanzen und eine vierfache Symmetrie für die zweite Größe, H_{c2}. Während die vierfache Symmetrie hauptsächlich auf die kubische magnetokristalline Anisotropie zurückzuführen ist, wird die zweifache Symmetrie auf die dipolaren Wechselwirkungen zurückgeführt. Diese werden berücksichtigt, indem die Bildung stehender Spinwellen anstelle einer gleichmäßigen Anregung der Magnetisierungsdynamik in Betracht gezogen wird. Durch Anpassung der analytisch hergeleiteten Gleichungen an die experimentellen Daten wird eine kontinuierliche Abnahme von K als Funktion der Temperatur extrahiert. Der Vergleich der extrahierten K-Werte, die zum einen aus den Resonanzen in der feldpolarisierten Phase und zum anderen aus H_{c2} gewonnen wurden, zeigt einen endlichen Unterschied. Dies deutet darauf hin, dass ein zusätzlicher vierfacher Symmetriebeitrag, wie die Austauschanisotropie, im Energie Funktional fehlt. Die Austauschanisotropiekonstante, die sich aus der nachfolgenden Analyse ergibt, stimmt gut mit derjenigen überein, die in der vorangegangenen numerischen Behandlung angenommen wurde, um den Unterschied in der Größe der Hybridisierungslücke zu kompensieren. Daraus lässt sich schließen, dass sowohl die kubische magnetokristalline als auch die Austauschanisotropie die Hauptbeiträge zu den Moden-Moden-Wechselwirkungen darstellen.

Contents

Contents

Introduction

The research field of magnonics, a neologism originating from the quantized excitations of spin waves (magnons), addresses the collective spin excitations in micro- and nanostructured logic and memory devices in form of spin waves. The foundation on which this area of research builds on are the wave like properties of magnetization dynamics. In analogy to light and sound waves, diffraction [Bir09; Man12; Grä20], refraction and reflection [Gie14; Sti16; Hio20], interference [Cho06; Per08; Pir11; Ber20; Pap21] and Doppler [Vla08; Cha14] effects are observed, just to name a few. Exploiting these characteristics allows to manipulate and steer spin waves in a controlled manner [Sch10; Dem11; Jam13; Gie13; Gru16; Kör17; Vog18; Zha19]. Despite many materials allow to study magnonic effects, the probably most important one is the insulating ferrimagnet yttrium iron garnet $Y_3Fe_5O_{12}$ (YIG) [Ser10]. Due to its ultra low magnetic damping $\alpha = 2.7(5) \times 10^{-5}$ [Kli17], which is the up to that the day record value, long life time and propagation distance of the magnons are observed. The insight gained into the general wave properties can nevertheless ultimately be applied to different materials. The research in the field of magnonics is, besides the interest in the fundamental physical procedures, mainly driven by the potential implementation in data processing devices [Chu17; Mah20]. The aim in this regard is to transfer, process and store information using spin waves as respective carriers. Towards conventional electronics, the encoding of information in angular momentum instead of electron charges enables to circumvent Joule heating and lowers the energy costs in general [Chu14]. In order to exploit the characteristics of spin waves for application in devices, the respective wave lengths should be reduced to values smaller than $100\,\mathrm{nm}$ [Chu15]. Since an efficient excitation of magnons by microwave antennae in this wave length regime, however, requires their dimensions to be also on the same length scales, the limits of feasibility are gradually reached. A workaround to bypass these constraints is the creation of a periodic modulation of the magnetization structure, for instance, by etching or depositing nanodots in the material [Tac12; Yu16]. In analogy to photonic crystals, these devices are referred to as magnonic crystals [Gul01]. Based on the tremendous amount of publications in this field, a vast number of review papers have been published in the last decade [Neu09; Kru10; Len11; Kra14;

Nik15; Chu17; Bar21].

An intrinsically periodic modulation of the magnetization properties in form of spin spirals or skyrmion lattices is found in a multitude of materials. Magnetic skyrmions are vortex-like spin swirls with particle-like character. The nanometer sized magnetic textures [Hei11] as well as the chiral magnetization configuration, in general, originate from the competition between several energy contributions [Nag13]. The ones which are responsible for the spin twisting in the material investigated in the framework of this thesis are the isotropic and anisotropic exchange interactions, the latter is also referred to as Dzyaloshinsky-Moriya interaction (DMI). An important property of skyrmions is the topological nature, which is characterized by their topological winding number. Since a continuous deformation from one magnetization configuration into another is prohibited in the case the respective winding numbers do not accord, skyrmions are said to be topologically protected [Nag13]. They are therefore relatively stable and exhibit a long lifetime. The findings of an, in general, chiral magnetic texture opened up a new, intriguing research field in physics. In the past years, different kind of skyrmions [Bac20], nucleation and annihilation processes [Jia15; Büt17], interactions with applied currents [Zha15a; Doh19; Yu20; Pen21] and generic magnetization excitations [Gar17], in particular interactions with magnons [Moc14; Iwa14; Lin14; Kov14; Sch14; Zha17], were subject to intensive studies, just to name a few. Additionally, the investigations are not just limited to the skyrmion host itself but are also extended to heterostructures [Ran21] and also hybrid systems with topological insulators and superconductors [Sou16; Vad18; Che19b; Div22], which promise interesting phenomena. A comprehensive summary of the state of the art in this research area is provided in [Bac20]. Besides fundamental research, skyrmions also attract interest in regard of applications in practical devices. Against the background of their size, stability and mobility [Sch12; Yu12], skyrmions are treated as potential candidates to be implemented in devices like a race track memory as information carriers [Fer13; Sam13; Iwa13; Mül17; Che19a; Wan19].

A specific class of these magnetic materials are the chiral magnets, which exhibit a non-centrosymmetric cubic crystal structure with space group $P2_13$ [Sch15]. Its elements share the same rich phase diagram, which comprises spin spirals with a perpendicular (helical) or canted alignment (conical) of the individual spins with respect to the pitch vector, a collinear alignment of the magnetization (field-polarized phase) and a skyrmion lattice [Müh09]. Regarding the electrical conductivity, all three groups, namely metals, semiconductors and insulators are represented in this class [Sch15]. The skyrmion hosting material investigated in this thesis is the insulating ferrimagnet copper-oxo-selenite Cu_2OSeO_3 (CSO). The bulk material, which is a member of the chiral magnet family, stands out for its very low magnetic damping of approximately $\alpha = (9.9 \pm 4.1) \times 10^{-5}$ at $5\,K$ [Sta17b], a value very close to the one observed in yttrium iron garnet. In addition to that,

with the recent observation of the tilted conical phase [Fen18] and more importantly a second, independent skyrmion lattice phase at low temperatures by Chacon *et al.* [Cha18] via small angle neutron scattering, further peculiarities could be found. For this reasons, the up to that point already extensively studied ferrimagnet attracted again a lot of attention. Compared to its counterpart close to T_c, the low temperature skyrmion phase extends over a wide field and temperature pocket, which leads to a lower sensitivity against fluctuations in these parameters. Finally, the combination with the low damping makes CSO an interesting candidate for studying the propagation characteristics of spin waves in all phases [Sek16; Sek20; Oga21], the interaction between magnons and skyrmions [Moc14; Iwa14; Lin14; Kov14; Sch14; Zha17] and the coupling to photons [Abd19; Kha21].

The mechanism, stabilizing these additional phases at low temperatures, is identified by numerical calculations to originate from the coupling to the underlying cubic lattice [Cha18]. In particular, it could be shown that the cubic magnetocrystalline anisotropy alone is sufficient to reduce the energy of the skyrmion lattice with respect to the other phases, making it the ground state of the system. Additional anisotropy terms might also play a non-negligible role in this regard, but their contributions can not be uniquely determined without further input from the experimental side. In this study only the effect on the magnetization configuration is investigated. The induced changes in the magnetization dynamics, however, remain unresolved. To this end, this thesis focuses on the numerical and experimental investigation of the collective spin excitations in the helimagnet CSO in presence of a cubic magnetocrystalline anisotropy. The results comprise on the one hand numerical calculations, which build on the previously established model [Müh09; Sch15], and on the other hand broadband microwave spectroscopy experiments, which already proved to be a novel technique to resolve the microwave absorption spectra [Ono12; Sch15].

This thesis is divided into three parts. In the first part, Part I, fundamental aspects are presented. In Chap. 1 the framework of micromagnetism is elaborated, which comprises the introduction of the relevant quantities, namely magnetization, energy contributions and effective field. In the second chapter Chap. 2, the equation of motion of magnetization dynamics is covered. The experimental setup in order to excite and detect the magnetization dynamics is introduced in Chap. 3. Here, two techniques of performing microwave spectroscopy experiments are presented.

The second part of this thesis, Part II, addresses the main focus of this work, namely the spin excitations in the insulating chiral magnet Cu_2OSeO_3. First, a general introduction of chiral magnets is given in Chap. 4. Subsequently, a more detailed description of the characteristics of one of its members, Cu_2OSeO_3, the material investigated in this study, will be presented in Chap. 5. In order to account for the eigenstates and eigenvalues of the magnetization dynamics of this particular group of magnets, the Ginzburg-

Landau model and the Landau-Lifshitz equation of motion are employed. The framework of the numerical model is presented in the following chapter, Chap. 6. Finally, in Chap. 7 the theoretical and experimental results are discussed. This chapter is structured as follows: Based on the findings reported in [Cha18], the resonance modes of the helical/conical, tilted conical, field polarized and skyrmion lattice phases are calculated numerically in presence of the cubic magnetocrystalline anisotropy. The results are presented in the first section. In these calculations mode hybridizations in the tilted conical and skyrmion lattice phase are observed. In the second section of this chapter, these interactions will be analyzed in more detail for the skyrmion lattice phase. The last part comprises the measurements of the angle and temperature resolved resonance conditions. The experimental results are accompanied by analytical and numerical calculations. Finally, this thesis concludes with a summary of the main results, which is presented in Chap. 8. Additional information is given in the appendix, which is the third part, Part III.

Part I

Preliminaries

Chapter 1

Introduction

In this chapter a short introduction of the quantity of interest, the magnetization, and the important interactions, it is subject to, will be presented. This small summary is based on the detailed description found in several textbooks [Blu01][Coe10][A H09] which for the interested reader we are referring to. The energy landscape, the sum of the individual interaction terms, which finally determines the physical properties of the magnetization, strongly depends on the material investigated. It is therefore not discussed here, but will be presented in regard of the Ginzburg-Landau model in the corresponding chapter in great detail.

1.1 Magnetization and magnetic field

The magnetization $\boldsymbol{M}$ is defined as the magnetic moment density [A G96]

$$\boldsymbol{M}(\boldsymbol{r}, t) = \frac{1}{\Delta V} \sum_{\Delta V} \boldsymbol{\mu}, \tag{1.1}$$

given in the unit volume ΔV. Despite the discrete nature of the magnetic moments $\boldsymbol{\mu}$, which are connected to the spin of the electrons and the nuclei, the magnetization is assumed to be a continuous differentiable vector field. This approximation is based on the strong exchange forces between neighboring magnetic moments, leading to an almost parallel alignment in a ferromagnet. Since the angle between the moments varies on length scales significantly larger than the atomic lattice spacing, this assumption is justified and the magnetization can be treated in a classical approach.

For temperatures below the Curie temperature T_c, the absolute value of the magnetization is assumed to be equal to the saturation magnetization, $|\boldsymbol{M}(\boldsymbol{r}, t)| = M_s(T)$ at every position in the sample. It is defined as the state of fully aligned magnetic moments. The critical temperature T_c strongly depends on the material investigated. While, for instance, in the case of ferrimagnet $Y_3Fe_5O_{12}$ (YIG) ($T_c > 550\,\mathrm{K}$ [Ars18]) measurements can be

conducted at room temperature, in the case of Cu_2OSeO_3 (CSO), the sample has to be cooled down to at least $T_c = 58\,\text{K}$ [Ono12].

In free space the relation between the two magnetic fields $\boldsymbol{B}$ and $\boldsymbol{H}$ is given by the linear relation,

$$\boldsymbol{B} = \mu_0\boldsymbol{H}. \tag{1.2}$$

The prefactor μ_0 entering the equation is the permeability constant of the vacuum. In the presence of a magnetic sample, its magnetization has to be included in the equation above, yielding

$$\boldsymbol{B} = \mu_0(\boldsymbol{H} + \boldsymbol{M}). \tag{1.3}$$

Since $\boldsymbol{M}$ and $\boldsymbol{H}$ are not necessarily correlated, the magnetic fields are no longer parallel. Assuming, however, a linear dependence on the magnetic field $\boldsymbol{H}$, the magnetization can be written in the form

$$\boldsymbol{M} = \chi\boldsymbol{H} \tag{1.4}$$

with the dimensionless quantity χ, which is referred to as magnetic susceptibility. Inserting this expression in Eq. 1.3, results in

$$\boldsymbol{B} = \mu_0(1 + \chi)\boldsymbol{H}. \tag{1.5}$$

It should be noted, that in the context of dipolar interactions, the fields within and outside of the boundaries of the magnetized body, have to be distinguished. Further information regarding the difference will be elaborated in Sec. 1.2.2.

1.2 Energy contributions

1.2.1 Exchange interaction

A generic form of the interaction between two spins $\boldsymbol{S}_i$ and $\boldsymbol{S}_j$ on the respective lattice sites i and j is given by [Udv03]

$$\mathcal{H} = \boldsymbol{S}_i\boldsymbol{\mathcal{J}}_{i,j}\boldsymbol{S}_j, \tag{1.6}$$

with the 3×3 interaction matrix $\boldsymbol{\mathcal{J}}_{i,j}$. This interaction matrix, in turn, can be divided into an isotropic and anisotropic contribution, while the latter consists of a symmetric and antisymmetric term.

Isotropic exchange interaction
The isotropic exchange interaction, which is mostly referred to as exchange interaction only, in the literature, is the origin of the order of the magnetic moments, as anticipated before. This strong but short ranging phenomena is of quantum mechanical nature, originating from the interplay of the

Coulomb interaction and the Pauli principle. For simplicity, the interaction is often limited to the next neighbor interaction and given in the established form, denoted as Heisenberg Hamiltonian [Coe10],

$$\mathcal{H} = -2\sum_{i<j} J_{i,j}\boldsymbol{S}_i\boldsymbol{S}_j. \tag{1.7}$$

Assuming the interaction to not depend on the lattice site, $J_{i,j}$, the measure of the interaction strength, is considered to be isotropic $J_{i,j} = J$. Depending on the sign of J, minimization of the Hamiltonian leads either to a parallel ($J > 0$) or an anti parallel alignment ($J < 0$) of the magnetic moments [Blu01] [A H09]. Based on the approximation, that the angle between neighboring spins is small allows for the sum over all lattice sites to be converted into a continuous model. The resulting energy density reads,

$$F_{\text{ex}}[\boldsymbol{M}] = \frac{A}{M_{\text{s}}^2}\left((\boldsymbol{\nabla} M_x)^2 + (\boldsymbol{\nabla} M_y)^2 + (\boldsymbol{\nabla} M_z)^2\right) \tag{1.8}$$

with exchange stiffness constant A. Deviations from a uniform alignment are penalized by the gradient terms, leading to an increase of the energy in the system.

Ansiotropic exchange interaction
The second exchange interaction to be considered is the antisymmetric anisotropic exchange, which can be found in systems with a broken inversion symmetry and strong spin orbit coupling. Due to their contributions, this interaction is nowadays also referred to as Dzyaloshinsky-Moriya interaction (DMI) [Dzy58; Mor60]. Its general form is given by,

$$\mathcal{H} = \sum_{i,j} \boldsymbol{D}_{i,j} \cdot \boldsymbol{S}_i \times \boldsymbol{S}_j. \tag{1.9}$$

In contrast to the isotropic exchange interaction, the DMI favors perpendicular orientation of the neighboring spins, in order to minimize its energy contribution. Depending on the symmetry of the system, the vector $\boldsymbol{D}_{i,j}$ is aligned either parallel or perpendicular to the distance vector, connecting lattice site i and j. The two cases distinguished are the bulk DMI, emerging in bulk crystals without inversion center, and the interface DMI, arising due to a lack of symmetry at the interfaces and surfaces. Using the same argument above, the discrete nature of the lattice can be ignored and the Hamiltonian is expanded in a Taylor series, resulting in the continuous form,

$$F_{\text{DM}}[\boldsymbol{M}] = D\boldsymbol{M}(\boldsymbol{\nabla} \times \boldsymbol{M}), \tag{1.10}$$

in the case of bulk DMI. The Dzyaloshinsky-Moriya interaction plays an important role in the case of chiral magnets like Cu_2OSeO_3. Due to the

competition between the isotropic and anisotropic exchange, the formation of spin helices and skyrmions arises. The third term, anisotropic symmetric exchange interaction, is symmetric under the exchange of both interacting spins. Its strength depends on the spin orientation relative to the distance vector between the lattice sites i and j. Based on its small magnitude compared to the isotropic exchange interaction, its contribution is often neglected [Sko05] and therefore it is not taken into account in the theoretical model, discussed in this thesis.

1.2.2 Dipolar interaction

The energy contribution, resulting from the magnetic dipole-dipole interaction between two magnetic dipoles $\boldsymbol{\mu_1}$ and $\boldsymbol{\mu_2}$ separated by the distance vector $\boldsymbol{r} = \boldsymbol{r}_1 - \boldsymbol{r}_2$ reads [Blu01],

$$E_{\mathrm{DD}} = \frac{\mu_0}{4\pi r^3}\Big(\boldsymbol{\mu_1} \cdot \boldsymbol{\mu_2} - \frac{3}{r^2}(\boldsymbol{\mu_1} \cdot \boldsymbol{r})(\boldsymbol{\mu_2} \cdot \boldsymbol{r})\Big). \tag{1.11}$$

Compared to the previously introduced exchange energy, the dipolar interaction is a rather long ranging but weak interaction. Due to the order of magnitude of this contribution, it alone would be therefore not sufficient enough to stabilize magnetic order in many magnetic materials [Blu01]. Seen from a macroscopic view, the magnetic field arising from all the individual microscopic dipoles is determined by the magnetic induction Eq. 1.3 and the Maxwell equation $\boldsymbol{\nabla B} = 0$ and results in the representation,

$$\boldsymbol{\nabla H}_{\mathrm{D}} = -\boldsymbol{\nabla M}. \tag{1.12}$$

This induced field is aligned anti parallel with respect to the magnetization and is therefore referred to as demagnetizing field. The presence of $\boldsymbol{H}_{\mathrm{D}}$ can be visualized in terms of magnetic charges in the volume and at the surface of the magnetic sample. While the charges in the volume cancel each other, the ones at the surface remain uncompensated due to the reduced symmetry at the boundaries, leading to the finite divergence of the magnetization. The energy density contribution arising from this effect is given by [Blu01],

$$F_{\mathrm{DD}}[\boldsymbol{M}] = -\frac{1}{2}\mu_0 \boldsymbol{H}_{\mathrm{D}}\boldsymbol{M} \tag{1.13}$$

which is integrated over the samples volume. In general, for an arbitrarily shaped sample, the calculation of the demagnetizing field is quite complicated due to its complex dependence on the position. In the special case of an ellipsoid, however, the magnetization and the resulting demagnetizing field are homogeneous, which reduces their correlation to the linear equation

$$\boldsymbol{H}_{\mathrm{D}} = \boldsymbol{N M} \tag{1.14}$$

with the 3×3 demagnetization tensor $\boldsymbol{N}$. If the Cartesian coordinate system (x, y, z) is aligned with respect to the principal axes of the ellipsoid, the demagnetization tensor can even be simplified to a diagonalized representation. Note, the entries of $\boldsymbol{N}$, the demagnetization factors, are governed by the constraint $\mathrm{tr}(\boldsymbol{N}) = 1$. Since they depend on the dimension ratios of the sample, this energy contribution is also referred to as shape anisotropy.

Due to the magnetization of the sample, the magnetic fields within and outside the material have to be distinguished. In the presence of an external field $\boldsymbol{H}_{\mathrm{ext}}$ the actual field within the solid, the internal field $\boldsymbol{H}_{\mathrm{int}}$, is given by the sum of both external and demagnetization field, reading,

$$\boldsymbol{H}_{\mathrm{int}} = \boldsymbol{H}_{\mathrm{ext}} + \boldsymbol{H}_{\mathrm{dem}}. \tag{1.15}$$

With the linear relation given for the external field, $\boldsymbol{B}_{\mathrm{ext}} = \mu_0 \boldsymbol{H}_{\mathrm{ext}}$, the internal magnetic induction $\boldsymbol{B}_{\mathrm{int}}$ is then written in the form,

$$\boldsymbol{B}_{\mathrm{int}} = \mu_0(\boldsymbol{H}_{\mathrm{int}} + \boldsymbol{M}) \tag{1.16}$$

$$= \mu_0(\boldsymbol{H}_{\mathrm{dem}} + \boldsymbol{M}) + \boldsymbol{B}_{\mathrm{ext}}. \tag{1.17}$$

1.2.3 Zeeman energy

The interaction between the magnetization and an externally applied field $\boldsymbol{H}_{\mathrm{ext}}$ is described by the Zeeman term, reading [A H09]

$$F_{\mathrm{Z}}[\boldsymbol{M}] = -\mu_0 \boldsymbol{H}_{\mathrm{ext}} \boldsymbol{M}. \tag{1.18}$$

This energy term is minimized by a parallel alignment of the magnetization with respect to the applied magnetic field.

1.2.4 Magnetic anisotropies

The last energy contribution to be considered, is the anisotropy governed by the underlying crystallographic structure. Arising from the interaction between the electron orbit and the crystal fields, the energetically favorable directions are related to the principal axes of the crystal lattice. As a consequence, the additional energy terms must therefore obey the symmetry of the system investigated. It should be noted that the anisotropy parameters are strongly temperature dependent. For experiments at low temperatures higher order terms might no longer be negligible and have to be taken into consideration.

Cubic magnetocrystalline anisotropy
In a cubic environment, the magnetocrystalline anisotropy to the lowest

order is written in the form [A G96]

$$F_{c0}[\boldsymbol{\alpha}] = K'\left(\alpha_1^2\alpha_2^2 + \alpha_2^2\alpha_3^2 + \alpha_3^2\alpha_1^2\right) \tag{1.19}$$

$$= \frac{K'}{2}\left(1 - \alpha_1^4 - \alpha_2^4 - \alpha_3^4\right), \tag{1.20}$$

with direction cosine vector $\boldsymbol{\alpha}$ [1]. The latter is defined as the projection of the magnetization on the crystallographic axes, denoted by the indices $i = \{1, 2, 3\}$. Assuming the principal axes of the sample to conform with the crystallographic axes, the representation of the anisotropy term chosen in this thesis is given by,

$$F_{c0}[\boldsymbol{M}] = \frac{K}{M_s^4}\left(M_x^4 + M_y^4 + M_z^4\right), \tag{1.21}$$

with $K = -\frac{K'}{2}$. Since the constant term does not have an effect on the equilibrium position and resonance condition of the magnetization, it will be omitted in the calculations. Depending on the sign of K, the magnetization tends to align either along the [100] ($K < 0$) or [111] ($K > 0$) direction.

Uniaxial anisotropy
In the case of ferromagnets with one preferred axis, the energy term, also referred to as uniaxial anisotropy is written in the form,

$$F_U = \frac{U}{M_s^2}\left(\boldsymbol{M} \cdot \hat{\boldsymbol{n}}_U\right)^2 \tag{1.22}$$

with the direction of the symmetry axis given by $\hat{\boldsymbol{n}}_U$. This additional term, exhibiting a twofold symmetry, results either in an easy axis ($U > 0$) or easy plane ($U < 0$) anisotropy, depending on the sign of U. It should be mentioned, that in thin magnetic films and multilayer systems, an in plane but also out of plane uniaxial anisotropy is often added to the energy functional, in order to take growth induced and interface effects into account [Far98; Wol04; Liu06; Hof10; Dec18].

Exchange anisotropy
Another anisotropy term, which will be taken into consideration in the theoretical analysis of CSO, is the exchange anisotropy,

$$F_{c1}[\boldsymbol{M}] = C\left((\partial_x M_x)^2 + (\partial_y M_y)^2 + (\partial_z M_z)^2\right). \tag{1.23}$$

This additional energy contribution is also allowed by the symmetry of the P2$_1$3 space group and was already included in the model by Bak and Jensen

---

[1] The components of the direction cosine vector are defined as $\alpha_i = M_i/M_s$. Here, index i refers to the crystal axes.

[Bak80]. In contrast to the cubic crystalline anisotropy, this term fixes the direction of the pitch vector, which reflects the orientation of the spin spirals. While for $C < 0$ the orientation along the [111] direction is energetically more favorable, for $C > 0$ the pitch aligns along the [100] direction. Further anisotropy terms following the symmetry requirements are presented in [Eve12], but will not be discussed in the course of this thesis.

1.3 Equilibrium position

Depending on the material investigated, the energy landscape consists of the sum of several energy contributions as listed above. Minimizing the resulting energy functional with respect to the magnetization allows to determine the ground state [A G96],

$$\delta_{\boldsymbol{M}} \int_V \sum_i F_i \, dV \overset{!}{=} 0. \tag{1.24}$$

The length of the magnetization is assumed to be constant in this approach, leaving the direction cosines as free variables. The variation of the energy functional leads to the so called Brown equation [Bro78; A G96; Aha01],

$$\boldsymbol{M} \times \boldsymbol{H}_{\text{eff}} = 0, \tag{1.25}$$

with the effective field defined as,

$$\boldsymbol{H}_{\text{eff}} = -\frac{1}{\mu_0} \frac{\delta F[\boldsymbol{M}]}{\delta \boldsymbol{M}}. \tag{1.26}$$

Here, $F[\boldsymbol{M}] = \sum_i F_i$, represents the sum over the respective energy contributions. The equilibrium condition Eq. 1.25 is fulfilled, if the magnetization is aligned parallel to the effective field. If the magnetization is deflected out of its equilibrium position, a torque acts on $\boldsymbol{M}$, leading to a precessional motion around $\boldsymbol{H}_{\text{eff}}$.

Chapter 2

Magnetization Dynamics

The investigation of the magnetization precession or dynamics, respectively, opens up the possibility to gain insights into the materials characteristics. Comparing the observed experimental data to the respective theoretical model, allows to extract the parameters of the individual interaction terms, contributing to the total energy functional. In this thesis the focus lies on the collective as well as the local response of the magnetization to an external driving field. Depending on the investigated regime, the experimental methods and theoretical model have to be adapted. Before introducing the established tools to excite and resolve its precessional motion in time and space in the following chapter Chap. 3, the equation of motion has to be derived.

The corresponding equation, which describes the temporal and spatial evolution of the magnetization, is called Landau-Lifshitz-Gilbert equation [Lan35; Gil55]. It is given by,

$$\frac{\mathrm{d}\boldsymbol{M}}{\mathrm{d}t} = \underbrace{-\gamma\mu_0\boldsymbol{M}\times\boldsymbol{H}_{\mathrm{eff}}}_{\text{precession}} + \underbrace{\frac{\alpha}{M_{\mathrm{s}}}\boldsymbol{M}\times\frac{\mathrm{d}\boldsymbol{M}}{\mathrm{d}t}}_{\text{damping}} \tag{2.1}$$

with gyromagnetic ratio $\gamma = \frac{ge}{2m_{\mathrm{e}}}$, Landé factor g, electron charge e, electron mass m_{e} and Gilbert damping parameter α. The time evolution of the magnetization is determined by the sum of a precession and a damping term. Deflected once out of the equilibrium position, the torque induced by the effective field, causes the magnetization to precess around the latter, as illustrated in Fig. 2.1 (a). Due to the order of magnitude of the prefactor $\gamma = 1.88 \times 10^{11}\,\mathrm{rad/sT}$ (obtained for Cu_2OSeO_3 [Sta17b]) and the saturation magnetization the resonance frequencies lie in the GHz regime for the materials investigated in this thesis. Introducing the additional damping term, with its strength given by the dimensionless parameter α, the magnetization is subject to a further torque pointing towards the equilibrium position. The resulting trajectory is therefore described by a spiral around

the effective field, indicated by the orange line in Fig. 2.1 (b). Unless not continuously driven by an external driving field, the magnetization therefore relaxes into the equilibrium state.
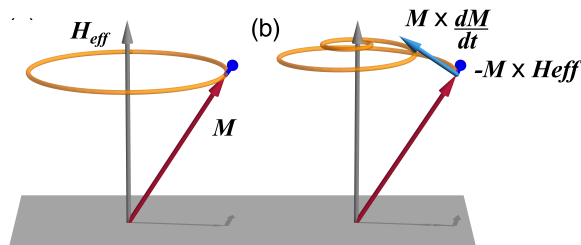
Figure 2.1: Trajectory (orange) of the magnetization vector (red) around its equilibrium position (gray). (a) Lossless precessional motion, driven by the precession term of Eq. 2.1 (dark blue). (b) Including the dissipative term, the magnetization is subject to an additional torque (light blue arrow), pointing towards the equilibrium position. The resulting magnetization trajectory is a spiral motion.

A general approach in order to solve the equation of motion, is to divide the magnetization into a homogeneous static and a dynamic part,

$$\boldsymbol{M} = \boldsymbol{M}_{\mathrm{s}} + \delta \boldsymbol{M}(t) \tag{2.2}$$

assuming, that the amplitude of the dynamic component is significantly smaller than the static one, $|\delta \boldsymbol{M}| \ll |\boldsymbol{M}_{\mathrm{s}}|$. Therefore, the change of the magnitude of $\boldsymbol{M}_{\mathrm{s}}$, caused by the precessional motion, is negligible, leaving $|\boldsymbol{M}_{\mathrm{s}}| = |\boldsymbol{M}| = M_{\mathrm{s}}$. For the dynamic component $\delta \boldsymbol{M}$, a plane wave ansatz is used,

$$\delta \boldsymbol{M}(t) = \delta \boldsymbol{M} \, e^{i(\boldsymbol{k}\boldsymbol{r} - \omega t)}, \tag{2.3}$$

exhibiting an explicit space and time dependence, characterized by the momentum vector $\boldsymbol{k}$ and resonance frequency ω, respectively. As already anticipated before, we investigate the collective and local magnetization dynamics. In the first case also called macrospin approximation, the neighboring spins are precessing with $\boldsymbol{k} = 0$ and therefore in phase. This case is referred to as ferromagnetic resonance (FMR). In the second case, the dynamic magnetization exhibits a finite wave vector, leading to a linear shift in phase between the neighboring spins. Therefore a wave, referred to as spin wave, propagates in the material. Both cases are illustrated in Fig. 2.2.

Depending on the orientation of magnetization, wave vector and surface normal, the spin waves exhibit different characteristics. For thin magnetic films a distinction is made between three main geometries: the Damon-Eshbach, backward volume and the forward volume geometry. They are defined as illustrated in Fig. 2.3. In the first two cases, the Damon-Eshbach and backward volume mode, the magnetization lies in plane. While $\boldsymbol{k}$ is

perpendicular to $\boldsymbol{M}_\mathrm{s}$ for the Damon-Eshbach geometry, the wave vector is aligned along the magnetization direction for the backward volume mode. For the last case, the magnetization is orientated perpendicular to the surface and the wave vector lies within the plane. This geometry is referred to as forward volume mode. Note, in the most general case, the angle between the wave vector and the magnetization direction takes on arbitrary values and is not just limited to these three geometries. Consequently this leads to a spin wave manifold, as it is shown for the case of an in plane applied magnetic field exemplary in [Bau15].
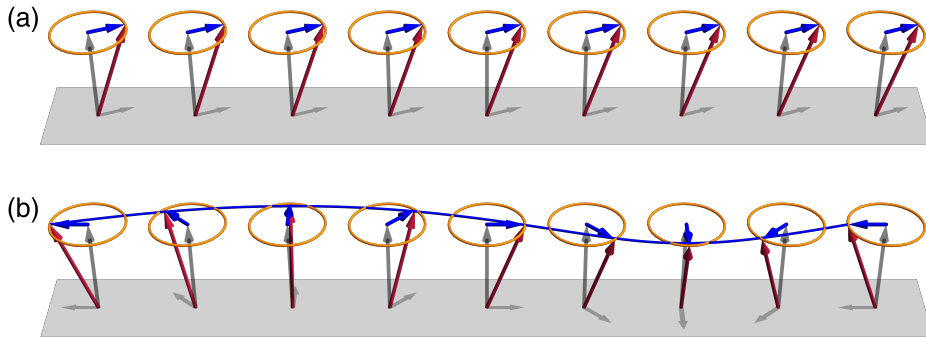
Figure 2.2: Sketch of a collective excitation for vanishing (a) and finite momentum $\boldsymbol{k}$ (b) at a certain time t.
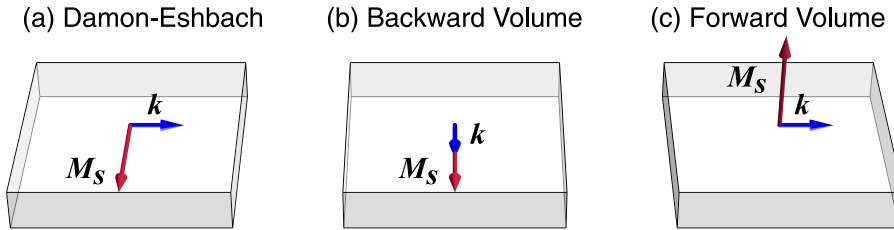
Figure 2.3: Sketch of the three main spin wave geometries. (a) Damon-Eshbach, (b) Backward volume (c) Forward volume

In order to solve the equation of motion, the effective field of the system investigated has to be calculated by means of Eq. 1.26. In this regard, the corresponding energy terms have to be determined first. After inserting the ansatz for the magnetization (Eq. 2.2) into the effective field, the latter is expanded up to the first order in $\delta\boldsymbol{M}$, leading to

$$\boldsymbol{H}_\mathrm{eff} \approx \boldsymbol{H}_\mathrm{eff}^0 + \boldsymbol{H}_\mathrm{eff}^1. \tag{2.4}$$

Here, the effective field is divided into two terms containing $\delta\boldsymbol{M}$ either to zeroth or first order, respectively, as indicated by the indices. Plugging

now the magnetization Eq. 2.2 and the approximation for the effective field Eq. 2.4 into the Landau Lifshitz equation Eq. 2.1 and keeping only terms linear in $\delta \boldsymbol{M}$, yields,

$$\frac{\mathrm{d}\delta \boldsymbol{M}(t)}{\mathrm{d}t} = -\gamma \Big(\delta \boldsymbol{M}(t) \times \boldsymbol{H}_{\mathrm{eff}}^0 + \boldsymbol{M}_{\mathrm{s}} \times \boldsymbol{H}_{\mathrm{eff}}^1 \Big) + \frac{\alpha}{M_{\mathrm{s}}} \boldsymbol{M}_{\mathrm{s}} \times \frac{\mathrm{d}\delta \boldsymbol{M}(t)}{\mathrm{d}t}. \quad (2.5)$$

Using the explicit time dependence of the dynamic component given in Eq. 2.3, the equation can then be written as, [1]

$$-\mathrm{i}\,\omega\,\delta \boldsymbol{M} = -\gamma \Big(\delta \boldsymbol{M} \times \boldsymbol{H}_{\mathrm{eff}}^0 + \boldsymbol{M}_{\mathrm{s}} \times \boldsymbol{H}_{\mathrm{eff}}^1 \Big) - \mathrm{i}\omega \frac{\alpha}{M_{\mathrm{s}}} \boldsymbol{M}_{\mathrm{s}} \times \delta \boldsymbol{M}. \quad (2.6)$$

Rearranging this formula, we introduce the vector $\mathcal{W}$, parameterizing the sum of all contributions,

$$0 = \underbrace{\mathrm{i}\,\omega\,\delta \boldsymbol{M} - \gamma \Big(\delta \boldsymbol{M} \times \boldsymbol{H}_{\mathrm{eff}}^0 + \boldsymbol{M}_{\mathrm{s}} \times \boldsymbol{H}_{\mathrm{eff}}^1 \Big) - \mathrm{i}\omega \frac{\alpha}{M_{\mathrm{s}}} \boldsymbol{M}_{\mathrm{s}} \times \delta \boldsymbol{M}}_{\mathcal{W} :=}. \quad (2.7)$$

Due to the linear dependence on $\delta \boldsymbol{m}$, Eq. 2.7 can be simplified by the equation system [A G96; Wai17]

$$0 = \mathcal{W}' \, \delta \boldsymbol{M} \quad (2.8)$$

with matrix $\mathcal{W}'$ defined as,

$$\mathcal{W}' := \begin{pmatrix} \partial_{\delta M_x} \mathcal{W}_x & \partial_{\delta M_y} \mathcal{W}_x & \partial_{\delta M_z} \mathcal{W}_x \\ \partial_{\delta M_x} \mathcal{W}_y & \partial_{\delta M_y} \mathcal{W}_y & \partial_{\delta M_z} \mathcal{W}_y \\ \partial_{\delta M_x} \mathcal{W}_z & \partial_{\delta M_y} \mathcal{W}_z & \partial_{\delta M_z} \mathcal{W}_z \end{pmatrix}. \quad (2.9)$$

Since Eq. 2.8 has to be fulfilled for every $\delta \boldsymbol{M}$, the determinant of $\mathcal{W}'$ has to vanish,

$$\mathrm{Det}[\mathcal{W}'] \overset{!}{=} 0. \quad (2.10)$$

Starting from the Landau Lifshitz Gilbert equation Eq. 2.1, the search for the resonance frequencies amounted to the solution of Eq. 2.10 for ω. Depending on the orientation of $\boldsymbol{M}_{\mathrm{s}}$ and $\delta \boldsymbol{m}$, respectively, $\mathcal{W}'$ can even be reduced to a 2×2 matrix.

Keeping only terms linear in α, results in general in three solutions for ω. Due to the dissipative contribution, these are complex numbers, divided into real and imaginary part,

$$\omega = \mathrm{Re}(\omega) + \mathrm{i}\,\mathrm{Im}(\omega) \quad (2.11)$$

From the real part of ω, $\mathrm{Re}(\omega) = 2\pi f(\boldsymbol{k})$, we obtain the dispersion relation, describing the evolution of the resonance frequency f as a function of wave

---

[1] For simplicity, the effective field $\boldsymbol{H}_{\mathrm{eff}}^1 := \boldsymbol{H}_{\mathrm{eff}}^1 / e^{i(\boldsymbol{k}\boldsymbol{r} - \omega t)}$ was redefined.

vector $\boldsymbol{k}$ at a fixed external field $\boldsymbol{H}_{\text{ext}}$.

Furthermore, the dispersion relation allows to calculate the group velocity, given by

$$\boldsymbol{v}_{\text{gr}} = \frac{\partial}{\partial \boldsymbol{k}} \text{Re}(\omega) = 2\pi \frac{\partial f}{\partial \boldsymbol{k}}. \tag{2.12}$$

It should be mentioned, that $\boldsymbol{v}_{\text{gr}}$ is in general not necessarily aligned with the wave vector, but adjusts its direction, depending on the orientation of $\boldsymbol{k}$ with respect to $\boldsymbol{M}_{\text{s}}$. Considering the main spin wave geometries, $\boldsymbol{v}_{\text{gr}}$ is aligned parallel, antiparallel and parallel to $\boldsymbol{k}$, for the Damon-Eshbach, backward volume and forward volume modes.

The imaginary part of ω is identified as the reciprocal relaxation time τ,

$$\text{Im}(\omega) = \frac{1}{\tau}. \tag{2.13}$$

Using additionally the expression for the group velocity, the attenuation length can be calculated accordingly,

$$L_{\text{att}} = v_{\text{gr}}\tau = \frac{v_{\text{gr}}}{\text{Im}(\omega)}. \tag{2.14}$$

Depending on the type of experiment conducted, the introduced quantities can be extracted from the obtained data. Since, as already stated, FMR and spin wave spectroscopy are covered in this thesis, a more detailed description will be given in the corresponding chapters.

Chapter 3

Experimental Techniques

3.1 Generation of a Microwave Driving Field

In order to excite magnetization dynamics continuously, the sample has to be subject to an external oscillating field. A basic approach to generate this alternating magnetic field in the desired frequency range is to drive a radio frequency current through a conductive material, serving as a waveguide. The magnetization couples to this driving field, resulting in a precessional motion of the former. Depending on the experiment, the design of this waveguide has to be chosen properly. A widely used approach is the shorted coplanar wave guide (CPW) [Bai03; Vla08; Bau14; Sti16], also referred to as antenna throughout this thesis. It consists of one signal and two ground lines, as shown in Fig. 3.1 (a). The crucial parameters of the antenna are the widths w_s and w_{gr} and the gap between the ground and signal line w_g. Assuming the conducting leads to be infinitely long, the generated magnetic field can be calculated by the 2D Biot-Sarvart law [Coe10]. The resulting alternating field for the design presented in Fig. 3.1 (a) is given in Fig. 3.1 (b) as a function of position. It consists of a symmetric in plane (red) and asymmetric out of plane (blue) component. While the in plane component is localized around the ground and signal lines, the out of plane driving field reaches its maximum strength within the gap. It should be mentioned that the calculation of the Biot-Saravat law was performed with a spatially independent current density. Due to the skin effect, which needs to be taken into account for an oscillating current, the current density is inhomogeneously distributed within the the transmission lines and is required to be calculated numerically using commercial software [Obs15; Här16]. The generated excitation field consequently differs from the approximated results presented in Fig. 3.1. The excitation efficiency strongly depends on the orientation of the magnetization with respect to the driving field direction. Since the alternating field exerts a torque on the magnetization, its strength is maximized by a perpendicular orientation of the latter with respect to the individual driving

field components. This is realized by saturating the magnetization along the antenna lines, since both in and out of plane driving field contribute to the magnetization excitation. On the basis of their different symmetry characteristics with respect to the center of the signal line, the excitation efficiency, however, depends on the side of the antenna considered. As it is shown in Fig. 3.1 (b), while the in plane oscillating field is symmetric in x, the out of plane component is antisymmetric in x. It follows that due to the superposition of both driving field components, on one side the excitation efficiency is enhanced, while it is reduced on the other side. This is know as amplitude non-reciprocity.

An important characteristic of the driving field is the excitation efficiency as a function of wave vector length $|\boldsymbol{k}|$. Since the wave vector of the driving field and the spin wave excited are directly correlated, the design of the antenna has to be chosen in accordance with the wave vector range under investigation. The distribution in momentum space is determined by calculating the fast Fourier transformation (FFT) of the excitation field. The normalized FFT of the in plane field is illustrated in Fig. 3.1 (c). From the distance between the center of the ground lines, $d = w_{\mathrm{s}} + w_{\mathrm{gr}} + 2w_{\mathrm{g}}$, the peak position of the first maximum can be estimated. As the dimensions of the antenna are likewise in the micrometer regime, it is usually fabricated directly on top of the magnetic film samples via optical lithography. In the case of a lamella-shaped sample, a preparation technique which is recently frequently employed for bulk crystals like CSO, the CPW is structured on top of a substrate and the lamella is placed on top of the antenna.

In addition to the width parameters of the antenna, introduced before, also the periodicity of the structure influences the line shape of the excitation spectrum. Increasing the repetition in a meander-like manner [Vla08] decreases the line width in momentum space, while using only one stripe line, leads to a broader range of the excited wave vectors. Depending on the purpose of the experiment, either a narrow or broad excitation spectrum might be advantageous: while for applications in the information technology a selective excitation of spin waves might be required, the characterization of a sample via the detection of the dispersion relation demands the full range of wave vectors.

For a homogeneous excitation of the magnetization dynamics, a spatially independent driving field is required. In these FMR experiments the dimensions of the CPW are extended to the millimeter regime and the samples are mounted face down on top of the wave guide. By placing the device either on the signal line or on the gap, the excitation geometry with respect to the magnetization direction can be chosen selectively. This results in a more dominant in plane or out of plane excitation, as illustrated in the spatial dependence of the driving field components shown in Fig. 3.1 (b). Since the chiral magnet CSO exhibits various types of modes, which are excited by both, alternating fields perpendicular and parallel to the magnetization

direction, the excitation geometry will play an important role.

3.2 Broadband FMR Spectroscopy

In the following, the well established measurement technique, namely absorption FMR, which is used for the indirect detection of magnetization dynamics, will be introduced. In this approach the magnetization is brought into resonance by sweeping either the external field or excitation frequency while the remaining parameter is set to be constant. The precessional motion, in turn, leads to a variation of the magnetic flux and an induced voltage in the metallic leads of the coplanar waveguide [Bil07a; Sch13; Sta16]. With this the transmission characteristics are altered. This change of transmission, reflecting the absorbed power by the magnetic sample, is then recorded as a function of the swept parameter. By analyzing the extracted line scans, finally, conclusions can be drawn on the properties of the material investigated. In the following two implementations, exploiting the concept of the absorption FMR, are distinguished.

3.2.1 Frequency Domain

In the first method, the measurements are performed in the frequency domain, sweeping the driving frequency while the external field strength is set to a constant value. This approach is advantageous for studying complex magnets like helimagnets, since it allows to stay in a certain temperature and field pocket while resolving the resonance conditions. The important device undertaking this task is the vector network analyzer (VNA), which simultaneously acts as a source and detector of the sinusoidal current. With a frequency range from $45\,\text{MHz}$ to $20\,\text{GHz}$ (Agilent PNA E8362A) a wide spectrum of the resonances of the material investigated in this thesis is covered. As illustrated in the schematic Fig. 3.2, the respective ports 1 and 2 of the VNA are connected to the device under test, which is given by the CPW and the sample placed face down on the latter. Note, in this case not a shorted CPW is employed. The whole assembly, which is mounted on a sample holder within the cryostat, is subject to an uniform magnetic field, generated by a rotatable electromagnet. Since the critical temperature of CSO amounts to a value of around $58\,\text{K}$, the operation at low temperature and therefore of the cryostat is required. The quantity detected in the frequency scans is the amplitude of the complex scattering parameter S_{12}, which is proportional to the transmitted microwave power. Here the arrangement of the indices represents the emitting and detecting port, respectively. The implementation of the VNA in the absorption FMR setup is a already well-established technique and has been used for many years now. We therefore will not elaborate a detailed description of the functionality of
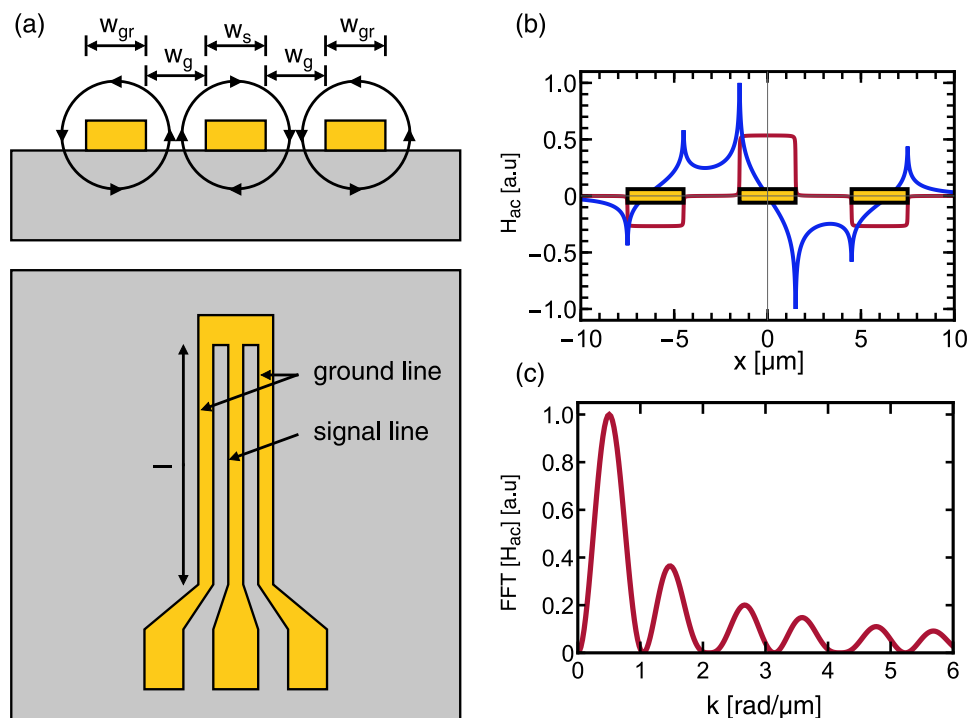
Figure 3.1: (a) Geometry of a shorted antenna on top of a substrate: front and top view. (b) Normalized in and out of plane driving field as a function of position x, drawn by red and blue lines. (c) Fast Fourier transformation of the out of plane driving field as a function of wave vector magnitude k.

the vector network analyzer and the data acquisition, but refer to [Bil07b; Bil07a; Neu06; Sch13; Sta16].

Since the recorded frequency traces are dominated by the transmission characteristics of the CPW and the whole setup, in general, the signal arising from the magnetization dynamics is not readily visible. On this account, two techniques aiming to remove the parasitic background are applied. The first one, the high field normalization, employs the difference between the dataset of interest $S_{12}(B)$ and an additional one $S_{12}(B_{\mathrm{ref}})$ obtained at a reference field B_{ref},

$$\Delta S_{12}(B) = S_{12}(B) - S_{12}(B_{\mathrm{ref}}). \qquad (3.1)$$

The latter is chosen high enough, so that in the given frequency range the line scan does not include any magnetic signal. It should be mentioned that, the background is often slightly field dependent and can therefore sometimes not be removed completely. Provided that the excitation field is homogeneous, the resulting resonance curve is expected to be of Lorentzian shape, as predicted by the calculations of the dynamic susceptibility [Cel97; Wol04; Kal06; Neu06; Dev13]. In reality, however, the experimental data is

often given by the combination of a symmetric ($\mathcal{F}_{\mathrm{L}}^{s}(f)$) and antisymmetric ($\mathcal{F}_{\mathrm{L}}^{a}(f)$) Lorentzian function [Cel97; Jos04; Wol04; Dec18],

$$
\begin{aligned}
A_{\mathrm{FMR}}(f) &\sim \mathcal{F}_{\mathrm{L}}^{s}(f)\cos\epsilon + \mathcal{F}_{\mathrm{L}}^{a}(f)\sin\epsilon \\
&\sim \frac{\Delta f \cos(\epsilon) + (f - f_0)\sin(\epsilon)}{\Delta f^2 + (f - f_0)}
\end{aligned}
\tag{3.2}
$$

which reflects the intermixing of the amplitude and dispersion [Jos04]. Here, f_0, Δf and ϵ describe the resonance position, line width and the mixing angle. This effect, which is observed for conducting but also insulating material might arise from the change of impedance of the CPW induced by the sample itself and should be taken into account for both experimental methods, the one utilizing the VNA and the one employing the lock in amplifier discussed below.

The second normalization technique, also referred to as derivative divide [Mai18], utilizes the difference quotient of neighboring data sets on the field axis,

$$
\delta S_{12}(B) = \frac{S_{12}(B + \Delta B) - S_{12}(B - \Delta B)}{S_{12}(B)},
\tag{3.3}
$$

with field step ΔB. It could be shown that this data manipulation in the field domain, in turn, results in a line shape in the frequency domain, which is then proportional to the derivative of Eq. 3.2 [Mai18].

3.2.2 Field Domain

In the second approach, the status of the external parameters is reversed, meaning that the excitation frequency is fixed, while the magnetic field strength is continuously swept. Instead of the vector network analyzer, a rf frequency generator and a Schottkey diode, which converts the transmitted rf current into a dc voltage, are integrated into the electrical circuit in order to generate and detect the oscillating current. For an improved signal-to-noise ratio, the extracted voltage is further processed by a lock-in amplifier. In order to allow the lock-in technique, the external field is superimposed by an additional small modulation field, which oscillates in the low-Hertz regime. As a consequences, the resulting field trace is therefore no longer proportional to the sum of a symmetric and antisymmetric Lorentzian function (analogous to Eq. 3.2), but to the sum of their derivatives with respect to H [Cel97; Wol04; Obs15; Dec18],

$$
A_{\mathrm{FMR}}(H) \sim \frac{-2(H - H_0)\Delta H \cos\epsilon + \left(\Delta H^2 - (H - H_0)^2\right)\sin\epsilon}{\left(\Delta H^2 + (H - H_0)\right)^2}
\tag{3.4}
$$

Here, H_0, ΔH and ϵ describe the resonance position, line width and the mixing angle. Note, this approximation only holds as long as the modulation field is small compared to the line with.
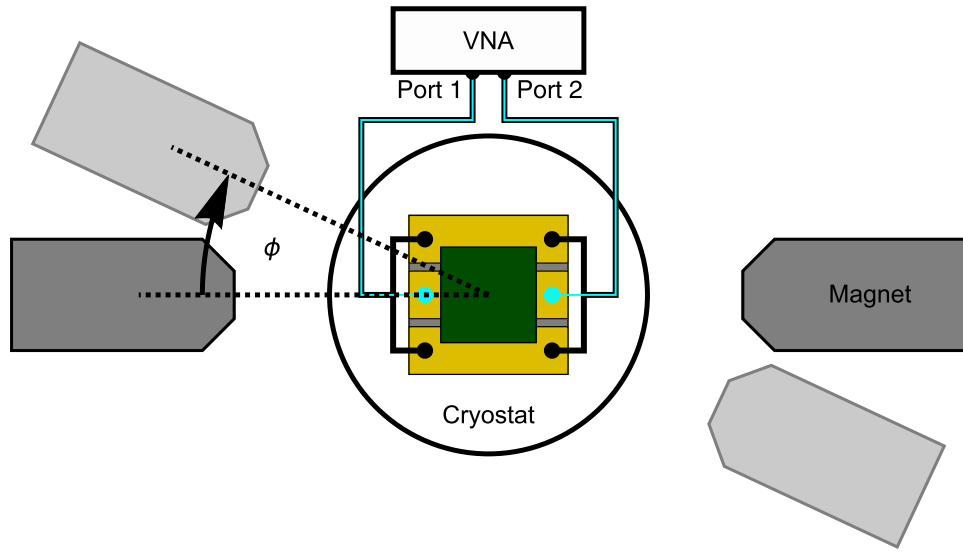
Figure 3.2: Schematic of the absorption FMR setup, utilizing a VNA as radio frequency current source and detector. The ports of the VNA are connected to the signal and ground lines of the CPW, with the sample placed on top. The external field is provided by a rotatable electromagnet, which allows for angle-resolved measurements.

Depending on the materials characteristics and especially the strength of the dynamic response, it is more advantageous to conduct the experiments with either the VNA or the lock-in amplifier. While the VNA measurements in general require less time, the lock-in technique provides a significantly better signal to noise ratio. If the sample under investigation exhibits a complex phase diagram, with one of the axes given by the external field, as it is the case for CSO, a continuous change of the magnetic field yields a likewise change of the magnetization configuration and consequently resonance condition. Therefore VNA measurements are suggested, if the detection of the phase diagram is the main focus of the experiment. As absorption FMR is also a well-established technique, we refer the interested reader to [Wol04; Obs15; Här16] for a more detailed description.

Part II

Spin excitations in the chiral magnet Cu$_2$OSeO$_3$

Chapter 4

Chiral Magnets

4.1 Overview

The competition between different kinds of magnetic interactions can lead to a deviation from a parallel alignment of the individual spins and a formation of spin helices instead. One group of magnets in which this particular magnetic order is observed are the chiral magnets, exhibiting a non-centrosymmetric cubic crystal lattice structure with space group $P2_13$. The interactions which are responsible for the spin twisting in these materials are the isotropic and anisotropic exchange interactions. The latter, which is also referred to as Dzyaloshinsky-Moriya interaction (DMI), arises from a broken structure inversion symmetry, given by surfaces or interfaces in general, or a non-centrosymmetric crystal structure, in combination with the relativistic spin-orbit coupling. In chiral magnets, spin spirals represent the energetic ground state of the magnetization at zero magnetic field up to the magnetic transition temperature T_c. Above T_c, thermal fluctuations are prevailing, and the magnetic order is suppressed. By adding an externally applied magnetic field as a second dimension, chiral magnets exhibit a rich temperature-field phase diagram. Depending on the position in this phase space, additional phases, referred to as conical and field-polarized state, emerge. A more detailed discussion is presented in the following section. Next to the formation of spin spirals, these materials also host vortex like spin structures, which are referred to as magnetic skyrmions. These three dimensional (3D) spin configurations are axially symmetric objects reminiscent of tubes, assumed to extend throughout the whole thickness of the sample [Mil13]. Nevertheless they should not be seen as rigid objects but more like flexible strings [Bac20]. It could be shown by Lorentz transmission electron microscopy (LTEM), that for certain conditions the skyrmion strings are no longer straight, but are twisting around another, leading to the formation of a braid-like structure [Zhe21]. While in the past years many publications could reproduce a two dimensional real space visualization of

skyrmions, the simultaneous observation of the third dimension remained an unsolved challenge. In 2021 Seki *et al.* [Sek21] successfully reproduced a 3D illustration of skyrmion strings, utilizing a X-ray tomography technique [Don17; Suz18]. Apart from elongated single skyrmions, they could also observe the emergence of structural defects, which comprises chiral bobbers [Ryb15; Zhe18; Ran21] and the coalescence of two skyrmions [Mil13].

In general, skyrmions crystallize in lattice structures, comprising a hexagonal [Müh09] or square [Kha21] order and are therefore often referred to as skyrmion crystals (SkX) in the literature. The lattice shape occurring in a material is not necessarily limited to one of the types given above. Depending on the position in the field-temperature space, both types of arrangements emerged in a robust metastable state in $Co_8Zn_8Mn_4$ [Kar16]. Next to a lattice, also isolated skyrmions could be observed [Bra19; Mey19] and, more important, artificially nucleated [Rom13; Jia15; Woo16; Hra17].

The skyrmion phase, at that time called A-phase, was first discovered experimentally in MnSi, a metallic chiral magnet, by small angle neutron scattering (SANS) in 2009 by Mühlbauer *et al.* [Müh09]. The experiments were supported by the numerical results from the phenomenological model based on the Ginzburg-Landau theory approach in the mean field approximation, revealing thermal fluctuations to be the stabilization mechanism of the skyrmion lattice. In subsequent experiments, skyrmions could also be observed in different materials, including further members of the aforementioned space group. Some of these are $Mn_{1-x}Fe_xGe$ [Shi13], $Mn_{1-x}Co_xSi$ [Pfl10], $Fe_{1-x}Co_xSi$ [Mün10; Yu10], FeGe [Yu11], GaV_4S_8 [Ehl16] and Cu_2OSeO_3 [Sek12c]. Despite their shared property of hosting spin spirals and magnetic skyrmions, these materials exhibit very different characteristics. Starting from the sample dimensions, skyrmion hosts comprise bulk crystals but also thin film systems [Hei11; Mac18; Man20], which range from millimeters to even a one atom layer thickness [Hei11]. A consequence of the reduced dimensionality, is the extension of the skyrmion pocket in the magnetic field - temperature space [Yu11]. Exhibiting a wider energetically more favorable phase range, reduces the sensitivity to field and temperature fluctuations. In this regard, the actual position of the skyrmion phase on the temperature axis is of importance and desirably equal to room temperature. While chiral magnets like MnSi, posses magnetic ordering only at low temperatures, the formation of skyrmions at ambient temperatures could be achieved in multilayer samples [Bou16; Woo16]. The latter are very interesting candidates, since the magnetic characteristics can be tuned in a very fine manner by the controlled growth process. Next to the temperature, also the skyrmion size strongly depends on the chosen material. The diameter might take on values between a few nanometers [Hei11] and a few micrometers [Jia15]. Here, it should be mentioned that the significant difference in length scales originates from the competition between different magnetic interactions [Nag13]. Finally, regarding the electrical conductivity,

all three groups, namely metals, semiconductors and insulators are represented [Sch15].

Behind the term skyrmion, a variety of different spin arrangements is hidden [Eve18]. The alignment of the spins at the skyrmion edges, pointing along the symmetry axis and of the one in the center pointing in the opposite direction, is shared by all skyrmion types. The spin configuration in between, however, depends on the energy terms contributing. Experimentally, Bloch [Müh09] and Néel [Kéz15] type, but also anti skyrmions [Nay17] could be observed. The kind of skyrmions which forms in the material investigated in this thesis, Cu_2OSeO_3, is of Bloch type.

Despite resulting from a field configuration, skyrmions exhibit a particle-like nature. As a consequence of their distinct spin texture, they are characterized by a finite topological winding number W. This integer-quantized value is defined as [Nag13],

$$W = \frac{1}{4\pi} \int \hat{\boldsymbol{n}} \cdot \left(\partial_x \hat{\boldsymbol{n}} \times \partial_y \hat{\boldsymbol{n}} \right) dx\, dy, \tag{4.1}$$

with the normalized local magnetization direction $\hat{\boldsymbol{n}}$. Here, the skyrmions are assumed to be aligned along the z direction. The winding number is a measure of how many times the magnetization field wraps around the order parameter space, given by the surface of a unit sphere. Unless possessing the same winding number, magnetization configurations can not be transformed into another by a continuous deformation. Therefore the topological unwinding, the transition from topologically non-trivial (skyrmion lattice) into topologically trivial states (helical, conical and field-polarized phase), requires the overcome of a certain energy barrier. The skyrmion is said to be topological protected [Müh09; Yu10; Nag13].

Apart from the generic interest in the rich field of fundamental physics, opened up by the skyrmions, the research is driven by prospects of the application in future magnetic storage devices. Based on the characteristics, dimension and stability, skyrmions are seen as a potential candidate to be implemented as information carriers. An application concept is the so called race track memory [Fer13; Sam13; Iwa13; Mül17; Che19a; Wan19]. In this proposal chains of skyrmions are driven along predefined lanes within a magnetic nanostripe and detected by a reading head measuring the magnetoresistance for example [Wan19]. The induced repulsive forces, which originate from the surface twists at the edges of a crystal lacking inversion symmetry, assure that the skyrmions are confined along the center of the lane [Mey14] and move in the desired direction. Compared to the common storage devices, the data is no longer encoded by the magnetization orientation but by the position of the skyrmions. It follows that due to the nanometer sized diameter, a high storage density might be achieved. Another advantage is the reduced energy consumption ascribed to the high mobility of the skyrmions. The transport of the latter requires only low

current densities [Sch12; Yu12] and is also achieved by the interaction with spin waves [Sch14; Zha15b; Din15; Zha17]. In the second case, even Joule heating can be avoided, due to the absence of a charge carrier flow. In order to integrate this topological protected spin texture in future applications, thin film materials, hosting skyrmions at room temperature, are required.

4.2 Phase Diagram

The generic temperature-field phase diagram, shared by all chiral magnets, is given in Fig. 4.1 (a). It is divided into four magnetic ordered phases, which are the helical, conical, field-polarized and skyrmion lattice phases. Besides these an intermediate and paramagnetic state is illustrated in the phase diagram. Since they are not of interest in this thesis, they will not be considered in the further course of the discussion. For temperatures far below T_c and fields below H_{c1} the spin configuration is given by a helix with vanishing cone angle as it is illustrated in Fig. 4.1 (b). The magnetization is said to be in a helical configuration. The helix is determined by its pitch vector $\boldsymbol{Q}$, with its length exhibiting a direct dependence on the ratio between the isotropic and anisotropic exchange constants, $Q \sim D/J$ [Müh09; Sch15]. Due to the sample shape and the cubic environment and therefore the resulting anisotropies, the direction of $\boldsymbol{Q}$ aligns along the easy axes of the crystal for zero and low external field values. Without a hysteretic field protocol, the helical phase is consequently divided into equally populated multi domain states, oriented along the energetically favorable directions, provided the sample is of spherical shape. By increasing the magnetic field, the helices are rotated out of their initial position and align along the field direction. Reaching the first critical field value H_{c1}, the helical phase experiences a spin-flop transition into the conical phase. The single spins deviate from a perpendicular alignment with respect to the pitch vector, resulting in a cone angle smaller than 90° as shown in Fig. 4.1 (c), which decreases with increasing field strength. At a field value of H_{c2} the spins are fully aligned along the field direction. This phase is referred to as the field-polarized state. The transition field into this phase is proportional to the square root of the temperature as shown in [Sch15]. Additionally the shape of the sample, represented by the demagnetization factors, enters the derived formula as a prefactor. In a small phase pocket, for temperatures close to T_c and magnetic fields close to H_{c1}, skyrmions form and build a lattice structure, in the plane perpendicular to the applied field. Depending on the material, the sample thickness and the orientation of the external field with respect to the underlying crystal structure, it extends over a wider field and temperature range [Ada12; Sch15]. A visualization of the respective spin texture is given in Fig. 4.1(d)-(e).
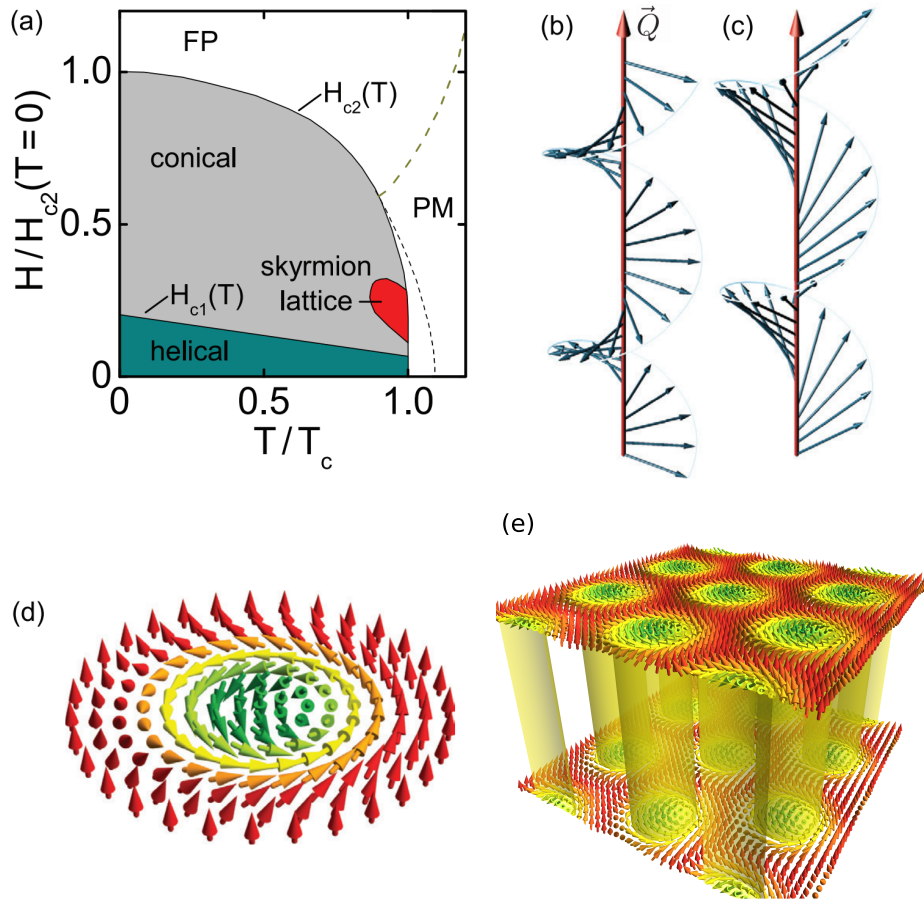
Figure 4.1: (a) Calculated phase diagram of a chiral magnet. (b)-(c) 3D illustration of the spin arrangement in the helical and conical phase. (d)-(e) Visualization of a single skyrmion and a 3D skyrmion lattice, in the plane perpendicular to the externally applied field. (a-d) Reprinted by permission from IOP Publishing Ltd: Journal of Physics D [Gar17] Copyright (2017). Figure (e) reproduced from [Mil13].

Here, the orientation of the magnetization is given by the arrows, while the colors highlight its out of plane component. A parallel and antiparallel alignment with respect to the external field is reflected by red and green colors. Note, the shown skyrmions are of Bloch type. Above the magnetic transition temperature T_c thermal fluctuations prevail and suppress the formation of magnetic order. It was found that under certain ambient conditions, the obtained phase diagram digresses from the one presented above, revealing additional rich features. The most important observation is the extension of the skyrmion pocket size in field and also temperature. It could be shown, that the skyrmion lattice, even though it might no longer be the ground state of the system, survives to temperatures down to approximately $0\,K$. One method which induces the above mentioned findings is applying mechanical pressure on the samples. Materials which were investigated for instance are MnSi [Nii15; Cha15] and [Sek17] Cu_2OSeO_3. Interestingly, it was also observed that applying a high enough pressure, T_c would increase drastically and skyrmions could even be obtained at room temperature in the helimagnet Cu_2OSeO_3 [Den20]. Another method established is the controlled cooling of the sample within an externally applied magnetic field, which is referred to as field-cooling. In numerous studies it was reported that it is sufficient enough to apply a field-cooling protocol with the magnetic field strength ranging between the skyrmion phase boundaries, to extend the latter to lowest temperatures in $Fe_{1-x}Co_xSi$ [Bau16] $Co_8Zn_8Mn_4$ [Kar16] and MnSi [Nak17; Oik16]. It should be mentioned that in the last reports the metastable skyrmion state was obtained by an additional quenching technique, characterized by a rapid cooling process. By means of the method described above also the insulator Cu_2OSeO_3 was further studied. In this regard a new phase, the tilted conical phase [Fen18] and most importantly a second, independent low temperature skyrmion phase [Cha18] was observed in the chiral magnet. It could be shown that the obtained phase diagrams are sensitive to the magnetic field direction with respect to the crystallographic axes of the cubic structure, due to the underlying magnetic anisotropies [Cha18; Ban19]. These results will be elaborated in more detail in the following chapter.

4.3 Dynamics

The individual phases described above, exhibit a distinct response to an external magnetic driving field. The investigation of the magnetization dynamics reveals insight into the sample characteristics, but requires an accurate model to predict the resonances to be measured. A generic excitation spectrum, comprising the resonance frequency as a function of externally applied magnetic field, is given in Fig. 4.2 for a spherical sample. The momentum of the excitation field is set to zero, resulting in a spatially uni-

form precession of the magnetization. The color code of the field ranges is matched to the phases, provided in the phase diagram Fig. 4.1 (a). It represents the helical (H), conical (C) , field-polarized (FP) and skyrmion lattice (S) phase and concurrently the energetically favorable state at the field values considered. The dot size of the spectrum represents the spectral weight of the modes, indicating the coupling efficiency to the driving field.
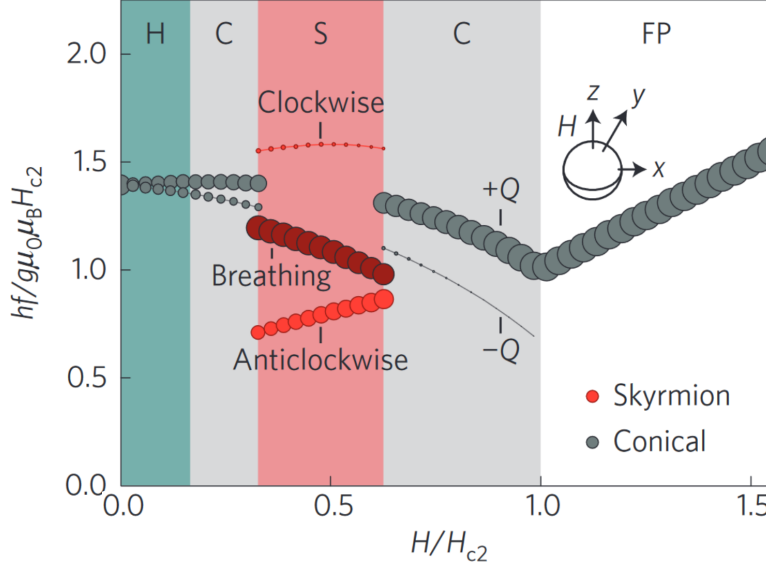
Figure 4.2: Calculated excitation spectrum as a function of externally applied magnetic field for a spherical sample. The illustration comprises the conical, Kittel and skyrmion modes. The dot size reflects the spectral weight of the respective resonance branch. Reprinted by permission from Springer Nature Customer Service Centre GmbH: Nature Materials [Sch15] Copyright (2015).

In the helical and conical phase, two excitation modes exhibit a finite spectral weight. Based on their propagation direction projected onto the pitch vector, they are referred to as $+Q$ (parallel) and $-Q$ (anti-parallel) modes. It should be noted that in this regard the designation propagation refers to the time domain and not real space. An illustration of the equilibrium state and the spin dynamics can be found in Fig. 4.3 (a-b). The periodic compression (red) and decompression (green) of the spin texture results in a screw like propagation along the pitch vector. The character of the collective spin dynamics, which is represented by the ellipticity and therefore the polarization, strongly depends on the demagnetization factors N_x and N_y within the plane perpendicular to the external field. It could be shown that for certain N_x and N_y values and field ranges, the Q modes diverge from the perfect circular motion and result in a linear polarization [Sta17a]. This results in a direction-dependent excitation efficiency in the

case of a linearly polarized driving field, which could be predicted theoretically and proven by broadband spectroscopy methods [Sta17a]. Due to the sample shape ($N_x = N_y$) chosen in the presented calculations, the two gyration modes are degenerate at zero magnetic field. For a differently shaped sample, the degeneracy is lifted and the modes can be distinguished. Neglecting anisotropies the field dependence of the Q modes can be calculated analytically [Kat87; Sch15].

Reaching the critical field value H_{c2} the $+Q$ mode smoothly merges into the field-polarized mode, while the spectral weight of the $-Q$ mode gradually decreases. This behavior is based on the helicity of the magnetization precession of the gyrational modes and the helicity of the uniform precession in the field-polarized phase. The spin excitation of the latter corresponds to the generic FMR behavior and can be therefore described by the Kittel formula [Kit48; Sch15]. The uniform magnetization of the $+Q$ mode possesses the same helicity as the Kittel mode, which are both precessing counterclockwise around their equilibrium. In the case of the $-Q$ mode, the uniform magnetization precesses in the opposite manner and does not comply to the inherent helicity in the Kittel mode [Sta17a].
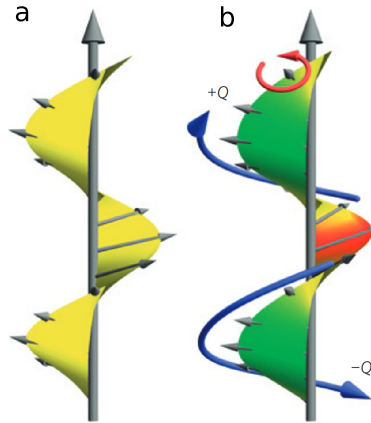
Figure 4.3: 3D illustration of the magnetic helix. (a) Equilibrium state. (b) The two conical excitation modes, propagating either along the pitch vector ($+Q$) or in the opposite direction (-Q). Reprinted by permission from Springer Nature Customer Service Centre GmbH: Nature Material [Sch15] Copyright (2015).

The skyrmion lattice exhibits three distinct eigenmodes which efficiently couple to the external driving field. Due to their characteristic time evolution, they are referred to as counterclockwise (CCW), clockwise (CW) and breathing (BR) mode. While the breathing mode possesses a similar field dependence as the $\pm Q$ modes, the resonance frequency of the counter clockwise and clockwise mode increases with increasing field. An import point to be mentioned is the sensitivity of the modes to the excitation geome-

try. While the gyrational modes couple to an in plane driving field with respect to the skyrmion plane, the breathing mode is only excited by an out of plane ac-field. These modes can therefore be selectively addressed in broad brand spectroscopy measurements as described in Sec. 3.1. Due to the low intensity, the clockwise mode was barely reported in preceding resonance experiments [Ono12; Sch15]. A visualization of the three modes for four time values within one period is given in Fig. 4.4. The snapshots are composed of the in-plane (arrows) and the out-of-plane (contour plot) magnetization components, with respect to the skyrmion plane. The magnetic field is applied perpendicular to the latter, pointing out the image plane. The color code therefore indicates a parallel (red) and antiparallel (green) alignment regarding the external field. From these illustrations the clear rotational and breathing character of the gyrational and breathing mode, respectively can be seen. Compared to the $\pm Q$ modes of the conical phase, the skyrmion lattice excitations require numerical calculations. At first predicted by Mochizuki [Moc12], they were extensively studied by Schwarze *et al.* [Sch15] in three different types of chiral magnets experimentally and theoretically. Since one part of this thesis is aiming to determine the effect of cubic anisotropies on the resonance spectra, the model developed in [Sch15] will be discussed in greater detail in Chap. 6. Before introducing the chiral magnet Cu_2OSeO_3, it should be noted that the above presented eigenmodes are excitations with finite spectral weight. Next to these, additional higher-order modes with a vanishing weight exist in the conical and skyrmion phase. While the conical modes were already observed experimentally at low temperatures by broadband spin wave spectroscopy measurements [Wei17], the higher order skyrmion modes could only be predicted [Wai17] [Gar17]. In the course of this thesis, we will present the hybridization between the uniform and higher order modes theoretically and experimentally, revealing the existence of the latter.
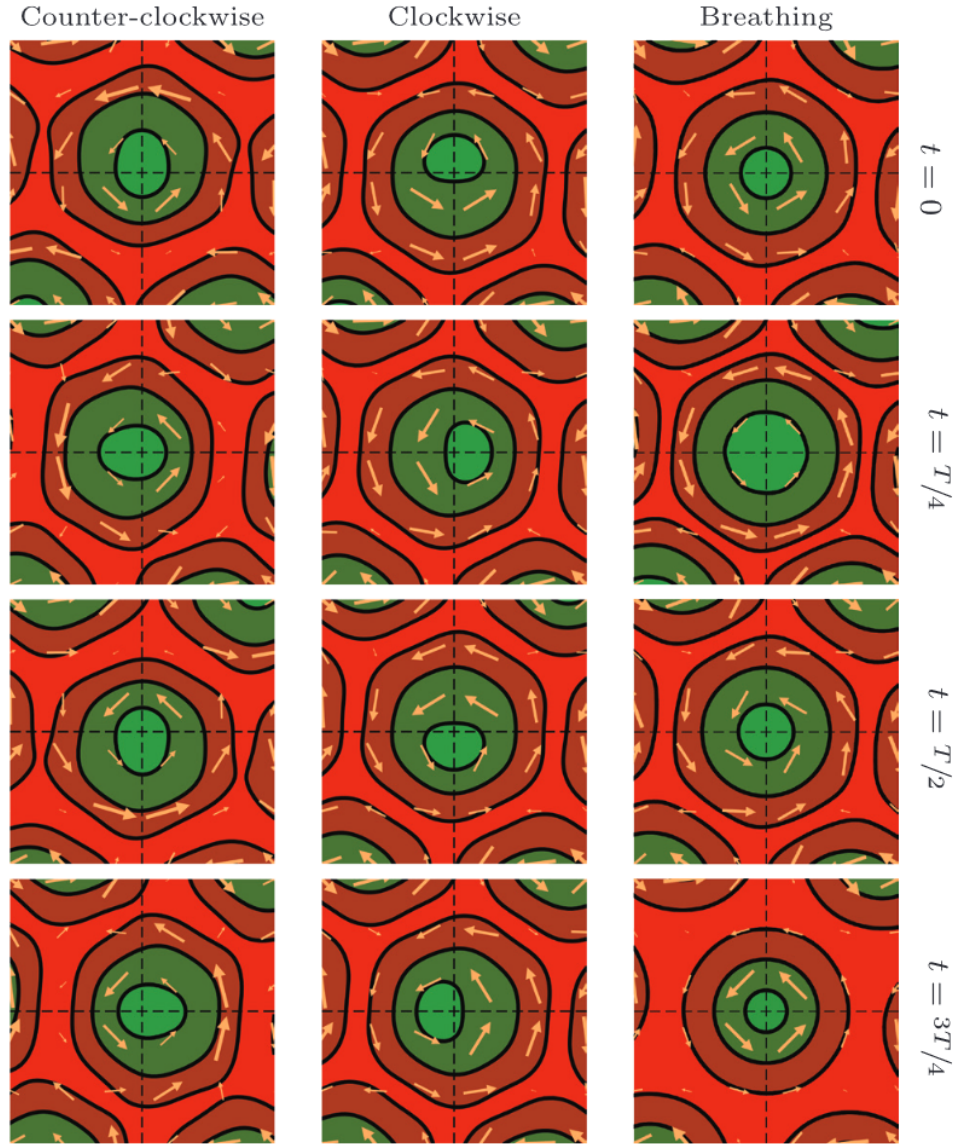
Figure 4.4: Visualization of the clockwise, counterclockwise and breathing mode of the skyrmion crystal in real space as a function of time. The magnetic field is applied perpendicular to the skyrmion lattice, pointing out of the image plane. The magnetization components are given by the arrows (in-plane) and contour plot (out-of-plane). In the case of the latter, the red colour represents a parallel and the green colour an antiparallel alignment with respect to the external field. Reprinted by permission from IOP Publishing Ltd: Journal of Physics D [Gar17] Copyright (2017).

Chapter 5

Helimagnet Cu_2OSeO_3

The helimagnet to be investigated in this thesis is the insulating compound Cu_2OSeO_3, which is a member of the cubic chiral magnets with space group $P2_13$. In Fig. 5.1a the crystal structure of the corresponding unit cell is illustrated. It consists of copper, oxygen and selenium atoms, indicated by light brown and light cyan, brown and green spheres. Here, the first two colors are both attributed to the copper sites, since these are divided into two groups, depending on their oxygen environments. The latter form either a square pyramid or a trigonal bipyramid, depicted by the yellow and brown faces, respectively. As indicated in the figure, the ratio amounts to 12 square pyramids and 4 bipyramids per unit cell. For simplicity, the corresponding lattice sites will be referred to as $Cu_{(2)}$ and $Cu_{(1)}$ in the following. Since only the copper atoms are contributing to the magnetic moment, selenium and oxygen will be excluded from the further discussion.

From high-resolution powder x-ray diffraction (XDR) [Bos08] and nuclear magnetic resonance (NMR) [Bel10] experiments it could be found, that magnetic moments on the $Cu_{(1)}$ and $Cu_{(2)}$ sites are aligned anti-parallel to each other as visualized by the arrows in Fig. 5.1b. This leads to the emergence of ferromagnetic J^{FM} (blue lines) and anti-ferromagnetic J^{AF} (red lines) coupling between the atoms. *Ab initio* density functional theory (DFT) calculations [Jan14] reveal, that these magnetic interactions are in turn divided into strong (S) and weak (W) couplings, with the strength represented by the thickness of the connection lines. As a consequence, the copper lattice sites form a spin 1 triplet tetrahedron, composed by one $Cu_{(1)}$ and three $Cu_{(2)}$ atoms, as the ground state of the system. The resulting effective spin moments of 1, given by the arrows in Fig. 5.1c, are in total then leading to a ferromagnetic order. However, due to the, up to now, neglected DM interaction, which favors a twisting of the effective spin moments, the parallel alignment is impaired. This competition finally leads to a long-ranging formation of a helical spin texture.

In Cu_2OSeO_3, this magnetic order persists up to a critical temperature
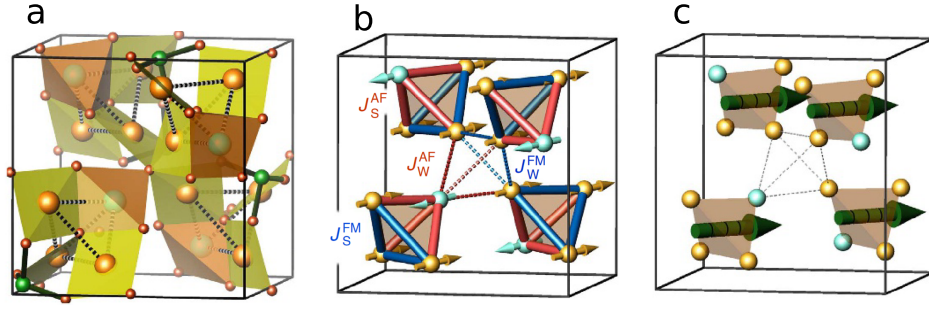
Figure 5.1: (a) Crystal structure of Cu_2OSeO_3. The unit cell consists of copper (light brown, light cyan), oxygen (brown) and selenium (green) atoms. The copper and oxygen atoms build square pyramids (yellow faces) and triangular bipyramids (brown faces). (b) Spin arrangement (arrows) and magnetic interactions (connection lines) of the Cu lattice sites. Further information is given in the main text. (c) Arrangement of the effective spin 1 triplets. Reprinted by permission from Springer Nature Customer Service Centre GmbH: Nature Communications [Jan14] Copyright (2014).

T_c of around $58\,\mathrm{K}$ [Ono12] and its respective periodicity takes values of around $60\,\mathrm{nm}$ [Ada12; Sek12b]. Apart from its particular magnetic characteristics, Cu_2OSeO_3 also exhibits a magnetic-field induced polarization and is therefore referred to as multiferroic [Sek12a; Liu13; Ruf15]. Since only the magnetic properties are of interest in this thesis though, the latter will not be further elaborated. At low temperatures, magnetic resonance spectroscopy revealed that the magnetic damping decreases significantly [Sta17b], approaching the record value of YIG [Onb14; Kli17]. This characteristic makes CSO an interesting candidate for studying magnon-skyrmion interactions and the realization of skyrmionics in future information devices, which, in turn, might be readily transferable to other materials, hosting skyrmions at room temperature. In this regard, also the large optical response, including Kerr and Faraday rotation [Ver16; Ver19] plays an important role. These effects are usually employed in microscopes, detecting the local magnetization and magnetization dynamics. As a chiral magnet, CSO shares a similar phase diagram, hosting skyr-mions only in a small temperature-field pocket close to T_c. However, as already mentioned before, this window could be extended on one hand to lower temperatures by thinning down the crystal [Sek16], applying strain [Sek17] and rapid cooling [Ban19] and on the other hand to even room temperature by applying mechanical pressure [Den20]. Here, the most relevant method in the light of future applications is the reduction of the sample dimensions. The size of the CSO crystals, which are grown by chemical vapor transport, is usually in the millimeter regime [Aqe21]. Although, grinding and polishing of the material allows to reduce the thickness to hundreds of micrometers, only by applying the cumbersome
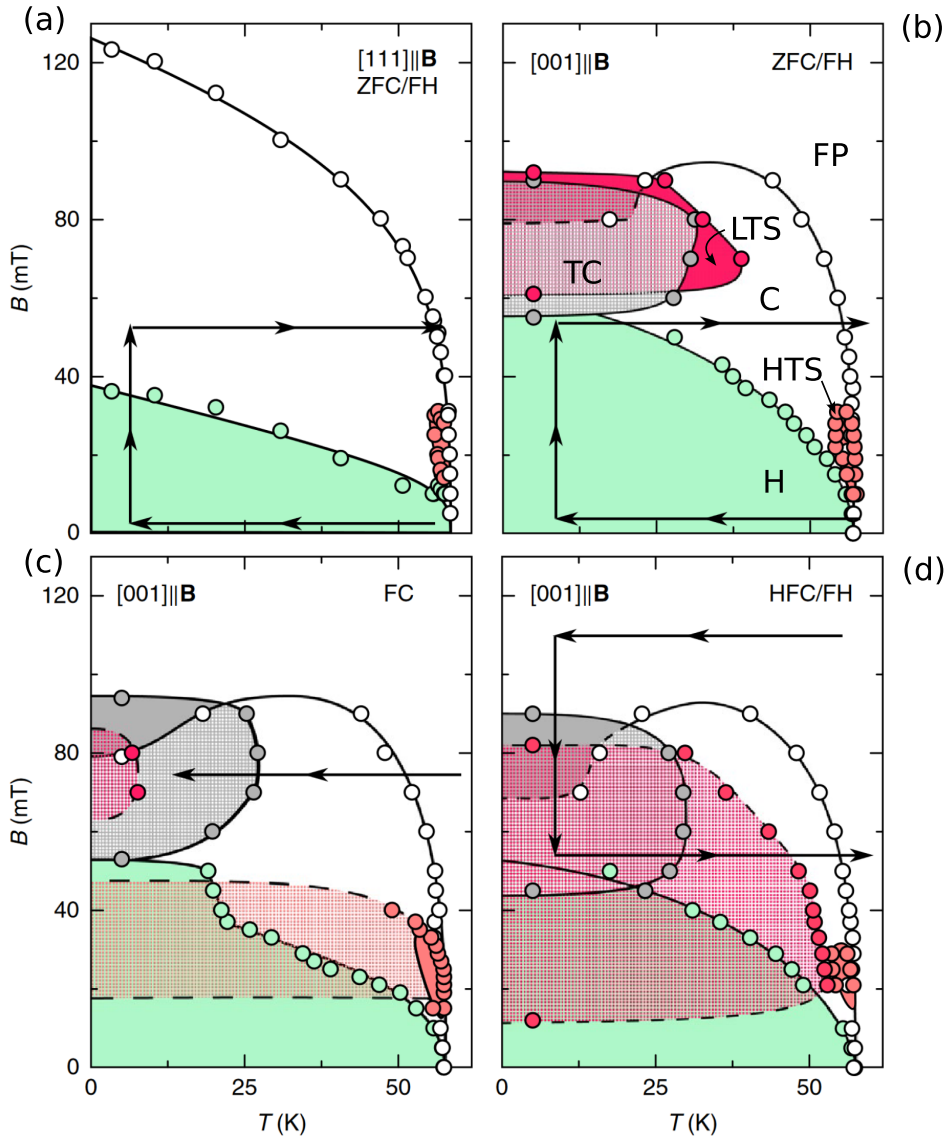
Figure 5.2: Phase diagrams for different field orientations parallel to the (a) [111] and (b) [001] crystallographic direction. The phase boundaries of the helical (H), conical (C), HTS, tilted conical (TC) and LTS are given by green, white, orange, gray and red circles and corresponding shaded area. The field-polarized phase is indicated by the notation FP. By applying defined cooling and heating protocols (b)-(d), a hysteretic behavior of the skyrmion phase can be visualized by an extension of the phase pocket, which originates from the topological protection, amongst others. Reprinted by permission from Springer Nature Customer Service Centre GmbH: Nature Physics [Cha18] Copyright (2018).

focused ion beam (FIB) etching technique dimensions down to 1-2 micrometer [Sek16] can be achieved. A further reduction of the thickness in turn can cause a twisting of the crystal. The effects arising from the thin and ultra thin film limit can therefore not be exploited, yet.

While in the publications mentioned above the extension of the high temperature skyrmion (HTS) phase, in field and temperature, was studied, Chacon *et al.* reported on the observation of an independent low temperature skyrmion (LTS) phase in a bulk CSO crystal [Cha18]. By conducting SANS measurements for different field directions with respect to the crystallographic axes of the samples, they discovered the emergence of additional features in the extracted phase diagrams. The results are shown in the upper row of Fig. 5.2 for the [111] (a) and [001] (b) directions. Next to the helical (green), conical (white) and HTS (orange) phase, they observed the tilted conical (gray), previously found by Fengjiao *et al.* [Fen18] and the second, thermodynamically disconnected, skyrmion phase (red). The latter only occurred for the case with the external field applied along the [001] direction. These findings reveal the cubic crystal environment and the resulting magnetic anisotropies to be the origin of this direction-dependent behavior. In their studies, they also employed different cooling and heating protocols, indicated by the black arrows in the diagrams, which are zero field cooling (ZFC), field heating (FH), field cooling (FC) and high field cooling (HFC). Considering the results obtained in the [001] configuration, Fig. 5.2b-d, emphasizes the hysteretic behavior of the skyrmion phase, which also originates from the intrinsic topological protection of the latter. Another important point to be mentioned, is the skyrmion nucleation process, induced by a continuous up and down sweep of the magnetic field strength within a small field range. By this field cycling technique, the intensity obtained from the skyrmion lattice increases, which indicates the growth of the skyrmion volume fraction within the sample. The details of this nucleation process are, however, not fully understood, yet. In order to support the experimental findings, also a theoretical approach, based on the already well established Ginzburg-Landau energy functional [Müh09; Sch15], is presented in this study. Building upon the previously obtained results, the focus of the current model lies on the induced changes arising from the additional cubic magnetocrystalline energy term. Further anisotropies, as considered in [Ban19], in general might also play a non-negligible role in the investigated material, but are not necessary for a qualitative understanding of the experimental data. Aiming to reproduce the emergence of the tilted conical and low-temperature skyrmion phase, first an appropriate anisotropy strength has to be determined. In Fig. 5.3 a, the phase diagram of the energetically favorable magnetization configuration, spanned by the dimensionless anisotropy value K and magnetic field B, is illustrated. For the temperature parameter, the Ginzburg-Landau coefficient r_0, which will be introduced in Chap. 6, a value of $r_0 = -1000$ is chosen in the presented calculations.

Here, a smaller constant r_0 refers to a lower temperature, while $r_0 = 0$ denotes the transition temperature T_c. It can be seen, that for approximately $K > 0.0001$, the conical phase no longer represents the ground state of the system for the whole field range, but the low-temperature skyrmion lattice emerges. Interestingly, also a square lattice is predicted to form within a certain K and B pocket. By increasing the anisotropy strength further, the pitch vector of the conical phase starts to tilt away from the [100] direction, leading to the tilted conical phase. Note, despite being the energetically more favorable configuration compared to the helical, conical and field polarized states, the formation of the tilted conical phase requires higher energy costs compared to the skyrmion lattice and is therefore only metastable.

Based on these findings the anisotropy strength is fixed to a value of $K = 0.0004$ and the theoretical predicted phase diagram, now with the dimensions temperature r_0 and external field B, is illustrated in Fig. 5.3 b. It should be mentioned that, however, in reality also the anisotropy exhibits a strong temperature dependence. Comparing these findings to the experimental data, for instance shown in Fig. 5.2(d), it is evident that, apart from the tilted conical phase, the theoretical model reproduces the obtained phase diagram accurately. It therefore can be concluded that the cubic magnetocrystalline anisotropy is the origin of the stabilization mechanism of the second skyrmion phase at lower temperatures.
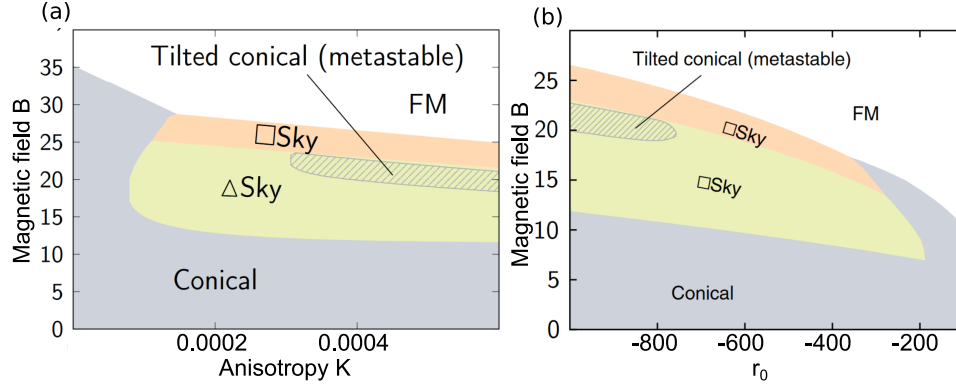
Figure 5.3: (a) Theoretically predicted phase diagram by the Ginzburg-Landau model as a function of anisotropy K and externally applied magnetic field B. K and B are given in dimensionless units. For certain K and B values the emergence of the skyrmion and tilted conical phase can be observed. Depending on the position in the phase space, the formation of a hexagonal or square skyrmion lattice is predicted. (b) Phase diagram as a function of temperature constant r_0 and magnetic field for a fixed anisotropy value $K = 0.0004$. Reprinted by permission from Springer Nature Customer Service Centre GmbH: Nature Physics [Cha18] Copyright (2018).

Chapter 6

Theoretical Model

Apart from influencing the magnetic texture, anisotropies also have an impact on the dynamic response of the magnetization for example in magnetic resonance experiments. In preceding studies [Sch15], cubic magnetocrystalline anisotropies were already taken into account in order to investigate in the induced changes at the helical-conical phase transition. The effect on the skyrmion resonances, however, was not elaborated since on one hand only the HTS phase was known at that time and on the other hand the anisotropy strength is negligible at temperatures close to T_c. With the shift of the focus towards the low temperature limit and the subsequent observation of the tilted conical and low temperature skyrmion phase, as a result of an increased magnetocrystalline anisotropy, the previous model is no longer accurate enough to reproduce the new features, but requires the implementation of additional energy terms. In this chapter the theoretical framework for calculating the magnetic texture and the resulting collective spin excitations in the chiral magnet are presented, which serves to support the experimental data obtained from broadband microwave experiments. The theoretical model is based on the well established Ginzburg-Landau energy functional and can be seen as a continuation of the calculations performed in [Sch15; Wai17]. The numerical results are produced by the *Wolfram Mathematica* code, created by Johannes Waizner during the course of his Phd thesis [Wai17] under the supervision of Professor Markus Garst. Previous results are published in [Sch15; Sta17b]. In order to take also anisotropies into account the code was adapted in close collaboration with Professor Markus Garst and extended by the magnetic cubic magnetocrystalline and later on also by the exchange anisotropy term. Owing to the new findings obtained from the experiments, the parameters were continuously adapted in the course of this thesis in order to reproduce the most recently obtained results. The numerical results are therefore presented in a chronological order. The chapter first introduces the Ginzburg-Landau energy functional, the determination of the equilibrium configuration of the magnetization and its

respective dynamics and closes with the actual implementation in the code. The most important equations and derivations of the theoretical model will be presented throughout this thesis. For a detailed understanding though, we refer to the Phd thesis of Johannes Waizner [Wai17] and the aforementioned publications [Sch15; Sta17b].

6.1 Ginzburg-Landau Theory

The theoretical approach for chiral magnets [Bak80; Nak80; Müh09] builds up on the framework of the phenomenological Ginzburg-Landau theory. This model in turn is an extension of the Landau theory of second order phase transitions, which considers a series expansion in powers of the slowly varying order parameter of the free energy functional, assuming the latter to be small around the phase transition. Limited to the fourth order, the energy functional is therefore given by,

$$F[\boldsymbol{M}] = \int d^3r \left(F_0[\boldsymbol{M}] + r_0 \boldsymbol{M}^2 + U \boldsymbol{M}^4 \right). \tag{6.1}$$

Due to the imposed time reversal symmetry, only even powers exhibit finite prefactors. The last to terms of the functional are governed by the phenomenological Ginzburg-Landau coefficients r_0 and U. While U has to be greater than zero for the system to be thermodynamically stable and is in general assumed to be constant, r_0 is set to be the only temperature dependent component. Expanded up to linear order, $r_0 \sim T - T_\mathrm{c}$ represents an explicit measure of the distance to the critical temperature T_c. The sign convention of r_0 is chosen to be negative in the ordered phase ($T < T_\mathrm{c}$) and positive in the paramagnetic phase ($T > T_\mathrm{c}$). It should be mentioned that material parameters, for instance the exchange constant, are also temperature dependent, but are assumed to be constant throughout the theoretical analysis. The first energy term in Eq. 6.1 represents the sum of the exchange interaction, DMI, demagnetization energy, Zeeman interaction and the cubic magnetocrystalline and exchange anisotropy, given by,

$$\begin{aligned} F_0[\boldsymbol{M}] = &\frac{1}{2} J (\nabla \boldsymbol{M})^2 + D \boldsymbol{M} (\nabla \times \boldsymbol{M}) + \frac{1}{2} \mu_0 \boldsymbol{M} \boldsymbol{N} \boldsymbol{M} - \boldsymbol{B} \boldsymbol{M} \\ &- \frac{K}{M_\mathrm{s}^4} \sum_i M_i^4 + C \sum_i (\partial_i M_i)^2. \end{aligned} \tag{6.2}$$

These contributions are characterized by their respective strengths, J, D, K and C, the demagnetization tensor $\boldsymbol{N}$, with $\mathrm{tr}(\boldsymbol{N}) = 1$ and the externally applied magnetic field B. Here, the notation $(\nabla \boldsymbol{M})^2 \equiv \partial_i M_j \partial_i M_j$ with Einstein's sum convention for the coordinates $i, j \in [x, y, z]$ is used. It should be mentioned, that the prefactor convention is chosen to match

the model in [Cha18], which differs slightly compared to the original approach published in [Müh09]. In contrast to the most recent adapted energy functional in [Cha18], we additionally extended our model by the exchange anisotropy, which is of the same order in the spin-orbit coupling as the cubic magneto crystalline term. While the latter might be sufficient to explain the appearance of the low temperature skyrmion phase, the exchange anisotropy is needed to account for the hybridization strength between the resonance branches, as will be discussed later. By including anisotropies in the theoretical model - apart from the shape anisotropy -, the magnetization orientation is subject to the underlying cubic environment of the crystal lattice. Given by its structure, the cubic anisotropy defines an easy and hard axis for the spontaneous magnetization and the exchange anisotropy determines a preferred orientation of the pitch vector, as stated in Chap. 1. It therefore results in a violation of the symmetry of a combined continuous rotation in real and spin space around the magnetic field axis. At this point, it should be mentioned that also further anisotropies are allowed by symmetry and might play an important role, for instance for the orientation of the skyrmion lattice with respect to the crystallographic axis [Müh09; Eve12; Wai17], but will not be taking into consideration in the framework of this thesis.

The energy density is determined by a vast parameter space, which however can be reduced by rescaling the energy functional. This is achieved by measuring the distance in units of pitch vector length Q, $\tilde{r} = Q r$ ($\tilde{\nabla} = Q\nabla$) and introducing the dimensionless magnetization and field quantities $\tilde{M} = \left(\frac{U}{JQ^2}\right)^{1/2} M$ and $\tilde{B} = \left(\frac{U}{(JQ^2)^3}\right)^{1/2} B$. The equation given above thus simplifies to,

$$
F[\boldsymbol{M}] = \kappa \int \mathrm{d}^3\tilde{r}\, \frac{1}{2}(\tilde{\nabla}\tilde{\boldsymbol{M}})^2 + \tilde{\boldsymbol{M}}(\tilde{\nabla}\times\tilde{\boldsymbol{M}}) + \frac{1}{2}\frac{\mu_0}{JQ^2}\tilde{\boldsymbol{M}}\boldsymbol{N}\tilde{\boldsymbol{M}} - \tilde{\boldsymbol{B}}\tilde{\boldsymbol{M}}
$$
$$
- \frac{K}{M_\mathrm{s}^4 U}\sum_i \tilde{M}_i^4 + \frac{C}{J}\sum_i (\tilde{\partial}_i \tilde{M}_i)^2 + \frac{r_0}{JQ^2}\tilde{\boldsymbol{M}}^2 + \tilde{\boldsymbol{M}}^4 \tag{6.3}
$$

with prefactor $\kappa = \frac{J^2 Q}{U}$. In the following, the tildes are omitted and the remaining parameters are redefined. [1] The equation to be considered in the subsequent analysis is therefore given by,

$$
F[\boldsymbol{M}] = \kappa \int d^3 r \left(\frac{1}{2}(\nabla\boldsymbol{M})^2 + \boldsymbol{M}(\nabla\times\boldsymbol{M}) + \tau\boldsymbol{M}\boldsymbol{N}\boldsymbol{M} - \boldsymbol{B}\boldsymbol{M} \right.
$$
$$
\left. - K\sum_i M_i^4 + C\sum_i (\partial_i M_i)^2 + r_0\boldsymbol{M}^2 + \boldsymbol{M}^4 \right). \tag{6.4}
$$

Here, $\tau \approx 0.88$ was already determined in [Sch15] for Cu_2OSeO_3. The characteristics of the model are hence only shaped by the strengths of the

---

[1] The parameters are redefined in the following way: $\tau \equiv \mu_0/2JQ^2$, $C \equiv C/J$, $K \equiv K/M_\mathrm{s}^4 U$

remaining prefactors B, r_0, K, and C. With these the equilibrium configuration of the system is calculated by minimizing the energy functional with respect to the magnetization, following

$$\left.\frac{\delta F[\boldsymbol{M}]}{\delta \boldsymbol{M}}\right|_{\boldsymbol{M}^{\mathrm{mf}}} = 0. \tag{6.5}$$

6.2 Magnetization Dynamics

The magnetization dynamics of a chiral magnet are calculated in a similar approach as presented in Chap. 2. However, in the following derivation the magnetization will not be given by a normalized vector field with constant length M_{s}, which hence does not allow the application of the previous results. The energy functional and magnetization vector are divided both into a static/mean-field and time dependent component,

$$F(\boldsymbol{r}, t) = F_{\mathrm{stat}}(\boldsymbol{r}) + \bar{F}(\boldsymbol{r}, t) \tag{6.6}$$

$$\boldsymbol{M}(\boldsymbol{r}, t) = \boldsymbol{M}_{\mathrm{mf}}(\boldsymbol{r}) + \delta \boldsymbol{M}(\boldsymbol{r}, t). \tag{6.7}$$

The temporal evolution of these terms are assumed to be described by a plane wave ansatz

$$F(\boldsymbol{r}, t) = \bar{F} e^{i(\boldsymbol{k}\boldsymbol{r} - \omega t)} \tag{6.8}$$

$$\delta \boldsymbol{M}(\boldsymbol{r}, t) = \delta \boldsymbol{M} e^{i(\boldsymbol{k}\boldsymbol{r} - \omega t)}. \tag{6.9}$$

with a linear response of the magnetization to the external stimulus, given by an oscillating magnetic field for instance.

The magnetization dynamics are governed by the Landau-Lifshitz equation of motion Eq. 2.1. Substituting the effective field Eq. 1.26 and neglecting dissipative contributions, the equation to be solved is written in the form,

$$\frac{\mathrm{d}\boldsymbol{M}}{\mathrm{d}t} = \gamma \boldsymbol{M} \times \frac{\delta F}{\delta \boldsymbol{M}}. \tag{6.10}$$

The next steps comprise the insertion of the expressions Eq. 6.6, Eq. 6.7 with the explicit time dependences Eq. 6.8, Eq. 6.9 into the equation given above and the subsequent expansion up to the first order in $\delta \boldsymbol{M}$. Finally, this protocol leads to a formula describing the vectorial amplitude of the dynamic magnetization components, reading [Wai17]

$$\delta \boldsymbol{M} = \left[\omega - i\gamma \boldsymbol{M}_{\mathrm{mf}} \times \left.\frac{\delta^2 F_{\mathrm{stat}}}{\delta \boldsymbol{M}^2}\right|_{\boldsymbol{M}^{\mathrm{mf}}}\right]^{-1} \left[i\gamma \boldsymbol{M}_{\mathrm{mf}} \times \left.\frac{\delta F}{\delta \boldsymbol{M}}\right|_{\boldsymbol{M}_{\mathrm{mf}}}\right]. \tag{6.11}$$

From this result, the resonance condition and maximum amplitude, respectively, is achieved by a vanishing denominator. Therefore the determination

of the resonance frequencies is reduced to the calculation of the eigensystem and the corresponding eigenvalues of the following matrix [Wai17],

$$\omega_{\mathrm{res}} = \mathrm{Im}\left[\mathrm{Eigenvalues}\left(\gamma \boldsymbol{M}^{\mathrm{mf}} \times \chi_0^{-1}\right)\right] \tag{6.12}$$

with fluctuation matrix $\chi_0^{-1} = \left.\frac{\delta^2 F_{\mathrm{stat}}}{\delta \boldsymbol{M}^2}\right|_{\boldsymbol{M}^{\mathrm{mf}}}$. For a comprehensive derivation of these results we refer to [Wai17].

6.3 Spectral Weight

Now with the previously derived equations at hand, the equilibrium configuration of the magnetization and its corresponding resonance conditions can be determined. The last quantity, which will be incorporated in the numerical treatment, is the so called spectral weight which illustrates the coupling efficiency to the external oscillating magnetic field. Due to its various and complex magnetic textures, the chiral magnet hosts a huge variety of eigenmodes, which are not just limited to the well established $\boldsymbol{Q}$ modes in the conical phase and the gyrational and breathing modes in the skyrmion phase, but also include higher order excitations of the modes, listed above. Since these excitations however, do not exhibit a finite macroscopic dipole moment and consequently can not efficiently couple to the driving field, they are hardly detectable in experiments. They are therefore referred to as dark modes and said to have a vanishing spectral weight. By including anisotropies in the theoretical considerations, certain resonance branches start to hybridize with each other, leading to a redistribution of the weight and experimentally accessible higher order modes.

In general, the coupling efficiency can be calculated by means of the dynamic susceptibility χ, resulting from the Landau Lifshitz Gilbert equation Eq. 2.1. Including dissipation, the imaginary part of χ gives the amplitude of the dynamic magnetization as a function of driving frequency, following a Lorentzian distribution. The spectral weight is therefore determined by the enclosed area of the Lorentzian function. Since damping is omitted in Eq. 6.12, $\delta \boldsymbol{M}$ no longer converges, but exhibits a singularity approaching the resonance condition. As a workaround, the prefactor of the Lorentzian function, after projection onto the driving field axis, will be used as a substitution instead. The following derivation is closely related to the approach presented in [Wai13].

The equation of motion Eq. 6.11 is first displayed in the reduced form,

$$\delta M^\alpha = \left[\left(\omega \mathbb{1} - \mathcal{W}\right)^{-1}\right]^{\alpha\beta} \mathcal{V}^\beta. \tag{6.13}$$

with $\mathcal{W} = \left(\gamma \boldsymbol{M}^{\mathrm{mf}} \times \chi_0^{-1}\right)$ and $\mathcal{V} = i\gamma \boldsymbol{M}_{\mathrm{mf}} \times \left.\frac{\delta F}{\delta \boldsymbol{M}}\right|_{\boldsymbol{M}_{\mathrm{mf}}}$. Application of the transition matrix $T^{ij} = v_j^i$, composed by the eigenvectors, $\mathcal{W}\boldsymbol{v}_i = \lambda_i \boldsymbol{v}_i$,

allows to introduce the diagonalized matrix representation $\widetilde{\mathcal{W}} = T^\dagger \mathcal{W} T$. The notation $\mathcal{A}^\dagger$ indicates the conjugate transpose of the respective matrix $\mathcal{A}$. The denominator of Eq. 6.13 is hence given by

$$\left[(\omega \mathbb{1} - \mathcal{W})^{-1} \right]^{\alpha\beta} = \left[\left(T(\omega \mathbb{1} - \widetilde{\mathcal{W}})T^\dagger \right)^{-1} \right]^{\alpha\beta} \tag{6.14}$$

$$= T^{\alpha\gamma} \frac{1}{\omega - \lambda_i} \left(e_i^\gamma e_i^\epsilon \right) T^{\dagger\epsilon\beta}. \tag{6.15}$$

With the unit vectors $\hat{e}_i$ acting on the transformation matrices, the corresponding eigenvectors are selected,

$$\left[(\omega \mathbb{1} - \mathcal{W})^{-1} \right]^{\alpha\beta} = \frac{1}{\omega - \lambda_i} v_i^\alpha (v_i^\beta)^*. \tag{6.16}$$

Inserting this result in the initial equation given above and projecting the latter onto the oscillating field axis $\hat{e}_{\mathrm{ac}}$, yields

$$e_{\mathrm{ac}}^\alpha \delta M^\alpha = \frac{1}{\omega - \lambda_i} e_{\mathrm{ac}}^\alpha v_i^\alpha (v_i^\beta)^* \mathcal{V}^\beta. \tag{6.17}$$

In this setup the dynamic free energy contribution is determined by the alternating field, $\frac{\delta F}{\delta M}\big|_{M_{\mathrm{mf}}} = \mu_0 H_{ac}$. We therefore arrive at the expression,

$$e_{\mathrm{ac}} \delta M = \frac{\mu_0}{\omega - \lambda_i} |e_{\mathrm{ac}} v_i|^2 (v_i)^* \left(M_{\mathrm{mf}} \times \right) v_i H. \tag{6.18}$$

Finally, the spectral weight of the respective resonance condition λ_i is defined as the prefactors on the right-hand side and will be implemented as the dot size in the field-frequency spectra.

6.4   Implementation in the Reciprocal Space

Due to the periodic nature of the helical/ conical and skyrmion lattice phase in real space, the respective magnetization textures will be converted to momentum space by a Fourier transformation,

$$M(r) = \sum_k m_k e^{ikr} \tag{6.19}$$

with momentum vectors k and the corresponding Fourier components m_k. Based on the same argument given above, the resulting momentum space is discretized and therefore forms a reciprocal lattice, spanned by the pitch vectors Q_i. As a result, an arbitrary momentum vector can be represented by the combination of a lattice vector Q and momentum vector q, limited to the first Brillouin zone, reading $k = Q + q$. In the case of the conical phase, the spin arrangement is given by,

$$M_{\mathrm{con}}(r) = M_0 \hat{Q} + A\,\hat{e}' \cos Qr + A\,\hat{e}'' \sin Qr \tag{6.20}$$

with the ferromagnetic component M_0 and orthonormal basis $\{\hat{\boldsymbol{Q}}_i, \hat{\boldsymbol{e}}'_i, \hat{\boldsymbol{e}}''_i\}$, $\hat{\boldsymbol{Q}}_i = \hat{\boldsymbol{e}}'_i \times \hat{\boldsymbol{e}}''_i$. In the presence of an external magnetic field, the pitch vector and therefore the one-dimensional reciprocal lattice aligns collinear with the field direction, if anisotropies are neglected. The latter is illustrated in Fig. 6.1 (a).

The magnetic texture in the case of a skyrmion lattice can be reproduced by a superposition of three spin helices [Müh09],

$$\boldsymbol{M}_{\mathrm{sky}}(\boldsymbol{r}) \approx \boldsymbol{M}_0 + \sum_{i=1}^{3} A_i \left(\hat{\boldsymbol{e}}'_i \cos \boldsymbol{Q}_i \boldsymbol{r} + \hat{\boldsymbol{e}}''_i \sin \boldsymbol{Q}_i \boldsymbol{r}\right) \qquad (6.21)$$

with the respective amplitudes A_i. It could be shown by minimizing the energy functional with this ansatz, that the helices exhibit the same phase, amplitude $A_j = A$ and pitch vector length $|\boldsymbol{Q}_i| = |\boldsymbol{Q}|$. Additionally, the momentum vectors are restricted to the plane perpendicular to the external field, taking on an angle of 120° with respect to each other. The resulting reciprocal lattice of the skyrmion phase is hence two-dimensional and spanned by two pitch vectors $\boldsymbol{Q}_1$ and $\boldsymbol{Q}_2$, following the hexagonal structure of the skyrmion lattice. A schematic is shown in Fig. 6.1(b). Regarding their different dimensionality, the calculations for the helical/conical/field-polarized and the skyrmion phase will be executed separately.

For the implementation in the numerical analysis, the various Fourier components are summarized in the vectorial representation, given by,

$$\boldsymbol{m}_{\mathrm{con}}(\boldsymbol{k}) = \{\boldsymbol{m}_0, \boldsymbol{m}_{\boldsymbol{Q}}, \boldsymbol{m}_{-\boldsymbol{Q}}, \boldsymbol{m}_{2\boldsymbol{Q}}, ...\}(\boldsymbol{q}) \qquad (6.22)$$

for the one-dimensional lattice and by,

$$\boldsymbol{m}_{\mathrm{sky}}(\boldsymbol{k}) = \{\boldsymbol{m}_0, \boldsymbol{m}_{\boldsymbol{Q}_1}, \boldsymbol{m}_{-\boldsymbol{Q}_1}, \boldsymbol{m}_{\boldsymbol{Q}_2}, \boldsymbol{m}_{-\boldsymbol{Q}_2}, \boldsymbol{m}_{\boldsymbol{Q}_1+\boldsymbol{Q}_2}, \boldsymbol{m}_{-\boldsymbol{Q}_1-\boldsymbol{Q}_2}...\}(\boldsymbol{q}) \qquad (6.23)$$

for the two-dimensional lattice. The individual elements consist of three spatial components, i.e. $\boldsymbol{m}_{\boldsymbol{Q}} = \{m_{\boldsymbol{Q}}^x, m_{\boldsymbol{Q}}^y, m_{\boldsymbol{Q}}^z\}$, which in turn are complex values, possessing a real and imaginary contribution. In general, the momentum space extends up to infinity, but will be limited by introducing a cutoff momentum Λ, so that $|\boldsymbol{Q}| \leq \Lambda$ is fulfilled. With that, only momenta marked by red dots are included in the analysis, as sketched in Fig. 6.1. While for the one-dimensional space Λ is just given by a multiple of $|\boldsymbol{Q}|$, in the case of the skyrmion lattice the cut off is defined by the radius $\Lambda(n, m) = |n \boldsymbol{Q}_1 + m \boldsymbol{Q}_2|$. The resulting rings are illustrated up to the third order in Fig. 6.1(b). Depending on the magnitude of the cut off momentum, the numbers of variables which must be taken into account, increases dramatically. Based on symmetry considerations, like the fixed angle between the momentum vectors and the restriction to the plane perpendicular to the external field, the number can be reduced significantly. Adding anisotropies

(a) 1D reciprocal space   (b) 2D reciprocal space
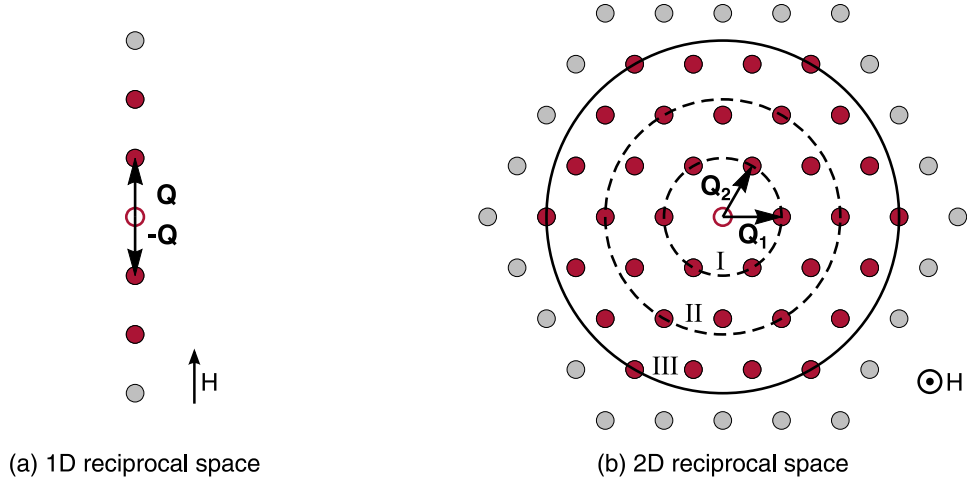
Figure 6.1: Visualization of the (a) 1D reciprocal space, comprising the helical, conical and tilted conical spin arrangement and (b) 2D reciprocal space of the skyrmion lattice. A more detailed description will be given in the main text.

to the theoretical model, however, breaks the aforementioned constraints, leading to a vast number of variables and therefore computational time.

In order to perform the numerical calculations in momentum space, the magnetization vector in the previous results, comprising energy and equation of motion, will be replaced by its converted representation Eq. 6.19. Inserting this Fourier transform into the energy functional Eq. 6.4 results in

$$
\begin{aligned}
F[\boldsymbol{m}] = \sum_{\boldsymbol{k}} \Bigg(&\frac{1}{2}(\boldsymbol{k}\boldsymbol{k})(\boldsymbol{m}_{\boldsymbol{k}}\boldsymbol{m}_{-\boldsymbol{k}}) + i\boldsymbol{m}_{-\boldsymbol{k}}(\boldsymbol{k}\times\boldsymbol{m}_{\boldsymbol{k}}) + r_0\boldsymbol{m}_{\boldsymbol{k}}\boldsymbol{m}_{-\boldsymbol{k}} \\
&+ \sum_{\boldsymbol{k_2},\boldsymbol{k_3},\boldsymbol{k_4}} (\boldsymbol{m}_{\boldsymbol{k}}\boldsymbol{m}_{\boldsymbol{k_2}})(\boldsymbol{m}_{\boldsymbol{k_3}}\boldsymbol{m}_{\boldsymbol{k_4}})\delta_{\boldsymbol{k}+\boldsymbol{k_2}+\boldsymbol{k_3}+\boldsymbol{k_4},0} \Bigg) \\
&+ \tau\Bigg(\boldsymbol{m}_0 N\boldsymbol{m}_0 + \sum_{\boldsymbol{k}\neq 0} \frac{(\boldsymbol{k}\boldsymbol{m}_{-\boldsymbol{k}})(\boldsymbol{k}\boldsymbol{m}_{\boldsymbol{k}})}{\boldsymbol{k}\boldsymbol{k}} \Bigg) - \boldsymbol{B}\boldsymbol{m}_0 \\
&- K \sum_{\boldsymbol{k},\boldsymbol{k_2},\boldsymbol{k_3},\boldsymbol{k_4}} \sum_i m_{\boldsymbol{k}}^i m_{\boldsymbol{k_2}}^i m_{\boldsymbol{k_3}}^i m_{\boldsymbol{k_4}}^i \delta_{\boldsymbol{k}+\boldsymbol{k_2}+\boldsymbol{k_3}+\boldsymbol{k_4},0} \\
&+ C \sum_{\boldsymbol{k}} \sum_i k_i^2 m_{\boldsymbol{k}}^i m_{-\boldsymbol{k}}^i.
\end{aligned}
\tag{6.24}
$$

The notation is chosen to coincide with the one applied in [Cha18]. Compared to the model presented in the mentioned publication ([Cha18]), the functional is additionally extended by the exchange anisotropy. By minimizing the energy, the equilibrium configuration of the magnetization is determined in analogy to Eq. 6.5.

With the magnetization and the resulting effective field given in momentum space, the Fourier transformation of the Landau-Lifshitz equation results in an equivalent representation as provided in Eq. 6.11,

$$\delta m_{\mathbf{Q}'''}^{b}(\mathbf{q}, \omega) =$$
$$\underbrace{\left[\omega \delta^{ib} \delta_{\mathbf{Q}\mathbf{Q}'''} + \frac{i\gamma}{\nu}(\mathbf{m}^{\mathrm{mf}} \times)_{\mathbf{Q}\mathbf{Q}''}(\chi_0^{-1})_{\mathbf{Q}''\mathbf{Q}'''}^{lb}(\mathbf{q}) \right]}_{\mathcal{W}_{\mathbf{Q}\mathbf{Q}'''}^{lb}(\mathbf{q})}^{-1} \left[\frac{i\gamma}{\nu}(\mathbf{m}^{\mathrm{mf}} \times)_{\mathbf{Q}\mathbf{Q}''}^{in} \xi_{\mathbf{Q}''}^{n}(\mathbf{q}, \omega) \right].$$

$$(6.25)$$

Here, the transformed fluctuation matrix [Müh09; Wai17] is given by,

$$(\chi_0^{-1})_{\mathbf{Q}\mathbf{Q}'}^{ij}(\mathbf{q})\delta_{\mathbf{q}',\mathbf{q}} = \frac{\partial^2 F}{\partial m_{-\mathbf{k}}^i \partial m_{\mathbf{k}'}^j}$$

$$= \left(\left(2\, r_0^2\, \delta^{ij} + \mathbf{k}^2\, \delta^{ij} + D^{ij}(\mathbf{k}) + 2\, i \sum_\alpha \epsilon_{i,j,\alpha,}\, k^\alpha \right) \delta_{\mathbf{Q}',\mathbf{Q}} \right.$$

$$+ 4\, \delta^{ij} \sum_{\mathbf{Q}''} (\mathbf{m}_{\mathbf{Q}-\mathbf{Q}'-\mathbf{Q}''}\mathbf{m}_{\mathbf{Q}''} + 2\, m_{\mathbf{Q}-\mathbf{Q}'-\mathbf{Q}''}^i m_{\mathbf{Q}''}^j)$$

$$\left. 2\, C(k^i)^2\, \delta^{ij}\, \delta_{\mathbf{Q}',\mathbf{Q}} - 12\, K \sum_{\mathbf{Q}''} \delta^{ij} \mathbf{m}_{\mathbf{Q}-\mathbf{Q}'-\mathbf{Q}''}\mathbf{m}_{\mathbf{Q}''} \right) \delta_{\mathbf{q}',\mathbf{q}}$$

$$(6.26)$$

with demagnetization energy,

$$D^{ij}(\mathbf{k}) = 2\tau \begin{cases} \dfrac{k^i k^j}{\mathbf{k}^2} & \text{for } kL \gg 1 \\ \delta^{ij} N^{ij} & \text{for } kL \ll 1 \end{cases}.$$

$$(6.27)$$

In the limit of large wavelengths compared to the samples dimension L, the interaction is determined by the demagnetization factors N_x, N_y and N_z, while for large k, the microscopic nature of the dipolar interaction has to be taken into account.

The last two elements are the matrix,

$$(\mathbf{m}^{\mathrm{mf}} \times)_{\mathbf{Q}\mathbf{Q}''}^{ij} \equiv \sum_{\mathbf{Q}'} \epsilon^{ijl} m_{\mathbf{Q}'}^j \delta_{\mathbf{Q}'+\mathbf{Q}'',\mathbf{Q}}$$

$$(6.28)$$

and the time dependent free energy component,

$$\xi_{\mathbf{Q}''}^{i}(\mathbf{q}, \omega) = - \left. \frac{\delta F(\mathbf{Q}'' + \mathbf{q}, \boldsymbol{\omega})}{\delta m_{\mathbf{Q}''}^{i}(\mathbf{q})} \right|_{\mathbf{m}^{\mathrm{mf}}}.$$

$$(6.29)$$

As aforementioned, the latter includes the alternating magnetic field. Likewise to the derivations in real space, also in momentum space the determination of the resonance frequencies and modes are obtained by solving

the respective eigenequation,

$$\mathcal{W}^{ij}_{\boldsymbol{Q}\boldsymbol{Q}'}(\boldsymbol{q})v^j_\alpha(\boldsymbol{Q}+\boldsymbol{q}) = \omega_\alpha v^i_\alpha(\boldsymbol{Q}+\boldsymbol{q}). \tag{6.30}$$

Here, eigenvalues and corresponding orthonormal eigenvectors are denoted as ω_α and $\boldsymbol{v}_\alpha(\boldsymbol{Q}+\boldsymbol{q})$, with

$$\sum_{j,\boldsymbol{Q}}\left(v^j_\alpha(\boldsymbol{Q}+\boldsymbol{q})\right)^*v^j_\beta(\boldsymbol{Q}+\boldsymbol{q}) = \delta_{\alpha\beta} \tag{6.31}$$

Again, for a comprehensive derivation of these equations we refer to [Wai13].

Chapter 7

Results

As aforementioned in the previous chapter, during the course of this thesis, several consecutive microwave spectroscopy experiments were performed. Building up on the gathered experiences, the primary focus and therefore the measurement protocols were constantly shifted, in order to reveal the intrinsic characteristics of the material investigated. With this new input from the experimental side, the theoretical model supporting these findings was adapted respectively. The obtained results will be therefore presented in a chronological order, to reflect the progress made.

The following chapter is divided into three parts. In the first part, the first broad-band microwave spectroscopy experiments and the supporting numerical calculations in the low-temperature regime, which builds upon the knowledge obtained in [Cha18], are presented. Subsequently, in the next section, the temperature dependence of the low-temperature skyrmion phase was investigated, with the main focus lying on the observed hybridization of the resonance modes. Finally, the chapter closes with an extensive study of the angle-dependence of the resonance condition in order to resolve the outstanding issues regarding the energy landscape arising from the underlying cubic lattice structure.

7.1 Microwave Spectroscopy of the Low-Temperature Skyrmion Phase

7.1.1 Experimental Results

The measurements presented in this chapter and published in [Aqe21] are performed on a cube-shaped, single-crystal of Cu_2OSeO_3 by Dr. Aisha Aqeel. With a temperature of $5\,K$ and the external magnetic field applied out of plane and therefore parallel to a [100] direction of the crystal lattice, all the prerequisites are met in order to populate the titled conical and low-temperature skyrmion phase in a certain field range, as observed

in [Cha18]. In order to resolve the resonance spectra the well established all-electrical broadband microwave spectroscopy, as described in Sec. 3.2, is utilized. At a fixed external magnetic field, the complex scattering parameter $S_{12}(f)$ as a function of frequency is recorded by means of a vector network analyzer in combination with a coplanar waveguide. In order to remove the spurious background and improve the signal-to-noise ratio, the high field normalization is applied, leaving $\Delta S_{12}(H)$ the data to be analyzed. Here, the reference field is chosen high enough, i.e. $B = 0.5\,\mathrm{T}$, so that the corresponding data set does not contain resonance modes in the frequency range under consideration. In the conducted experiments, two excitation geometries, simply by moving the sample from the center of the signal line to the gap, are employed. As can be seen in Sec. 3.1, the sample is therefore subject to a dominant in-plane excitation field in the first case and a dominant out-of-plane excitation field in the second case. Nevertheless it should be mentioned, that due to larger dimensions of the sample compared to the CPW, the excitation field will be always a combination of both geometries. If not mentioned otherwise, the sample is placed on the center of the signal line in the following. In previous studies [Moc12; Sch15; Sta17a] it could already be observed, that the application of the oscillating field along certain directions allows to selectively address the different resonance modes of a chiral magnet. Based on these findings, a similar dependence is expected also for the resonance modes in the low-temperature skyrmion phase and will be taken into consideration for the assignment of the latter.

Before elaborating the complex excitation spectra, the measurement protocol established will be discussed in more detail. This defined routine is required for a reproducible outcome due to the hysteretic behavior of the material. In the first step the sample is cooled down to a temperature of $5\,\mathrm{K}$, without an external field applied. This process is referred to as zero-field cooling. Subsequently the magnetic field is ramped up to $120\,\mathrm{mT}$, exceeding H_{c2} for the sample shape investigated, with the purpose of saturating the magnetization and ensuring a collinear alignment. From this point on, the external field is decreased stepwise until reaching the LTS phase, which emerges around $70\,\mathrm{mT}$. Here, at each field value, a frequency sweep is performed. This accumulation of frequency scans will be denoted as H^{init} in the following. The cubic magnetocrystalline anisotropy reduces the energy of the skyrmion lattice with respect to the topologically trivial phases, making it the ground state of the system. However, its respective signatures are found not to be the prevailing contributions to the microwave spectra. These observations originate from the fact that indeed the volume fraction covered by the skyrmion lattice is small, compared to the one assigned to the conical texture. Its is apparent to conclude, that the system is trapped in a local energy minimum and a certain energy barrier must be overcome to establish the formation of topological winding and the associated charge. To overcome this energy barrier and increase the skyrmion number, a con-

trolled field cycling protocol is established. Starting at $70\,\mathrm{mT}$, the external field is continuously decreased to $62\,\mathrm{mT}$ and increased back to the initial field strength. This process is defined as one field cycle, indicated by cycle number $n = 1$. After the cycling protocol, frequency sweeps are carried out either under a decreasing or increasing magnetic field, which is denoted by H^n_{decr} or H^n_{incr}, respectively.

A generic microwave spectrum without field cycling is illustrated in Fig. 7.1(a). Here, dark colors are reflecting a strong absorption induced by the resonant precessional motion of the magnetization. Following the measurement protocol described above, the data acquisition starts at fields, well above H_{c2}. Decreasing the magnetic field leads to a likewise decrease of the resonance position, characteristic for the Kittel mode in the field-polarized phase. However, due to the low magnetic damping at low temperatures, additionally standing spin waves are excited, which are assigned to the replicas of the Kittel mode. The latter is identified by its significantly larger spectral weight. The formation of these additional modes is of great interest, especially on the background of a nonreciprocal spin wave propagation in non-centrosymmetric helimagnets [Gar17], but they will not be further discussed in the context of this thesis. A more detailed study can be found in [Che21]. Below the critical field value H_{c2}, the typically smooth transition into the $+Q$ mode exhibits significant discontinuities, which are attributed to the onset of the tilted conical phase. A further reduction of the magnetic field, in turn, displays an evolution of the resonance frequencies akin to the rotational modes of the conical phase at high temperatures. Also in the conical phase multiple resonance branches are detected, indicating the formation of standing spin waves. In the following, however, only the two prominent ones will be discussed. Here, yellow circles are introduced to highlight the field dependence of the respective resonance frequencies. In the subsequent measurements, shown in Fig. 7.1(b)-(c), the effect of the field cycling is illustrated. As previously described, the resonance spectra are composed of two different sets of frequency traces, H^{init} and H^n_{decr}, separated by the dashed green line. For a moderate cycling number, as given in Fig. 7.1(b), the data set of H^{15}_{decr} already reveals significant changes in the resonances, compared to the results depicted in Fig. 7.1(a). While the spectral weights of the rotational modes of the conical phase decrease, additional resonance branches at lower frequencies are emerging. Further increasing the number of field cycles to $n = 140$ in Fig. 7.1(c), enhances the described effect, leading to distinct resonance modes in the low frequency regime. The similar evolution under the applied field, compared to the counterclockwise and breathing mode of the high temperature skyrmion phase, and the fact that the corresponding spectral weight is increasing with the number of cycles allows to attribute these modes to the low-temperature skyrmion phase. Cyan circles are added to highlight the field dependence of the resonance branch, which is associated with the counterclockwise mode. In the interest of clarity the approximate
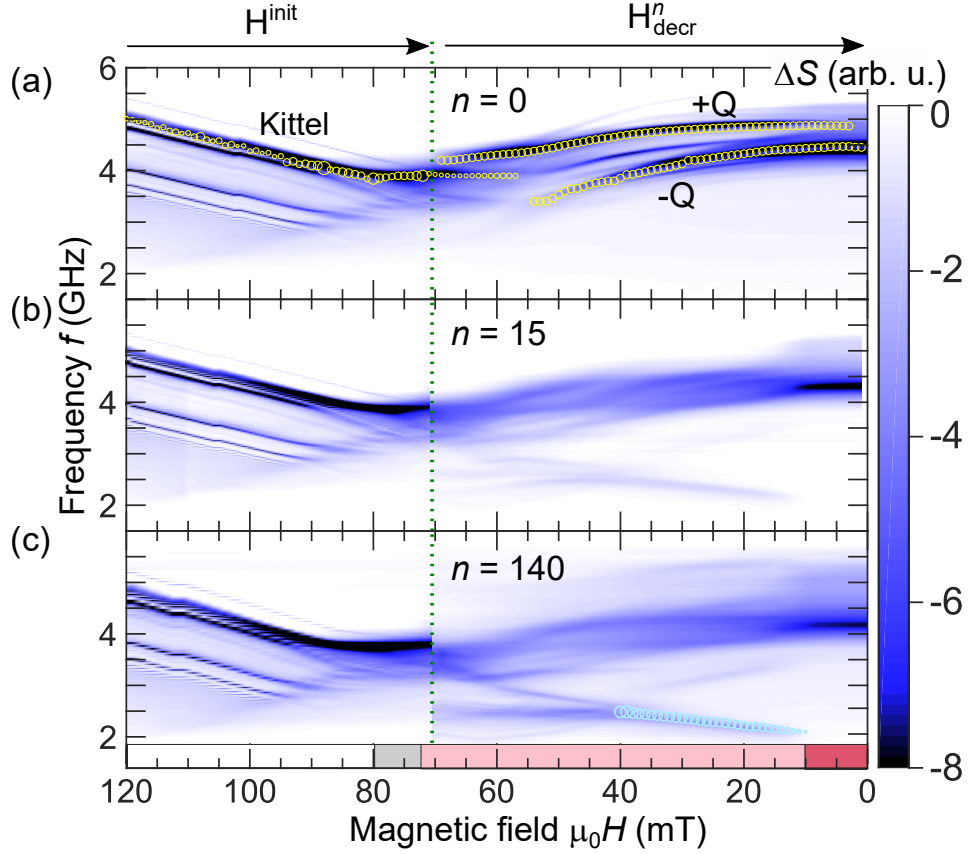
Figure 7.1: Evolution of the microwave spectra as a function of number of field cycles n. The normalized microwave absorption intensity ΔS is represented by the color gradient, with dark colors indicating a strong absorption. The first part of the spectra, the left hand side with respect to the dashed green line, is recorded during an initial H^{init} scan down to $70\,\text{mT}$. The second part is covered by a H^{n}_{decr} scan, after n preceding field cycles. By applying the field cycling protocol, the volume fraction of the conical and tilted conical phase decreases, while the one of the low-temperature skyrmion phase increases. This can be observed by the decrease of the spectral weight of the conical and tiled conical resonance modes (yellow open symbols) and the emergence of low frequency modes (cyan open symbols), which are associated with the LTS phase. Resonance positions are obtained from Lorentzian fits applied to the individual frequency sweeps. The color bar at the bottom indicates the individual phases. The field-polarized, tilted conical, hexagonal skyrmion lattice and oblique skyrmion lattice phases are reflected by white, gray, light red and red colors. Figure taken from [Aqe21].

phase boundaries of the different magnetic phases are indicated by the color shading of the external field at the bottom of Fig. 7.1(c). While white and gray illustrate the field-polarized and the tilted conical phase, respectively, the skyrmion boundaries are given by the light red and red color. The latter is divided into two pockets, due to the potential formation of an elongated low-temperature skyrmion (eLTS) lattice phase, which will be elaborated later.

In order to gain more insight into the characteristics of the additional modes appearing, the different driving field distributions arising from the two opposed excitation geometries are exploited, as summarized in Fig. 7.2. From previous studies [Moc12; Sch15; Sta17a] it is already known, that the resonance modes in the field-polarized and conical phase, as well as the gyrational modes in the skyrmion state couple to an in-plane ac-field, while only the breathing mode is sensitive to an out-of-plane driving field. It stands to reason that a similar behavior is therefore also expected to be observed in the low-temperature limit. In contrast to the results presented in Fig. 7.1, the two spectra are in each case composed by frequency sweeps, which are recorded under an increasing H_{incr}^{140} and decreasing H_{decr}^{140} external field, both after 140 field cycles. It allows hence to study also the effect of the field cycling on the frequency sweeps for field values above the cycling region. In the in-plane configuration, represented by the spectrum on the left hand side of Fig. 7.2, the most prominent excitation is the one in the high field limit, assigned to the Kittel mode and its numerous replica of the field-polarized phase. In the field regime of interest, inside the boundaries of the LTS phase, the spectral weight however is distributed over a wide frequency range due to the coexistence of the conical and skyrmion modes. Despite its multiple features, the focus is guided to the low frequency resonance branch, highlighted by the open cyan symbols. Originating from the monotonous increase in frequency with a likewise increasing field, its field dependence resembles the one of the counter clockwise mode of the HTS phase. It is therefore assigned to its counterpart in the low-temperature limit. Moving the sample towards the gap, as shown in the inset on the right hand side, the strength of in-plane oscillating field component, acting on the magnetization, is attenuated, while the one of the out-of-plane component is enhanced. As a consequence, the total absorbed microwave power is reduced significantly, as expected from the arguments given above. While only weak remnants of the excitations assigned to the CCW mode are visible, another resonance branch, which is divided into three segments, gains more intensity. Here, orange symbols are introduced as a guide to the eye. This mode, covering the whole field range, exhibits an increase in resonance frequency with decreasing field, which is, up to now, only known from the field evolution of the breathing mode. Supported by the numerical calculations presented later, it is therefore assigned to the breathing mode in the anisotropic case. Interestingly, its features also clearly extend down
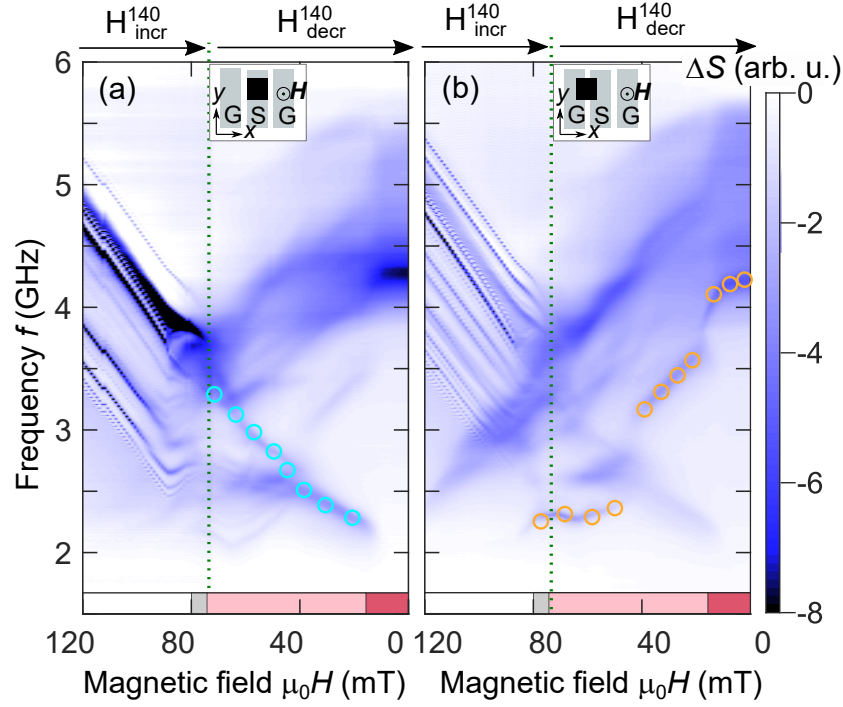
Figure 7.2: Microwave spectra recorded for two different excitation geometries, as schematically illustrated by the insets. By centering the sample on the signal line (a) it is subject to a dominant in-plane excitation field, while placing it on the gap (b) the out-of-plane ac-field is prevailing and mainly driving the magnetization dynamics. The shown results are each obtained from the two independent measurements routines, H_{incr}^{140} and H_{decr}^{140}, after 140 field cycles. The excitation branches associated with the counterclockwise and breathing mode are highlighted by the open cyan and orange symbols. Resonance positions are obtained from Lorentzian fits applied to the individual frequency sweeps. The color bar at the bottom indicates the individual phases. The field-polarized, tilted conical, hexagonal skyrmion lattice and oblique skyrmion lattice phases are reflected by white, gray, light red and red colors. Figure taken from [Aqe21].

to zero-field. As it will be discussed in regards of the numerical results, these resonances might originate from an oblique distortion of the skyrmion lattice at lower fields, as predicted in [Cha18].

In order to support this anticipated assumption from the experimental side, the respective resonance frequencies of the LTS and conical phase in the low-field limit have to be compared. For this reason, two microwave spectra recorded after different cooling and cycling protocols are contrasted in Fig. 7.3. On the left hand side (Fig. 7.3(a)), the results obtained after $n = 70$ cycles are illustrated, resembling the one shown in Fig. 7.1. Here, the spectrum is mainly dominated by the skyrmion resonances in the field range of interest. For the measurements collated in Fig. 7.3(b), the magnetization configuration was first reset by exceeding temperatures well above T_c and a subsequent zero-field cooling process. Starting at $0\,\text{mT}$, frequency sweeps are performed under an increasing magnetic field, afterwards. With the applied cooling protocol, the spin texture is expected to decay into a multi domain helical/conical state at low magnetic fields, with the pitch vectors aligning along the easy axes, predefined by the anisotropies [Sch15; Cha18]. Enhancing the magnetic field, causes the helices to rotate out of their preset alignment and orientate parallel with respect to the field direction. Consequently, a single domain state is formed. As it is obvious from the shown line scans, the signatures of the low-temperature skyrmion phase, namely the low frequency resonance branches, are not present in the excitation spectrum, given on the right hand side. It is determined only by the resonance frequencies of the $\pm Q$ modes of the conical and tilted conical phase and the Kittel mode of the field-polarized state. Comparing now the resonance positions of both data sets around zero magnetic field, discloses a distinct difference, suggesting indeed a different magnetic texture as its origin. This leads to the assumption that, due to the applied cycling and field sweep routine in combination with the hysteretic character of the skyrmions, the LTS phase exceeds down to low magnetic fields in a metastable, but robust state in the microwave spectra presented. More precisely, based on the resolved jump in frequency at around $\mu_0 H = 12\,\text{mT}$, which indicates the transition into an oblique lattice structure according to the numerical findings discussed later on, the resonances in the low-field limit are assigned to the elongated skyrmion lattice phase.

7.1.2 Theoretical Results

Parts of the numerical results presented in this section are published in [Aqe21]. The numerical treatment of our theoretical model is divided up with regard to the dimensionality of the employed reciprocal lattices, as elaborated in Sec. 6.4. In the first part of this section the topologically trivial states, including helical, conical, tilted conical and field-polarized phase, are discussed, while in the second part the analysis of the skyrmion
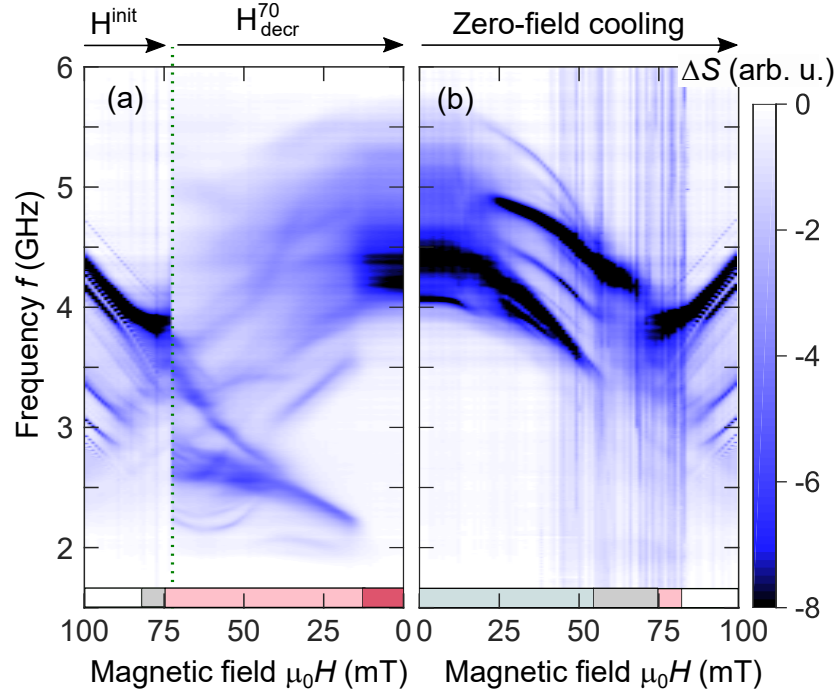
Figure 7.3: Comparison of excitation spectra obtained for two different measurement protocols. (a) Composition of a H^{init} and H^{70}_{decr} data set. (b) Spectrum recorded for an increasing external field, after reseting the magnetization by an initial zero-field cooling process. Emphases is put on the different resonance conditions in the low-field limit. The color bars at the bottom indicate the individual phases. The field-polarized, tilted conical, helical/conical, hexagonal skyrmion lattice and oblique skyrmion lattice phases are reflected by white, gray, light green, light red and red colors. Figure taken from [Aqe21].

lattice phase is covered.

1D Reciprocal Space

The main focus of this work is on the unrevealed effect of cubic magnetic anisotropies on the collective spin excitations of a chiral magnet. The latter, however, requires first the determination of the equilibrium configuration of the magnetization, which in interest of completeness, will be likewise presented in a comprehensive execution. The magnetic texture, minimizing the energy functional given by Eq. 6.24 is obtained by solving equation Eq. 6.5 for the fixed parameter set r_0, τ, K, N_i and B [1]. For this step, a

---

[1] Note, as elaborated in Chap. 6, these parameters are dimensionless. In the interest of clarity, the tilde notation is, however, omitted.

default configuration of the magnetization, determined by an initial set of pitch vectors and Fourier components (Sec. 6.4), is fed into the minimization algorithm. Here it should be mentioned that, in general, these start parameters have a significant impact on the resulting equilibrium state. In addition to that, the result also strongly depends on the symmetries imposed on the reciprocal lattice and the corresponding Fourier components of the magnetization. Therefore, in order to approach the global and not just a local minimum configuration, several different default parameters are used for the minimization routine. The setup established for the calculations is given in the following. The sample coordinate system is chosen to coincide with crystallographic directions, i. e. $x \parallel [100]$, $y \parallel [010]$, $z \parallel [001]$. If not stated otherwise, the external magnetic field is applied along the $[001]$ direction and the Ginzburg-Landau coefficient is set to $r_0 = -1000$ in accordance with [Cha18]. Finally, the investigated sample shape is a sphere with demagnetization factors $N_x = N_y = N_z = \frac{1}{3}$ and the respective dipolar interaction strength of $\tau = 0.88$, obtained from previous studies [Sch15]. With this, only anisotropy value K and magnetic field strength B enter the theoretical model as free parameters.

In the following the results inferred from the minimization routine will be discussed. The data are presented as a function of field, determined for various anisotropy values, which are ranging between $K = 0.0003 - 0.0004$. From previous studies [Cha18] these anisotropy strengths are proven to be sufficient enough to enable the formation of the tilted conical and low-temperature skyrmion phase.

For the characterization of the magnetization configuration, the enclosed angles between the pitch vector of the spin helices and the crystallographic axes will be analyzed first. In Fig. 7.4(a) - (b) the tilt angles ϕ and θ, which result from the projection onto the $[100]$ and $[001]$ direction, respectively, are illustrated. Note, by definition, the latter displays also the deviation from the applied field direction. It is therefore instructive to start the discussion with these observations. For a given anisotropy value of $K = 0.0003$ the magnetization texture remains in a conical configuration with the static magnetization component aligned collinear with the external field. The additional energy term, appears to not have any effect on the equilibrium position of the spin helices. When increasing K slightly, the tilt angle θ reaches finite values for a certain field range. The pitch vector starts to tilt, but relaxes back into its prior equilibrium position, for an increasing external field. Exceeding a certain anisotropy strength, $\boldsymbol{Q}$ does no longer align with the $[001]$ direction at higher field values, but abruptly increases its inclination. Moreover, also the first transition into the tilted state occurs in the form of a discontinuity. The tilt angle ϕ, given in Fig. 7.4(a), displays a similar field and anisotropy dependence as θ. Due to the initial perpendicular alignment with the $[100]$ axis, the direction of the canting is reversed though. The angle decreases for an increasing magnetic field. With
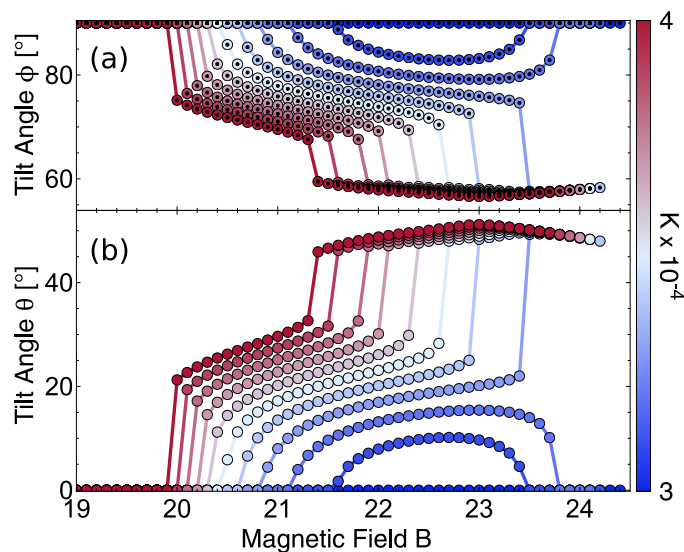
Figure 7.4: Calculated tilt angles of the pitch vector $\boldsymbol{Q}$ with respect to the [100] (a) and [001] (b) crystallographic direction for various anisotropy values K as a function of applied field B. The remaining parameters are set to $r_0 = -1000$, $\tau = 0.88$ and $N_i = 1/3$.

the components of the pitch vector extracted from the numerical data, it follows that the deflection is confined to the $[001] - [110]$ plane. These findings can be easily verified by calculating the respective tilt angle $\phi' = \arccos \frac{\sin \theta}{\sqrt{2}}$ of a unit vector restricted to this plane, by inserting the extracted angle θ. The results obtained are given by the small black dots in Fig. 7.4(a). The pitch vector therefore indeed cants from the easy to the hards axis of the cubic magnetocrystalline anisotropy. It should be mentioned that the sign of the obtained angles and with this the tilting direction are results of the default configuration set at the beginning of the calculation. Due to the four equivalent directions, the tilted conical phase is expected to decay into an equally populated multiple domain state.

Besides the orientation of the pitch vector, also the respective wavenumber $|\boldsymbol{Q}|$ is subject to the additional energy term. The field dependence of the pitch length calculated for various anisotropy values is summarized in Fig. 7.5. As it was observed in regard of the tilt angles, the anisotropy does not affect $|\boldsymbol{Q}|$ for a given strength of $K = 0.0003$. Increasing K, the helix cants towards the [111] direction and simultaneously the length of the pitch vector decreases, until continuously relaxing back into the conical state with $|\boldsymbol{Q}| = 1$. At larger anisotropy constants the field dependences are divided into two ranges, enclosed by the sudden changes, which are attributed to the ones resolved in Fig. 7.4. The overall course is governed by a decrease of the wavenumber under an increase of the magnetic field. The wavelength
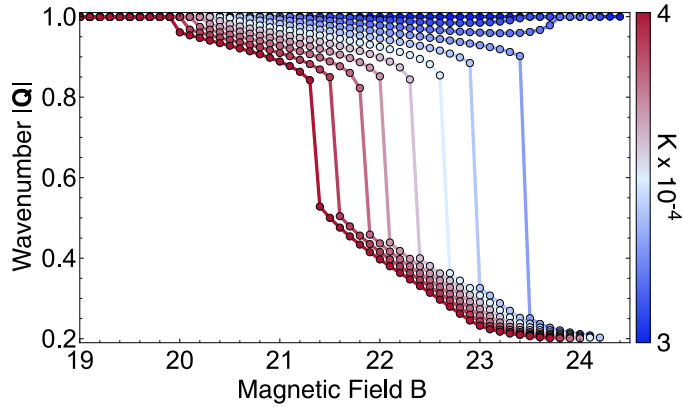
Figure 7.5: Calculated length of the pitch vector $\boldsymbol{Q}$ for various anisotropy values K as a function of applied field B. The remaining parameters are set to $r_0 = -1000$, $\tau = 0.88$ and $N_i = 1/3$.

of the modulation given in real-space is therefore increasing. Note, the obtained results reproduce the ones presented in [Cha18] largely, but exhibit also considerable deviations. This discrepancy might originate from different employed symmetries of the one-dimensional reciprocal lattice in combination with the corresponding Fourier components of the magnetization, as discussed in Sec. 6.4.

The application of the Fourier transform, allows to visualize the magnetization texture in real-space for the obtained equilibrium configurations. In Fig. 7.6 a three-dimensional representation of the individual spin helices is illustrated for the anisotropy strength set to $K = 0.0004$ and $B = 0$, 19, 20.5 and 22. The field range is chosen to comprise all the modulated textures associated to the one-dimensional momentum space. The direction of the externally applied field is given by the blue arrow, on the left hand side. In accordance with the chosen color code, a collinear alignment of the magnetization with the magnetic field is likewise reflected by blue, while a perpendicular orientation is indicated by white arrows. The first two configurations calculated at $B = 0$ and $B = 19$ are the well established helical and conical state, which differ by the deviation from the perpendicular alignment of the spins with respect to $\boldsymbol{Q}$ in the case of the latter. Traversing the phase transition into the tilted conical state, the pitch vector deviates from a parallel alignment with respect to the external field and tilts towards the [111] direction. By further increasing the magnetic field strength, the energy landscape of the chiral magnet is mainly dominated by the Zeeman interaction, favoring a collinear alignment between the magnetization and the external field. With this more spins align along the field direction, resulting in a localized winding of the magnetization and consequently a longer wave length of the modulation, as shown in Fig. 7.6e.
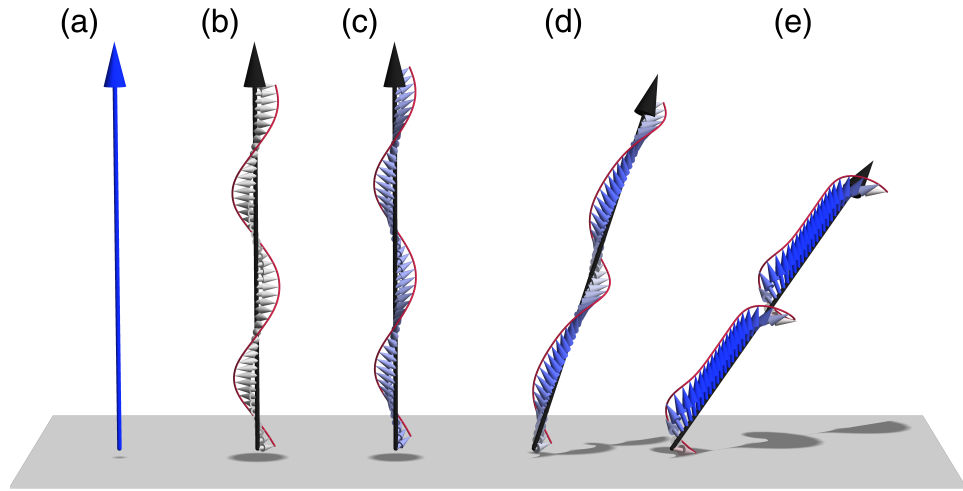
Figure 7.6: 3D visualization of the evolution of the spin helices under increasing magnetic field. The anisotropy strength is set to $K = 0.0004$ and the magnetic field to $B = 0$ (b), $B = 19$ (c) $B = 20.5$ (d) $B = 22$ (e). The remaining parameters are set to $r_0 = -1000$, $\tau = 0.88$ and $N_i = 1/3$. The blue arrow (a) on the left hand side displays the external field direction. The color code of the magnetization reflects the orientation with respect to the applied field. A collinear alignment is given by blue, while a perpendicular alignment is indicated by white.

In real-space imaging experiments on chiral magnets the main focus is on the resolution of the skyrmion lattice plane, perpendicular with respect to the externally applied field. While in this configuration the magnetization of the helical and conical state is uniform within the plane, provided the pitch vector is aligned along the field direction, from the results presented above a periodic structure for a finite canting angle of the pitch vector is expected to be displayed. In Fig. 7.7(a)-(b) two dimensional maps of the normalized z component of the static magnetization are illustrated, obtained for the states given in Fig. 7.6(d)-(e), i.e. with the field set to $B = 20.5$ and $B = 22$. A collinear alignment with the magnetic field is indicated by blue, whereas red, which is not clearly represented in these plots, corresponds to an anti-parallel orientation. In the depictions beneath, Fig. 7.7(ii)-(iv), the individual magnetization components, resolved for the coordinates indicated by the black arrows, are shown. For the comparison to the conical phase, the distance is measured in units of $2\pi/Q_c$, with pitch vector length Q_c obtained in the conical state. In general, for a line scan oblique with respect to the pitch vector, the periodic behavior is imposed on all magnetization components for the modulated states. In the case of the helical and conical phases, it is expected to be described by a sinusoidal function. As displayed in Fig. 7.7(ii)-(iv), this description can not be applied, indicating a

deviation from the screw-like arrangement of the spins, in the tilted conical states. Increasing the external field further, the Zeeman interaction enforces the formation of ferromagnetic domains, resulting in a localized winding of the magnetization, as anticipated before. Consequently, the wave length in real-space increases whereas the pitch vector length decreases. Note, since Fig. 7.7 illustrates the projected magnetization, a scaling factor, dependent on the angle between plane and pitch vector, is required for the conversion into the actual pitch length. In conclusion, the canting of the pitch vector is expected to be easily observed in a perpendicular field configuration, by the appearance of a periodic modulated magnetization. It should be mentioned that, however, the twisting of the spins at the surface, which arises from the DMI interaction [Mey14], might not be negligible and therefore diminish or even mask the signatures of the tilted conical phase.

With the mean field configuration obtained from the minimization algorithm, the resonance frequencies and modes are calculated by the eigenvalue equation given by Eq. 6.30. The setup is chosen in accordance with the previous results, i.e. the sample investigated is of spherical shape and the external magnetic field is aligned along the [001] direction of the crystallographic lattice. For now, the analysis is limited to the resonances of the topologically trivial state, comprising field-polarized, tilted conical and conical states. Additionally, if not stated otherwise, the calculations are performed at the Γ-point, indicating a uniform excitation of the dynamic magnetization.

In Fig. 7.8 the field dependence of the resonance frequencies, determined for various anisotropy strengths K, is presented. The spectral weight (Eq. 6.18), which serves as a measure for the coupling efficiency to the oscillating magnetic field, is reflected by the size of the symbols. In the interest of clarity, for this general discussion of the effect of the cubic anisotropy on the spectra, a cut off for the spectral weight is introduced in the last two panels. The whole spectra, which comprise a multitude of excitation modes, will be discussed in more detail later on. As already observed in preceding studies [Sch15], the eigenmodes are only driven by an ac-field perpendicular with respect to the pitch vector and the static magnetic field, respectively. Due to the canting of the pitch vector, however, the tilted conical modes might also be sensitive to an out plane driving field. Since the efficiency is smaller than the chosen cut off value in the numerical results presented beneath, the corresponding resonances are excluded from the spectra. For the illustration purpose, the field and frequency axes are normalized by the critical transition field $B_{c2,0}$ and the critical field frequency $\nu_{c2}^{int} = \frac{g\mu_B\mu_0 H_{c2,0}^{int}}{2\pi\hbar}$. Here, $B_{c2,0}$ and $H_{c2,0}^{int}$ are extracted in absence of the cubic anisotropy, as indicated by the index 0. Note, in contrast to the experimental data, the field axis is displayed in ascending order.

The calculations obtained in the case of $K = 0$, shown in Fig. 7.8(a),
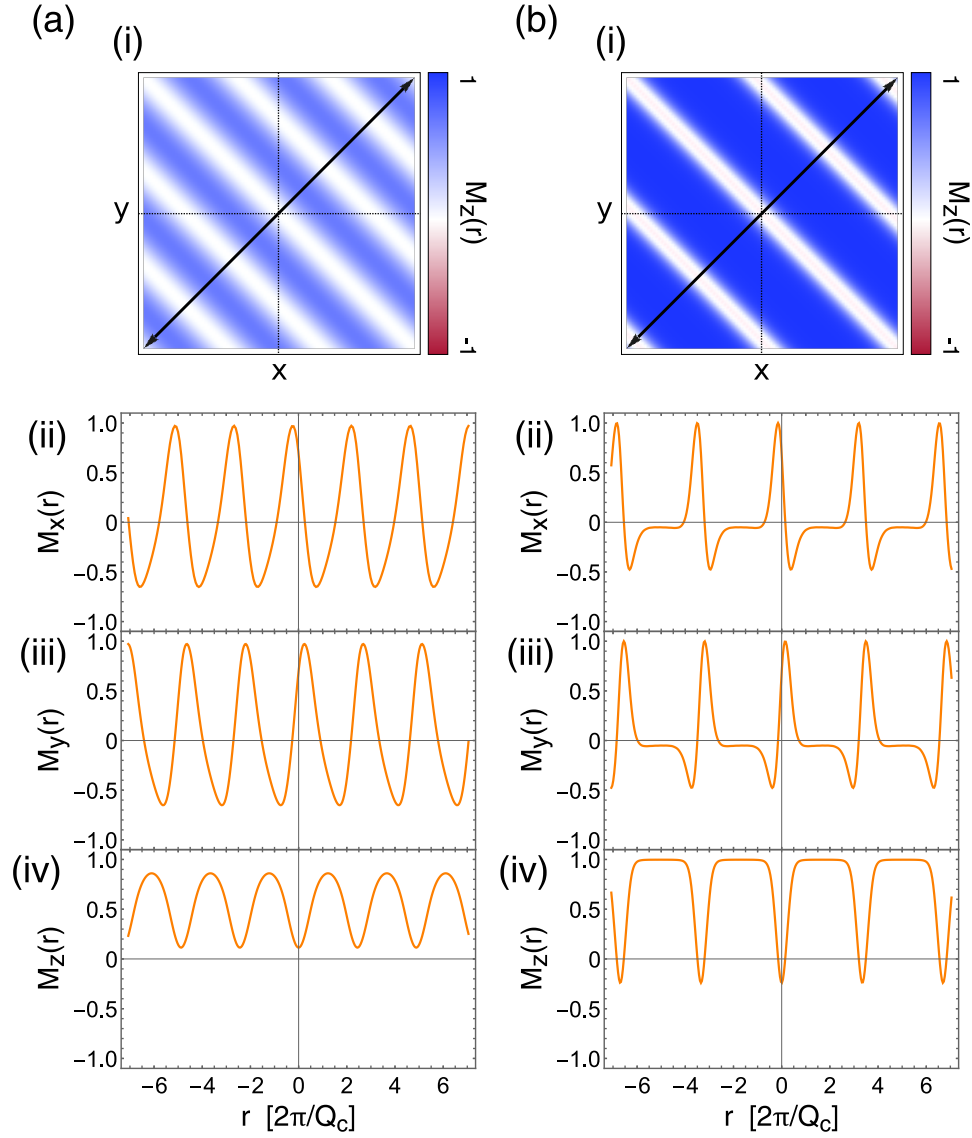
Figure 7.7: Visualization of the magnetization configuration of the tilted conical phase within the plane perpendicular to the external field for $B = 20.5$ (a) and $B = 22$ (b). (i) 2D maps of the z component of the magnetization, with blue and red color indicating a parallel and anti parallel alignment with respect to the magnetic field. (ii)-(iv) Line scans of the individual components along the black arrows, given in (a) and (b). Coordinate r is given in units of Q_c, defined as the pitch vector length of the conical state.
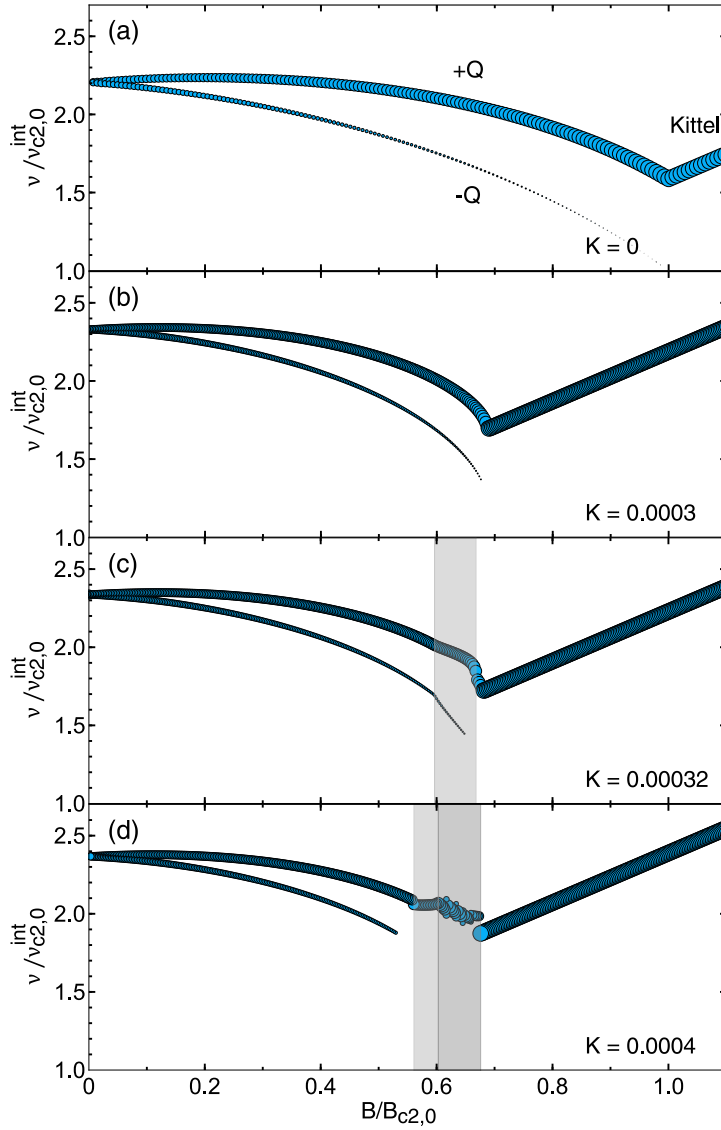
Figure 7.8: Theoretically predicted spectral weights (symbol size) for a spherical sample calculated for different anisotropy values K. Field and frequency axes are normalized by $B_{c2,,0}$ and $v_{c2,0}^{int}$, respectively. Here, the spectral weight indicates the coupling efficiency to an driving field perpendicular to the external magnetic field. The remaining parameters are set to $r_0 = -1000$, $\tau = 0.88$ and $N_i = 1/3$. The gray and dark gray shadings in the last two panels highlight the two different tilted conical phases.

reproduce the well-established universal excitation spectrum as expected. In the conical phase, the two resonance branches are identified as the $\pm Q$ modes. Due to the chosen sample shape, they are degenerate at zero magnetic field. Approaching the phase transition into the field-polarized state, the $+Q$ mode merges smoothly into the Kittel mode, while the spectral weight of the $-Q$ mode continuously decreases. For a value of $K = 0.0003$, the magnetization configuration is still not effected by the anisotropy as already elaborated in the field dependence of the tilt angle and pitch length given in Fig. 7.4 and Fig. 7.5. The overall appearance of the corresponding excitation spectrum resembles therefore the results presented in Fig. 7.8(a). The additional energy term, however, changes the slope of the rotational modes and increases the frequency of the benchmarks $\nu(B_{c2,K})$ and $\nu(0)$. In combination with the reduced critical field $B_{c2,K}$, the spectrum appears to be compressed with respect to the field axis. In the field-polarized state, the anisotropy enters the Kittel mode as a field-independent contribution. The additional energy term leads to a shift in frequencies towards higher values, with the slope remaining unchanged.

Exceeding an anisotropy strength of $K = 0.0003$, leads to a finite angle between the pitch vector and the external field direction and with this to the formation of the tilted conical phase, as presented above. As a consequence, the resonance branches of the conical phase do no longer decrease continuously as a function of field, but exhibit several anomalies originating from the additional phase transition. In panel Fig. 7.8(c), the excitation spectrum calculated with the anisotropy strength set to $K = 0.00032$ is shown. From the results discussed in Fig. 7.4 it could be observed that for this K value, the first transition from the conical phase is rather smooth, while the second transition back into the conical phase from the tilted conical phase is accompanied by a sudden jump with regard of the tilt angle. As can be seen in the respective microwave spectrum, these distinct phase transitions are also reflected in the field-dependence of the resonance frequencies. The onset of the first phase transition is marked by the smooth change of slope around $B = 0.6\,B_{c2,0}$. In this field range, indicated by the gray shading, the resonance frequencies are changing continuously until reaching a field value of around $B = 0.65\,B_{c2,0}$. At this point the resonance spectrum exhibits a clear discontinuity, which is attributed to the abrupt change in the tilt angle. The pitch vector is again aligned with the external field and the magnetization dynamics correspond to the ones of the conical modes, which, in case of the $+Q$ mode smoothly connects to the Kittel mode of the field-polarized phase.

Finally, in the last panel, Fig. 7.8(d), the excitation spectrum, obtained from the calculations with the anisotropy strength fixed to a value of $K = 0.0004$, is visualized. Before evaluating these findings its is instructive to recall again the results of the magnetization configuration with respect to the tilt angle. Due to the enhanced anisotropy strength, the canting of the

pitch vector is no longer continuous but governed by a sudden increase of θ. In addition to that, the magnetization does not relax back into a conical configuration, but tilts even further into the [111]-crystal direction. This transition is also indicated by an abrupt change of the tilt angle and marks an additional phase. Finally, the phase transition into the field-polarized state is no longer mediated by the conical phase, but occurs directly from the tilted conical phase. As could already be seen above, these changes in the magnetic texture are also reflected in the field dependence of the excitation frequencies. The transition into the first tilted conical phase can be identified by the discontinuity of the $+Q$ resonance branch, at a field value of approximately $B = 0.55\,B_{c2,0}$. Its respective excitation frequencies, which are highlighted by the gray shading, are characterized by an almost field independent curve progression. At a field value of around $B = 0.6\,B_{c2,0}$ a second anomaly in the form of a sudden change of slope emerges, which indicates the aforementioned additional canting of the pitch vector. Interestingly, despite its smooth variation in the magnetization configuration, this second region, indicated by the dark gray shading, exhibits a multitude of discontinuities in the frequency domain accompanied by a repeated change of the spectral weight. It should be mentioned that the field evolution of the resonance frequencies is masked by the introduction of the spectral weight cut off in this illustration, but will be evaluated in more detail later on. Originating from the sudden spin-flop at the transition field, the tilted conical modes do not merge smoothly into the Kittel mode anymore. A clear frequency gap between these resonance branches is predicted to be observed.

Before resolving these kinks and discontinuities originating from the additional energy term in an expanded view, it is instructive to return to the universal microwave spectrum, calculated in absence of the cubic anisotropy. In general, the presentation is limited to the well-established $\pm Q$ and the Kittel modes, as given in Fig. 7.8(a). Besides the clockwise and counter-clockwise modes, the conical phase however hosts a multitude of higher order modes, which could also be experimentally resolved in [Wei17], despite their small spectral weight. Due to their lack of a macroscopic dipole moment they are also referred to as dark modes in the following. The theoretically predicted real-space visualization of the magnetization dynamics for the first 16 modes, lowest in frequency, is illustrated in Fig. 7.9 for a certain time t. As anticipated before, the cubic anisotropy is not included in the calculations and the external field, $B = 15$, is chosen to arrange the formation of a spin helix with a cone angle smaller than $90°$. The individual spin sites along one helix period, indicated by the gray symbols, are given in a polar presentation for reasons of simplicity. The amplitude of the respective dynamic z component of the magnetization is displayed by the black symbols. The color code for the enclosed areas emphasizes the orientation of $\delta M_z(t)$ with respect to the pitch vector direction, ranging from an anti-parallel (red) to a parallel alignment (blue). Note, for illustration
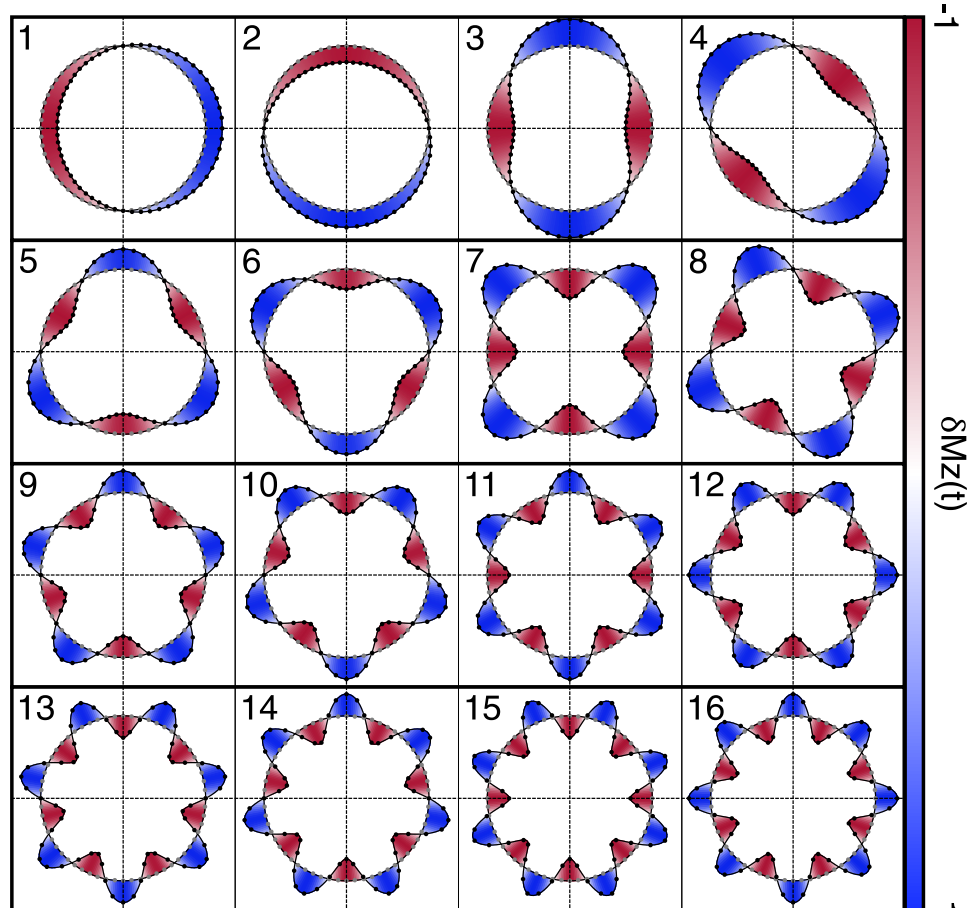
Figure 7.9: Theoretically predicted real-space visualization of the z component of the dynamic magnetization at a certain time t for the first 16 modes. The calculations are performed in absence of the cubic anisotropy at a magnetic field strength of $B = 15$, corresponding to the conical phase for a spherical sample. The remaining parameters are set to $r_0 = -1000$, $\tau = 0.88$ and $N_i = 1/3$. The gray symbols are attributed to the equilibrium position of the spin sites along one helix period, which is mapped onto a circle for reasons of simplicity. The corresponding dynamic component of the magnetization is given by the black symbols. The color code for the enclosed areas indicated a negative (red) or positive (blue) of $M_z(t)$. Note, for the illustration, the latter was multiplied by a scaling factor of 3.

purposes, the amplitude of $\delta M_z(t)$ was multiplied by a scaling factor of 3. The obtained modes are arranged in an ascending order with respect to their resonance frequencies. Characterized by their node number, they are divided into groups of two, comprising each an element with clockwise and counterclockwise sense of rotation, apart from modes 3, 4 and 7, 8. While the former group shows only an oscillating motion, the latter exhibits both a rotational and oscillating magnetization dynamics. The first two modes are the extensively studied $\pm Q$ resonance branches of the conical phase. Due to their finite magnetic dipole moment compared to the others, they likewise exhibit a finite spectral weight and are therefore very likely to be excited in broadband microwave experiments. Interestingly, apart from this group, the elements of the remaining ones are degenerate. They all demonstrate the same field dependence as the clockwise mode, only shifted along the frequency axis. This can also be observed for an anisotropically shaped sample.

With these observations in mind, the microwave spectra obtained in the case of $K = 0.00035$ and $K = 0.0004$ will be discussed in more detail. The field range, normalized by the anisotropy dependent transition field $B_{\text{c2},K}$, is set to limit the focus mainly on the tilted conical phase, as given in Fig. 7.10. Additionally, the frequency axis is expanded to take also higher order modes into account. The presentation of the excitation spectra is chosen to coincide with the ones described above. Compared to Fig. 7.8, however, the spectral weights are extended by the contribution arising from an out-of-plane oscillating field, represented by the gray symbols. Here, it should be mentioned that the coupling efficiency to this field direction is non-zero, but rather small. On that account, an additional scaling factor of 3 was introduced in order to highlight the latter. Besides the spectral weights, more importantly the general field dependence of the resonance frequencies, given by the black dots, is displayed. This allows to visualize also the modes, exhibiting a vanishing spectral weight. In the conical phase, which exceeds up to a field value of around $B = 0.85\,B_{\text{c2},K}$ in Fig. 7.10(a), four distinct resonance branches are visible in the plot range, employed. While the first two are the $\pm Q$ modes, the last ones are identified as mode number three and four in regard of Fig. 7.9. Interestingly, the degeneracy of these is lifted, in contrast to the results extracted from the isotropic model. Traversing the boundary of the titled conical phase, the increase of the tilt angle and the simultaneous decrease of the wavenumber is accompanied by a significant change in slope for the said modes. Excluded from this is the $+Q$ mode, which mainly remains constant under an increase of the magnetic field strength. Conversely, the spectrum of the second region of the tilted conical phase, ranging between $B = (0.93 - 1)\,B_{\text{c2},K}$, is subject to fundamental changes and stands out for a high degree of complexity. The initially distinctively separated resonance branches undergo a drastic decrease in slope, leading to an accumulation of a multitude of higher order modes in the frequency range considered. The
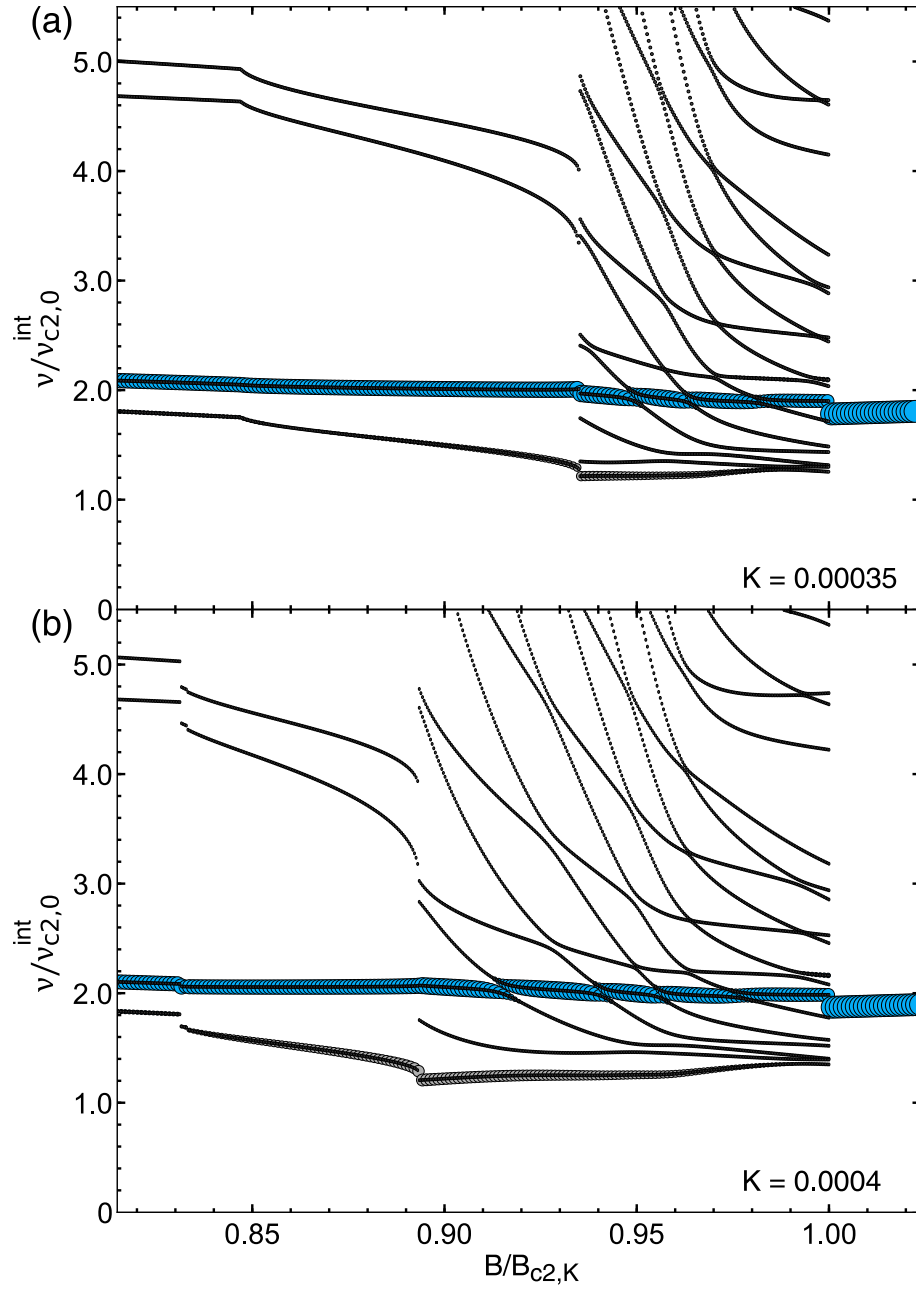
Figure 7.10: Theoretically predicted spectral weights (symbol size) for a spherical sample calculated for different anisotropy values K. Field and frequency axes are normalized by $B_{c2,,0}$ and $\nu_{c2,0}^{int}$, respectively. Here, the spectral weight indicates the coupling efficiency to a driving field perpendicular to the external magnetic field. The remaining parameters are set to $r_0 = -1000$, $\tau = 0.88$ and $N_i = 1/3$.

$+Q$ mode, remaining the dominant mode, exhibits only minor changes in its general field dependence. With increasing field the frequencies decrease but subsequently increase again, in accordance with the reversed increase and decrease of the tilt angle, as displayed in Fig. 7.4. This change of slope is, however, barely noticeable. On the other hand its progression is crossed by several higher order modes, resulting in the alternating decrease and increase of the spectral weight at the interaction points. With specific reference to these observations, a description in terms of anti-crossing or hybridization is more accurate. At no time, the resonance branches are degenerate. The hybridization mechanism is not limited to the $+Q$ mode only, but can also be resolved for the interaction among higher order modes. Interestingly, the frequency gap, which serves as an indication of the interaction strength, varies strongly, depending on the hybridization modes. This suggest that, a certain selection rule is imposed by the underlying crystal lattice. In the case of the second mode, which exhibits a finite spectral weight, a slight increase of the resonance frequencies with a likewise increasing field is observed. Its respective time evolution is characterized by a clockwise rotational motion akin to the $-Q$ mode of the conical phase. In contrast to the isotropic case, however, the dynamic response of the magnetization is susceptible to an out-of-plane driving field, as indicated by the gray symbols. The corresponding coupling efficiency is decreasing for both cases, approaching the conical and the field-polarized phase, respectively from the internal transition field of the tilted conical phase at a field of around $B = 0.93\, B_{\mathrm{c}2,K}$. In the bottom panel Fig. 7.10(b) the results, obtained for an anisotropy strength of $K = 0.0004$, are depicted. The most striking change in the microwave spectrum is the shift of the field boundary of the second tilted conical region, induced by an earlier inclination of the pitch vector regarding the field value. Comparing the field range $B = (0.93-1)\, B_{\mathrm{c}2,K}$ of both plots, reveals a high resemblance of the field dependence of the individual resonance branches. The spectrum calculated for the larger anisotropy values therefore appears to be an extension of the results displayed in Fig. 7.10(a) towards lower field values, which allows for further hybridizations.

As anticipated before, in absence of the cubic anisotropy, the eigenvectors of the conical state exhibiting the same number of nodes are degenerate, except for the $\pm Q$ modes. By introducing the additional energy term, however, the rotational symmetry is broken, which, in turn, leads to different resonance frequencies of the individual excitation modes. As a consequence the degeneracy is lifted. For illustration purposes, the resulting frequency difference $\Delta\nu$ between the modes of the individual groups is depicted for a field range covering the conical and the first region of the tilted conical phase in Fig. 7.11(a). Due to the multitude of modes and hybridizations, a precise allocation of the resonance branches can not be ensured, which substantiates the exclusion of the second area of the tilted conical phase in this discussion. The results display the field dependence of $\Delta\nu$ between modes

with node number $n = 2, 4, 6, 10$ and 24, obtained for $K = 0.0004$. Here, $n = 2$, given by the red symbols, corresponds to the well-established $\pm Q$ modes. Independent of the anisotropy, the latter exhibit a finite frequency difference, which increases with increasing external field. The illustrated slope within the conical phase, ranging up to a field value of approximately $B = 0.8 \, B_{c2}$, is therefore not significantly affected by the cubic anisotropy. Passing through the transition field into the tilted conical phase, the slope of the $-Q$ mode experiences a sudden decrease, while the $+Q$ mode remains constant, as shown in the excitation spectrum in Fig. 7.10(b). This observation is reflected in the respective increase of the frequency difference in Fig. 7.11(a). The eigenvalues of the first higher order modes, given by the light red symbols, on the other hand are susceptible to the cubic environment of the crystal structure and the resulting anisotropy contribution. Commencing at zero-field, the frequency difference between the $n = 4$ modes displays a large value of around $\nu = 0.6 \, \nu_{c2,0}^{int}$, which even surpasses the maximum value obtained for the $\pm Q$ modes. With increasing field, the gap between the branches is first decreasing until the transition field, only to rise again in the regime of the tilted conical phase, similar to the $\pm Q$ modes, as observed before. In the case of the remaining higher order modes, the effect of the additional energy term on the resonance positions in the conical state is extremely small. Only for a finite tilt angle of the pitch vector with respect to the external field, the frequency difference can be quantified, revealing a linear increase as a function of magnetic field strength. In accordance with the excitation spectrum, presented above, the slope of $\Delta \nu$ increases for an increasing node number n.

The significantly different response of the first higher order modes with $m = 3, 4$ originates from their unique time evolution of the dynamic magnetization. As elaborated before, in contrast to the remaining modes, the excitation of the dynamic magnetization component projected onto the pitch vector is not determined by a rotational, but an oscillating motion, mainly limited to certain axes. From the real-space visualizations in Fig. 7.9, it is obvious that these axes do not coincide for the modes discussed, but are shifted by $\pi/4$. It consequently stands to reason that the magnetization experiences a different energy landscape in the respective cases, which results in a finite frequency difference. In order to approach this argument, the dynamic anisotropy contribution,

$$E_K(\delta \boldsymbol{M}(t)) = \left\langle \left(\delta M_x(t)\right)^4 + \left(\delta M_y(t)\right)^4 + \left(\delta M_z(t)\right)^4 \right\rangle \qquad (7.1)$$

will be evaluated for eigenstates with equal number of nodes. Here, the bracket notation indicates the average along a helix period. In this discussion the first four modes of the conical phase ($B = 15$), concerning their frequencies, will be taken into consideration. It should be mentioned that these eigenstates are obtained from calculations performed in absence of the

magnetocrystalline anisotropy. In Fig. 7.11(b) the extracted time evolution of $E_\mathrm{K}\big(\delta\boldsymbol{M}(t)\big)$ for the said modes within one period T is displayed. For the $\pm Q$ modes, assigned to the numbers $m = 1$ (blue) and 2 (light blue), the graphs show both a sinusoidal time dependence, which are determined by the rotational motion in combination with the fourfold symmetry of the cubic anisotropy. The mean values, around which the curves are oscillating, are slightly different which in turn leads to a small discrepancy in the resonance frequencies. In the case of mode numbers $m = 3$ (light red) and 4 (red) the effect of the cubic environment on the resonance modes is no longer negligible. While the time delay between these modes is not of importance for the discussion, the amplitudes of $E_\mathrm{K}\big(\delta\boldsymbol{M}(t)\big)$ are playing the decisive role with regard to the resonance position in the frequency domain. As anticipated before, the dynamics of the magnetization are best described in terms of an oscillating rather than a rotational motion. The time evolution of $E_\mathrm{K}\big(\delta\boldsymbol{M}(t)\big)$ is therefore not expected to display a fourfold symmetry as obtained for the $\pm Q$ modes. From the real-space representation it can be seen, that the individual components of $\delta\boldsymbol{M}(t)$ oscillate dominantly along the [100]- and [110]-directions, for mode numbers $m = 3$ and 4, respectively. Since the [100] directions reflect the easy axes of the system, the absolute value of the energy contribution is higher and with this also the resonance frequencies of mode number 4.

(a)

(b)
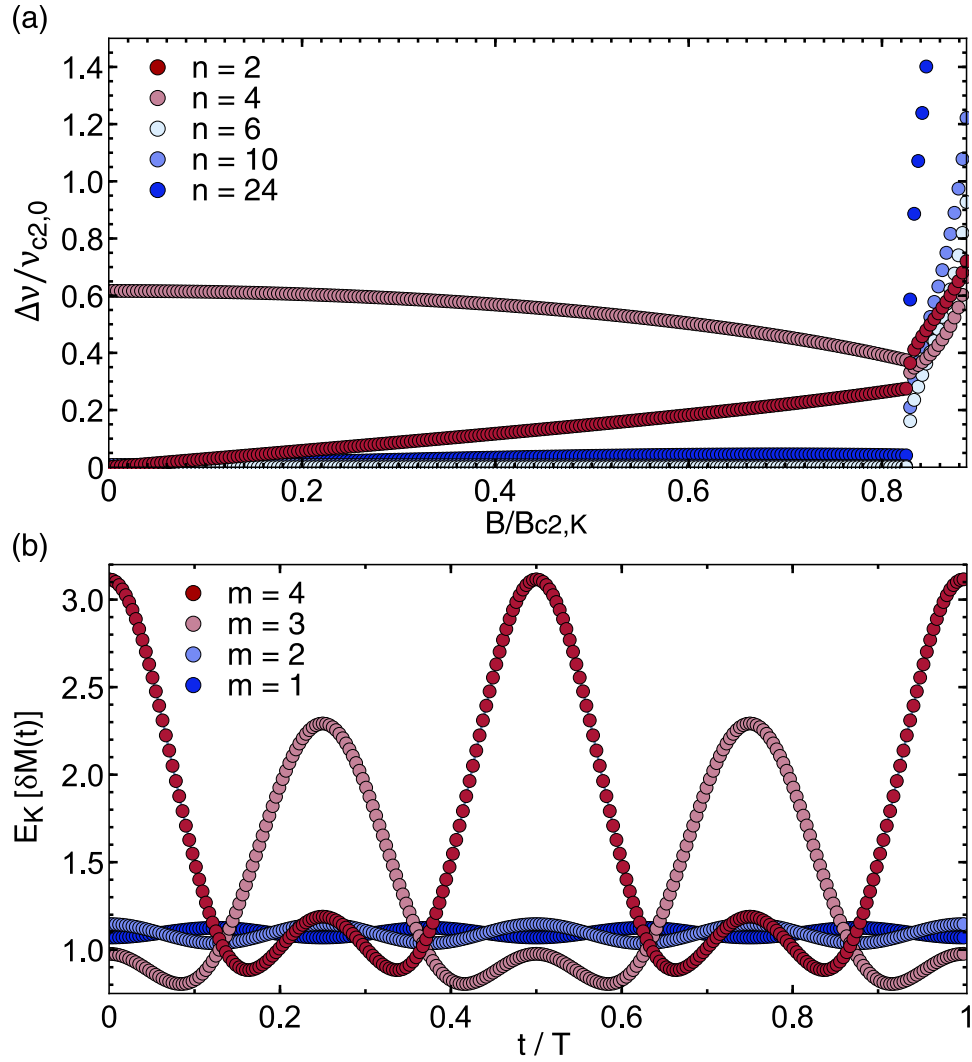
Figure 7.11: (a) Theoretically predicted frequency difference between modes with the same number of nodes (n) for a spherical sample calculated for an anisotropy value of $K = 0.0004$. Field and frequency axes are normalized by $B_{c2,K}$ and $\nu_{c2,0}^{int}$, respectively. In the interest of simplicity, the conical and first region of the tilted conical phase is displayed. (b) Time evolution of the dynamic anisotropy contribution. The remaining parameters are set to $r_0 = -1000$, $\tau = 0.88$, $B = 15$ and $N_i = 1/3$.

2D Reciprocal Space

In order to evaluate the effect of an underlying cubic lattice structure on the magnetization texture in the topologically nontrivial state and its corresponding dynamic response to an external driving field, the same protocol as described above will be employed. In the first step, the magnetization configuration is calculated by minimizing the energy functional with respect to the two pitch vectors and Fourier components of the individual lattice sites. The number of parameters entering the numerical treatment is determined beforehand by the cutoff introduced in the two dimensional reciprocal lattice. For the calculations presented here, the momentum space is restricted to five rings (c.f. Sec. 6.4), if not stated otherwise, which results in a total number of $2 \cdot 3 \cdot 91 + 3 \cdot 2 = 552$ variables. With the magnetization representing a physical and therefore real quantity, it follows that $\boldsymbol{m_{-Q} = m_Q^*}$ and consequently instead only $2 \cdot 3 \cdot 46 + 3 \cdot 2 = 282$ parameters are taken into consideration. In contrast to the analysis in the high temperature limit [Wai17], this number can not be further reduced by means of symmetry arguments, since the magnetocrystalline anisotropy explicitly breaks the rotational symmetry. This results in cumbersome calculations with high computation times on the one hand and an increase in sensitivity concerning the start parameters on the other hand. In this regard, the adjustment of only a few parameters might lead to the convergence of the minimization algorithm and consequently relaxation into an equilibrium configuration, which might not necessarily correspond to the global, but a local minimum. It follows that the implementation of various start parameters is required. As default configuration a superposition of three spin helices, reproducing a skyrmion lattice, is chosen. By rotating the individual components around the field axis with certain angles and adding noise on top, a set of starting parameters is generated. Note that the orientation of the pitch vectors with respect to the crystallographic axes will play an important role in the case of an oblique lattice, due to the reduced symmetry. Another method comprises the usage of previously obtained results, calculated with the same external parameters, but slightly different magnetic field value as starting point. With this restriction, the performance of the minimization for an increasing or decreasing magnetic field with a small step size mimics the employed measurement protocol, described above, and additionally leads to a smooth change of the magnetization configuration as a function of field.

Besides the external magnetic field value, only the strength of the cubic magnetocrystalline anisotropy enters the energy functional as a free parameter, in accordance with the setup introduced before. As a reminder, the remaining constants are set to $r_0 = -1000$, $N_i = 1/3$ and $\tau = 0.88$ and the field is aligned along the [001] or z axis, respectively. Consequently, the skyrmion lattice, in real and reciprocal space, forms in the $x - y$ plane, perpendicular to the predefined external field direction.

In the following, the field dependence of the magnetization configuration, calculated for various anisotropy values will be discussed. Compared to the one-dimensionally modulated states, even small K values induce significant changes in the magnetic texture. The results presented below cover therefore an extended parameter range of $K = 0 - 0.0004$. The quantities which display the characteristics of the skyrmion lattice are the pitch vector lengths and the orientation with respect to each other, represented by the enclosed angle ϕ.

In Fig. 7.12, first the wavenumbers of the lattice vectors $\boldsymbol{Q}_1$ and $\boldsymbol{Q}_2$ are given as a function of the external field. The corresponding results are indicated by closed and open symbols. Since for wide field ranges these values coincide, colored lines are added as a guide to the eye. It is instructive to begin the discussion with the isotropic case, $K = 0$, depicted by the dashed black line and the dark blue symbols. Here, we distinguish between two cases, which arise from the different restrictions on the pitch vector parameters: in the first case (dashed black line) the calculations are performed for a hexagonal lattice configuration, i.e. $|\boldsymbol{Q}_1| = |\boldsymbol{Q}_2|$ and $\phi_{1,2} = 120°$ denoting the enclosed angle between both vectors, while in the second case (blue dots) no restrictions are applied, leaving both pitch vectors independent of one another. Starting in the high field limit, the data sets show the same slight increase of the wavenumbers under a decreasing external field. At approximately $B = 29$ the slope exhibits a sudden change indicating an increase of $|\boldsymbol{Q}_1|$ and $|\boldsymbol{Q}_2|$ and therefore an increase of the skymrion density. In general, in the vicinity of $B_{c2,0}$, the energy functional is minimized by either spin helices with small cone angles ($B < B_{c2,0}$) or by a collinear alignment of the spins with the given field direction ($B \geq B_{c2,0}$). Due to the construction of a two dimensional reciprocal lattice within the plane perpendicular to the z axis, and a skyrmion lattice serving as default configuration, the minimization algorithm however is not likely to relax into a nonmodulated or one-dimensionally modulated state. As a consequence, at external field values even higher than the critical transition field the formation of a skyrmion lattice is still the result of the minimization routine. In order to approach the energetically more favorable field-polarized state, however, the pitch vector length is rather small and with this the distance between the skyrmions rather larger. The magnetization configuration is therefore mainly given by a fully aligned state. Traversing now the aforementioned discontinuity at around $B = 29$ the skyrmion density starts to increase significantly, while the volume fraction of the field-polarized state is decreasing. It is evident that a parallel alignment of the magnetization with the external field is now associated with higher energy costs, in contrast to the modulated spin texture. Finally, for field values in the vicinity of $B = 15 \approx 0.5B_{c2}$, the wavenumbers stabilize and reach a value close to one. A further decrease of the field strength below $B = 6$ reveals that the imposed restrictions on $\boldsymbol{Q}_1$ and $\boldsymbol{Q}_2$ lead to two different lattice structures. While in the first case, the
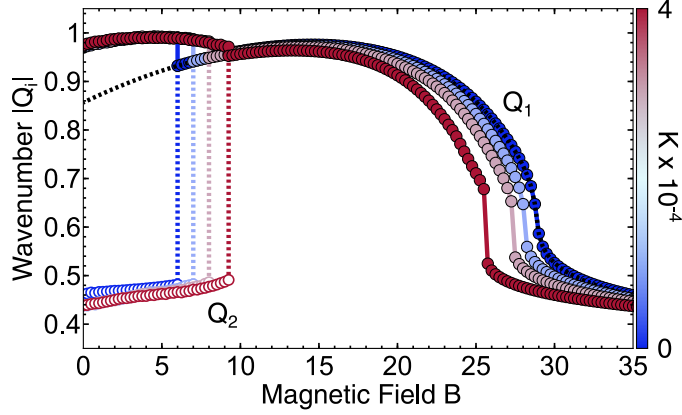
Figure 7.12: Calculated pitch vector lengths $|\boldsymbol{Q}_1|$ (closed symbols) and $|\boldsymbol{Q}_2|$ (open symbols) for various anisotropy values K as a function of applied field B. Colored lines are given as a guide to the eye. The dashed black line illustrates the results obtained in the isotropic case with the lattice fixed to a hexagonal configuration. The remaining parameters are set to $r_0 = -1000$, $\tau = 0.88$ and $N_i = 1/3$.

wavenumbers are decreasing continuously, the curve progressions of $|\boldsymbol{Q}_1|$ and $|\boldsymbol{Q}_2|$ no longer coincide in the second case. This indicates that the deviation from a hexagonal lattice structure is energetically more favorable. As a consequence, the calculations result in an oblique distortion of the lattice and finally in an elongation of the skyrmions, which are referred to as elongated skyrmions. Interestingly, this deformation can be observed despite the lack of the anisotropic crystal environment. Nevertheless, emphasis should be put on the fact that the calculations are performed in the low-temperature regime, far below the critical temperature T_c. Without the cubic magnetocrystalline anisotropy, the stabilization mechanism of the LTS phase, the skyrmion lattice does not form the ground state of the system and is not predicted to be resolved. For finite K values, a similar field dependence as in the isotropic case is displayed. An increase of the anisotropy strength leads on one hand to an extension of the eLTS phase and a shift of the sudden change of the wavenumbers towards lower field values on the other hand. The latter accompanies the decrease of the critical transition field B_{c2} for higher anisotropy strength as shown in Fig. 7.5. Note that, due to the additional direction-dependent energy contribution, no restrictions are applied to the pitch vector components in these calculations.

The second quantity, which characterizes the skyrmion lattice, is the orientation of the pitch vectors with respect to each other and the crystallographic axes. In the following, the corresponding angles are denoted by $\phi_{1,2}$ and ϕ_i, with index $i = \{1, 2\}$. Here, angle ϕ_i relates to the x-axis and [100] direction. The extracted field dependencies are illustrated in Fig. 7.13. The
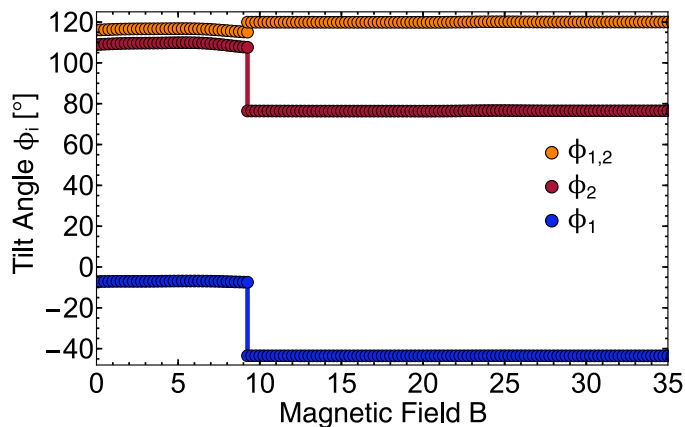
Figure 7.13: Calculated tilt angles ϕ_i of the pitch vectors $\boldsymbol{Q}_1$ (blue) and $\boldsymbol{Q}_2$ (red) with respect to the [100] crystallographic direction as a function of applied field B. The angle enclosed by both vectors $\phi_{1,2}$ is indicated by the orange symbols. The remaining parameters are set to $r_0 = -1000$, $\tau = 0.88$, $N_i = 1/3$ and $K = 0.0004$

blue, red and orange symbols are assigned to the parameters ϕ_1, ϕ_2 and $\phi_{1,2}$ respectively. Note, in the interest of clarity the discussion is limited to the data obtained for an anisotropy strength of $K = 0.0004$. Starting again in the high field limit, it is evident that the skyrmion lattice is of hexagonal shape, since the enclosed angle amounts to $\phi_{1,2} = 120°$ and both vectors show the same length, as elaborated before. Over the wide range down to $B = 9$, $\phi_{1,2}$ exhibits a field-independent behavior. The same observation holds for the orientation of the individual lattice vectors. Given the hexagonal configuration, the actual directions of the pitch vectors with respect to the crystal structure are, however, not predefined by the energy terms taken into account. As a consequence, the orientation of the skyrmion lattice is degenerate and only depends on the default parameters of the initial magnetization configuration, fed into the minimization algorithm. For a fixed direction of the skyrmion lattice a higher-order energy potential, which for instance displays a sixfold symmetry, is required [Müh09; Eve12].

For the chosen anisotropy strength, the magnetization undergoes a phase transition into the elongated skyrmion phase at a field value of $B = 9$, as already elaborated in Fig. 7.12. The sudden change of the wavenumbers is additionally accompanied by a reorientation of the individual pitch vectors and a slight decrease of the angle enclosed by them. By diverging from the rotationally symmetric configuration, the skyrmions are now subject to the underlying crystal structure. Due to the extension of the skyrmions along one direction, the in-plane component of the magnetization parallel to this axis is increased. In order to reduce the arising energy costs, the elongated skyrmions align along the crystallographic axes. This results in

four energetically equal directions for a non-zero anisotropy strength K.

With the results obtained from the minimization protocol and the application of the Fourier transform, the magnetic texture can be visualized in real-space, in analogy to Fig. 7.6. In the following, 3D representations of the skyrmion lattice, calculated at a moderate anisotropy strength of $K = 0.0002$ and two different field values, are illustrated. Note that, due to the symmetry along the field direction, the illustrations are limited to the plane perpendicular to the latter, for reasons of simplicity. The visualizations are comprised by a vectorial representation of the magnetization configuration, indicated by arrows and a color gradient, which highlights the corresponding out-of-plane component of the magnetization. The color gradient, ranging from blue to red, represents a parallel and anti-parallel alignment with respect to the external field direction. A vanishing z component is encoded by a white color. With the magnetic field set to a value of $B = 15$, the chiral magnet hosts the well-established hexagonal skyrmion lattice, as given in Fig. 7.14. The localized windings, which are of Bloch type due to the bulk DMI in Cu_2OSeO_3, are embedded in a ferromagnetic background aligned along the external field. In contrast, the center spin of each skyrmion is pointing in the opposite direction, as highlighted by the red color.

A decrease of the field strength below a certain value, in this case $B = 8$, leads to a finite difference in length of the pitch vectors and a slight distortion of the enclosed angle, as anticipated before. This imbalance, which mainly originates from the abrupt reduction of one wavenumber, is conversely resulting in an increase of the helix period in real-space. The implication on the magnetization configuration is depicted in Fig. 7.15, representing the results obtained with the external field set to $B = 5$. Instead of a circularly and rotationally symmetric arrangement of the spins, the lattice in real-space is characterized by an elongation of the skyrmions along one of the crystallographic easy axis of the system. Here, the orientation in the illustration depends on the default parameters of the magnetization configuration. In order to distinguish this specific phase from the hexagonal lattice, it is also referred to as elongated low-temperature skyrmion phase, as introduced before. In the limit of a vanishing pitch vector length, the eLTS texture resembles a spin helix, aligned perpendicular with respect to the external field.

In order to account for the excitation frequencies of the two dimensionally modulated states, the eigenvalue equation Eq. 6.30 with the mean field configuration substituted by the previously determined results from the minimization protocol, will be evaluated. Since the main focus of this section lies on the effects, which the cubic magnetocrystalline anisotropy imposes on the resonance spectra of the topologically nontrivial states, only the respective anisotropy strength K and the external magnetic field remain the free parameters of the theoretical model. The Ginzburg-Landau parameter, the
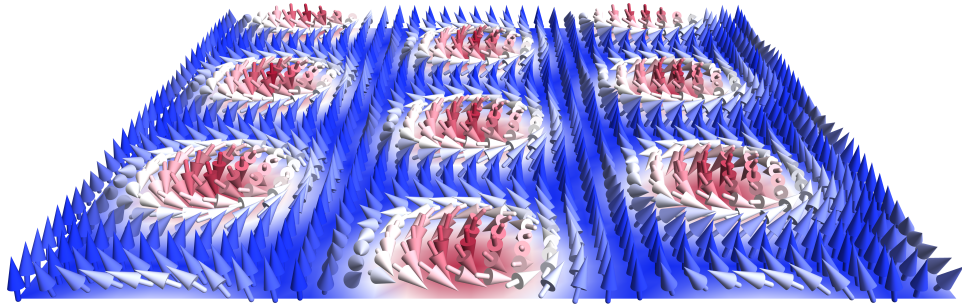
Figure 7.14: 3D visualization of the skyrmion lattice, forming in the plane perpendicular to the external field. The magnetization direction is represented by the arrows, while the color coding is highlighting the out-of-plane component of the magnetization. Blue and red indicate a parallel and anti-parallel alignment with respect to the magnetic field.
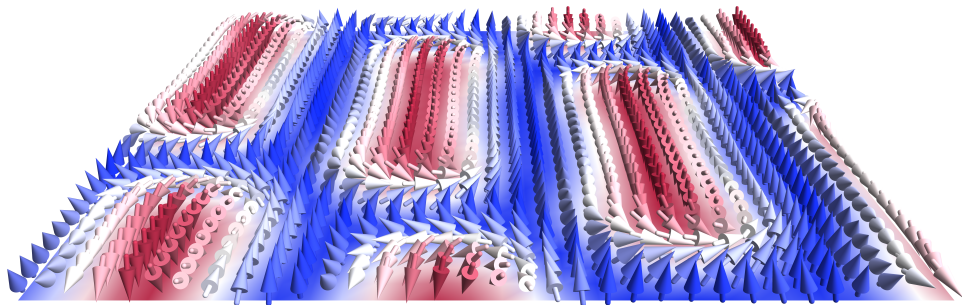
Figure 7.15: 3D visualization of the elongated skyrmion lattice, forming in the plane perpendicular to the external field. The magnetization direction is represented by the arrows, while the color coding is highlighting the out-of-plane component of the magnetization. Blue and red indicate a parallel and anti-parallel alignment with respect to the magnetic field.

dipolar interaction strength and the demagnetization factors on the other hand read $r_0 = -1000$, $\tau = 0.88$ and $N_i = 1/3$. Additionally, in accordance with the measurement setup introduced before, the magnetization is assumed to be subject to a spatially homogeneous driving field, if not stated otherwise.

The field dependence of the resonance frequencies, shown in Fig. 7.16, summarizes the results obtained from calculations with the anisotropy constant set to $K = 0$, 0.0002 and 0.0004. The illustrations are composed in a similar manner as in the 1D case by the generic microwave spectrum, given by the gray symbols, and the spectral weight, which is encoded in the symbol size, in order to highlight the modes accessible in a broad-band microwave experiment. The direction-dependent coupling efficiency in regard of the magnetic driving field, is highlighted by the employed color code. While an out-of-plane sensitivity is depicted by blue symbols, an in-plane driving field is indicated by the red colors. Here, the separation into red and dark red allows to differentiate between the x and y component of the oscillating field. For the frequency and field axis again $\nu_{c2,0}$ and $B_{c2,,0}$, respectively, are chosen as reference, with the transition field inferred from previous results in the one-dimensional reciprocal space. Note, the excitation spectra, presented in the following, are illustrated for the whole field range covered in the previous discussion. The area, in which the skyrmion lattice actually minimizes the energy functional, however, is rather limited. In the interest of clarity, the corresponding phase boundaries are therefore highlighted by the gray shading.

In the top panel of Fig. 7.16, the field dependence of the excitation frequencies, calculated in absence of the cubic anisotropy, is displayed. It should be mentioned that, in this specific case a hexagonal lattice, i.e. $|\boldsymbol{Q}_1| = |\boldsymbol{Q}_2|$ and $\phi_{1,2} = 120°$, is preconditioned in order to emphasize the difference between the high- and low-temperature skyrmion phase. In reminiscence of previous results [Sch15], the microwave spectrum is dominated by three resonance branches. Based on their distinct progression under an increasing field and the additional sensitivity to the excitation geometry, these modes are identified as the CCW, breathing and CW mode, sorted in an ascending order regarding the respective frequency. Note, due to its small coupling efficiency on one side and the finite symbol size of the excitation spectrum on the other side, the clockwise mode is barely recognizable in this illustration. Besides these prevailing modes, the skyrmion lattice hosts a multitude of further resonance branches which do not couple to the driving field, based on the lack of a dynamic macroscopic dipole moment. They are not expected to be observed in broad-band microwave experiments and are therefore referred to as dark modes, as mentioned above. Without the additional energy term, at no time the skyrmion lattice does form the ground state of the system in the low-temperature limit [Cha18]. The corresponding field range of energy stability, indicated by the gray shading, is thus not present in the spectrum

displayed.

Increasing the anisotropy strength to $K = 0.0002$ and lifting the restriction of the pitch vector parameters induces fundamental changes in the resonance spectrum, as illustrated in Fig. 7.16(b). Originating from the transition into an oblique lattice, indicated by the discontinuities at a field value of around $B = 0.25\,B_{\mathrm{c2,,0}}$, the microwave spectrum is clearly divided into two distinct parts. In the high-field range, the field dependencies of the resonance frequencies resemble the ones obtained in the isotropic case, $K = 0$, to a great extent. While the resonance frequencies of the modes sensitive to an in-plane driving field are increasing with field, the mode, which is efficiently coupling to an out-of-plane ac-field, exhibits a negative slope. With specific reference to the intersection point between the breathing and the corresponding darker mode, however, the respective resonance branches no longer cross each other, but reveal an anti-crossing or hybridization instead, combined with a shift of the spectral weight towards the resonances of the dark mode. The same effect, but less pronounced, can also be observed for the clockwise and counterclockwise modes at $B = 0.3\,B_{\mathrm{c2,,0}}$ and $B = 0.7\,B_{\mathrm{c2,,0}}$, respectively. The hybridization counterparts of these differ from the one, interacting with the breathing mode. Interestingly, not every mode crossing leads to repulsion of the resonance branches, which can be seen, for instance, in the case of the counterclockwise and breathing mode. It stands to reason that the mode-mode interaction is subject to a selection rule mediated by the cubic anisotropy.

The second part of the spectrum, attributed to the elongated skyrmion lattice phase, is also determined by three dominant resonance branches, based on their finite spectral weight. The one lowest in frequency monotonically decreases with decreasing field and is susceptible to an in-plane ac-field, akin to the character of the counterclockwise mode of the hexagonal lattice. Besides a small offset in frequency, it continues the progression of the latter. The spectral weight, however, decreases remarkably. The second mode, on the contrary, reveals a finite response of the magnetization dynamics to an out-of-plane driving field. Taking also the slight increase in frequency under a decreasing field into account, it stands to reason that it can be identified as the counterpart of the breathing mode in the oblique lattice. Compared to the CCW mode, the transition into the eLTS phase can be identified by the significant shift in frequency instead of a drop in the coupling efficiency. Even though the third mode displays a similar field dependence as the breathing mode, they, nevertheless, differ in the sensitivity with respect to the excitation geometry. The last mode namely is again driven by an in-plane ac-field, which agrees with the character of the clockwise mode. Interestingly, due to the reduced symmetry of the elongated skyrmions, the orientation of the oscillating field with respect to skyrmion lattice plays an important role, regarding the coupling efficiency of the gyrational modes. While the first mode is mainly driven by an oscillating field

along the y direction, the third mode is dominating under an oscillating field along the x direction. Here, these axes correspond approximately to the long and short axes of the skyrmions. A more detailed description will be elaborated later on.

The most striking effect of an enhanced anisotropy strength (Fig. 7.16(c)) on the excitation spectrum is the increased hybridization gap size, most clearly visible in the case of the breathing mode. Here, increasing K by a factor of two likewise doubles the frequency difference between these two interacting branches. This dependence conversely suggests that, by detecting the hybridization gap experimentally, conclusions can be drawn on the anisotropy strength. A detailed study, building up on these findings is presented in the subsequent chapter. In this, the evolution of the hybridization gap as a function of temperature and with this anisotropy constant, is addressed from the experimental and theoretical side. Besides the interaction strength, the spectrum reveals further minor changes. On the one hand, with increasing K and consequently decreasing transition field $B_{c2,K}$ the general field range of the low-temperature skyrmion phase moves to lower field values. On the other hand the boundary between the hexagonal and oblique lattice, shifts slightly towards higher field values, which in turn extends the stable range of the eLTS phase. In addition to that, a change in the anisotropy strength leads to an overall shift of the energies and excitations frequencies, respectively of the resonance branches. Since this effect differs between the individual modes, the counterclockwise mode approaches the breathing mode, while the frequency difference with respect to the clockwise mode increases. Finally, the emerging change of slope of the breathing mode at a field value of around $B = 0.65\, B_{c2,,0}$, forms a local minimum in the case of $K = 0.0004$.

As anticipated before in regard of the experimental data, the resonance frequencies in the low-field limit were assigned to the breathing mode branch of the eLTS phase instead of the helical/conical modes, based on the sensitivity to an out-of-plane driving field and the number of cycling routines. Interestingly, a skyrmion lattice does not form the ground state of the system in this regime though. Add to that the fact that in the anisotropy strength range considered the transition into an oblique lattice structure is at no time energetically more favorable than the one-dimensionally modulated states, as indicated by the gray shading in Fig. 7.16(b)-(c). This leads to the assumption that based on the topological protection and the associated energy cost of the unwinding process the elongated skyrmion phase can survive even in the low-field limit, but in a metastable configuration only.

Apart from the shift along the frequency axis, it stands to reason that the cubic magnetocrystalline anisotropy also affects the general mode structure, as already indicated by the emergence of a mode-mode interaction. In order to quantify this assumption, the time evolution of the dynamic magnetization, calculated for a fixed anisotropy strength K and field value B,
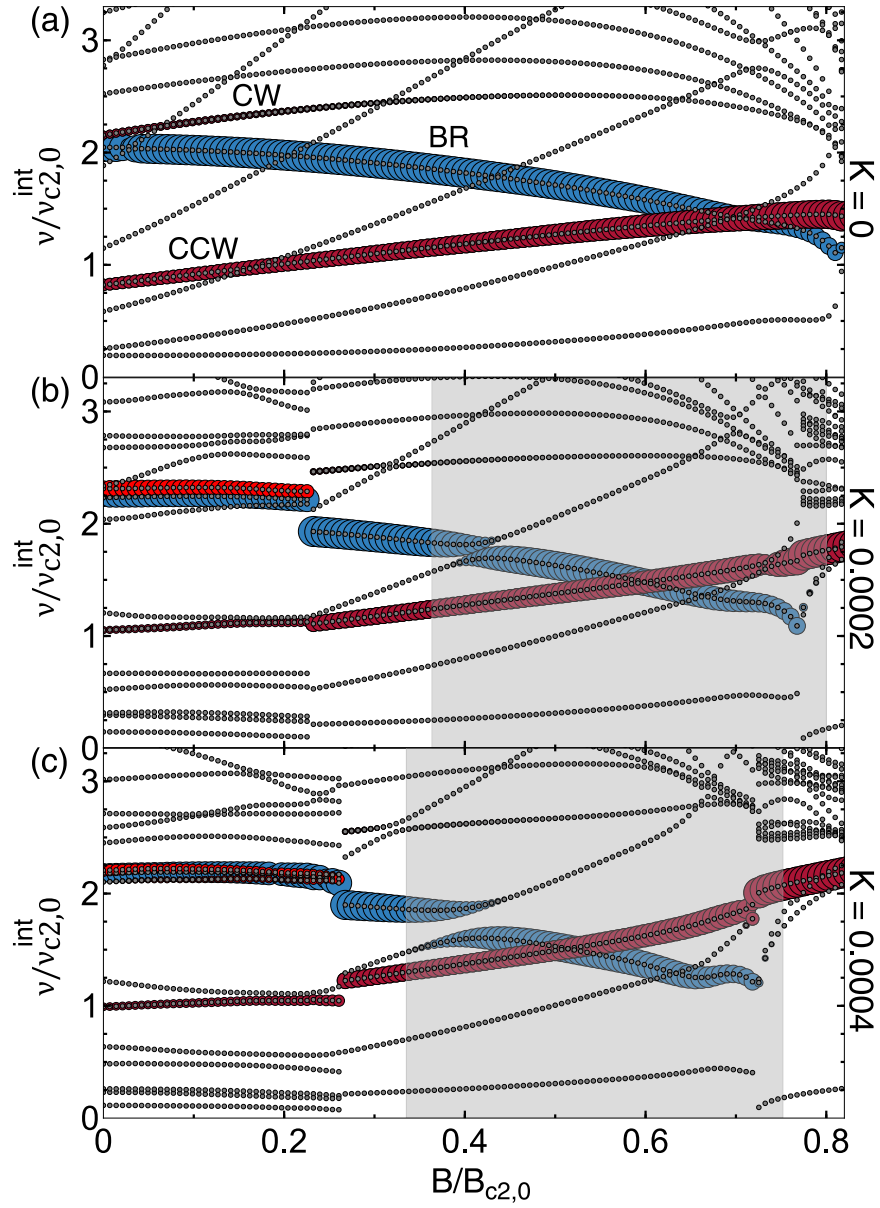
Figure 7.16: Theoretically predicted field dependence of the resonance frequencies for a spherical sample calculated for different anisotropy values K. Field and frequency axes are normalized by $B_{c2,,0}$ and $v_{c2,0}^{int}$, respectively. The spectral weight, which indicates the coupling efficiency to the driving field, is represented by the symbol size. The corresponding colors reflect an in-plane and out-of-plane driving field by red and blue. Additionally, a distinction is made between the x (red) and y (dark red) component of the oscillating field. The range in which the skyrmion lattice forms the ground state is highlighted by the gray shading. The remaining parameters are set to $r_0 = -1000$, $\tau = 0.88$ and $N_i = 1/3$.

will be evaluated. Note, in the interest of simplicity the discussion is limited to the dynamic out-of-plane component $\delta M_z(t)$, only. For the illustration of the induced changes, first the time development of the spatial distribution of $\delta M_z(t)$ is visualized for the isotropic case, $K = 0$. With the field set to $B = 0.4B_{c2,0}$ the skyrmions are arranged in a hexagonal lattice structure. The results, presented in Fig. 7.17, comprise the visualization of the counterclockwise, breathing and clockwise mode, and their respective hybridization counterparts, similar to the ones shown in [Wai17]. In this reference a detailed classification regarding their spatial structure of the first 16 skyrmion lattice excitations can be found. The resonance modes discussed here are arranged in an descending order regarding their excitation frequency. Here, T corresponds to the respective time period. The color gradient is chosen to match the previously employed setup, indicating a collinear alignment by blue and an anti-parallel orientation with respect to the external field by red. The color white reflects a vanishing out-of-plane component of the dynamic magnetization. From the presented images it is evident that the additional modes exhibit a similar nodal-like structure, characterized by a alternating deviation out of the equilibrium position. Based on the number of nodes, they are denoted as sextupole (6), octupole (8) and dectupole (10) modes in the following. Concerning their evolution under time, all of the modes discussed reveal a clockwise sense of rotation.

Introducing now the anisotropy term ($K = 0.0002$) in the energy functional, imposes significant changes of the spatial distribution of $\delta M_z(t)$ as collated in Fig. 7.18. Due to the hybridization mechanism, the presented modes appear to be a superposition of the interacting modes, exhibiting additionally the features of the hybridizing counterpart. This effect is most clearly seen in the case of the breathing mode. In the isotropic case, at certain times $t = 0$ and $t = 2T/4$ the structure of the dynamic z component is given by a radial symmetric profile. The deviation from the equilibrium position reaches its maximum values, visualized by the dark blue and red color. Taking now also the anisotropy term into account in the theoretical model, this symmetry is broken. The spatial distribution of $\delta M_z(t)$ reveals an imprinted nodal structure akin to the pattern of the octupole mode. The merging of the two modes is most evident at times $t = T/4$ and $t = 3T/4$. While the breathing mode, in absence of the anisotropy, experiences a zero-crossing at these times, the hybridization manifests itself in the appearance of the nodal structure of the octupole mode in the snapshots, calculated for a finite K value. A similar effect can also be observed in the remaining illustrations.

Finally, in addition to the excitations of the hexagonal lattice presented above, the character of the three dominant modes in the oblique skyrmion lattice will be discussed. The visualization of the respective time evolution of $\delta M_z(t)$, obtained for $K = 0.0002$ and $B = 0.1B_{c2,0}$, is displayed in Fig. 7.19. Here, the modes are arranged in a descending order, concerning their reso-
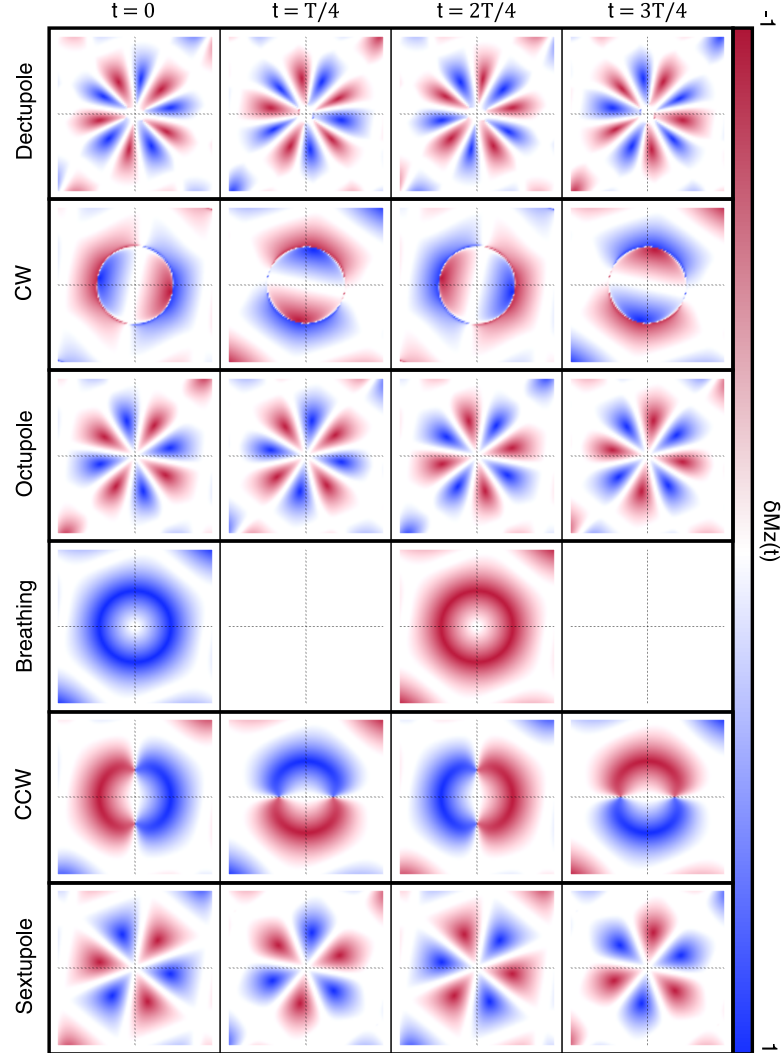
Figure 7.17: Calculated real-space images of the time evolution of the three uniform skyrmion modes and their respective hybridization counterparts for $K = 0$ and $B = 0.4B_{c2,0}$. The remaining parameters are set to $r_0 = -1000$, $\tau = 0.88$ and $N_i = 1/3$. From top to bottom, the modes are identified as the dectupole, clockwise (CW), octupole, breathing, counterclockwise (CCW) and sextupole mode. T is the corresponding time period. The quantity presented in this illustration is the z component of the dynamic magnetization. A parallel alignment with respect to the external field is indicated by blue, while an antiparallel orientation is given by red. Here, the applied field is pointing out of the image plane.
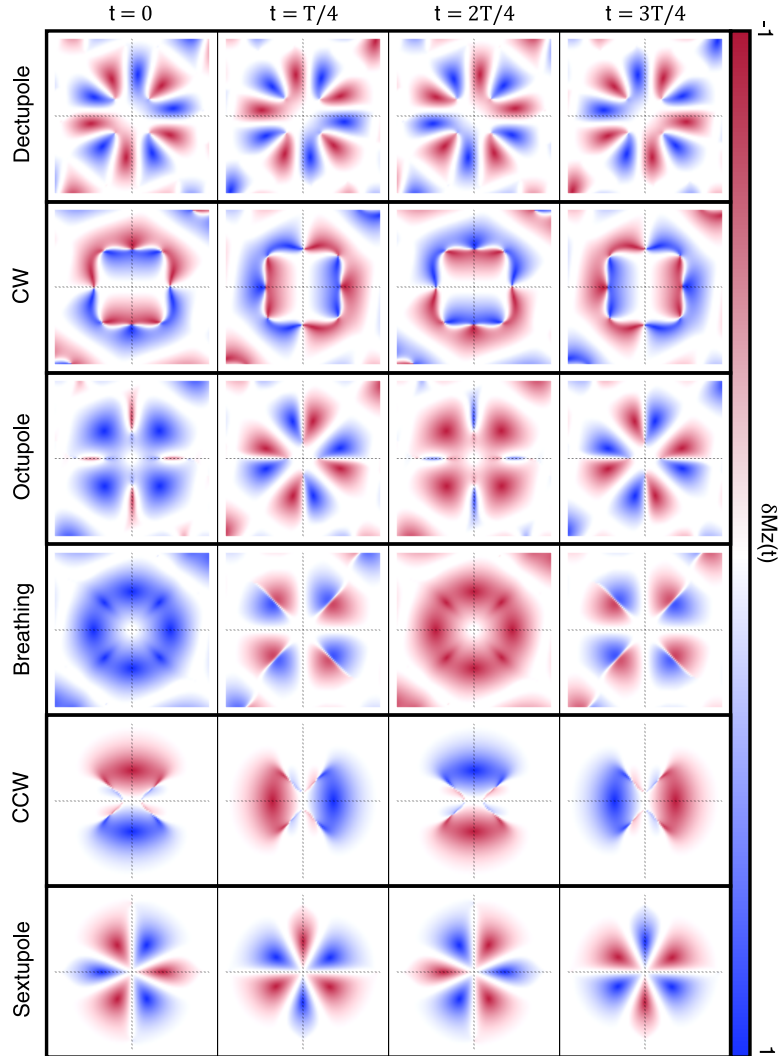
Figure 7.18: Calculated real-space images of the time evolution of the three uniform skyrmion modes and their respective hybridization counterparts for $K = 0.0002$ and $B = 0.4B_{c2,0}$. The remaining parameters are set to $r_0 = -1000$, $\tau = 0.88$ and $N_i = 1/3$. From top to bottom, the modes are identified as the dectupole, clockwise (CW), octupole, breathing, counterclockwise (CCW) and sextupole mode. T is the corresponding time period. The quantity presented in this illustration is the z component of the dynamic magnetization. A parallel alignment with respect to the external field is indicated by blue, while an antiparallel orientation is given by red. Here, the applied field is pointing out of the image plane.

nance frequency. For reasons of clarity, besides the dynamic magnetization component, also the skyrmion edges, inferred from the static magnetization configuration, are depicted. They are given by the dashed black lines in the individual snapshots. The first mode illustrated is the one exhibiting similar characteristics, regarding the field dependence and sensitivity with respect to the driving field direction, as the clockwise mode of the hexagonal lattice. In addition to that, from the real-space images also a similar profile of the spatial distribution of $\delta M_z(t)$ is visible. As depicted in Fig. 7.17 and already discussed in [Wai17], the clockwise mode structure is divided into two rings of opposite sign, which rotate around the center. Similar features can also be observed in the case of elongated skyrmions in the top panel of Fig. 7.19 at times $t = 0$ and $t = 2T/4$. A homogeneous excitation is, however, disturbed by several nodes along the skyrmion edge. Taking also the remaining images, calculated at times $t = T/4$ and $t = 3T/4$ into account, the sense of rotation appears to be clockwise. This resonance branch is therefore identified as the counterpart of the CW mode and referred to as $\mathrm{CW_{eLTS}}$ in the following. Comparing the time evolution of the spatial profile of the second mode with the ones present in the hexagonal lattice, it is evident that it resembles the one of the breathing mode. While at time $t = 0$, $\delta M_z(t)$ points mainly along the external field direction, it reverses its sign at $t = 2T/4$, leading to an alternating shrinking and expanding of the skyrmion core. Interestingly, at times $t = T/4$ and $t = 3T/4$ also a nodal structure, as it could be observed in the hybridizing breathing mode in Fig. 7.18, forms in center. In this case, however, not an octupole but quadrupol structure is visible. A similar observation can be made between the individual skyrmions. The last mode, which exhibits a finite spectral weight, is the one lowest in frequency shown in the bottom panel of Fig. 7.19. Its resonant motion is highly reminiscent of the CCW mode in the high-temperature skyrmion lattice, which is characterized by only one ringlike structure. From the sequence of snapshots a counterclockwise sense of rotation can be identified.

A more simplified insight into the mode characteristics is given by the time dependence of the homogeneous magnetization $\delta \boldsymbol{M}_0(t)$, extracted from the respective eigenvector $\delta \boldsymbol{M}(t)$. In Fig. 7.20 the change of $\delta \boldsymbol{M}_0(t)$ is illustrated for the three modes discussed above. Here, the individual components, x, y and z are depicted by red, green and blue colors. In the case of the $\mathrm{CW_{eLTS}}$ mode of the oblique skyrmion lattice, which is shown in the top panel, it is evident that $\delta \boldsymbol{M}_0(t)$ oscillates within the $x - y$ plane in a clockwise manner, as could also be observed from the real-space illustration of the excitation in Fig. 7.19. Due to the vanishing x component, the rotational motion is, however, strongly elliptical. As a consequence the $\mathrm{CW_{eLTS}}$ mode is therefore almost linearly polarized along the y direction. In contrast to that, the in-plane components of $\delta \boldsymbol{M}_0(t)$ in the case of the $\mathrm{CCW_{eLTS}}$ mode (bottom panel) are almost equal in amplitude. The resonant excitation is only slightly diverging from a circular motion and with this from a circular
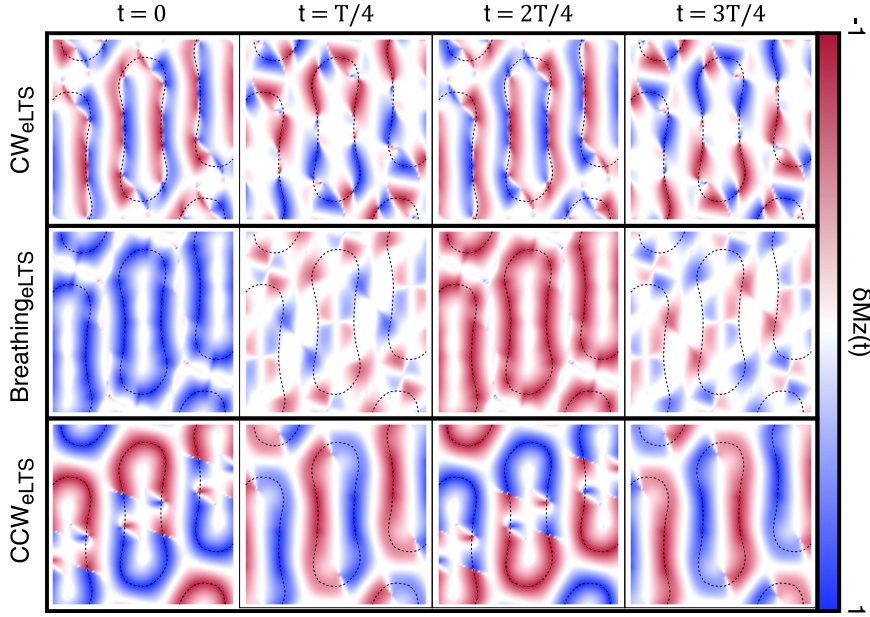
Figure 7.19: Calculated real-space images of the time evolution of the three dominant skyrmion modes of the oblique lattice for $K = 0.0002$ and $B = 0.1B_{c2,0}$. The remaining parameters are set to $r_0 = -1000$, $\tau = 0.88$ and $N_i = 1/3$. From top to bottom, the modes are referred to as $\mathrm{CW_{eLTS}}$, $\mathrm{Breathing_{eLTS}}$, $\mathrm{CCW_{eLTS}}$ mode based on their resonant motion. T is the corresponding time period. The quantity presented in this illustration is the z component of the dynamic magnetization. A parallel alignment with respect to the external field is indicated by blue, while an antiparallel orientation is given by red. Here, the applied field is pointing out of the image plane.

polarization. As can be inferred from the signs of the individual components, the sense of rotation is counterclockwise. The time evolution shown for the second mode, the one with a breathing like character, is limited to the z or out-of-plane direction only. In accordance with the counterpart in the high-temperature skyrmion phase it oscillates along the external field direction and is consequently linearly polarized. Interestingly, besides these three dominant modes, also higher order modes in the elongated skyrmion lattice show a finite change of the homogeneous magnetization in contrast to the ones in the hexagonal lattice [Wai17]. This finite macroscopic magnetic dipole moment is required for the resonance modes to be accessible in microwave experiments. They are therefore more likely to be excited and subsequently detected.

The consequence of these distinct oscillating motions is a different sensitivity of the coupling efficiency in regard to the driving field direction
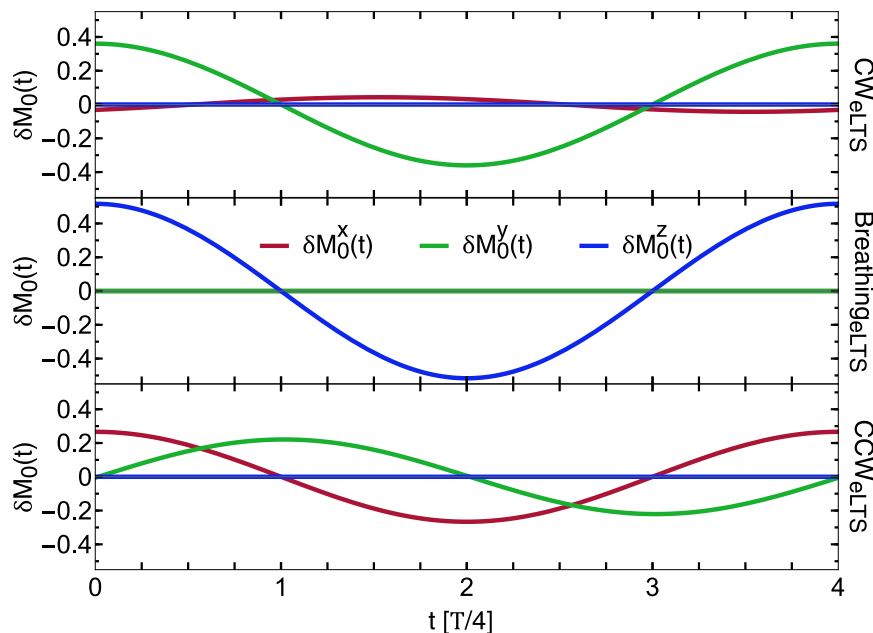
Figure 7.20: Time evolution of the homogeneous magnetization $\delta \boldsymbol{M}_0(t)$ of the three dominant skyrmion modes of the oblique lattice for $K = 0.0002$ and $B = 0.1 B_{\mathrm{c2,0}}$. The remaining parameters are set to $r_0 = -1000$, $\tau = 0.88$ and $N_i = 1/3$. The modes are arranged in an descending order, concerning their resonance frequency. T is the corresponding time period.

[Gar17]. For the individual modes its is maximized if the ac-field concurs with the respective polarization direction, i.e. out-of-plane excitation geometry in the case of the breathing mode and in-plane excitation geometry for the gyrational modes. Note, a linearly polarized ac-field is given by the superposition of a left- and right-circularly polarized driving field. Therefore both the clockwise and counterclockwise modes are excited simultaneously by a linearly polarized in-plane field, in the triangular skyrmion lattice. In previous studies [Sta17a], however, it could be experimentally and theoretically observed that the coupling efficiency changes also by a reorientation of the sample with respect to the CPW and ac-field direction, respectively. The requirement for these findings is a finite difference in demagnetization factors, which are assigned to the axes perpendicular to the external field. This imbalance leads to a different ellipticity of the CW and CCW modes and consequently different spectral weight, compared to the uniform case $N_x = N_y$. It should be mentioned that these findings are not just limited to the skyrmion modes, but can also be observed in the $\pm Q$ modes of the helical/conical phase as reported in the given reference. The peculiarity of the additional modes in the oblique skyrmion lattice is the emergence of elliptically polarized magnetic moment, despite a uniform sample shape, as

shown above. In Fig. 7.21(a) the resulting angle dependence of the coupling efficiency of the two modes, susceptible to an in-plane driving field is displayed. The presented results are obtained for an anisotropy strength of $K = 0.0002$ and a field value of approximately $B = 0.1B_{c2,0}$. Here, ϕ is defined as the angle, which is enclosed by the x axis, which coincides with the [100]-direction, and the driving field direction. The values of the spectral weight are ranging between 0 and 1 and reflect either no or a maximum excitation of the respective mode. Note that, for illustration purpose, the maximum value of the clockwise mode is chosen as reference. Compared to the Kittel mode, the coupling to the ac-field is only half as efficient. For the high-frequency mode, given by the red symbols, a strong correlation between the coupling efficiency and the field orientation is clearly visible. While with the ac-field applied approximately along the x direction the spectral weight vanishes, a maximum excitation of this mode is achieved by rotating the driving field by around 90°, which corresponds roughly to the y axis. This behavior originates from the almost linearly polarized oscillating motion of the homogeneous magnetization in the case of the CW_{eLTS} mode. In the case of the low-frequency mode, displayed by the dark red symbols, the maximum response of the magnetization dynamics is significantly smaller. In contrast to the first mode, however, the amplitude does not vary as strongly under the evolution of the rotation angle but remains finite. The excitation of this mode is therefore predicted to be observed in the experiments independent of the orientation of the driving field, due to the almost circular motion of $\delta M_0(t)$, as shown in Fig. 7.20. Compared to the clockwise mode, the maximum amplitude is achieved in this case by the application of the ac-field along the x and no longer the y axis. In order to relate the orientation of the elongated skyrmions to the coordinate system, the real-space visualization of the respective static magnetization configuration is illustrated on the right hand side, in Fig. 7.21(b). Given by the established color gradient is the z component of the magnetization. The x and y directions are indicated by the black arrows, the large axis of the polarization ellipses P_{cw} and P_{ccw} by the cyan and yellow arrows, and the ac-field h_{ac} direction is depicted by the green one. It should be mentioned that the directions of maximum amplitude in both cases do not exactly concur with the individual polarization directions or crystallographic [100] and [010] axes, which might arise from the slightly asymmetric shape and arrangement of the skyrmions. Since the angle mismatch is, however, rather small, the easy axes of the crystal structure and with this the orientation of the elongated skyrmions might be identified. In conclusion, while the coupling efficiency of the low-frequency mode does not exhibit a strong angle-dependence, the high-frequency mode can be selectively addressed by applying the driving field in certain directions. Reversely it follows that from an angle-dependent measurement of the spectral weight, the orientation of the elongated skyrmion lattice might be determined, as long as further anisotropy terms do not play an impor-

tant role. It should be mentioned that, however, the standard broadband microwave spectroscopy technique as described in Chap. 3 is not suitable for these experiments since the sample is usually attached to the coplanar waveguide. Consequently, the requirement of a decoupled crystallographic and driving field direction is not met and a different measurement technique has to be employed. One option might be to structure multiple CPWs on top of the sample, which are rotated with respect to each other and therefore the crystal axes. Nevertheless, in this case it has to be considered that due to the finite size of the antenna the sample is subject to an inhomogeneous driving field, exciting spin waves rather than the FMR mode.

In order to summarize the observations obtained from the experiments and the numerical model, the respective excitation spectra are collated in Fig. 7.22. The compilation comprises the data shown on the one hand in Fig. 7.1 and Fig. 7.8(d) and in Fig. 7.2 and Fig. 7.16 on the other hand. Note, in accordance with [Cha18] an anisotropy value of K = 0.0004 is chosen for the numerical results. The field axes are normalized by the critical field strength H_{c2} and the frequency axes by the corresponding value $f_{c2} = f(H_{c2})$. Despite the additional energy contribution in form of the cubic magnetocrystalline anisotropy, the spectra given in Fig. 7.22(a) - (b) display strong similarities to previous results in the high-temperature regime [Sch15]. Originating from the abrupt distortion from the preceding collinear alignment with the external field and with this the formation of the tilted conical phase, both spectra, however, exhibit a change of slope and discontinuities just below H_{c2}. As suggested by the numerical results, the latter are attributed to the appearance of anti-crossings with higher-order resonance branches in the one-dimensionally modulated state. The formation of standing spin waves, due to the low magnetic damping, does not allow a precise extraction of the resonance positions though, leaving the hybridizations unresolved and therefore unconfirmed. Approaching the low magnetic field regime, the difference in frequency between the resonance branches is predicted to decrease, resulting in a degeneracy at $B = 0\,\text{mT}$ in the case of $N_i = 1/3$. The finite gap in the experimental data reveals, however, a deviation from the initially assumed cube or spherical shape of the sample investigated. It should be mentioned that the spectral weight, as displayed in Fig. 7.22(b), is obtained from the projection onto an in-plane oscillating magnetic field. Even though the tilted conical modes might also couple to an out-of-plane ac-field, the corresponding data are omitted based on the low excitation efficiency.

In contrast, the establishment of different excitation geometries allows to selectively address the resonance modes of the skyrmion lattice, as indicated in the last two panels, Fig. 7.22(c) - (d), by the differently colored symbols. With the driving field aligned within the skyrmion plane, the dynamic response of the magnetization is attributed to the gyrational clockwise and counterclockwise modes. Due to lack of spectral weight of the former, the
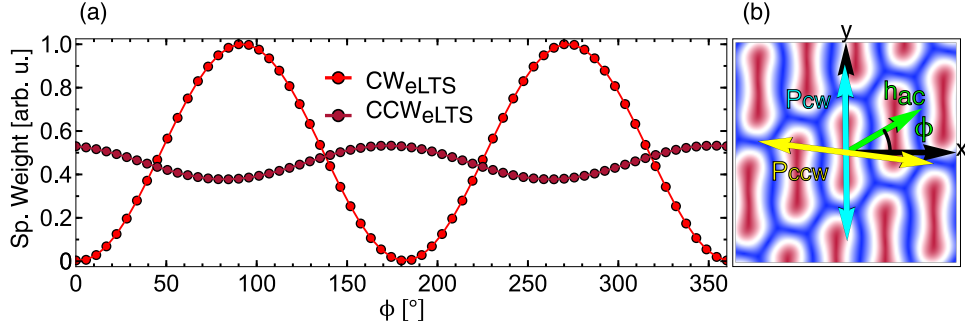
Figure 7.21: (a) Spectral weight of the CW_{eLTS} (red) and CCW_{eLTS} (dark red) modes as a function of driving field direction ϕ. (b) Visualization of the z component of the static magnetization, aligned parallel (blue) or antiparallel (red) with respect to the external field. The arrows given by the black, cyan and green colors indicate the x and y, polarization and driving field direction $\boldsymbol{h}_{ac}$. The parameters are set to $r_0 = -1000$, $\tau = 0.88$, $N_i = 1/3$, $K = 0.0002$ and $B = B_{c2,0}$.

discussion, however, focuses on the CCW (cyan symbols) mode only. In both, experimental and theoretical data, the field dependence of the CCW mode is highly reminiscent of the isotropic case in the HTS phase. In accordance to the latter, the resonance frequencies continuously decrease with a likewise decreasing magnetic field. Conversely, the resonances of the breathing mode (orange symbols), dominant under an out-of-plane driving field, are demonstrated to steadily increase as a function of applied field in the high-temperature skyrmion lattice. Subject to the effect of the magnetic anisotropy in the low-temperature limit, the progression of the breathing mode is predicted to deviate from the described field dependence though, disclosing several anomalies. Just below H_{c2} a local minimum is observed, followed by two discrete gaps at $H = 0.6\,H_{c2}$ and $H = 0.4\,H_{c2}$ in regard of the calculated spectrum. The first one arises from an anti-crossing with a dark octupole mode, while the second one at lower magnetic field indicates a distortion of the hexagonal lattice into an energetically more favorable elongated configuration. A visualization of the magnetic texture for the described states is given in the insets Fig. 7.22(i)-(ii). In the recorded microwave spectra also three distinct resonance branches are resolved, which bear a high level of resemblance to the ones calculated numerically. While the two in the high-field limit are unambiguously ascribed to the breathing mode, the resonance branch at lower fields might also originate from the helical/conical modes, which are expected to form the ground state in this field range. For this reason further experiments are employed, which however confirmed that the observed signatures cannot be attributed to the dynamic response of the spin spirals. These findings therefore suggest that,

at low magnetic fields, the unwinding into a topologically trivial state is not realized, but indeed the survival of a metastable skyrmion phase with an elongated lattice structure. Note, the shift of the CCW and breathing mode with respect to each other might arise from the discrepancy between the sample shapes, investigated in the experiments and calculations, and from the anisotropy strength chosen in the theoretical model.
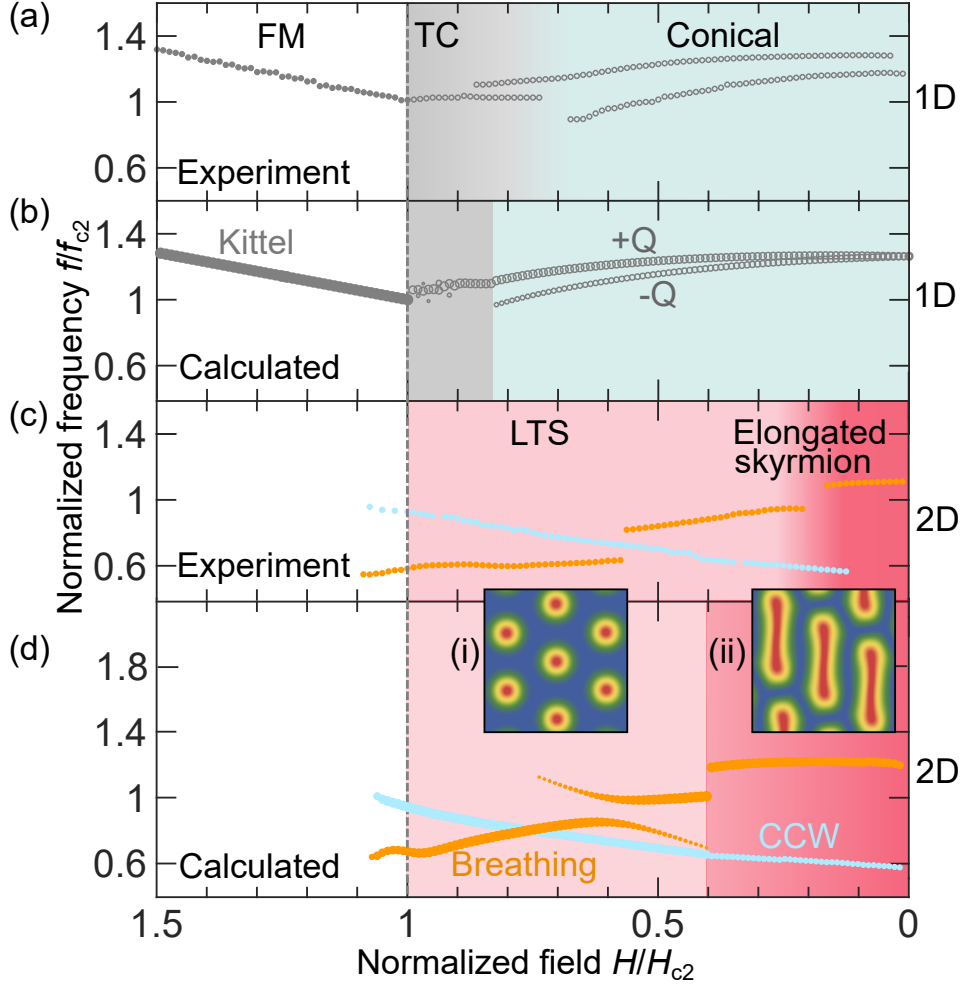
Figure 7.22: Comparison between the experimentally (a), (c) and theoretically (b), (d) obtained microwave spectra. Field and frequency axes are normalized by their corresponding values obtained at the critical transition field H_{c2}. Gray symbols indicate the resonances modes in the field-polarized (closed) and conical and tilted conical phase (open). In the skyrmion lattice phase two excitation branches are extracted, which are attributed to the counterclockwise (cyan symbols) and breathing (orange symbols) modes. (i),(ii) Visualization of the calculated magnetization configuration, displaying the triangular and elongated skyrmion lattice. The color shading indicates the individual phases. The field-polarized, tilted conical, helical/conical, hexagonal skyrmion lattice and oblique skyrmion lattice phases are reflected by white, gray, light green, light red and red colors. Figure taken from [Aqe21].

7.2 Investigation of the Skyrmion Resonance Mode Hybridization

The results presented above reveal that, besides mediating the stabilization mechanism for skyrmions at lowest temperatures [Cha18], the cubic lattice environment induces also significant changes in the respective magnetization dynamics. The most prominent one, is the anomaly in the breathing mode, which originates from the hybridization with a dark octupole mode. Since the previous measurements are, however, only obtained at one temperature, the evolution of these additional features as a function of anisotropy strength remains unresolved. Conversely, the questions arise if the obtained mode interactions, characterized by the frequency gap size, allow to draw conclusions on the anisotropy strength and if further anisotropy terms are also contributing and are required to be taken into consideration. In the following section these open questions are addressed from the experimental and theoretical side, by means of microwave spectroscopy experiments and numerical calculation of the excitation spectra, as established before. Parts of the numerical results presented in this section are published in [Tak21; Lee21].

7.2.1 Experimental Results

The experimental findings presented in this section are collated from two independent microwave spectroscopy experiments. The first contribution, published in [Lee21], comprises the results from measurements, which are performed on two bulk crystals of Cu_2OSeO_3 by Oscar Lee and Christian Back. Here, two sample shapes, namely a cuboid and a platelet, are investigated. In both cases the sample dimensions range in the millimeter regime, with a size of $1.6 \times 1.6 \times 1.0$ mm^3 and $1.9 \times 1.4 \times 0.3$ mm^3, respectively. In addition to that, the crystals are cut such that the surface normals coincide with the corresponding [001]-directions. In order to populate the low-temperature skyrmion phase the magnetic field is applied out of plane, i.e. along the thickness direction during the frequency sweeps. In accordance with the previous experiments, the samples are placed face-down on the coplanar waveguide. Since its dimensions are similar to the ones of the samples and therefore also in the millimeter regime, the generated driving field, acting on the magnetization, is assumed to be homogeneous. In the second experiment, microwave spectroscopy is conducted by Rina Takagi ([Tak21]) on a lamella shaped sample, which is cut out of a Cu_2OSeO_3 crystal, by focused ion beam etching (FIB). This process allows, in general, to reduce the sample dimensions to the micrometer regime, but more importantly to thin down the sample and therefore reduce the dimension ratios significantly. Here, for the lamella investigated, the thickness amounts to 1 μm, which is one to two orders of magnitude smaller than its length and width. Also

in this experiment the static field is applied along the thickness direction, which corresponds to a [001]-direction of the crystal lattice, as the remaining surface normals. In contrast to the measurements on the bulk crystals, the lamella shaped sample is placed on two microwave antennae, which are structured on a silicon substrate. Due to the micrometer sized signal and ground lines, the main excitation of these lies at a finite wave number. As a consequence, the magnetization is no longer driven homogeneously, leading to the excitation of spin waves instead.

It is important to mention that, technically speaking, in these two experiments two different skyrmion phases are investigated. While for the bulk crystals at low temperatures the second, independent skyrmion phase is populated, in the case of the lamella sample the high-temperature skyrmion lattice is extended down to lowest temperatures by a rapid cooling process. Despite the different routes through the phase diagram, the effects which the cubic magnetocrystalline anisotropy induces on the dynamic response of the magnetization however remain the same. It allows therefore to directly compare the obtained experimental results and additionally to draw conclusions on the effects arising from the demagnetization energy.

In both experiments a VNA-based spectroscopy setup, as introduced in Sec. 3.2 is employed. Since the measurement routines, but also the data processing accord, only the ones of the first experiment on the bulk samples are presented in the following. For a detailed description of the measurement procedure on the lamella sample we refer to [Tak21] and previous publications [Sek16; Sek17; Sek20]. The investigation of the bulk crystals builds upon the findings of the broadband microwave spectroscopy experiments on the low-temperature skyrmion phase, presented in the preceding section. For the detection of the dynamic response of the skyrmion lattice it was shown that first the respective volume fraction is required to be increased by the established field-cycling protocol. In order to execute this step, the external field, which is ramped up to the reference field $B = 0.3\,\mathrm{T}$ before each measurement procedure, is reduced to a value, which corresponds to the skyrmion pocket. Within the respective field range, the external field is then increased and decreased continuously n times. If not stated otherwise, the number of field-cycles, performed during the measurements, amounts to $n = 400$. From this point on, the scattering parameter S_{ij}, with $i, j = \{1, 2\}$, is recorded as a function of frequency, either under an increasing or decreasing field, which is again referred to as H_{incr}^n or H_{decr}^n. Finally, both scans are combined to generate a complete excitation spectrum. Note that in order to reduce the spurious background arising from the setup itself, the individual frequency sweeps are normalized with respect to the data set recorded at the reference field. The application of the normalization technique is indicated by the absolute values notation $|S_{11}|$ and $|S_{21}|$ in the following. Since both crystals are significantly larger than the signal line of the CPW, the magnetization dynamics are simultaneous driven by the in- and out-of-plane

component of the oscillating magnetic field. Consequently, the combination of the two excitation geometries allows to excite and detect both the gyrational and breathing modes. The adjustment of the sample position with respect to the CPW during the experiment is therefore not required.

In order to elaborate now, how an enhanced anisotropy strength affects the magnetization dynamics, the measurement protocol described before is executed for a wide temperature range. The microwave spectra obtained for both sample shapes (platelet(a) and cuboid(b)) are contrasted in the top panel of Fig. 7.23. The employed color gradient, ranging from white to black, indicates no or a high microwave absorption due to the resonant motion of the magnetization within the resonance modes. As aforementioned, the quantity visualized here is the normalized scattering parameter $|S(f)|$.

Focusing first on the results obtained at 4 K in the case of the platelet sample, reveals similar signatures as displayed in Fig. 7.2. At high magnetic fields, which corresponds to the field-polarized phase, the magnetization dynamics are determined by the Kittel mode, characterized by the linear decrease of the resonance frequencies under a likewise decreasing field strength. Due to the formation of standing spin waves mediated through the low magnetic damping, several replica of the Kittel modes are resolved additionally. Here, the resonance positions of the branch with the highest amplitude, which are obtained from Lorentzian fits, are highlighted by the open gray symbols for illustration purposes. Since, however, the main focus of this study lies on the excitation modes of the skyrmion lattice phase, these resonance branches are not further investigated. For a wide field range, slightly below the transition field H_{c2}, the excitation modes reminiscent of the LTS lattice emerge. The most evident signature is the repulsion of the breathing and octupole mode, which is visualized by the open red symbols. Besides these, also the counterclockwise mode, depicted by the open purple symbols, but also a faint indication of the clockwise mode, is evident. Note, also in the skyrmion lattice the resonance branches are accompanied by replica based on the excitation of standing spin waves. Reducing the magnetic field further leads to an unwinding of the topologically non-trivial texture and the formation of the conical spin spirals. Its individual resonance branches are, however, hidden by the overall blurry absorption signal, but are identified by the distinct evolution as a function of field strength.

Despite the increase of the temperature and thereby consequent decrease of the anisotropy strength the overall appearance of the microwave spectra remains unaffected. Until a temperature of 20 K, besides the resonant excitations of the field-polarized and conical phase, also the signatures of the gyrational modes and the hybridization between the breathing and octupole modes are still clearly visible. Add to that the fact that also the respective phase boundaries and frequencies appear to be barely affected. In contrast to these findings, it is however obvious that the hybridization gap is decreasing significantly when increasing the temperature. At a value of 22 K a faint
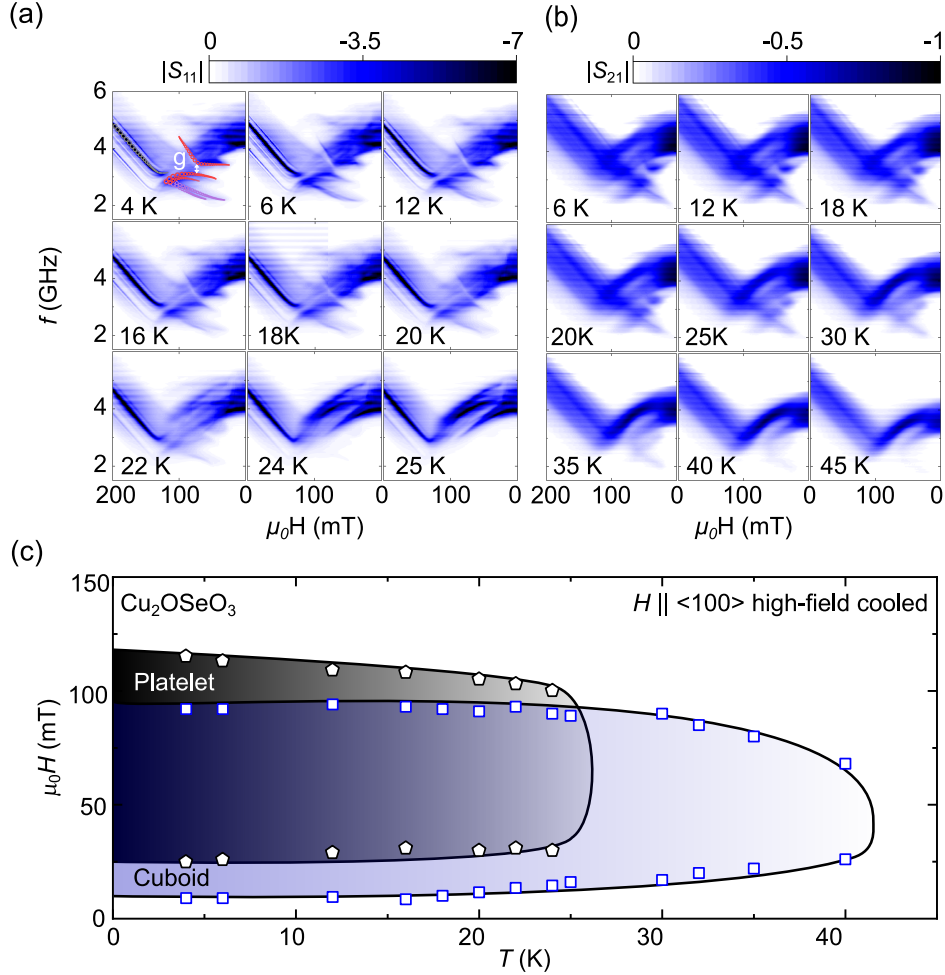
Figure 7.23: Evolution of microwave spectra as a function of temperature obtained for a (a) platelet and (b) cuboid sample shape. The color gradient represents the normalized microwave absorption intensity $|S_{11}|$ and $|S_{21}|$, respectively. For the population of the low-temperature skyrmion phase during these measurements the external field is applied along the crystallographic [001]-direction. In order to highlight the field-dependence of the breathing and CCW mode, the respective resonance frequencies are extracted from Lorentzian fits and depicted by open red and purple symbols, respectively. (c) Phase boundaries of the low-temperature skyrmion pocket for both sample shapes, extracted from the excitation spectra. Figure taken from [Lee21]

signal from the clockwise and counterclockwise modes is still detectable, while the breathing mode is masked by the prevailing conical modes. The features of the mode-mode interaction are no longer visible. Finally, at around 24 K the signature arising from the LTS phase vanishes suddenly and the microwave spectra exhibit only the Kittel and conical modes. Here, the small discontinuity at around 100 mT is attributed to the onset of the tilted conical phase.

On the right hand side of Fig. 7.23, the measurement results obtained on the cuboid sample are illustrated. The main difference, apart from the overall smaller signal-to-noise ratio, which might arise due to a rougher sample surface, is the position of the resonance branches of the skyrmion lattice with respect to the field and frequency axes. Compared to the platelet, first the hybridization range of the breathing and octupole mode is shifted towards smaller field values. It is no longer masked by the conical modes and can be therefore clearly distinguished from these. In addition to that, the intersection point of the breathing and counterclockwise mode can also be found at lower magnetic fields. It is evident that despite the crossing of their respective resonance branches, these modes do not interact with each other, i.e. a hybridization cannot be observed. Interestingly, in the case of the cuboid sample, the metastable skyrmion lattice phase can be extended to significantly higher temperature values. Even at 40 K faint remnants of the skyrmion excitations can still be detected. Finally at a temperature of 45 K these features disappear and the field dependence of the resonance frequencies is given by the universal spectrum of a chiral magnet.

By means of the presented microwave spectra, the evolution of the phase boundaries of the LTS phase of both samples is extracted as a function of temperature. They are displayed in Fig. 7.23(c). Here, the black shading corresponds to the platelet-shaped sample and the blue one is obtained for the cuboid. It can be seen that the width of the respective field range amounts approximately to the same value, but is shifted to higher values in the case of the platelet sample. In contrast, as discussed above, the temperature range in which the skyrmion lattice survives is larger for a cuboid-shaped sample. The extracted ratio between the two samples is given by a factor of approximately 1.5.

Despite the significant difference in the dimension ratios the microwave spectroscopy experiments on the quenched skyrmion lattice state in the lamella sample result in similar excitation spectra. We therefore refrain from a renewed description of the general appearance of these but guide the focus to an additional anomaly, not resolved in the previous frequency scans. With specific reference to the evolution of the CCW mode as a function of the external field a discontinuity is observed in the microwave spectra recorded on the lamella sample. In the numerical results given in Fig. 7.16 such an anomaly in the CCW resonances was already observed and identified to originate from the hybridization with a sextupol mode. For the assumed sample

shape in these calculations, $N_i = 1/3$, it is predicted to emerge very close to the transition field H_{c2}, though. As a consequence, this additional feature is masked by the prevailing excitation of the tilted conical and field-polarized modes in the experiments. By reducing the thickness and therefore increasing the contribution from the demagnetizing energy this crossing is shifted towards lower field values, as will be illustrated below, and therefore allowed to be detected. In Fig. 7.24 an expanded view around both hybridization regions of the microwave spectrum performed at 20 K is shown. While on the left hand side, Fig. 7.24(a), the interaction between the breathing and octupole mode is depicted, the right hand side, Fig. 7.24(b), highlights the crossing of the counterclockwise and sextupole mode. For illustration purpose, a different color code is chose in the spectra, with the corresponding dark colors indicating a strong absorption, induced by the dynamic response of the excited modes. The black triangular symbols, added to the graphs, are the extracted resonance positions from Lorentzian fits of the individual frequency sweeps as shown in Fig. 7.24(c)-(d). Here, the data are displayed by the black open circles, with the corresponding fits given by the solid lines. The field dependence of the resonance frequencies, obtained in the case of the breathing-octupole hybridization, agrees well with the results presented above. A clear bending of the breathing mode branch is resolved with a gap size of several hundreds of MHz. Conversely, the interaction between the CCW and sextupole modes is considerably less pronounced, as predicted by the numerical results. Instead of two distinct peaks, the hybridization with a second mode is revealed by an emerging shoulder in the Lorentzian profile of the frequency scans. A gap between the two resonance branches is barely apparent. Nevertheless, these features serve as an indication of the existence of a second dark skyrmion lattice mode, which is, without the hybridization mechanism mediated by the cubic anisotropy, not accessible in microwave spectroscopy experiments.

The quantity to be used for the characterization of the mode interaction strength is the minimum gap size between the respective resonance branches. By applying Lorentzian fits as shown in Fig. 7.24(c), the frequency difference as a function of external field B, $\Delta f(B) = f_1(B) - f_2(B)$, with mode index 1 and 2 is extracted. From this, the minimum gap size is obtained by $g = \min\{\Delta f(B)\}$. This step is performed for all samples and temperatures and finally provides a temperature evolution of g. The collated results are discussed, in combination with the numerical determined gap size, later on.

7.2.2 Theoretical Results

In order to support the experimental findings from the theoretical side, we draw on the Ginzburg-Landau model, including first only the magnetocrystalline anisotropy as additional energy term, if not stated otherwise. By construction of the parameters, only r_0 is assumed to be temperature de-
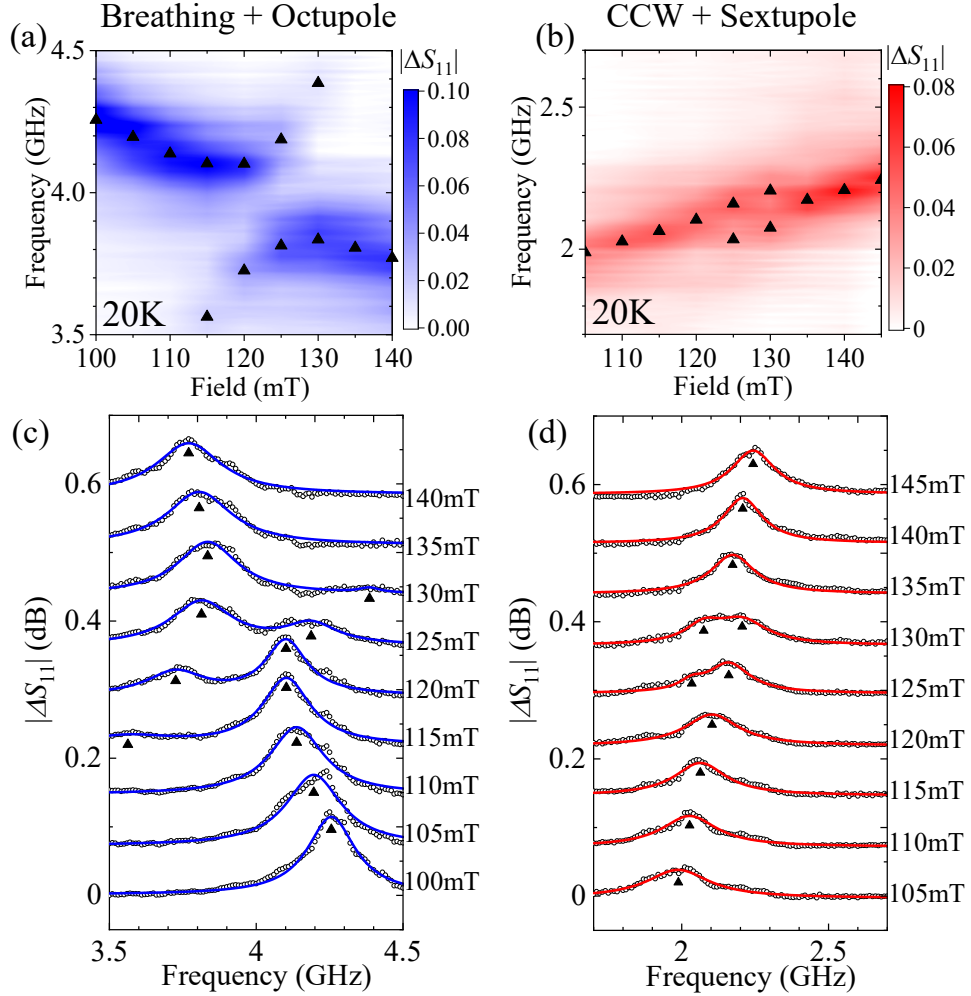
Figure 7.24: Expanded view of the (a) breathing-octupole and (b) CCW-sextupole mode hybridization regions of the microwave spectrum obtained at 20 K on the lamella sample. The color gradients represent the normalized microwave absorption intensity $|\Delta S_{11}|$. For the population of the low-temperature skyrmion phase during these measurements the external field is applied along the crystallographic [001] direction. In order to highlight the field dependence of the resonance branches, the respective excitation frequencies are depicted by triangular symbols. They are extracted from Lorentzian fits of the individual frequency sweeps, as illustrated in (c) and (d). Here, the data are given by open symbols, while the fitting curves are shown by the solid lines. Figure taken from [Tak21]

pendent, at the beginning. However, taking also the anisotropy into account, which likewise exhibits a strong temperature dependence, this assumption no longer holds. This results in a two-dimensional parameter space, regarding the temperature, which requires a workaround to limit the analysis to only one variable. By minimizing the energy functional, we obtain that the saturation magnetization M_s is directly proportional to the coefficient r_0. Additionally, M_s can be connected to the internal critical field by the internal susceptibility χ_{con}^{int} in the conical phase by,

$$M_s = H_{c2,0}^{int}\chi_{con}^{int}, \tag{7.2}$$

with $\chi_{con}^{int} \approx 1.76$ and $H_{c2,0}^{int}$ given in absence of the cubic anisotropy [Sch15]. In the limit of small K, the contribution of the anisotropy to the internal critical field can be neglected and hence the approximation $H_{c2,K}^{int} \approx H_{c2,0}^{int}$ is justified. With this, Eq. 7.2 is assumed to be valid also for finite K values. By choosing now the normalization protocol for the resonance frequencies, as already anticipated,

$$\nu_{c2,0}^{int} = \frac{g\mu_0\mu_B}{2\pi\hbar}H_{c2,0}^{int} \tag{7.3}$$

one obtains an estimate for the physical units, by extracting g, M_s and $H_{c2,0}^{int}$, respectively, from the measurements. The coefficient r_0 is therefore reduced to a scaling factor and the temperature dependence can quantitatively be reproduced by only adapting the anisotropy strength K. In the following $r_0 = -1000$ is chosen to match the previously obtained results.

For the translation between experiments and numerics, a conversion factor for the anisotropy still has to be determined. From the theoretical analysis in [Cha18] it could be observed, that $\tilde{K}_c^{th} \approx 0.0001$ marks the threshold for the stabilization of a low-temperature skyrmion lattice. It should be noted, that in order to avoid confusion the tilde notation was reintroduced for dimensionless variables. On the other hand, experimental findings [Cha18] suggest that this value corresponds to,

$$\tilde{K}_c^{exp} = \frac{K_{\sigma,c}}{\mu_0 H_{c2,0}^{int}M_s} \approx 0.07 \tag{7.4}$$

with anisotropy constant $K_{\sigma,c}$ given in units of energy density. In combination with the results obtained in [Hal18], which comprises the temperature dependence of K, our numerical data are therefore expected to provide an appropriate estimate of the resonance spectra for the investigated temperatures. In order to determine the hybridization gap from the theoretical side, we calculate the microwave excitation spectra for a wide anisotropy range, in analogy to Fig. 7.16. Since the discussion is limited only to the skyrmion resonances, the effect on the topologically trivial states will not be taken into consideration in this discussion. Anticipated by the experimental data, the sample shape and with this the demagnetizing energy, is playing

a non-negligible role in regard to the position of the mode branches with respect to each other and potentially also the interaction strength between those. Therefore, the analysis comprises two cases, including a spherical and lamella geometry, with the respective demagnetization factors given by $N_i = 1/3$ and $N_x = 0.06, N_y = 0.03, N_z = 0.91$.

In Fig. 7.25 we compare the microwave spectra of both systems (sphere: (a), lamella (b)), calculated at a moderate anisotropy strength of $K = 0.0002$ and dipolar strength of $\tau = 0.88$. As already introduced before, the spectra comprise the general field dependence of the resonance frequencies (gray dots) and the respective coupling efficiency to the oscillating magnetic field, implemented by the dot size. For the normalization of the field axes the respective critical field values $B_{c2,K}$ are chosen. The discussion focuses mainly on the well-established gyrational and breathing modes, but will also include higher order modes on account of the hybridization mechanism. It should be mentioned, that like the breathing and clockwise mode also the CW mode exhibits a finite spectral weight, which however is comparatively small and therefore masked by the chosen dot size of the spectrum. The color code, representing the direction of the driving field, is defined in the following. While blue is attributed to a parallel alignment along the surface normal, red corresponds to a driving field orientated within the skyrmion lattice plane. For reasons of clarity, orange circles are introduced to highlight the weak CW - dectupole and CCW - sextupole mode interactions. As expected from previous results [Sch15], both data sets bear a high level of resemblance. The contribution from the demagnetizing energy obviously does also not effect the generic appearance of the universal spectrum at low temperatures. A clear difference, however, is the larger spacing in frequency between the breathing and counterclockwise modes. The calculations reveal that, the thinner the sample, the higher and the lower the positions of the breathing and counterclockwise mode, respectively, in the frequency domain. We therefore observe that the intersection point between those branches is moving towards the critical transition field $B_{c2,K}$ and consequently out of the energetically stable field range, in accordance with the measurements presented in Fig. 7.23. In contrast, the shift of the counterclockwise mode to lower frequencies, leads to a likewise shift of the hybridization region with the sextupole mode to lower magnetic field strengths. This allows to detect the said anti-crossing in the case of the lamella sample, as observed in Fig. 7.24.

Interestingly, as can be seen from the spectra, not every mode crossing leads to a repulsion induced by the magnetocrystalline anisotropy. This suggests that the latter imposes a symmetry selection rule for the hybridization mechanism. In order to ascertain the allowed mode interactions, we calculate the inner product $\langle v_\alpha, v_\beta \rangle$ of the normalized eigenvectors, given by the eigenvalue equation Eq. 6.30. This quantity describes the projection of the eigenvectors onto each other and consequently the degree of linear
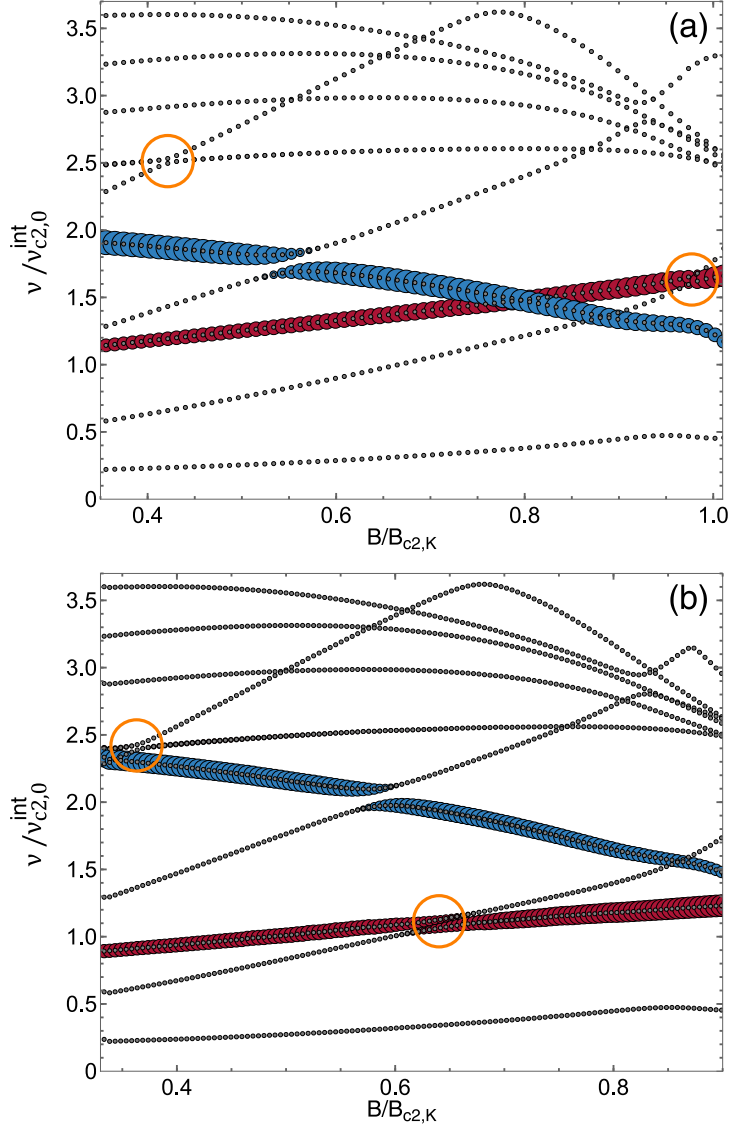
Figure 7.25: Theoretically calculated excitation spectra as a function of $B||[001]$ for a spherical (a) and lamella (b) shaped sample (gray symbols). The coupling efficiency to the oscillating magnetic field is reflected by the size of the colored symbols. Here, blue corresponds to the out-of-plane and red to the in-plane component of the latter. Due to their small interaction strength, orange circles were added to highlight the CW - dectupol and CCW - sextupol mode anti-crossing. The magnetocrystalline anisotropy strength is fixed to a value of $K = 0.0002$. The remaining parameters are set to $r_0 = -1000$ and $\tau = 0.88$. For the normalization of the field axes the respective transition fields $B_{c2,K}$ are chosen.

dependence. A finite value of the inner product is therefore an indication of the lifting of the initial orthogonality of the eigenvectors and a corresponding mode interaction. In Fig. 7.26 the inner product of the clockwise (orange), counterclockwise (red) and breathing (blue) mode, calculated from the data presented in Fig. 7.25(b) is illustrated. It is evident by comparing both figures that all curves reach a maximum value in the given field range, which corresponds to the position of the minimum gap size in the excitation spectrum of the lamella. Conversely, the amplitudes of the inner products appear not to be connected to the size of the gaps.

For a more comprehensive analysis, the determination of the inner product is extended to cover the range of modes given in the spectrum. With the selection rule presumably explained by symmetry arguments, the real-space configuration of the dynamic magnetization, shown in Fig. 7.17, will be first characterized regarding its number of symmetry axes m, similar to [Wai17]. In the interest of completeness, for the additional four modes we refer to [Wai17]. In the following, the modes are numbered in an ascending order, i.e. mode number 1 corresponds to the one lowest in frequency. Here, the reference point is chosen to be at $B/B_{c2,K} = 0.4$ in Fig. 7.25(a). Deducing the number of symmetry axes is straightforward for the resonance modes with the indicators 1, 2, 3, 4, 7, and 10 which is correlated to the number of nodes. Due to its rotational symmetry, the breathing mode (5) is a special case. In this context, m is assigned to infinity. The remaining modes 6, 8 and 9 stand out based on their more complex appearance. Conversely, they are divided into two ringlike structures, which do not necessarily exhibit the same pattern of motion. The number of symmetry axes might therefore be dependent on time and the rings need to be characterized individually. Since for those modes, the inner and outer rings have the same symmetry properties, only one indicator m is attributed to them. A summary of this categorization is given in Table 7.1. In addition to that, the polarization of the change of the homogeneous magnetization $\delta \boldsymbol{M}_0$ is extracted for the individual modes in absence of the cubic anisotropy. In the case of the well studied gyrational and breathing modes, $\delta \boldsymbol{M}_0$ rotates in the plane perpendicular with respect to the external field and oscillates along the external field direction, respectively. For the higher-order excitations, the polarization is determined by the symmetry of the mode profile and does not necessarily concur with the overall rotational sense. Due to a symmetric real-space distribution of $\delta \boldsymbol{M}(t)$, the respective modes do not exhibit a rotating dipole moment. The polarization is therefore oscillating along the z direction, which is given by the static field.

The inner product obtained for the considered modes at again a field value of $B/B_{c2,K} = 0.4$ is now presented in Table 7.2. It should be mentioned, that only a distinction between a finite and zero inner product is made, indicated by 1 and 0, respectively. Despite its clear dependence, the depicted results remain unchanged under increasing or decreasing the exter-
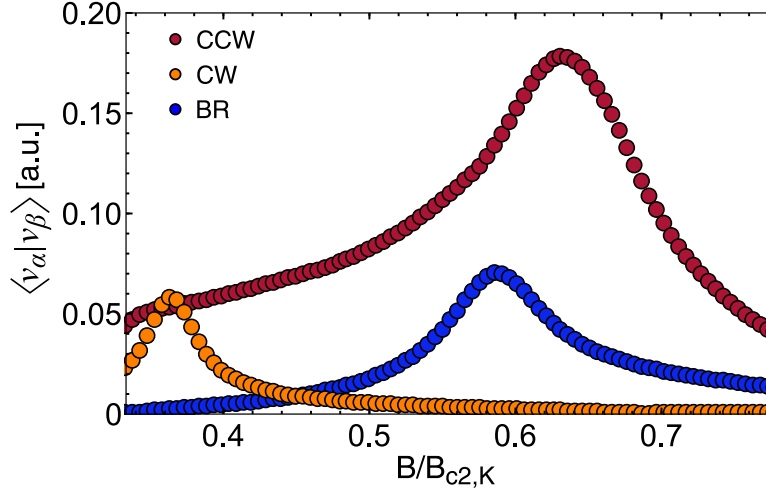
Figure 7.26: Calculated inner product $\langle v_\alpha, v_\beta \rangle$ of the interacting resonance branches, as a function of field. The eigenmodes are extracted from the resonance spectrum Fig. 7.25(b), obtained for the lamella sample. The data points display the CCW - sextupole (red), CW - dectupole (orange) and BR - octupole (blue) mode hybridization.

Table 7.1: Number of symmetry axis m, polarization and character of the time evolution of the respective resonance modes.

Mode	Symmetry axes m	Polarization	Character
1	2	linear-oop	quadrupole cw
2	3	elliptical-ip	sextupole cw
3	1	elliptical-ip	CCW
4	4	linear-oop	octupole cw
5	∞	linear-oop	BR
6	1	elliptical-ip	CW
7	5	elliptical-ip	dectupole cw
8	4	linear-oop	quadrupole cw*
9	3	elliptical-ip	sextupole cw/ccw
10	4	linear-oop	quadrupole ccw

nal field. From this table it is evident that the breathing mode, even though it is crossing the CW, dectupole, CCW and sextupole branches, does not hybridize with the listed modes. The same observation holds for the CW and octupole mode. In general, it can be concluded that from the symmetry arguments the magnetocrystalline anisotropy imposes a selection rule, which allows hybridizations between states with either only odd or only even m and additionally with rotational symmetry ($m = \infty$) and even m. From the point of view of the polarization, which is connected to the symmetry of the mode structure, only modes which are polarized in the same plane, are allowed to interact with each other.

As already mentioned in regard of the experiments, we exploit the hybridization gap as a characteristic of the interaction strength. Applying the same definition introduced before, the gap size g is collected for all three hybridizations from the numerically calculated spectra. The results, given in units of $\nu_{c2,0}^{\mathrm{int}}$ are summarized in Fig. 7.27 as a function of anisotropy strength K. The red and orange symbols represent the gap size of the CCW-sextupole and CW-dectupole coupling, whereas blue symbols indicate the one observed for the breathing-octupole hybridization. Here, open symbols correspond to the platelet, while closed symbols are extracted from the excitation spectra obtained for a spherical sample. From these curves, we observe that on the one hand the interaction strength strongly depends on the modes hybridizing and scales linearly with the anisotropy strength. In order to serve as a guide to the eye, linear fits to the results of the sphere, illustrated by the solid lines, are added to the data. On the other hand it is evident that the demagnetization provides only a minor contribution, suggesting the anisotropy to be the main cause for the anti-crossing.

For a comprehensive analysis of the temperature evolution, the gap size is extracted from the various microwave spectra obtained in both experiments and summarized in Fig. 7.28. The data points displayed in red (open symbols: platelet, closed symbols: cube) correspond to the bulk crystals, whereas the orange symbols represent the results from the lamella sample. The additional dashed red line serves as a guide to the eye. It should be mentioned that the intersection point with the abscissa is set to coincide with the observations reported in [Hal18]. There, the anisotropy is observed to vanish at a value of around $40\,\mathrm{K}$. Due to the vanishing coupling strength, the hybridizations of the clockwise and counterclockwise modes are not taken into consideration in this discussion. Despite originating from differently shaped samples, the obtained data sets reveal a very similar temperature dependence. In all three cases, the gap size increases with decreasing temperature stemming from the growth of the anisotropy strength. Additionally, also the finite momentum of the excited magnetization in the case of the lamella experiment, which results from the spatial distribution of the driving field, appears to have no significant effect on these results. For the comparison with the theoretically estimated gap size, the extracted values of Fig. 7.27

Table 7.2: Scalar product of the eigenvectors $\delta\boldsymbol{M}$ of the first ten excitation modes of the skyrmion lattice. For simplicity a finite value is given by 1 while a vanishing scalar product is indicated by 0.

Mode	1	2	3 (CCW)	4	5 (BR)	6 (CW)	7	8	9	10
1	1	0	0	1	1	0	0	1	0	1
2	0	1	1	0	0	1	1	0	1	0
3 (CCW)	0	1	1	0	0	1	1	0	1	0
4	1	0	0	1	1	0	0	1	0	1
5 (BR)	1	0	0	1	1	0	0	1	0	1
6 (CW)	0	1	1	0	0	1	1	0	1	0
7	0	1	1	0	0	1	1	0	1	0
8	1	0	0	1	1	0	0	1	0	1
9	0	1	1	0	0	1	1	0	1	0
10	1	0	0	1	1	0	0	1	0	1

are converted to physical units as described above. Note, a strong anisotropy is associated with a low temperature value. For simplicity, the maximum value of the experimentally determined M_s is substituted, leaving the linear dependence as shown in Fig. 7.27 unchanged. The results are illustrated by the dashed blue line, reminiscent of the course provided by experimental data. The theoretically predicted gap size, nevertheless, deviates by a factor of around 2-3. Since the error arising from the unit conversion is assumed to be small compared to the one stated above, this result suggests that further energy terms might have to be included in the discussion. For this reason, the effect of the exchange anisotropy, which was already introduced in Eq. 6.4, on the magnetization dynamics will be investigated in the following.

Before arriving at the point of evaluating the gap size, it is necessary first to perform again the minimization routine of the energy density, now with the additional energy contribution included. By adding this further temperature dependent variable, however, the dimension of the free parameter space is increased by one. This requires, in principle a systematic approach of calculating the mean-field configuration for all various constellations of these parameters. Given that they ultimately can not be uniquely determined by the experiment though, we drawn upon the preceding results in order to simplify the analysis in the following. From the previous measurement it was concluded that the cubic magnetocrystalline anisotropy is identified as the main stabilization mechanism of the low-temperature skyrmion phase. In addition to that, in combination with the microwave spectroscopy data, presented above, the numerical treatment reveals it to be also the main contribution to the observed hybridization mechanism. Based on these findings, we invoke the measurements of K in [Hal18], which also provide an estimate of the anisotropy strength required in the theoretical model, and
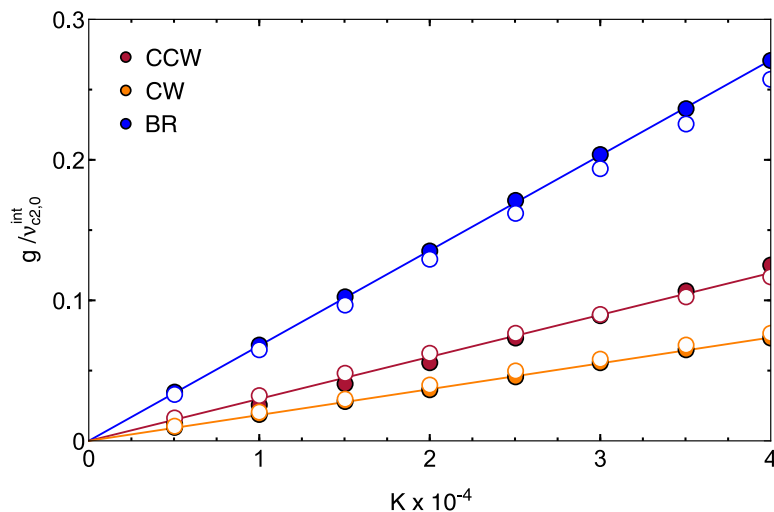
Figure 7.27: Theoretically predicted hybridization gap sizes as a function of anisotropy strength K in units of $\nu_{c2,0}^{int}$. The data points are extracted from microwave spectra calculated in the case of a spherical (closed symbols) and lamella (open symbols) shaped sample. Illustrated are the breathing-octupole mode (blue), clockwise-dectupole mode (orange) and counterclockwise-sextupole mode (red) hybridization gaps. Colored lines are added as guides to the eyes. The remaining parameters are set to $r_0 = -1000$ and $\tau = 0.88$.

fix the parameter therefore to a moderate value of $K = 0.0002$. With also the Ginzburg-Landau parameter, the dipolar strength and the demagnetization factors set to $r_0 = -1000$, $\tau = 0.88$ and $N_i = 1/3$ only the external field B and exchange anisotropy strength C enter the model as variables. In analogy to the previous numerical treatment, the mean-field configuration is determined as a function of the external field for various C values. Note, since the sign of the exchange anisotropy constant is not predefined, this step is executed for both, positive and negative values. Finally, by means of substituting this newly obtained magnetization configuration, the resonance frequencies are calculated by evaluating the eigenvalue equation Eq. 6.30 for the given range of parameters B and C.

In Fig. 7.29 two microwave spectra, determined in presence of the exchange anisotropy term, are depicted. In order to highlight the importance of the sign of C, the chosen amplitude of the constant is kept the same while the sign is reversed: in the top panel (a) the exchange anisotropy constant is set to $C = 0.2$, whereas the results presented in the bottom panel (b) are calculated for $C = -0.2$. In both cases the cubic magnetocrystalline anisotropy parameter is fixed to $K = 0.0002$, as motivated above. For illustration purposes of the changes induced by the additional anisotropy term, the spectra
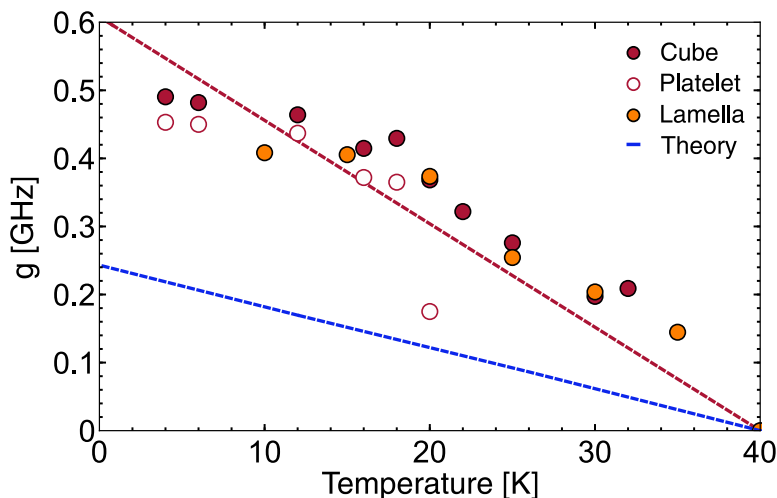
Figure 7.28: Comparison between the experimentally and numerically extracted gap sizes g of the breathing-octupole mode hybridization as a function of temperature. The results obtained from the experiments on the bulk and lamella samples are given by the red (cube: closed, platelet: open) and orange circles, respectively. The dashed red line serves as a guide to the eye. The dashed blue line represents the values obtained from the theoretical model, converted to physical units. Note that, the intersection point of both lines with the abscissa is chosen to be consistent with the observations reported in [Hal18].

should be compared to the data shown Fig. 7.25(a). The color code and the symbol size convention is chosen in regard with the above mentioned excitation spectrum. Additionally, for the normalization of the external field again the respective critical field values $B_{c2,K,C}$ are chosen. Note that also the latter are affected by the additional energy contribution as indicated by the extended index. The most striking difference between these two excitation spectra for this amplitude of C is the sign dependent enlargement or reduction of the breathing-octupole mode hybridization gap size, with respect to the case, calculated in absence of the exchange anisotropy. While in the top panel, the gap size reaches a value which is almost double the one obtained in Fig. 7.25(a) and therefore equal to the one observed in the experiments, in the bottom panel the anti-crossing in principle does not occur. Only the small discontinuity in the spectral weight of the breathing mode at the intersection point, reveals a potential interaction with the octupole mode. Besides these findings, also deviations of the CW - dectupol mode interaction strength in both spectra can be observed. In contrast to the spectrum determined in the $C = 0$ case, here, the gap size increases strongly, independently of the sign of the exchange anisotropy. For reasons of clarity, orange circles are introduced to highlight the CW - dectupol mode

115

interaction. While in the top panel an increase of a factor of approximately 5 is extracted, in the bottom panel g is enhanced by a factor of around 4.5. Due to the vanishing spectral weight, however, this mode interaction is predicted not to be accessible in microwave spectroscopy experiments. Another interesting observation is the fact that, at least in the frequency range of interest, no further hybridizations are induced by the additional energy term, but only the ones mediated by the cubic magnetocrystalline anisotropy get more or less pronounced.

A continuous increase or decrease of the gap size as a function of $|C|$ in the case of a positive or negative sign, as the results above might indicate, is actually not observed after evaluating the remaining spectra. In Fig. 7.30 the respective amplitude dependence of the extracted gap sizes are contrasted. It should be mentioned that, here, the discussion is limited to the hybridization gap between the breathing and octupole mode only. In the interest of clarity, the results, which are obtained without the additional contribution from the exchange anisotropy are also added to the graph. They are illustrated by the blue symbols and given as a function of K, with the bottom x axis, representing the corresponding scale. The red ($C > 0$) and orange ($C < 0$) data points are obtained from the microwave spectra, which are calculated for a fixed cubic magnetocrystalline anisotropy constant set to $K = 0.0002$, but various exchange anisotropy strengths. They are depicted as a function of $|C|$ with the respective x axis given by the top one. Due to the finite K value in these calculations, the gap sizes at $|C| = 0$ coincide with the last data point of the data set given in blue, as indicated by the dashed black line. Interestingly, independent of the sign of C, after exceeding certain exchange anisotropy strengths the gap sizes amount to a value 2-3 times larger than the one obtained for only one additional energy term. However, the curve progressions taken for reaching this value differ significantly. While for a positive sign of C the linear increase of g continues, the competition between both anisotropies leads first to a decrease of the gap size, in the case of $C < 0$. Reaching a value of around $C = -0.2$ the exchange anisotropy prevails, which finally causes an continuous increase of the gap size again. These observations originate from the fact that depending on the sign of C either the [100] or [111] crystal lattice directions minimize the energy contribution arising from the exchange anisotropy, as elaborated above. Considering the linear increase of g in the experiments, it stands to reason that, provided the exchange anisotropy is indeed strong enough to influence the gap size, the sign of the respective prefactor C is suggested to be positive. While a negative constant C would first lead to a decrease of g, a sudden sign change would result in a discontinuity in the temperature evolution. Both features are not resolved in the experimentally determined gap size collated in Fig. 7.28. To summarize, the inclusion of only the magnetocrystalline anisotropy is not sufficient to reproduce the magnitude of the gap size obtained from the experiments. By means of implementing
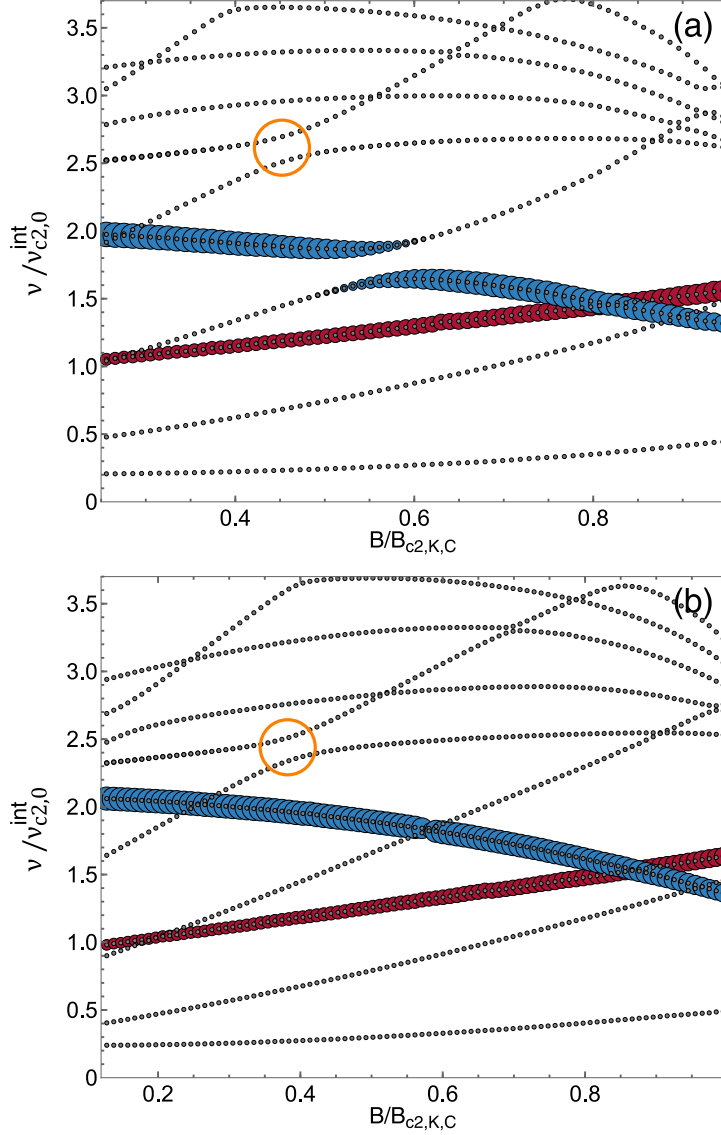
Figure 7.29: Theoretically calculated excitation spectra as a function of $B\|[001]$ for a spherically shaped sample, with the magnetocrystalline anisotropy set to $K = 0.0002$ and exchange anisotropy to $C = 0.2$ (a) and $C = -0.2$ (b) (gray symbols). The coupling efficiency to the oscillating magnetic field is reflected by the size of the colored symbols. Here, blue corresponds to the out-of-plane and red to the in-plane component of the latter. The remaining parameters are set to $r_0 = -1000$ and $\tau = 0.88$. For the normalization of the field axes the respective transition fields $B_{c2,K,C}$ are chosen.

the exchange anisotropy in the numerical model, the discrepancy between measurements and theory allows to be reduced, but the emergence and the respective strength of C remains to be verified. In addition to that, further anisotropy terms arise due to the cubic environment of the crystal lattice and might need to be taken into account for a comprehensive analysis.
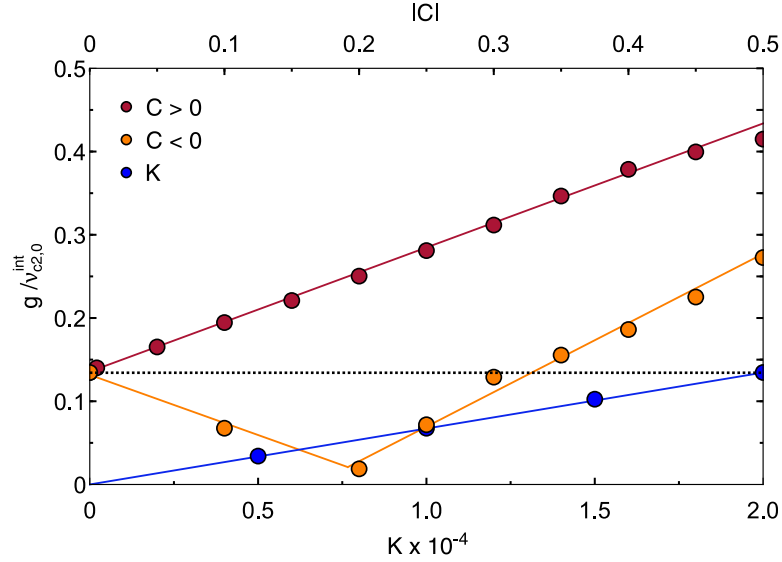
Figure 7.30: Theoretically predicted hybridization gap size of the breathing-octupole mode interaction as a function of anisotropy strength K and C, respectively, in units of $\nu_{c2,0}^{int}$. The data points are extracted from microwave spectra calculated in the case of a spherically shaped sample, with the remaining parameters set to $r_0 = -1000$ and $\tau = 0.88$. Note, two case are distinguished in the following. Given by the blue symbols are the previously discussed results (Fig. 7.27), which are obtained in absence of the exchange anisotropy. Here, g is shown as a function of K with the respective x axis given at the bottom. In the case of the remaining two data sets, depicted by red ($C > 0$) and orange ($C < 0$) symbols, the cubic magnetocrystalline anisotropy strength is fixed to $K = 0.0002$ in the calculations and g is displayed as a function of exchange anisotropy strength C. The respective x axis is given at the top. Colored lines are added as guide to the eyes.

7.3 Angle-Resolved Microwave Broadband Spectroscopy

A well-established technique for verifying the existence of anisotropy contributions and quantifying the corresponding strengths, comprises the sampling of the energy landscape in terms of the orientation-dependent resonance condition. In these experiments the magnetization is excited using an ac-magnetic field, while the direction of the static magnetic field is rotated in a controlled manner around predefined with respect to the reference frame. These are usually chosen to coincide with the lattice structure, in order to simplify the subsequent analytic treatment. As a consequence of the reorientation of the external field, the effective field and the resulting equilibrium configuration of the magnetization are varied. It therefore precesses at different resonance frequencies, reflecting the angle-dependence of the underlying anisotropic energy landscape. Conclusions are finally drawn on the individual energy terms, by comparing the obtained results to the theoretically predicted resonance frequencies, which in certain cases can be derived analytically. This measurement protocol can also be utilized for studying helimagnets, like the bulk crystal Cu_2OSeO_3, provided the magnetic field and temperature parameters are chosen to match the non-modulated spin state, e.g. field-polarized phase. The aim of the following chapter is to elaborate remaining open questions from preceding studies in regard of undetermined anisotropy contributions present in the chiral magnet Cu_2OSeO_3. In the first part, the focus lies on the investigation of the field-polarized phase. With the magnetization fully aligned, however, anisotropy terms given by a gradient representation like the previously discussed exchange anisotropy, vanish and consequently do no contribute to the angle-dependence of the resonance position. Since anisotropies are known to determine also the transition field from the conical into the field-polarized phase [Sch15], the second part of this chapter comprises the study of the critical field value B_{c2} as a function of angle and temperature. In the interest of clarity, first the theoretical treatment of these quantities will be presented. It comprises the analytical derivation of the respective equations and the subsequent comparison to the numerically obtained results. These derived equations are finally applied to the excitation spectra resolved in the microwave spectroscopy experiments, in the second part.

7.3.1 Derivation of the angle-dependent FMR condition

In order to support the experimental and numerical findings, the dependence of the resonance frequencies on the magnetic field direction with respect to the sample and crystallographic axis will be derived analytically. The calculations to be performed will follow the protocol of solving the lossless Landau-Lifshitz equation of motion Eq. 2.1 given in Chap. 2. Assuming the

magnetization to form ferromagnetic order aligned parallel to the externally applied magnetic field and M_s to be constant, the energy density functional is determined by

$$F = \tau \boldsymbol{M} \mathcal{T}(\phi_\mathrm{D}, 0) \boldsymbol{N} \mathcal{T}^{-1}(\phi_\mathrm{D}, 0) \boldsymbol{M} - K \sum_i M_i^4 - \boldsymbol{B} \boldsymbol{M} \qquad (7.5)$$

only, with demagnetization energy, cubic magnetocrystalline anisotropy and Zeeman interaction. As anticipated before, gradient terms are not included in the discussion due to the spatially uniform alignment of the magnetization. The prefactors of the individual energy terms are chosen to match the dimensionless units notation, introduced in Chap. 6. For the comparison to the experimental data, the equations will be finally converted to physical dimensions. The direction dependence of the resonance condition originates from the orientation of the magnetization with respect to the crystallographic axes on the one hand and the principle axes of the sample on the other hand. Here, the [100]-axes of the lattice are aligned with the laboratory coordinate system given by the $\hat{\boldsymbol{e}}_x$, $\hat{\boldsymbol{e}}_y$ $\hat{\boldsymbol{e}}_z$ unit vectors, while the principle axes of the sample are rotated around the [001] or z direction by means of the rotation matrix $\mathcal{T}$,

$$\mathcal{T}(\phi, \theta) = \begin{pmatrix} \cos\phi\cos\theta & -\sin\phi & \cos\phi\sin\theta \\ \sin\phi\cos\theta & \cos\phi & \sin\phi\sin\theta \\ -\sin\theta & 0 & \cos\theta \end{pmatrix} \qquad (7.6)$$

and angle ϕ_D. Here, the notation $^{-1}$ indicates the inverse of the rotation matrix $\mathcal{T}$. In general, anisotropic energy contributions counteract a parallel alignment of the magnetization with the external field, provided the latter is not applied along one of the corresponding easy axes. Since, however, the actual deviation from the collinear alignment with the magnetic field and the resulting frequency difference is negligible, as discussed in the appendix Appendix B, the assumptions made are justified.

By taking the derivative of the free energy, the effective field is calculated by $\boldsymbol{B}_\mathrm{eff} = -\frac{\delta F}{\delta \boldsymbol{M}}$. Inserting the ansatz for the time-dependent magnetization vector, $\boldsymbol{M} = \boldsymbol{M}_\mathrm{s} + \delta\boldsymbol{M}$, and expanding up to the first order in the dynamic magnetization component results in the following effective fields,

$$\boldsymbol{B}_\mathrm{eff}^0 = \begin{pmatrix} -B_x - 4KM_x^3 \\ -B_y - 4KM_y^3 \\ -B_z - 4KM_z^3 \end{pmatrix}$$
$$+ \begin{pmatrix} \tau(M_x(N^+ + N^- \cos 2\phi_\mathrm{D}) + M_y N^- \sin 2\phi_\mathrm{D}) \\ \tau(M_y(N^+ - N^- \cos 2\phi_\mathrm{D}) + M_x N^- \sin 2\phi_\mathrm{D}) \\ 2\tau M_z N_z \end{pmatrix}, \qquad (7.7)$$

$$\boldsymbol{B}_{\text{eff}}^{1} = \begin{pmatrix} -12KM_x^2\delta M_x + \tau\left(\left(N^+ + N^-\cos 2\phi_{\text{D}}\right)\delta M_x + N^-\delta M_y\sin 2\phi_{\text{D}}\right) \\ -12KM_y^2\delta M_y + \tau\left(\left(N^+ - N^-\cos 2\phi_{\text{D}}\right)\delta M_y + N^-\delta M_x\sin 2\phi_{\text{D}}\right) \\ -12KM_z^2\delta M_z + 2\tau N_z\delta M_z \end{pmatrix}$$

$$(7.8)$$

with indices 0 and 1 indicating the order of the dynamic magnetization component $\delta\boldsymbol{M}$ and notation $N^+ = N_x + N_y, N^- = N_x - N_y$. The integration of these in the reduced Landau-Lifshitz equation given in Eq. 2.7 leads to the matrix,

$$\mathcal{W}' = (\mathcal{W}_1', \mathcal{W}_2', \mathcal{W}_3') \qquad (7.9)$$

which is composed by the three column vectors,

$$\mathcal{W}_1' = \begin{pmatrix} i\omega + \tau M_z N^-\sin 2\phi_{\text{D}} \\ -B_z + 4K\left(3M_x^2 M_z - M_z^3\right) - \tau M_z\left(N^+ - 2N_z + N^-\cos 2\phi_{\text{D}}\right) \\ B_y - 4K\left(3M_x^2 M_y - M_y^3\right) + 2\tau N^-\left(M_y\cos 2\phi_{\text{D}} - M_x\sin 2\phi_{\text{D}}\right) \end{pmatrix}$$

$$(7.10)$$

$$\mathcal{W}_2' = \begin{pmatrix} B_z - 4K\left(3M_y^2 M_z - M_z^3\right) + \tau M_z\left(N^+ - 2N_z - N^-\cos 2\phi_{\text{D}}\right) \\ i\omega - \tau M_z N^-\sin 2\phi_{\text{D}} \\ -B_x + 4K\left(3M_x M_y^2 - M_x^3\right) + 2\tau N^-\left(M_x\cos 2\phi_{\text{D}} + 2M_y\sin 2\phi_{\text{D}}\right) \end{pmatrix}$$

$$(7.11)$$

$$\mathcal{W}_3' = \begin{pmatrix} -B_y + 4K\left(3M_y M_z^2 - M_y^3\right) \\ B_x - 4K\left(3M_x M_z^2 - M_x^3\right) \\ i\omega \end{pmatrix}$$

$$+ \begin{pmatrix} \tau\left(M_y\left(N^+ - 2N_z - N^-\cos 2\phi_{\text{D}}\right) + M_x N^-\sin 2\phi_{\text{D}}\right) \\ -\tau\left(M_x\left(N^- - 2N_z + N^-\cos 2\phi_{\text{D}}\right) + M_y N^-\sin 2\phi_{\text{D}}\right) \\ 0 \end{pmatrix} . \qquad (7.12)$$

The resonance frequencies are calculated by the determinant of $\mathcal{W}'$, which equates to zero, as derived in Eq. 2.10.

In order to obtain the angle-dependence of the resonance condition, the magnetization- and field-components are transformed into a spherical coordinate representation, reading

$$\boldsymbol{M} = M_{\text{s}}\left(\sin\theta\cos\phi, \sin\theta\sin\phi, \cos\theta\right)^{\text{T}} \qquad (7.13)$$

$$\boldsymbol{B} = B_0\left(\sin\theta\cos\phi, \sin\theta\sin\phi, \cos\theta\right)^{\text{T}}, \qquad (7.14)$$

with polar and azimuthal angles θ and ϕ. In the interest of clarity, the corresponding coordinate system is illustrated in Fig. 7.31. As anticipated before, the lab frame axes coincide with the crystallographic directions, i.e. $\hat{\boldsymbol{e}}_x||[100]$, $\hat{\boldsymbol{e}}_y||[010]$ and $\hat{\boldsymbol{e}}_z||[001]$, which are given by the black arrows. The direction of the magnetization, characterized now by θ and ϕ, is indicated by the orange arrow. Based on the assumption that both magnetization and external field are collinear, the latter is omitted in the illustration. In the

following, the focus of the analysis is limited to a rotation of the magnetic field within the plane spanned by either the [100]- and [010]-directions or [001]- and [110]-directions. Since the former is aligned parallel to the CPW in the experiments described beneath, a rotation within this plane will be referred to as "in-plane", while a rotation within the [001]-[110] plane will be referred to as "out-of-plane" rotation. The corresponding sense of rotation is highlighted by the dashed red and dashed blue line.

For $\theta = \frac{\pi}{2}$ and consequently a rotation confined to the [100]-[010] plane the predicted resonance frequencies are given by,

$$\nu = \gamma\sqrt{B_1 + B_2 + B_3} \tag{7.15}$$

with the individual components

$$
\begin{aligned}
B_1 &= B_0^2 + 3B_0 K M_0^3 + 4\left(KM_0^3\right)^2 - B_0\tau M_0\left(N^+ - 2N_z\right) \\
&\quad + 2\tau^2 M_0^2\left(N^-\right)^2 \\
B_2 &= -\tau M_0 N^-\left(12KM_0^3 + 3B_0 - 2\tau M_0\left(N^+ - 2N_z\right)\right)\cos 2\phi \cos 2\phi_{\mathrm{D}} \\
&\quad + \left(3B_0 - 2M_0\left(N^+ - 2N_z\right)\tau\right)\sin 2\phi \sin 2\phi_{\mathrm{D}} \\
B_3 &= KM_0^3\left(12KM_0^3 + 5B_0 - 4\tau M_0\left(N^+ - 2N_z\right)\right)\cos 4\phi.
\end{aligned}
\tag{7.16}
$$

This result represents a superposition of a twofold and fourfold symmetry, originating from the demagnetization and anisotropy energy, respectively. In the limit of a vanishing anisotropy strength, $K = 0$, the above given field components are reduced to,

$$
\begin{aligned}
B_1 &= (B_0 + 2\tau M_0(N_y - N_x))(B_0 + 2\tau M_0(N_z - N_x)) \\
B_2 &= -\tau M_0\left(N_x - N_y\right)\left(3B_0 - 2M_0\left(N_x + N_y - 2N_z\right)\tau\right)\left(\cos 2\left(\phi - \phi_{\mathrm{D}}\right) - 1\right) \\
B_3 &= 0.
\end{aligned}
\tag{7.17}
$$

Furthermore, in the case of a parallel alignment of the external field and one of the principal axes of the sample, for instance the x axis, i.e. $\phi = \phi_{\mathrm{D}} = 0$, the above equations reduce to the representation of the well-known Kittel formula [Kit48],

$$\nu = \gamma\sqrt{\left(B_0 + 2\tau M_0(N_y - N_x)\right)\left(B_0 + 2\tau M_0(N_z - N_x)\right)} \tag{7.18}$$

On the other hand, assuming the sample to be of a symmetric shape with respect to the rotation plane, $N_x = N_y$ holds and the spatial dependence, arising from the demagnetization energy vanishes. Its contribution is reduced to a frequency offset, given by the difference $N_x - N_z$. The obtained
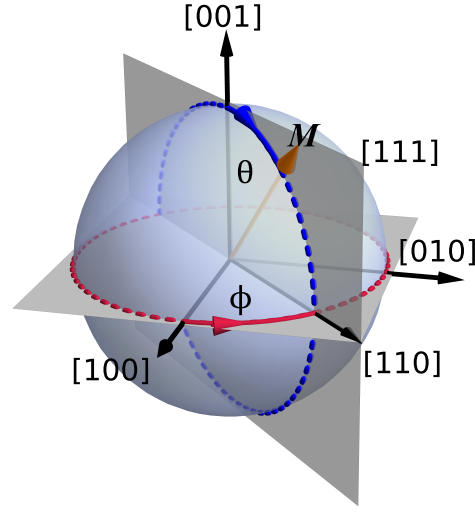
Figure 7.31: Schematic of the coordinate system. The laboratory coordinate system spanned by the unit vectors $\hat{e}_x$, $\hat{e}_y$ and $\hat{e}_z$ is aligned with the crystallographic axes [100], [010] and [001], which are indicated by the black arrows. Given by the orange arrow, is the magnetization direction, defined by the angles θ and ϕ. The rotation of the external field will be limited to the planes spanned by the [100]- and [010]- directions and the [001]- and [110]-directions in the analytical model. The respective sense of rotation is visualized by the dashed red and blue lines.

resonance condition is therefore composed by,

$$
\begin{aligned}
B_1 &= \left(B_0 + 4KM_0^3\right)^2 \\
B_2 &= -2M_0(N_x - N_z)\tau(B_0 + 4KM_0^3\cos 4\phi) \\
B_3 &= +KM_0^3\left(12KM_0^3 + 5B_0\right)(\cos 4\phi - 1)
\end{aligned}
\tag{7.19}
$$

and only governed by a four fold symmetry. For a spherical or also cube-like sample, $N_x = N_z$, the second component $B_2 = 0$ vanishes.

In order to visualize the derived equations, the resonance frequency given as a function of angle is illustrated in Fig. 7.32(a), (c) for the two cases of a spherical $(N_i = 1/3)$ and cuboid $(N_x = 0.25, N_y = 0.35, N_z = 0.4)$ shaped sample. As specified before, the polar angle is set to $\theta = \frac{\pi}{2}$, which confines the rotation to the [100]-[010] plane. The figures are both composed of the numerical results, generated by the *Mathematica* code as described above and the analytic results obtained from the derived equations. The individual contributions are indicated by the symbols and dashed lines, respectively. The calculations are performed for a fixed temperature and field value, set to $r_0 = -1000$ and $B = 2B_{c2}$ [2] and various anisotropy strengths K. The

---

[2] The used critical field value B_{c2} complies with the one obtained for a spherical sample.

values used for the calculations are $K = 0$, $K = 0.00005$ and $K = 0.0002$, reflected by the cyan, light and dark blue coloring. Note, the case $K = 0$ is omitted in Fig. 7.32(a), since the resonance frequency does not exhibit an angle-dependence and remains constant. As predicted by equation Eq. 7.19, for a spherical sample and therefore in absence of the demagnetization contribution, the angle-dependence of the resonance frequencies is determined by a fourfold symmetry only, with offset and amplitude of the oscillations increasing with increasing K value. Diverging from a symmetric sample shape, the resonance condition is given by a superposition of a two- and fourfold symmetry, as illustrated in Fig. 7.32(c). In both figures it is evident that the analytical model diverges from the numerical results for certain field configurations. These discrepancies arise from the fact that the magnetization orientation deviates from a parallel alignment with respect to the external field, as anticipated before. A more elaborate description is presented in Appendix B. Since the frequency mismatch is, however, rather small, the assumptions made hold and the derived equation is applicable.

In the limit of small K, a series expansion of equation Eq. 7.15 up to first order in K results in

$$\nu = \gamma \left(\sqrt{B_1 + B_2} + \frac{B_3}{2\sqrt{B_1 + B_2}} \right) \tag{7.20}$$

with

$$B_1 = (B_0 + 2\tau M_0(N_y - N_x))(B_0 + 2\tau M_0(N_z - N_x))$$
$$B_2 = -\tau M_0 \left(N_x - N_y \right) \left(3B_0 - 2M_0 \left(N_x + N_y - 2N_z \right) \tau \right) \left(\cos 2 \left(\phi - \phi_{\mathrm{D}} \right) - 1 \right)$$
$$B_3 = K M_0^3 (3(B_0 - 4M_0(N_x - N_y)\tau \cos 2\phi \cos 2\phi_{\mathrm{D}})$$
$$+ (5B_0 - 4M_0(N_x + N_y - 2N_z)\tau) \cos 4\phi).$$
$$\tag{7.21}$$

Applying again the external field along one of the [100]-directions, $\phi = \pi/2$, and assuming the principal axes of the sample to coincide, $\phi_{\mathrm{D}} = 0$, the resonance condition is written in the form

$$\nu = \gamma \left(\sqrt{(B_0 + 2\tau M_0(N_x - N_y))(B_0 + 2\tau M_0(N_z - N_y))} \right.$$
$$\left. + 4K M_0^3 \frac{(B_0 + \tau M_0(N_x + N_z - 2N_y))}{\sqrt{(B_0 + 2\tau M_0(N_x - N_y))(B_0 + 2\tau M_0(N_z - N_y))}} \right) \tag{7.22}$$

As presented in Appendix C, this expression can be simplified to

$$\nu = \gamma \left(\sqrt{(B_0 + 2\tau M_0(N_x - N_y))(B_0 + 2\tau M_0(N_z - N_y))} + 4K M_0^3 \right), \tag{7.23}$$

which reflects the sum of the Kittel mode and a term linear in K, weighted by the saturation magnetization M_0. This equation and the results, extracted

from the numerical calculations for the sample shapes discussed above, are plotted in Fig. 7.32(b),(d) as a function of K. It can be seen that both the analytical model and the numerical data are in a good agreement.

For the analysis of the experimental data, the dimensionless parameters given by the equations derived above need to be converted into physical units. Following the notation introduced in Chap. 6, the corresponding resonance condition reads

$$\omega = \mu_0 \gamma \sqrt{H_1 + H_2 + H_3} \tag{7.24}$$

with the individual components defined as

$$
\begin{aligned}
H_1 &= H_0^2 + 3H_0 \frac{K}{\mu_0 M_\mathrm{s}} + 4 \left(\frac{K}{\mu_0 M_\mathrm{s}} \right)^2 - \frac{1}{2} H_0 M_\mathrm{s} \left(N^+ - 2N_z \right) \\
&\quad + \frac{1}{2} M_\mathrm{s}^2 \left(N^- \right)^2 \\
H_2 &= -\frac{1}{2} M_\mathrm{s} N^- \left(12 \frac{K}{\mu_0 M_\mathrm{s}} + 3H_0 - M_\mathrm{s} \left(N^+ - 2N_z \right) \right) \cos 2\phi \cos 2\phi_\mathrm{D} \\
&\quad + \left(3H_0 - M_\mathrm{s} \left(N^+ - 2N_z \right) \right) \sin 2\phi \sin 2\phi_\mathrm{D} \\
H_3 &= \frac{K}{\mu_0 M_\mathrm{s}} \left(12 \frac{K}{\mu_0 M_\mathrm{s}} + 5H_0 - 2M_\mathrm{s} \left(N^+ - 2N_z \right) \right) \cos 4\phi.
\end{aligned}
\tag{7.25}
$$

7.3.2 Derivation of B_{c2} (I)

For the determination of the field boundary between the conical and field-polarized phase, the free energy Eq. 6.4 is minimized with respect to the magnetization configuration similar to the approach given in [Wai17]. Assuming the spin texture to form a single domain helix in the mean-field limit, the ansatz used in the following calculations is parameterized by

$$\boldsymbol{M}(\boldsymbol{r}) = M_0 \hat{\boldsymbol{e}}_3 + A \cos(\boldsymbol{Q} \cdot \boldsymbol{r}) \hat{\boldsymbol{e}}_1 + A \sin(\boldsymbol{Q} \cdot \boldsymbol{r}) \hat{\boldsymbol{e}}_2 \tag{7.26}$$

with the pitch vector $\boldsymbol{Q} = Q \left(\sin \theta \cos \phi, \sin \theta \sin \phi, \cos \theta \right)^\mathrm{T}$, $(\boldsymbol{Q} || \hat{\boldsymbol{e}}_3)$, and the orthonormal right-handed basis $\hat{\boldsymbol{e}}_1 \times \hat{\boldsymbol{e}}_2 = \hat{\boldsymbol{e}}_3$. In addition to that, in order to derive B_{c2} analytically, the pitch vector is assumed to be parallel to the external field, $\boldsymbol{Q} || \boldsymbol{B}$, and distortions of the helix configuration arising from the cubic anisotropy to be negligible. It should be mentioned that due to its explicit spatial dependence, the magnetocrystalline anisotropy contribution is evaluated over one helix period $2\pi/Q$. In contrast to that, only the static magnetization component M_0 is taken into account in the case of the demagnetizing energy, since local dipole fields average out [Wai17].
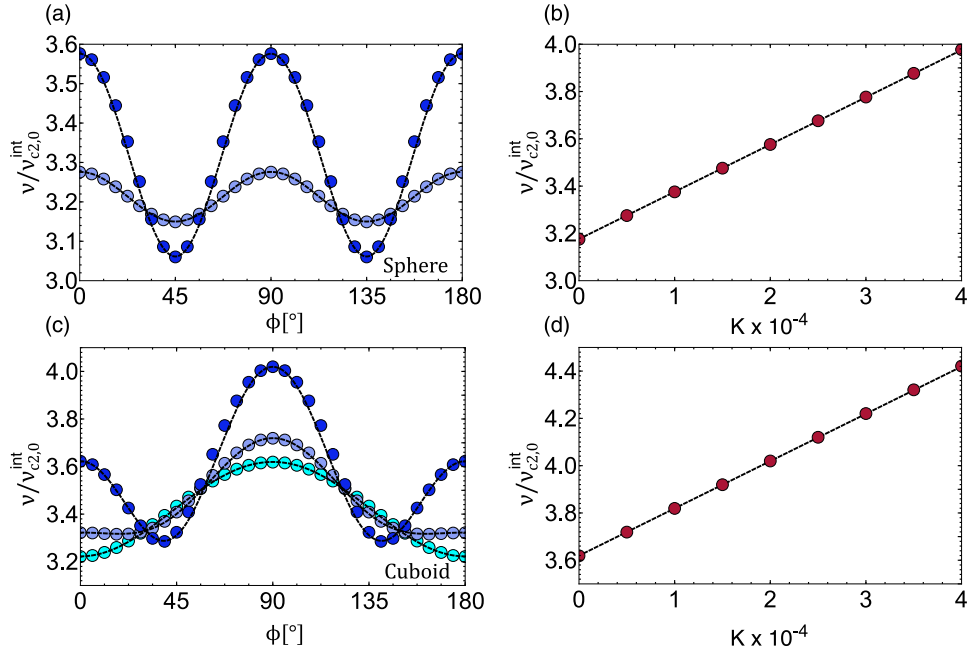
Figure 7.32: (a)-(c) Resonance frequency ν as a function of external field direction ϕ in the case of a spherical (top panel) and cuboid (bottom panel) sample shape, normalized with respect to $\nu_{c2,0}^{int}$. Given by the symbols are the numerical data, obtained for anisotropy values set to $K = 0$ (cyan) $K = 0.00005$ (light blue) and $K = 0.0002$ (dark blue). The corresponding analytical results, following Eq. 7.15, are illustrated by the dashed black lines. (b)-(d) Resonance frequency ν as a function of anisotropy strength K with the external field applied along the x direction, normalized with respect to $\nu_{c2,0}^{int}$. While the numerical data is represented by the symbols, the analytical approximation Eq. 7.23 is given by the dashed black lines. The dipolar strength, Ginzburg-Landau parameter and field strength are set to $\tau = 0.88$, $r_0 = -1000$ and $B = 2B_{c2} = 76$.

In-plane rotation

Inserting the magnetization configuration Eq. 7.26 into Eq. 6.4 and minimizing with respect to the pitch vector length Q and modulation amplitude A yields

$$Q \rightarrow 1 \tag{7.27}$$

$$A \rightarrow \frac{(2\sqrt{8M_0^2 - 3KM_0^2(1 - \cos 4\phi) + 4t + 2})}{\sqrt{3K(7 + \cos 4\phi) - 32}}. \tag{7.28}$$

In the last step the results of Eq. 7.27 is already substituted. Note that, in accordance with [Eve12; Wai17] the notation $t = r_0/(JQ^2) - 1$ is introduced. In the limit of $A = 0$, which marks the transition into the field-polarized

state, the uniform magnetization component is given by

$$M_0 \to \frac{\sqrt{2}\sqrt{-1-2t}}{\sqrt{8-3K(1-\cos 4\phi)}}. \tag{7.29}$$

Minimizing the energy functional with respect to M_0 and solving this equation for the external field strength B with the results obtained above, leads to

$$B_{c2} = \sqrt{-\frac{1}{2} - t} \frac{\left(B_1 + B_2 + B_3 - B_4\right)}{\sqrt{8-3K(1-\cos 4\phi)}^3}, \tag{7.30}$$

which is composed by

$$\begin{aligned}
B_1 &= 4(3Kt+4) - 2(3K-8)(N_x+N_y)\tau \\
B_2 &= (16-3K)(N_x-N_y)\tau \cos 2\phi \\
B_3 &= 2K(8+10t+3(N_x+N_y)\tau) \cos 4\phi \\
B_4 &= 3K(N_x-N_y)\tau \cos 6\phi
\end{aligned} \tag{7.31}$$

In absence of the magnetocrystalline anisotropy, the transition field is reduced to the following expression

$$B_{c2} = \frac{1}{2}\sqrt{-1-2t}\Big(1 + (N_x+N_y)\tau - (N_x-N_y)\tau \cos 2\phi\Big). \tag{7.32}$$

Applying the field along one of the principal axes of the sample, here $\phi = 0$ (x axis), yields

$$B_{c2} = \xi(1 + N_x\chi) \tag{7.33}$$

with $\tau = \chi/2$ and $\xi = \frac{1}{2}\sqrt{-1-2t}$, which corresponds to homogeneous magnetization component in the limit of negligible K. This equation recovers the results from previous publications [Sch15; Wai17]. It should be mentioned that M_0 deviates slightly from the preceding studies on account of a different prefactor convention in the energy functional. Taking also the cubic anisotropy into consideration in the given field configuration, $\phi = 0$, B_{c2} is written in the form

$$\begin{aligned}
B_{c2} &= \frac{1}{2}\sqrt{-1-2t}\Big(1 + 2N_x\tau + K(1+2t)\Big) \\
&= \frac{1}{2}\sqrt{-1-2t}\Big(1 + 2N_x\tau - 4K(\frac{1}{2}\sqrt{-1-2t})^2\Big) \\
&= \xi(1 + N_x\chi) - 4K\xi^3,
\end{aligned} \tag{7.34}$$

which represents Eq. 7.33 extended by a term linear in K.

Out-of-plane rotation
In the case of a rotation within the [001]-[110] plane, $\phi = \pi/4$, the helix amplitude reads

$$A \to \frac{2\sqrt{32M_0^2 - 3KM_0^2\left(7 - 4\cos 2\theta - 3\cos 4\theta\right) + 16t + 8}}{\sqrt{3K\left(25 + 4\cos 2\theta\right) + 3\cos 4\theta\right) - 128}}. \tag{7.35}$$

Since the pitch vector length Q is only determined by the interplay between the exchange and DMI energy and their respective prefactors, the result of Eq. 7.27 is used. At the phase transition A is set to zero and the uniform magnetization component is given by

$$M_0 \to \frac{2\sqrt{2}\sqrt{-1 - 2t}}{\sqrt{32 - 3K\left(7 - 4\cos 2\theta - 3\cos 4\theta\right)}}. \tag{7.36}$$

Performing the minimization protocol as described above, the critical field strength yields

$$B_{c2} = \sqrt{-\frac{1}{2} - t}\frac{\left(B_1 + B_2 + B_3 + B_4\right)}{\sqrt{32 - 3K\left(7 - 4\cos 2\theta - 3\cos 4\theta\right)}^3}, \tag{7.37}$$

with the individual field components

$$\begin{aligned}
B_1 &= 64\left(2 + (N_x + N_y + 2N_z)\tau\right) - 6K\left(16 + 4t + 9(N_x + N_y)\tau + 10N_z\tau\right) \\
B_2 &= \left(32K(4 + 5t) + (57K - 64)(N_x + N_y)\tau + 2(64 - 9K)N_z\tau\right)\cos 2\theta \\
B_3 &= 6K\left(16 + 20t + (N_x + N_y + 10N_z)\tau\right)\cos 4\theta \\
B_4 &= -9K(N_x + N_y - 2N_z)\tau\cos 6\theta.
\end{aligned} \tag{7.38}$$

In the limit of vanishing K, equation Eq. 7.37 simplifies to

$$B_{c2} = \frac{1}{2}\sqrt{-1 - 2t}\left(1 + \frac{1}{2}(N_x + N_y + 2N_z)\tau - \frac{1}{2}(N_x + N_y - 2N_z)\tau\cos 2\theta\right) \tag{7.39}$$

If the external field is applied along the [111] direction, $\theta = \arccos 1/\sqrt{3}$, the transition field is determined by

$$\begin{aligned}
B_{c2} &= \frac{1}{2}\sqrt{-1 - 2t}\frac{\left(3 - 5K - 4Kt + 2(1 - K)(N_x + N_y + N_z)\tau\right)}{3\sqrt{K - 1}^3} \\
&= \xi\frac{\left(3 - 3K + 8K\xi^2 + (1 - K)\chi\right)}{3\sqrt{1 - K}^3} \\
&\approx \xi\left(1 + \frac{1}{3}\chi\right) + K\frac{\xi}{6}\left(3 + 16\xi^2 + \chi\right)
\end{aligned} \tag{7.40}$$

Note, in the second step the identity $N_x + N_y + N_z = 1$ is used, while in the third step the expression is expanded up to the linear order in K.

For the examination of the validity of the analytic approach, the derived equations are compared to the results calculated numerically. In Fig. 7.33(a)-(b) the angle-dependence of B_{c2} for a rotation in the planes spanned by the [100]- and [010]-directions and the [001]- and [110]-directions is illustrated. The numerical data, given by the symbols, are obtained from several minimization routines with different magnetization start parameters, in order to approach the global minimum for each angle configuration. The analytic model in form of equations Eq. 7.30 and Eq. 7.37 is represented by the solid lines. Each plot combines several data sets, calculated for different anisotropy strengths, which range from low to high values as indicated by the color gradient. The remaining parameters are again set to $r_0 = -1000$, $\tau = 0.88$ and $N_i = 1/3$, which limits the focus of the discussion to the changes of B_{c2} arising from the cubic magnetocrystalline anisotropy only. As visualized in the top figure, the distinct energy landscape of the latter is imprinted directly on the phase boundary between the conical and field-polarized state. In both, analytical and numerical results, the angle-dependence of B_{c2} exhibits a fourfold symmetry. In this configuration the minimum value for the transition field is obtained, if the external field is applied along the easy axes. For anisotropy values up to $K = 0.0002$, the analytical model is in a good agreement with the numerically obtained results. Exceeding, however, this threshold, it is evident that the numerical data only change slightly with increasing K, apart from the hard axes in this plane at $\phi = 45°, 135°$. They therefore can no longer be described by a sinusoidal function, as it is predicted by the analytic model. Similar findings are also observed in the case of an out-of-plane rotation, which is illustrated in the bottom figure. In the limit of small K, the angle-dependence of B_{c2} is characterized by the combination of a two and fourfold symmetry. Compared to the in-plane rotation of the magnetic field, however, the discrepancy between the analytical and numerical model is significantly smaller even for larger K values. Interestingly, for the field angle set to approximately $\theta \approx 57.4°$, which corresponds to the hard axis of the system, and $\theta \approx 67.5°$, both analytic and numerical results are in a good agreement for all anisotropy values chosen.

The deviation between the analytical model and the numerical data arise from the simplified ansatz only to consider the $A \to 0$ limit in the derivation of B_{c2}, instead of taking the actual field-dependence of M_0 into account. In general, minimizing the energy functional Eq. 6.4 with respect to M_0 and substituting A by Eq. 7.28 leads to three solutions for the uniform magnetization component. The one representing the correct solution of M_0
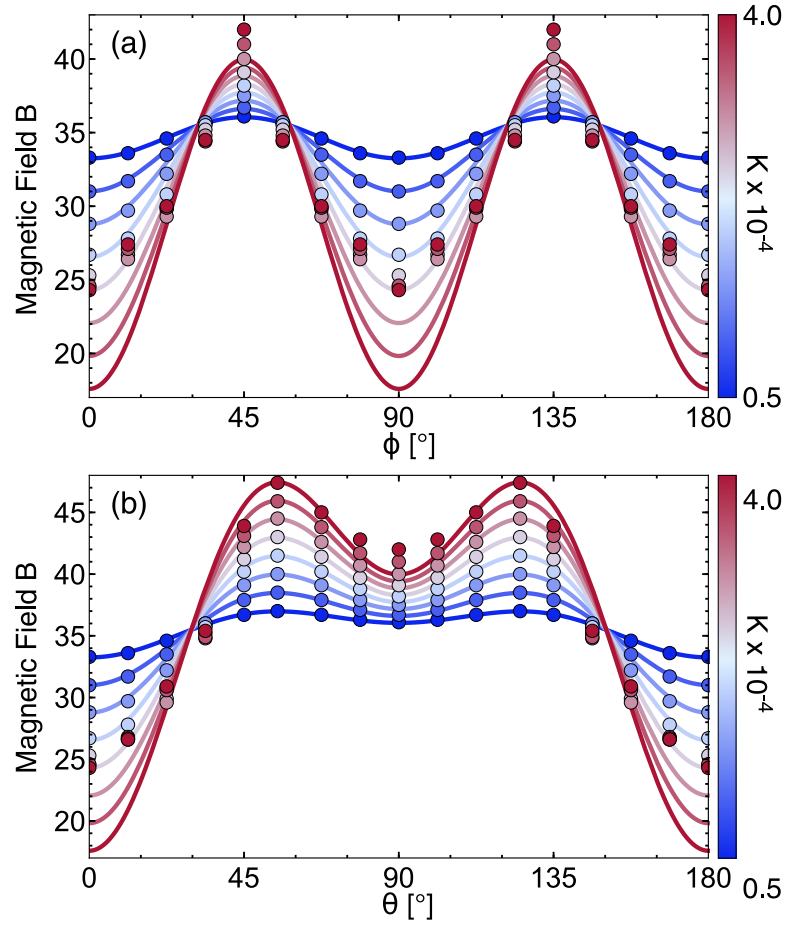
Figure 7.33: Angle-dependence of transition field B_{c2} in the (a) in-plane and (b) out-of-plane configuration calculated for various anisotropy strengths K and a spherical sample shape. The figures are composed by the results obtained numerically and analytically, illustrated by the symbols and lines, respectively. The remaining parameters are set to $r_0 = -1000$ and $\tau = 0.88$.

for an in-plane rotation in the small ϕ case is given by

$$
M_0 = \frac{(1 - i\sqrt{3})M_0^{II}}{2^{2/3}\left(M_0^I + \sqrt{108M_0^{II\,3}M_0^{III\,3} + M_0^{I\,2}}\right)^{1/3}}
$$
$$
- \frac{(1 - i\sqrt{3})\left(M_0^I + \sqrt{108M_0^{II\,3}M_0^{III\,3} + M_0^{I\,2}}\right)^{1/3}}{62^{1/3}M_0^{III}}
$$

(7.41)

with the individual components

$$
\begin{aligned}
M_0^I &= 27BK^2(3 + 5\cos 4\phi)^2(28 - 15K + 3K\cos 4\phi)^2 \\
&\quad \cdot (-32 + 21K + 3K\cos 4\phi) \\
M_0^{II} &= 1/2(-64 + 60K + 36Kt + 2(-32 + 21K)(N_x + N_y)\tau \\
&\quad + (-64 + 45K)(N_x - N_y)\tau\cos 2\phi + 6K(6 + 10t + (N_x + N_y)\tau)\cos 4\phi \\
&\quad + 3K(N_x - N_y)\tau\cos 6\phi) \\
M_0^{III} &= K(3 + 5\cos 4\phi)(28 - 15K + 3K\cos 4\phi)
\end{aligned}
$$

(7.42)

and represents a complex number. The respective field-dependence of the real ($\mathrm{Re}[M_0]$) and imaginary ($\mathrm{Im}[M_0]$) part of the uniform magnetization is illustrated in Fig. 7.34 by the solid lines for the case $\phi = 0$. The dipolar interaction strength, demagnetization factors and the Ginzburg-Landau parameter are set to $\tau = 0.88$, $N_i = 1/3$ and $r_0 = -1000$ in accordance with the numerical data presented in Fig. 7.34. From the derived equation, B_{c2} is in general obtained by the intersection point of $M_0(B)$ and M_0 in the limit of $A \to 0$ (Eq. 7.29), which is indicated by the horizontal dashed red line. As a physical quantity, however, M_0 is requested to be only composed by a real component. In the configuration discussed this requirement is only fulfilled for anisotropy values up to $K = 0.00015$, coinciding with the K-range in which the analytical model reproduces the numerical results in Fig. 7.34. Increasing the anisotropy strength further reveals that, $M_0(B)$ becomes complex before reaching $M_0(A \to 0)$. As a consequence $M_0(B)$ increases continuously as long as the imaginary part is zero and subsequently jumps to $M_0(A \to 0)$ the moment $\mathrm{Im}[M_0]$ exhibits finite values. These observations are reflected also in the numerical data, given by the symbols. Note, for $K = 0.00035$ (red symbols) the cubic anisotropy is strong enough to induce a tilting of the pitch vector away from the magnetic field direction and therefore the formation of the likewise called tilted conical phase. Since in the analytical model a misalignment between pitch vector and external field is excluded, this feature is not resolved in the corresponding graph.

The determination of B_{c2} by equating Eq. 7.41 and Eq. 7.29 is highly nontrivial and will obviously not results in a solution in the large-K limit, as elaborated above. The transition field can however be extracted, by

exploiting the fact that the sudden change into a complex number of Eq. 7.41 originates from a change of sign of the expression $108 M_0^{II3} M_0^{III3} + M_0^{I2}$, under the square root. Setting this term to zero and solving for B, leads to

$$B_{c2} = \frac{2}{3} \frac{\sqrt{2}}{\sqrt{3}} \sqrt{\frac{(-2 - 4N_x \tau + 3K(1 + t + N_x \tau))^3}{(4 - 3K)^2 K(3K - 7)}}. \tag{7.43}$$

The obtained B_{c2} values are represented by the dashed black lines in Fig. 7.34. It should be mentioned that the applicability of this procedure of finding the transition field strongly depends on parameters like the field angle ϕ. Due to its complexity, B_{c2} can not always be determined analytically.

7.3.3 Derivation of B_{c2} (II)

In the second approach of calculating B_{c2}, the assumption is made that the magnetization amplitude is set to be constant, $\boldsymbol{M}(\boldsymbol{r}) = M_s \hat{\boldsymbol{n}}(\boldsymbol{r})$, and consequently the physical properties only depend on the orientation of $\boldsymbol{M}$, given by the unit vector $\hat{\boldsymbol{n}}(\boldsymbol{r})$. With the reduced degrees of freedom, there is no need to stabilize the energy functional by the implementation of the higher order Ginzburg-Landau terms, which simplifies Eq. 6.2 to

$$\begin{aligned}
\mathcal{F} = & \frac{\rho_s}{2} \left[(\nabla_i \hat{n}_j)^2 + 2Q \hat{\boldsymbol{n}} (\nabla \times \hat{\boldsymbol{n}}) \right] + \frac{\mu_0}{2} M_s^2 \hat{\boldsymbol{n}} \mathcal{T}(\phi_D, 0) \boldsymbol{N} \mathcal{T}^{-1}(\phi_D, 0) \hat{\boldsymbol{n}} \\
& - \mu_0 M_s \hat{\boldsymbol{n}} \hat{\boldsymbol{H}}_0^{\text{ext}} - K \sum_i \hat{n}_i^4 + C M_s^2 \sum_i (\partial_i \hat{n}_i)^2,
\end{aligned} \tag{7.44}$$

with exchange stiffness constant $\rho_s = 2 J M_s^2$ and pitch vector length $Q = D/J$. The obtained equations can hence directly be applied to the experimental data. For the illustration of the effect, the exchange anisotropy induces on the transition field, it is also introduced in the energy functional above. Note, the prefactor convention is chosen in accordance with [Wai17]. Analogous to Sec. 7.3.2, in the further course, the magnetization configuration is assumed to be given by a helix representation,

$$\hat{\boldsymbol{n}} = \cos(\theta_c) \hat{\boldsymbol{e}}_3 + \sin(\theta_c) \cos(\boldsymbol{Q} \cdot \boldsymbol{r}) \hat{\boldsymbol{e}}_1 + \sin(\theta_c) \sin(\boldsymbol{Q} \cdot \boldsymbol{r}) \hat{\boldsymbol{e}}_2 \tag{7.45}$$

with the modulation amplitude parameterized by the cone angle θ_c. In addition to that, the direction of the uniform magnetization component and pitch vector $\boldsymbol{Q}$ is set collinear to the external field orientation and a distortion of the spin helix is neglected.
Inserting the helix ansatz Eq. 7.45 into the energy functional Eq. 7.44 and evaluating the spatially dependent energy contributions by integration along
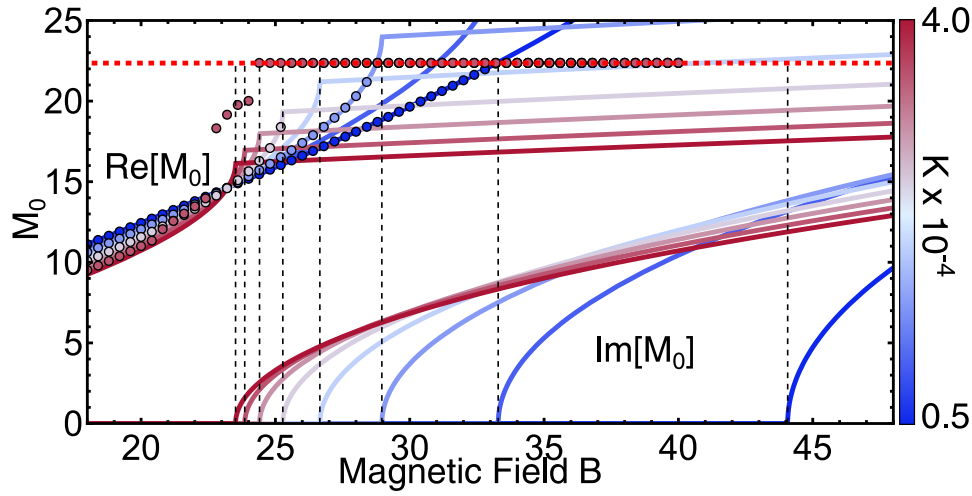
Figure 7.34: Field-dependence of the real and imaginary part of M_0 for various anisotropy values K. The figure illustrates the results derived in equation Eq. 7.41 (solid lines), with the magnetic field direction set to an angle of $\phi = 0$. The remaining parameters are set to $r_0 = -1000$, $\tau = 0.88$ and $N_i = 1/3$. For the comparison, the numerical data, which correspond to the previously discussed findings in Fig. 7.33(a), are added to the graph (symbols). The critical transition field, derived analytically in Eq. 7.43, is drawn by dashed black line. At this field value, M_0 is given by Eq. 7.29, as indicated by the dashed red line. A more detailed description is provided in the main text.

the pitch direction and over one helix period, yields

$$\mathcal{F} =$$

$$- \mu_0 M_s H_0 \cos \theta_c - \frac{1}{2} Q^2 \rho_s \sin^2 \theta_c$$

$$+ \frac{\mu_0 M_s^2}{4} \cos^2 \theta_c \left(2 N_z \cos^2 \theta + (N_x + N_y + (N_x - N_y) \cos 2(\phi_D - \phi)) \sin^2 \theta \right)$$

$$- \frac{1}{32} K \Big(\cos^4 \theta_c (21 + 4 \cos 2\theta + 7 \cos 4\theta + 8 \cos 4\phi \sin^4 \theta)$$

$$+ \frac{3}{8} \sin^4 \theta_c \left(53 + 4 \cos 2\theta + 7 \cos 4\theta + 8 \cos 4\phi \sin^4 \theta \right)$$

$$+ 12 \sin^2 \theta \cos^2 \theta_c \sin^2 \theta_c \left(9 + 7 \cos 2\theta - 2 \cos 4\phi \sin^2 \theta \right) \Big)$$

$$+ \frac{1}{32} C M_s^2 Q^2 \Big(18 + 14 \cos 2\theta + \cos 2(\theta - 2\phi)$$

$$- 2 \cos 4\phi + \cos 2(\theta + 2\phi) \Big) \sin^2 \theta_c \sin^2 \theta.$$

$$(7.46)$$

Minimizing with respect to the cone angle and subsequently setting θ_c to zero, allows to solve the resulting equation for H_0. In this limit it reflects the critical transition field H_{c2}, which reads,

$$H_{c2} = \frac{1}{2} M_s (\sin^2 \theta (N_x + N_y + (N_x - N_y) \cos 2(\phi_D - \phi)) + 2 N_z \cos^2 \theta)$$

$$+ \frac{Q^2 \rho_s}{\mu_0 M_s} - \frac{K}{16 \mu_0 M_s} (9 + 20 \cos 2\theta + 35 \cos 4\theta + 40 \cos 4\phi \sin^4 \theta)$$

$$- \frac{C M_s^2 Q^2}{32 \mu_0 M_s} (11 - 4 \cos 2\theta - 7 \cos 4\theta - 8 \cos 4\phi \sin^4 \theta)$$

$$(7.47)$$

In the following, analogous to the preceding derivations, rotations of the static field within the planes spanned by the [100]- and [010]-directions and the [001]- and [110]-directions will be discussed. For the in-plane rotation, $\theta = \pi/2$, the described minimization routine leads to

$$H_{c2} = \frac{1}{2} M_s \left((N_x + N_y) + (N_x - N_y) \cos(2(\phi_D - \phi)) \right) + \frac{\rho_s Q^2}{\mu_0 M_s}$$

$$- \frac{K}{2 \mu_0 M_s} (3 + 5 \cos(4\phi)) - \frac{2 C M_s^2 Q^2}{\mu_0 M_s} \cos^2 \phi \sin^2 \phi.$$

$$(7.48)$$

If the external field is applied along one of the principal axis of the sample, i.e. $\phi = 0$ and if assuming $\phi_D = 0$, the above equation simplifies to

$$H_{c2} = M_s N_x + \frac{\rho_s Q^2}{\mu_0 M_s} - \frac{4K}{\mu_0 M_s}. \tag{7.49}$$

Additionally, in the absence of the cubic anisotropy, $K = 0$, the critical field values reads

$$H_{c2} = M_s N_x + \frac{\rho_s Q^2}{\mu_0 M_s}, \tag{7.50}$$

which reproduces the already established result [Gar17; Wai17]. Rotating the magnetic field within the plane determined by [001]- and [110]-directions, i.e. $\phi = \pi/4$, the phase transition between the conical and field-polarized state occurs at a value of

$H_{c2} =$

$$\frac{1}{2}M_s \left(((N_x + N_y) + (N_x - N_y)\sin(2\phi_D))\sin(\theta)^2 + 2N_z\cos(\theta)^2\right) + \frac{\rho_s Q^2}{\mu_0 M_s}$$
$$+ \frac{K}{8\mu_0 M_s}(3 - 20\cos(2\theta) - 15\cos(4\theta)) - \frac{CM_s^2 Q^2}{4\mu_0 M_s}\sin^2\theta(5 + 3\cos 2\theta).$$

$$(7.51)$$

Finally, in the special case of a parallel alignment of the static field with respect to the [111] direction, which is given by $\theta = \arccos(1/\sqrt{3})$, the equation reduces to

$$H_{c2} = \frac{1}{3}M_s + \frac{\rho_s Q^2}{\mu_0 M_s} + \frac{8K}{3\mu_0 M_s} - \frac{2CM_s^2 Q^2}{3\mu_0 M_s}. \qquad (7.52)$$

For the illustration of the obtained results, equations Eq. 7.48 and Eq. 7.51 are plotted in Fig. 7.35 as a function of the external field direction, determined by the angles ϕ and θ, respectively. Since the angle-dependence of H_{c2} is governed by all three anisotropy terms taken into account, the transition field will be visualized for several parameter sets, in order to highlight the individual contributions. The variables set to be constant in the following are the susceptibility $\chi_{\mathrm{con}}^{\mathrm{int}} = \frac{\mu_0 M^2}{\rho_s Q^2} = 1.76$ [Sch15], saturation magnetization $\mu_0 M_s = 0.13\,\mathrm{T}$ [Sta17b] and sample frame orientation, given by $\phi_D = 0$. While the susceptibility is almost temperature independent [Bau10; Wai17], the magnetization amplitude is extracted at a temperature of around $5\,\mathrm{K}$. As a reference, H_{c2} calculated for a spherical sample and in absence of the additional anisotropies, is added to the figures (dashed black line). In the top panel the interplay between the magnetocrystalline anisotropy and demagnetization energy is visualized first. For the anisotropy strength a value of around $K = 600\ \mathrm{J/m^3}$ is assumed, which corresponds to the specified temperature of $5\,\mathrm{K}$ [Sta17b]. It should be mentioned that for the latter a different sign convention was chosen with respect to the cited publication. Regarding the shape anisotropy, two cases are contrasted: on one hand a spherical ($N_i = 1/3$, (a)) and on the other hand a cuboid ($N_x = 0.25, N_y = 0.35, N_z = 0.4$, (b)) shaped sample. In the left figure, which corresponds to the isotropic case concerning the shape contribution, the previously obtained results from the Ginzburg-Landau model Fig. 7.33 are reproduced quantitatively. Comparing the relative difference between the maximum and minimum field values, suggest a dimensionless anisotropy constant of approximately K = 0.00016, which is in a good agreement with the findings reported in [Hal18]. Provided the sample shape deviates from a uniform appearance, the demagnetization energy does not only add to a

constant offset of H_{c2}, but also induces a additional spatial dependence of the latter in the form of a two fold symmetry, as indicated by the dashed lines ($K = 0$). The resulting superposition of both anisotropies is given by the solid lines. In the bottom panel of Fig. 7.35 additionally the exchange anisotropy is taken into consideration. In the interest of simplicity, the sample shape investigated is chosen to coincide with a sphere, which reduces the discussion to the comparison between the exchange and cubic magnetocrystalline anisotropy. On the left hand side, the angle-dependencies of the individual energy terms are highlighted by setting the parameter of the respective counterpart to zero. The data, illustrated by the dashed lines, are obtained in the absence of the exchange anisotropy and reflect the results, already presented in Fig. 7.35(a). Given by the solid lines, is the angle-dependence of the transition field calculated for a pitch vector length $Q = 2\pi/60$nm [Ada12; Ono12; Sch15] and exchange anisotropy constant of $C = 0.17 \times 10^{-12}$ J/m, which corresponds to 5 % of the exchange constant J at 30 K [Sek16]. It should be mentioned that this value was not experimentally determined, but chosen for illustration purposes only. From this figure it is evident that both energy contributions modulate the transition field in a similar manner. The fundamental difference is, however, the constant shift of the field range to smaller values induced by the cubic magnetocrystalline anisotropy. In the right figure, finally the effect on H_{c2} of both energy terms combined is presented, comparing the cases of a positive (solid lines) and negative (dashed lines) sign of C. Due to the similar curve progression, the combination results either in a decrease or increase of the modulation amplitude. At first glance, an additional energy term like the exchange anisotropy might be masked in the angle-dependence of the transition field by a prevailing cubic magnetocrystalline anisotropy. Since, however, on the one hand the offset in H_{c2} and on the other hand the modulation amplitude are characteristic for a certain anisotropy strength, hidden anisotropy contributions are suggested to be easily resolved, when properly analyzing the experimental data.

7.3.4 Experimental Results

In order to sample the energy landscape induced by the underlying cubic lattice structure, angle-resolved broad-band microwave spectroscopy experiments are performed on two Cu_2OSeO_3 crystals for a wide temperature range. As motivated in the theoretical discussion above, the focus is placed on the resonance frequencies of the Kittel mode, but also on the field value of the phase transition between the conical and field-polarized state. The detection of these quantities as a function of the field direction allows to visualize the contributing energies and to extract the respective parameters. To distinguish the observed effects from the ones which arise from the shape anisotropy, two sample geometries, a cuboid and a sphere, are compared.
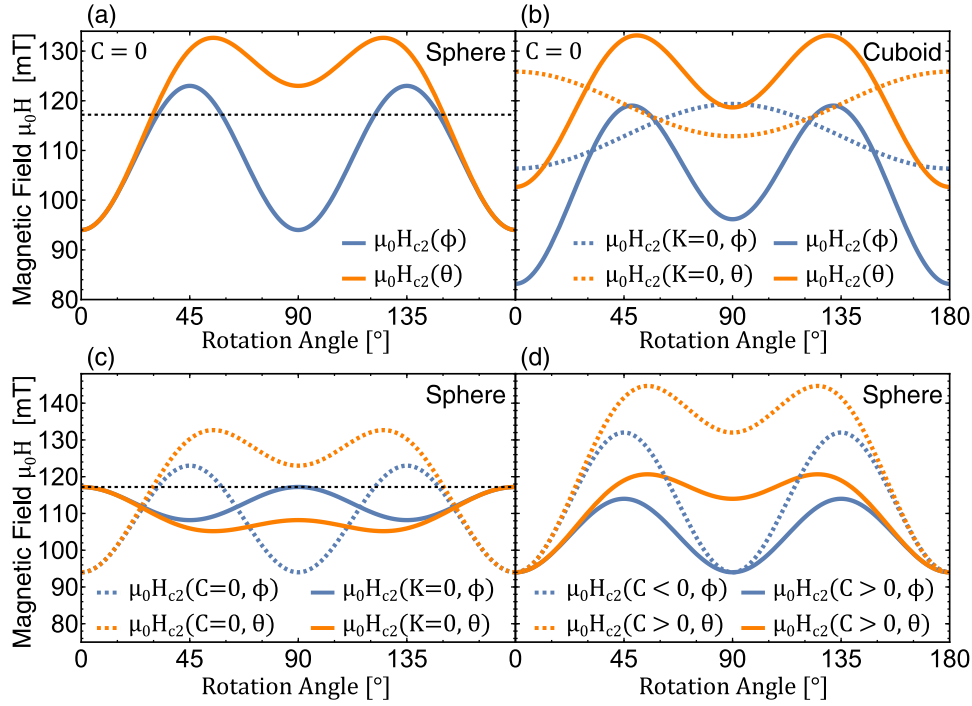
Figure 7.35: Angle-dependence of transition field $\mu_0 H_{c2}$ for various parameter sets. Each figure is composed of the results obtained for an in- (ϕ) and out-of-plane (θ) rotation, according to equations Eq. 7.48 and Eq. 7.51. While in the top panel the contribution induced by the magnetocrystalline and shape anisotropy are illustrated, in the bottom panel the magnetocrystalline and exchange anisotropy are compared. For this purpose a spherical (a),(c),(d) and cuboid (b) sample are collated. The dashed black line indicates the transition field of a spherical sample in absence of additional anisotropies. A more detailed description is given in the main text.

Cuboid Sample

The first sample to be investigated is a crystal of cuboid shape with lateral dimensions of $1.65 \times 1.65 \times 1.8 \, \text{mm}^3$ and the surface normals orientated along the [100] directions of the crystal lattice. The demagnetization factors, which correspond to these dimension ratios are approximately $N_{x,y} = 0.343$ and $N_z = 0.314$ [Aha98]. For the excitation and detection of the magnetization dynamics, the sample is placed on a coplanar waveguide, with the long axis oriented perpendicular with respect to the CPW plane. In the measurement setup utilized, this plane corresponds also to the one in which the magnetic field is applied. It follows that, in this configuration the contribution arising from the shape anisotropy is expected to be suppressed and the rotation of the external field is restricted to the plane spanned by the [100]- and [010]- directions. The angle-dependence of the resonance condition is therefore predicted to be only determined by the symmetries of the underlying crystal lattice and its induced anisotropies. In order to avoid a vanishing coupling efficiency between the driving field and the magnetization, due to a parallel alignment of these quantities, the sample is placed on one of the gaps Sec. 3.1. With this, the magnetization is, nevertheless, mainly subject to the in-plane component of the ac-field, but it also driven by the out-of-plane component, which is at any angle configuration perpendicular with respect to it. The measurement principle employed in the case of the cuboid sample is the broadband microwave spectroscopy technique utilizing the vector network analyzer, which is described in Sec. 3.2. At a fixed temperature, field direction and field strength the complex scattering parameter S_{ij} is recorded as a function of frequency in steps of $800 \, \text{kHz}$. In order to reduce the background contribution and enhance the signal-to-noise ratio, two normalization techniques are established. Depending on the varying background, either the derivative technique, $\delta S_{12} = (S_{12}(H + \Delta H) - S_{12}(H - \Delta H)) / S_{12}(H)$ [Mai18] or the high-field normalization $\Delta S_{12} = S_{12}(H) - S_{12}(H_{\text{ref}})$ is applied. For several data sets it is additionally required to remove the remaining background by a linear fit. Since the focus of this study lies on the angle-dependence of both the resonance condition in the field-polarized phase, but also the critical transition field H_{c2}, the range of the external field is chosen to cover all magnetic phases.

A visualization of several microwave spectra, recorded at $50 \, \text{K}$, is given in Fig. 7.36. The data represent the field dependence of the resonance frequencies obtained at four different field directions, with the respective angles set to $\phi = 0°, 30°, 60°$ and $90°$. It should be mentioned that angle ϕ refers to the lab frame. Here, for the illustration of the results, the high-field normalization technique is applied. The amplitude of the microwave absorption, denoted as A in the following, is reflected by the color gradient. While a vanishing intensity is given by dark blue, a high absorption is indicated by lighter colors. Note that, each spectrum is normalized with reference
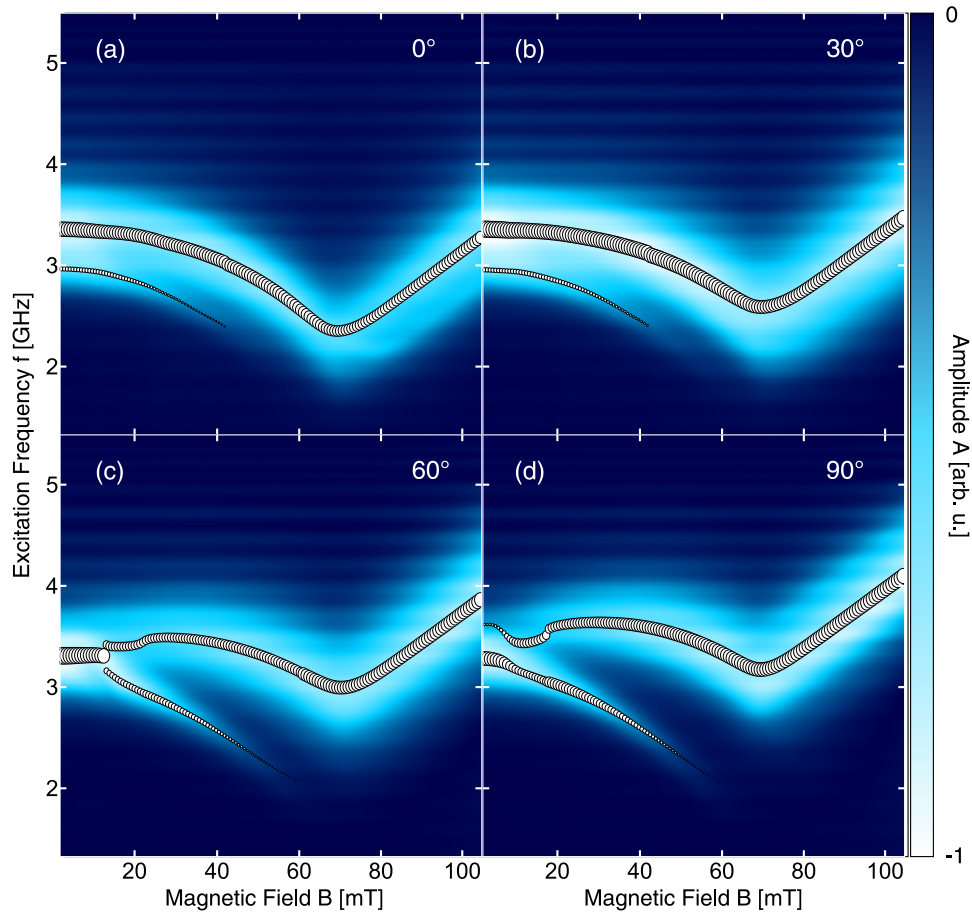
Figure 7.36: Microwave absorption spectra recorded at a temperature of 50 K for various field configurations. The external field is set to $\phi = 0°, 30°, 60°$ and $90°$. The background color, which is characterized by the color gradient, reflects the absorption intensity A. Note, every spectrum is normalized with respect to its minimum value. Resonance frequencies and respective peak amplitudes are extracted by Lorentzian fits, applied to the individual frequency scans. The obtained quantities are illustrated by the white symbols and the corresponding symbol size.

to its minimum value. The data are complemented by the resonance conditions, which are obtained from Lorentzian fits, applied to the individual line-scans. The extracted frequencies are indicated by the white symbols. In addition to that, the respective peak amplitude is implemented by the symbol size, in order to highlight the coupling efficiency of the individual modes to the driving field. The overall appearance of the microwave spectra at this temperature is determined by the well-established universal spectrum of a chiral magnet, comprising the helical/conical and field-polarized

139

states with their characteristic resonance branches. A clear difference between these is, however, observed in the low-field limit. Despite the different field-configuration, the two spectra in the top panel bear a strong similarity, regarding the field-dependence of the excitation modes. A slight shift towards higher frequencies is found in Fig. 7.36(b) though in the field region above 70 mT. Interestingly, the two conical modes are clearly non-degenerate at zero magnetic field in both spectra, despite the same lateral dimensions of the crystal within the plane of rotation. The approximation of an ellipsoidal sample shape, as it is assumed in the treatment of the demagnetization contribution, does obviously not hold in this case. Rotating the magnetic field further, leads to a wider frequency spacing between the two conical modes and a shift of spectral weight from the $+Q$ to the $-Q$ mode, as shown in Fig. 7.36(c)-(d). As a consequence the $+Q$ mode appears to vanish in the small field limit. It should be mentioned, that in this field region a clear distinction between one or two peaks can no longer be made. The actual resonance position might therefore not be reproduced correctly by the added fit results. This change in spectral weight originates from the field and also demagnetization factor dependent polarization of the conical modes [Sta17a]. By adjusting the external field angle, the polarization direction can be tuned such that it does not match the one of the driving field anymore, leading to a reduction of the excitation efficiency, as it is case for the $-Q$ mode in Fig. 7.36(a)-(b). Apart from the obvious changes, these few data sets already reveal a clear contradiction. For the given sample shape and the set temperature, at which the cubic magnetocrystalline anisotropy should be absent, neither the excitation frequencies of the Kittel mode nor the transition field H_{c2} are predicted to demonstrate any angle-dependence. While H_{c2} only varies slightly in the shown spectra, which agrees with the given argument, the resonance branch in the field-polarized phase is however continuously shifted towards higher values. This significant increase and the resulting disentanglement of both quantities contradicts the theoretical model. A more detailed discussion will be given in the regard of the respective angle and temperature evolutions, later on. Note that the field-independent wave-like signatures, which are visible in all four spectra, are artefacts induced by the normalization technique.

Before arriving at the point of analyzing these dependencies, all recorded microwave spectra are required to be evaluated, by extracting the corresponding resonances from the individual frequency scans. Depending on the chosen normalization technique, different fit functions have to be applied. By subtracting a reference trace, measured at a high field value, the general Lorentzian profile remains unchanged. For these data sets equation Eq. 3.4 is utilized. Applying, however, the difference technique, as it is introduced in [Mai18], the manipulated frequency sweeps are given by the derivative of

the Lorentzian function. Therefore,

$$A'_{\text{FMR}}(f) = \frac{2A}{\left((f-f_0)^2 + \Delta f^2\right)^3} \Big(-\Delta f \left(-3(f-f_0)^2 + \Delta f^2\right) \cos\epsilon$$
$$+ (f-f_0)\left((f-f_0)^2 - 3\Delta f^2\right)\sin\epsilon\Big) \tag{7.53}$$

with peak amplitude A, resonance position f_0 and linewidth Δf, is used for fitting the obtained line-scans. In Fig. 7.37(a) a processed microwave absorption trace as a function of frequency is displayed. The experiment is conducted at a temperature of $55\,\text{K}$ and a magnetic field strength set to $B = 175\,\text{mT}$, which corresponds to the phase parameters of the field-polarized state. Here, for the subtraction of the background contributions the difference technique is applied. In addition to that, the data are normalized to a maximum amplitude of one. The figure comprises the measurement results, which are indicated by the blue line, and the respective fit, given by the red lines. The fitting curve, in turn, is composed by the sum of two single peak fits, which are illustrated by the dashed black lines. Due to the chosen normalization, they are determined by the profile of the derivative of the Lorentzian function, as elaborated above. Interestingly, even at this high temperature, at which the multiple replica of the Kittel mode, originating from standing spin waves, are expected to be suppressed due to the higher magnetic damping, more than one peak is required for reproducing the data correctly. In the high-temperature limit, the number of peaks can be easily estimated from the profile of the frequency sweeps. Decreasing the sample temperature, however, leads to a significant increase of this number due to the aforementioned arguments. The microwave spectra therefore stand out for a high degree of complexity, as illustrated exemplarily in Fig. 7.37(b) by the blue line. Here, the line-scan is performed at a temperature of $6\,\text{K}$ and an external field set to $B = 175\,\text{mT}$. The data might be reproduced by adding further Lorentzian functions to the fitting algorithm, an overfitting is nevertheless very likely. As a consequence, the obtained resonance positions would not accord with the physical ones. In order to still get an estimate of the angle-dependence of the resonances and the critical field value, we refrain from the cumbersome multi peak fitting routine and introduce the amplitude-weighted frequencies f_{R},

$$f_{\text{R}} = \frac{\sum |A(f_i)| \cdot f_i}{\sum |A(f_i)|} \tag{7.54}$$

which will be focused on in the following. Here, f_i denotes the excitation frequency while $A(f_i)$ indicates the respective amplitude of the dynamic response of the magnetization. These quantities are illustrated in Fig. 7.37(b) by a red color. Assuming the Kittel mode and its replica to evolve in the same manner as a function of the field direction, this averaged value is only shifted along the frequency-axis with respect to the uniform mode.
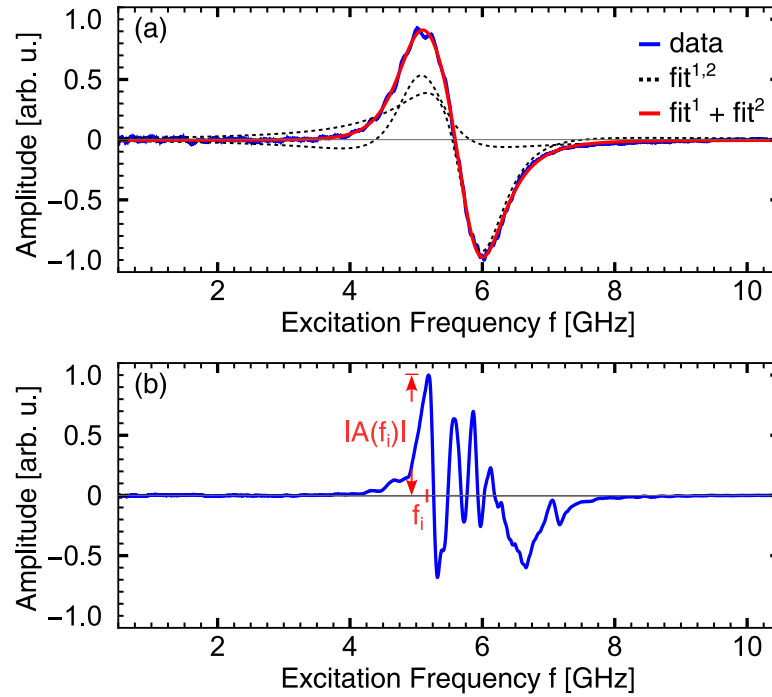
Figure 7.37: (a) Signal amplitude A as a function of excitation frequency f recorded at a temperature of $55\,\mathrm{K}$ and external field strength of $175\,\mathrm{mT}$. The figure comprises the raw data given by the blue line and the respective two-peak Lorentzian fit illustrated by the red lines. The individual Lorentzian functions are given by the dashed black lines. (b) Absorption A as a function of excitation frequency f recorded at a temperature of $6\,\mathrm{K}$ and external field strength of $175\,\mathrm{mT}$.

The first part of the analysis comprises the study of the evolution of the Kittel mode as a function of the external field direction. For this purpose the frequency sweeps, which are recorded in the field-polarized phase, are collated for each spectrum. The background contribution, which is attributed to the microwave absorption due to the whole microwave cable assembly of the setup, is removed afterwards by applying the derivative technique, as described above. Finally from the normalized data sets, the line-scans measured at the same field and temperature value are grouped, which leads to a microwave spectrum, characterized by the excitation frequency and the magnetic field direction. In Fig. 7.38, two spectra obtained at the same field strength of $B = 175\,\mathrm{mT}$ but different temperature are contrasted. On the left hand side, Fig. 7.38(a), the angle-dependence of the resonance frequencies at a temperature of $55\,\mathrm{K}$ is shown. The signal amplitude of the microwave traces, here in the derivative representation, is given by the background color, indicating positive values by red and nega-

tive ones by a blue color. A vanishing amplitude is given by white. It should be mentioned that each individual line-scan is normalized with respect to the maximum absolute value of its signal amplitude. In addition to that, in the interest of clarity, the color gradient is rescaled with respect to the maximum and minimum value of the whole spectrum. In order to highlight the curve progression of the resonances, they are extracted by fitting and the amplitude-weighted resonance method from each frequency sweep and added on top of the processed data. The corresponding results are visualized by the white and gray symbols, respectively. In this compilation, the angle-dependent change in frequency, already emerging in the microwave spectra discussed in Fig. 7.36, is clearly visible. Emphasis should be placed on the fact that the cubic magnetocrystalline anisotropy, which is expected to be zero at this temperature [Hal18], can be indeed excluded as its main origin. The respective angle-dependence would be of a fourfold symmetry instead of a twofold symmetry, as it is evident in the shown spectrum. The energy contribution complying with the resolved angle-dependence is the shape anisotropy, arising from the demagnetization field. Since the edge lengths of the crystal in the plane in which the magnetic field is rotated, are the same, the resulting effect in the ellipsoid approximation is predicted to vanish though. The origin therefore remains concealed. Note, a variation of the field strength at the sample position, induced by rotating the magnet, could be ruled out due to a preceding field calibration. The measured discrepancy amounts to a maximum value of $\pm 0.06\,\mathrm{mT}$, which has a negligible effect on the resonance position. On the right hand side, Fig. 7.38(b), the measurement results obtained at a temperature of $20\,\mathrm{K}$ are depicted. Apart from the, in general, more complex appearance of the individual line-scans, due to the formation of standing spin waves, the spectrum exhibits now a distinct change in the angle dependent profile. While the oscillation amplitude around the mean value is increased, another local maximum at the prior minimum occurs. The angle-dependence appears to be determined by a superposition of a two- and fourfold symmetry. The last contribution is expected to arise from the cubic magnetocrystalline anisotropy, which at this temperature possesses a finite strength. Interestingly, despite the alignment of the crystal lattice and the principal axes of the sample, the spectrum appears to be slightly asymmetric due to a angular shift between these contributions.

In order to quantify the parameters of the respective energy terms, the amplitude-weighted resonance position is extracted for each field and temperature value, as described above. A compilation of the angle-dependencies of the resonance frequencies in the field-polarized phase, resolved at a magnetic field strength of $B = 161\,\mathrm{mT}$, is illustrated in Fig. 7.39 (symbols). Each data set corresponds to one temperature, as indicated by the color gradient on the right hand side. While blue colors reflect low temperatures, red colors represent the measurements at high-temperatures. It should be mentioned
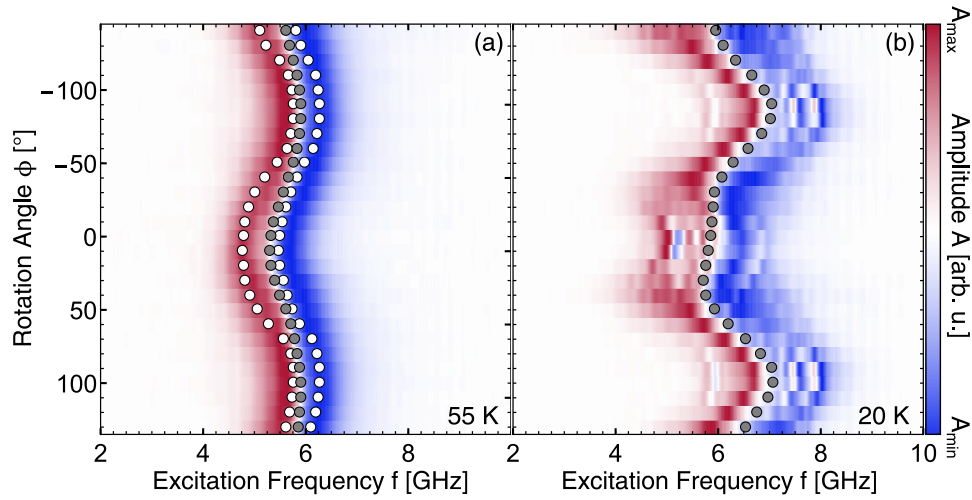
Figure 7.38: Angle-dependence of the normalized microwave excitation spectra in the frequency-domain for the cuboid-shaped sample. The figure illustrates the results obtained at (a) 55 K and (b) 20 K and a magnetic field strength of $B = 175\,\mathrm{mT}$. In addition to that the resonance frequencies extracted by Lorentzian fits and the amplitude-weighted resonance method are given by the white and gray symbols, respectively.

that, for illustration purposes, a frequency offset of $0.3\,\mathrm{GHz}$ (i - 1) is added to the traces. Here, integer i denotes the trace index, which is set to $i = 1$ for the measurements conducted at 55 K. These data sets are then subsequently fitted by applying equation Eq. 7.24 and its components given by Eq. 7.25. The parameters, entering the fit formula as variables, are reduced to the anisotropy strength K, demagnetization factors N_x and N_y and the orientation of the sample coordinate system ϕ_D with respect to the one of the crystal lattice. In addition to that, an additional angle, ϕ_off, is required to be introduced in order to compensate the shift between the crystal coordinate system and the lab frame. It nevertheless does not hold any physical meaning. The remaining parameters are set to be constant in the respective fitting procedure, since the external field value H_0 is recorded during the measurement, saturation magnetization M_s of the sample is determined by a superconducting quantum interference device (SQUID) in Appendix E and the gyromagnetic ratio $\gamma = 1.88 \times 10^{11}\,\mathrm{rad/sT}$ is taken from [Sta17b]. Note that, the third demagnetization factor is substituted by $N_z = 1 - N_x - N_y$. The fitting curves obtained for the field set to $B = 161\,\mathrm{mT}$ are drawn in Fig. 7.39 by the respective colored lines. Finally, employing a least square fit, allows to simultaneously analyze all data sets recorded at the same temperature value, despite their different field strengths. This allows to increase the precision of the obtained fit parameters.

The data points, visualized in Fig. 7.40, are therefore a result of fitting
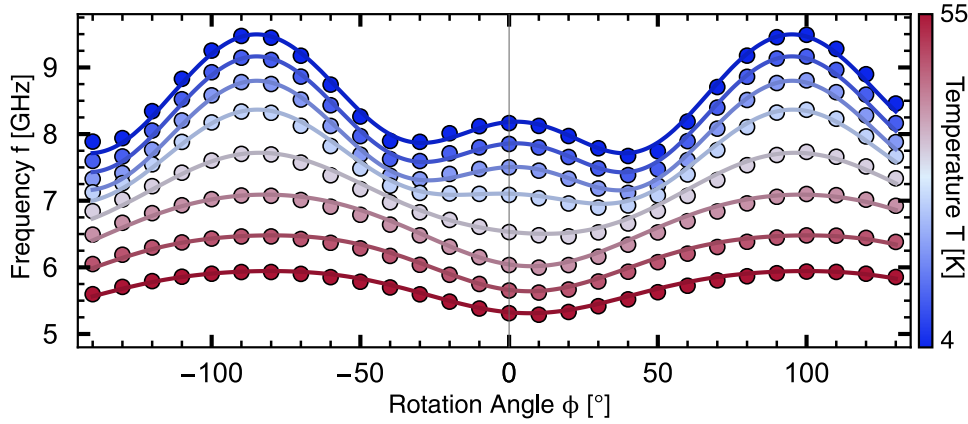
Figure 7.39: Angle-dependence of the amplitude-weighted resonance position for various temperature values. The extracted results from this method are visualized by the symbols. The color gradient on the right hand side, represents the set temperature. It ranges from low to high values, which is indicated by blue and red colors. The fitting curves obtained from the first fitting routine are drawn by the solid lines. Note, for illustration purposes, a frequency offset of $0.3\,\mathrm{GHz}\ (i$ - $1)$ is added to the traces. Here, integer i denotes the trace index, which is set to $i = 1$ for the measurements conducted at $55\,\mathrm{K}$.

several data sets for different magnetic fields. Note that in all figures the extracted error bars are masked by the chosen symbol size. In the following, the focus is placed on the temperature evolution of the demagnetization factors and the anisotropy strength. The discussion is first limited to the results, shown in Fig. 7.40(a),(c). In the top panel, the extracted demagnetization factors N_x and N_y are given for temperatures ranging between 4 and $55\,\mathrm{K}$, by orange and red symbols. From this, it can be seen that the parameters vary slightly, the difference between them, however, remains nearly constant. A certain trend as a function of temperature is not evident. The increase of the oscillation amplitude in the angle-dependencies, which is observed for a decreasing temperature value, arises therefore dominantly from the increase of the saturation magnetization. This behavior is in general in a good agreement with the expected results. The obtained values however by far do not match the actual sample shape. With an average of $N_x = 0.06$, $N_y = 0.28$ and consequently $N_z = 0.66$ the resolved shape corresponds to a rod, with its long axis aligned parallel to the x axis. By considering the amplitude-weighted resonance positions instead of the excitation frequencies of the Kittel mode, the individual traces, as a function of field-direction, might be shifted along the frequency-axis, as mentioned above. In order to compensate this artificial offset the fitting algorithm finally adapts N_z and outputs a larger or smaller value with respect to the

actual one. The resolved increase of a factor of approximately two is hence not surprising. The huge difference between the remaining demagnetization factors on the other hand cannot be explained. It is evident that this twofold symmetry contribution is not correctly described in regard of the demagnetization energy and originates from another effect. In the bottom panel, the anisotropy strength K is illustrated as a function of temperature by the closed blue symbols. Starting from a value of approximately $K = 600 \, \text{kJ/m}^3$ in the low-temperature limit, K continuously decreases under an increasing temperature until reaching a value of around $40 \, \text{K}$. Above this threshold, the anisotropy strength appears to converge and finally approaches a value slightly below zero. The inferred trend agrees well with the results presented in [Hal18]. Interestingly, also in this publication a change of sign is observed in the range of 30-40 K. It, however, is not unambiguously confirmed due to the accuracy of the estimates taken in the analysis. If indeed the change of sign detected in the microwave experiments is of a physical origin, can also not uniquely be determined. On the one hand, the consideration of the amplitude-weighted resonances, instead of the actual resonance frequencies, in the fitting procedure might induce an increase or decrease of the anisotropy strength. On the other hand, if the unidentified spatial contribution is not correctly reproduced by a twofold symmetry, but also comprises higher order terms or asymmetries, the values of K might also be affected. It can be concluded that, the angle-dependent measurements provide a good estimate of the cubic magnetocrystalline anisotropy in the low-temperature limit, the unexpected twofold symmetry can, however, not be explained by the shape anisotropy term.

In order to evaluate to what extent the fitting results of the cubic anisotropy depend on the model employed, the energy functional is complemented by two uniaxial anisotropy terms, resulting in

$$
\begin{aligned}
\mathcal{F} = \ & \frac{1}{2}\mu_0 \boldsymbol{M} \mathcal{T}(\phi_{\text{D}}, 0) \boldsymbol{N} \mathcal{T}^{-1}(\phi_{\text{D}}, 0) \boldsymbol{M} - \mu_0 \boldsymbol{M} \boldsymbol{H}_0 - \frac{K}{M_s^4} \sum_i M_i^4 \\
& - \frac{U_1}{M_s^2} \left(\boldsymbol{M} \cdot \boldsymbol{k}_1 \right)^2 - \frac{U_2}{M_s^2} \left(\boldsymbol{M} \cdot \boldsymbol{k}_2 \right)^2 .
\end{aligned}
\tag{7.55}
$$

Here, the corresponding constants are denoted as U_1 and U_2 and the direction of the symmetry axes are given by

$$
\begin{aligned}
\boldsymbol{k}_1 &= (\cos \phi_{U_1}, \sin \phi_{U_1}, 0) \\
\boldsymbol{k}_2 &= (0, 0, 1),
\end{aligned}
\tag{7.56}
$$

with angle ϕ_{U_1} indicating the deviation from the [100]-crystal lattice direction. In addition to that, the demagnetization factors are fixed to the values calculated for the given sample shape. The respective energy contribution therefore provides no longer an angle-dependent term, since $N_x = N_y$, but
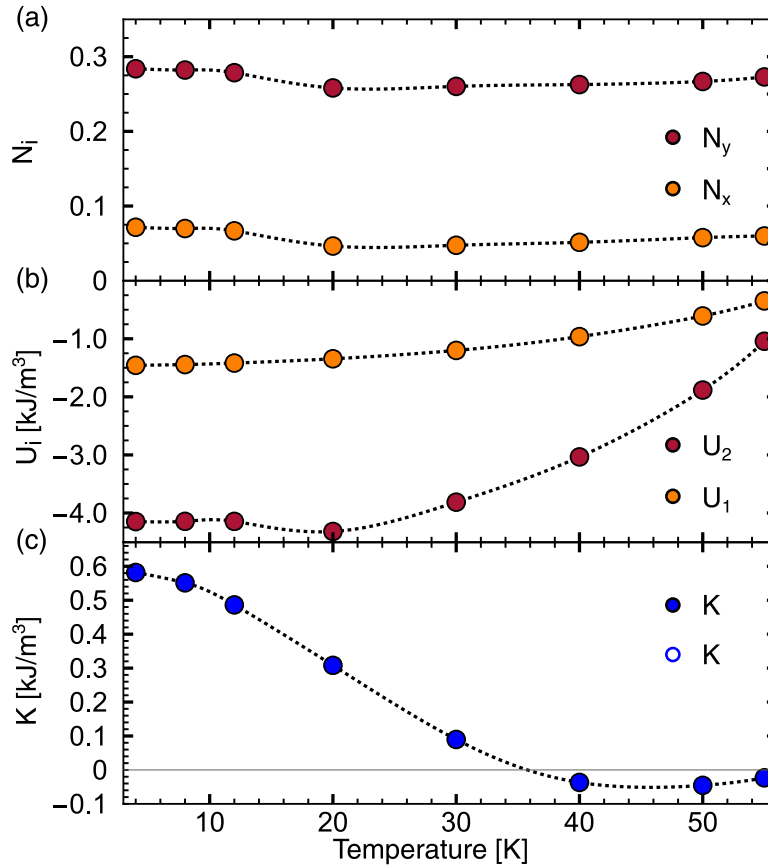
Figure 7.40: Visualization of the extracted fit parameters. (a) Temperature evolution of the demagnetization factors N_x, N_y. (b) Uniaxial anisotropy strengths U_1 and U_2 as a function of temperature. (c) Temperature dependence of the cubic magnetocrystalline anisotropy constant K. The results corresponding to the first fit routine are given by the closed symbols, while the ones obtained from the second one are illustrated by the open symbols. It should be mentioned that the obtained anisotropy strengths are equivalent and therefore the open symbols are hidden by the closed ones.

induces mainly a constant shift along the frequency-axis. Due to the chosen symmetry axes, it finally allows to disentangle the twofold symmetry from the frequency offset. It should be mentioned that the implementation of both anisotropies is a phenomenological approach to compensate these unpredicted effects.

Following the steps of solving the Landau-Lifshitz equation of motion, presented in Sec. 7.3.1, leads to the general resonance condition Eq. B.6 for the adapted energy functional. Applying the restriction for the demagnetization factors and setting $\phi_\mathrm{D} = 0$ reduces this expression to,

$$
\omega^2 =
$$

$$
\mu_0^2 \gamma^2 \left[H_0^2 + 4 \left(\frac{K}{\mu_0 M_\mathrm{s}} \right)^2 + 2 \left(\frac{U_1}{\mu_0 M_\mathrm{s}} \right)^2 + H_0 \left(3 \frac{K}{\mu_0 M_\mathrm{s}} + \frac{U_1}{\mu_0 M_\mathrm{s}} - 2 \frac{U_2}{\mu_0 M_\mathrm{s}} \right. \right.
$$

$$
\left. - M_\mathrm{s}(N_x - N_z) \right)
$$

$$
+ \frac{U_1}{\mu_0 M_\mathrm{s}} \left(6 \frac{K}{\mu_0 M_\mathrm{s}} + 2 \frac{U_1}{\mu_0 M_\mathrm{s}} - 4 \frac{U_2}{\mu_0 M_\mathrm{s}} + 3 H_0 \right.
$$

$$
\left. - 2 M_\mathrm{s}(N_x - N_z) \right) \cos \left(2(\phi - \phi_{U_1}) \right)
$$

$$
+ 6 \frac{K}{\mu_0 M_\mathrm{s}} \frac{U_1}{\mu_0 M_\mathrm{s}} \cos \left(2(\phi + \phi_{U_1}) \right)
$$

$$
+ \frac{K}{\mu_0 M_\mathrm{s}} \left(12 \frac{K}{\mu_0 M_\mathrm{s}} + 4 \frac{U_1}{\mu_0 M_\mathrm{s}} - 8 \frac{U_2}{\mu_0 M_\mathrm{s}} + 5 H_0 - 4 M_\mathrm{s}(N_x - N_z) \right) \cos (4\phi) \left. \right].
$$

$$
(7.57)
$$

By means of this equation, the fitting routine, elaborated above, is repeated. In this analysis, besides the magnetocrystalline anisotropy strength K, the uniaxial anisotropy constants U_1 and U_2 and the direction of the corresponding symmetry axis, in terms of ϕ_{U_1}, enter the fit formula as variables. The remaining parameters are again set to be constant. In Fig. 7.40(b) the determined temperature evolution of U_1 and U_2 is depicted. While the data points of the in-plane anisotropy term, the one inducing the twofold symmetry, are given by the orange symbols, the ones of the out-of-plane contribution are indicated by red. In case of anisotropy strength U_1, the absolute value of the amplitude is continuously increasing with decreasing temperature. A more detailed analysis reveals, that the temperature dependence is actually determined by M_s^2. For this reason the respective term in the resonance conditions in turn scales linearly with the saturation magnetization, which agrees with the behavior of the one resulting from the demagnetization energy. Regarding the constant U_2, a similar trend is recorded, except for the last three data points. In contrast to the in-plane anisotropy, a clear dependence on M_s or higher orders, however, cannot be identified. The fact that it appears to vanish at the critical temperature of around $58\,\mathrm{K}$, reveals that

it is correlated to the saturation magnetization though. It should be kept in mind that the amplitude of U_2 arises mainly from the frequency offset with respect to the FMR mode, but also covers for the shifts from the in-plane anisotropy and also the demagnetization term, as can be seen from Eq. 7.57. An actual out-of-plane anisotropy might also be existent, but can not be distinguished from these contributions. In Fig. 7.40(c) the anisotropy strength K, inferred from the fitting procedure, is visualized by open symbols. Since the obtained results are equivalent to the ones extracted before, they are hidden by the blue symbols. It follows that, despite the different energy terms, both fit equations reproduce the data appropriately and account for the frequency shift and the $\cos 2\phi$ contribution in the same manner.

The second quantity to be investigated is the critical field value H_{c2} as a function of the magnetic field direction and temperature. Identical to the routine above, first the resonance positions are determined for all frequency scans by the weighted amplitude method. Note, in order to determine H_{c2} from the individual spectra, the field range chosen in the analysis covers the onset of the conical/tilted conical phase and the field-polarized state. From these data sets the field value, which corresponds to the minimum frequency, is then attributed to H_{c2}. Finally, the values inferred from the measurements at the same temperature are collated. The resulting angle-dependence of H_{c2} is illustrated in Fig. 7.41. Here, the data points are indicated by the symbols. The color gradient on the right hand side indicates the set temperature, ranging from low to high values, given by blue and red colors. The measurements at $50\,\mathrm{K}$ demonstrate that the transition field varies only slightly with the external field direction. The corresponding angle-dependence appears to exhibit a twofold symmetry, the obvious distortion, however, might hint at further contributions. Decreasing the temperature leads to the formation of a clear fourfold symmetry pattern. Its respective oscillation amplitude and mean value are increasing under a decreasing temperature. Finally, in the low-temperature limit it dominates the overall appearance of the angle-dependence. In contrast to the results observed in the field-polarized phase, the behavior of the critical transition field is no longer dominated by the unexpected twofold symmetry, but follows mostly the theoretical model. In accordance with equation Eq. 7.48, the contribution to the angle-dependence arising from the shape anisotropy is predicted to be negligible, due to the symmetric sample shape. The only energy term remaining, which shapes the profile of H_{c2}, is the cubic magnetocrystalline anisotropy, which is evident from the measurements results.

As motivated in the beginning, the comparison of the angle-resolved critical field value with the theoretical model, also allows to draw conclusion on the energy landscape of the investigated material. The advantage over the analysis of the Kittel mode, however, is the access to the gradient terms, which in the case of a collinear alignment and homogeneous excitation of the magnetization do not contribute to the dynamic response. In the fol-
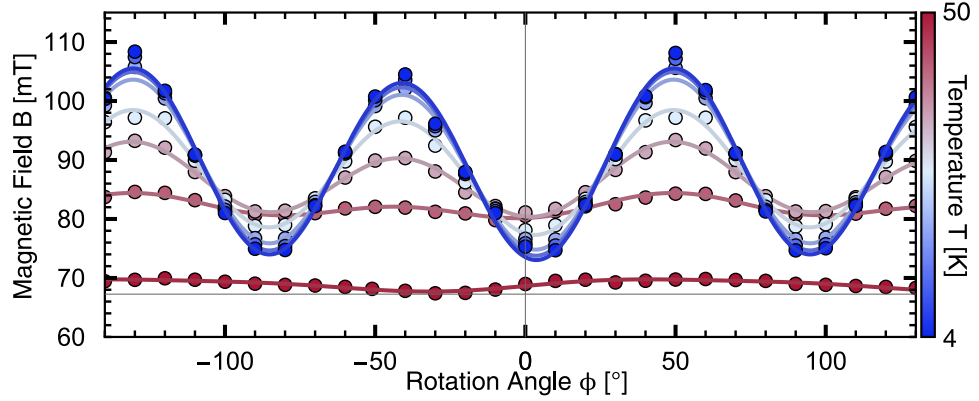
Figure 7.41: Angle-dependence of the critical transition field H_{c2} for various temperature values. The measurement results extracted from the fitting procedures are visualized by the symbols. The color gradient on the right hand side represents the set temperature. It ranges from low to high values, which is indicated by blue and red colors, respectively. The fitting curves obtained from the first fitting routine are drawn by the solid lines.

lowing, two different approaches, in analogy to the preceding discussion, are presented. The first one is based on the energy functional given in Eq. 7.44, whose spatial dependence is determined by the cubic magnetocrystalline and shape anisotropy. The corresponding equation for the critical transition field is presented in Eq. 7.48. In the second model, the demagnetization energy is again complemented by two uniaxial anisotropies, as demonstrated in Eq. D.1. Following the same steps as elaborated above, leads to an expression for H_{c2} which is given in Eq. D.5. The equation, which finally will be used for the fitting routine is reduced to

$$H_{c2} = M_s N_x + \frac{\rho_s Q^2}{\mu_0 M_s} + \frac{K(3 + 5\cos 4\phi)}{2\mu_0 M_s} - \frac{U_1\left(2 + 6\cos\left(2\left(\phi - \phi_{U_1}\right)\right)\right)}{4\mu_0 M_s}.$$
(7.58)

Note, due to the symmetric shape, i.e. $N_x = N_y$, the demagnetization field does not affect the spatial dependence of H_{c2}. It provides nevertheless a constant offset, as can be seen by the first term in the equation above. In addition to that, also the out-of-plane uniaxial anisotropy and the exchange stiffness term only enter the equation as constants. Since the individual contributions can not be unambiguously assigned, the additional anisotropy is therefore neglected in the following.

In the first model, the fitting parameters are the demagnetization factors N_x, N_y and the orientation of the principal axis with respect to the crystal axis ϕ_D, the cubic magnetocrystalline anisotropy strength K and the exchange stiffness constant ρ_s. In the second approach, the demagnetization factor is fixed to $N_x = 0.343$ and the variables are extended by the uniaxial

anisotropy strength U_1 and the respective direction of the symmetry axis given by ϕ_{U_1}. For the remaining parameters, the saturation magnetization and the pitch vector length, we refer again to the results of the SQUID measurements from Appendix E and to the findings, $Q = 2\pi/60\text{nm}$, from previous publications [Ada12; Ono12; Sch15]. In Fig. 7.42 the obtained fit parameters are illustrated. First, the focus is placed on the results of the model, including only the shape anisotropy. The respective demagnetization factors N_x and N_y are given by red and orange symbols in the top panel, Fig. 7.42(a). For the wide temperature range between 4 and 40 K, the two factors are nearly constant and amount to almost the same value. The contribution to the angle-dependence of H_{c2} is therefore obviously negligible. At 50 K, the values of both N_x and N_y decrease significantly, while the difference between them increases. This finite difference is required to reproduce the slight two fold symmetry at this temperature. The absolute values of the demagnetization factors are, however, not uniquely determined, since the sum of them contributes only to the field offset. The variation from the real values, will then be compensated by adapting ρ_s in the fitting algorithm. The extracted exchange stiffness constant is visualized in Fig. 7.42(b) by the orange symbols. With increasing temperature ρ_s decreases monotonously. From a more detailed analysis it is observed that it actually scales with M_s^2. This trend agrees with the finding that the internal conical susceptibility $\chi_{\text{con}}^{\text{int}} = \mu_0 M_s^2/\rho_s Q^2$ is nearly temperature independent [Bau10]. In the bottom panel, Fig. 7.42(c), the temperature evolution of the cubic magnetocrystalline anisotropy strength is depicted. Here, the data points assigned to the first model are given by the blue symbols. The curve progression is determined by a monotonous decrease of K under an increasing temperature. Emphasis is placed on the fact that the anisotropy strength remains positive over the whole temperature range and finite up to a value of 40 K. At 50 K it finally reaches zero. Apart from the high-temperature limit, the obtained results agree with the ones obtained in the field-polarized phase, presented above. Nevertheless, a significant difference between these results is evident for the whole temperature range.

In the second fit procedure the twofold symmetry is accounted for by the in-plane uniaxial anisotropy. Its respective strength is visualized in Fig. 7.42(a) by the open symbols. Similar to the demagnetization factors discussed above, U_1 does not vary much as a function of temperature. Only at higher temperatures it appears to slightly decrease. Due to the simultaneous decrease of M_s the effect on the oscillation amplitude is however smaller than the one in the case of the demagnetization energy. For the values of the exchange stiffness constant a significant discrepancy between the two models is evident in Fig. 7.42(b). The data of the second set, given here by the open symbols, are approximately 1.5 times larger than the one of the first fit routine. Also the slope in general appears to be different, but is demonstrated to scale also with M_s^2 as a function of temperature. This

observation originates from the fact that, the in-plane uniaxial anisotropy influences the angle-dependence of H_{c2}, but also provides a finite offset. This additional contribution, which reduces H_{c2} due to the positive sign of its respective strength U_1, is finally compensated by an increase of ρ_s. The last parameter extracted is the anisotropy strength K, illustrated in Fig. 7.42(c) by the open symbols. Apart from small deviations, its obtained curve progression is highly reminiscent of the one of its counterpart in the first fit model. Also here, K decreases continuously as a function of temperature, until reaching approximately zero at $50\,\mathrm{K}$.
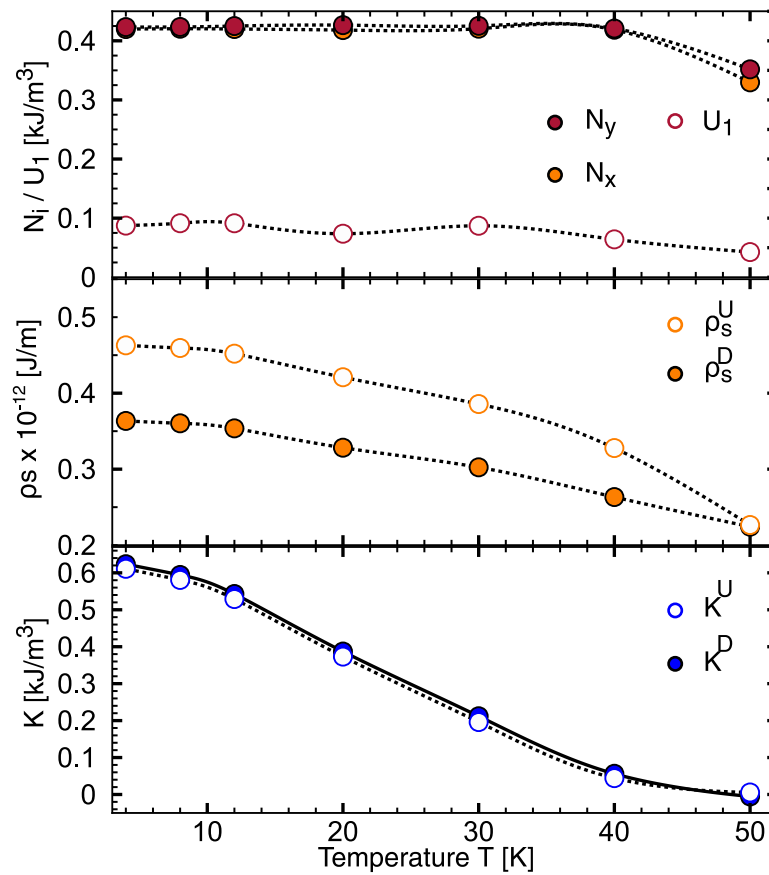
Figure 7.42: Visualization of the fit parameters extracted from the measurements of the critical field in the case of the cuboid sample. (a) Demagnetization factors N_x, N_y and uniaxial anisotropy strength U_1 as a function of temperature. (b) Temperature dependence of the exchange stiffness constant ρ_s. (c) Temperature evolution of cubic magnetocrystalline anisotropy K. The results corresponding to the first fit routine are given by the closed symbols, while the ones obtained from the second one are illustrated by the open symbols.

Finally, comparing the extracted fit parameters of these two quantities, the resonance frequencies in the field-polarized phase on one hand and the critical transition field on the other hand, confirms the observations, which emerged already in the compilation of the microwave spectra in Fig. 7.36. While the angle-dependence of the phase transition between the conical/tilted conical and field-polarized state can be ascribed to the shape and cubic magnetocrystalline anisotropy and therefore agrees with the theoretical model, the evolution of the resonances of the Kittel mode reveals an unexpected dominant twofold symmetry, which no longer can be explained in terms of the demagnetization energy. As a workaround, an additional uniaxial anisotropy term is required to be implemented in the energy functional in order to account for this dependence on the magnetic field direction. The parameters extracted from the two fit models can, however, not be compared, due to this additional contribution. From these observations it can be concluded that only the dynamic response of the magnetization is subject to the additional contribution, the magnetization configuration itself, however, remains unaffected. It follows also that the energy functional is in principle sufficient to describe the physical properties, the ellipsoidal approximation of the cuboid sample is valid and in this regard the magnetization does not decay into various domains and edge effects are of minor importance, despite the finite sample size. Regarding the anisotropy strength K, similar temperature dependences are observed. The values extracted in the field-polarized phase are, however, smaller and also change sign in the high-temperature limit. This discrepancy might hint at additional gradient energy terms, like the exchange anisotropy, which only contribute to the critical transition field, as elaborated above. Since the undefined contribution to the angle-dependence, which on first glance appears to be of a twofold symmetry, might also comprise higher order and also asymmetric terms, the fit results are likely to be impaired. It therefore does not allow to draw conclusions in this regard.

The fact that the measurements regarding the magnetization configuration agree well with the theoretically predicted results, but the ones of the dynamic response do not, suggests that the assumptions made in the respective approach are insufficient. A property of the magnetization dynamics, which is not considered in the calculations up to now is the explicit spatial dependence characterized by the wave vector $\boldsymbol{k}$. As spin waves are evidently excited in the microwave experiments though, the effect of a finite momentum on the dispersion will be elaborated in the following. In Fig. 7.43 the resonance frequencies of the field-polarized phase are plotted as a function of the field direction ϕ for a wide wave vector range. In accordance with the calculations presented above the magnetic field is rotated in the x-y plane, the field strength is fixed to $B = 2B_{c2,0} = 76$ and the remaining parameters are set to $r_0 = -1000$, $\tau = 0.88$ and $N_i = 1/3$. Regarding the wave vectors, two cases are differentiated. The data points given by the closed

symbols are calculated for a wave vector parallel to the x axis. The results indicated by the open symbols are obtained for a parallel alignment of k with the z direction. In the interest of completeness, also the uniform mode ($k = 0$), drawn by the dashed black line, is added to the figure. In the top panel, Fig. 7.43(a), the angle-dependence extracted for the isotropic case ($K = 0$) is illustrated. For spin waves propagating along the z direction, which is perpendicular to the one of the external field, the dispersion does not dependent on the field orientation ϕ and is therefore constant. The corresponding frequencies in this configuration decrease under a decreasing wave vector amplitude and approach the one of the uniform mode. Conversely, if the wave vector is parallel to the x axis and hence in the plane of the magnetic field, the frequency is no longer constant, but strongly depends on the orientation between k and B. For a better understanding of the presented calculations we refer to the analytically derived dispersion relation in [Gar17],

$$
\hbar\omega(\boldsymbol{k}) = \ 2\mathcal{D}Qk_z \\
+ \sqrt{(\mathcal{D}k^2 + g\mu_B\mu_0 H_{\text{int}})\left(\mathcal{D}k^2 + g\mu_B\mu_0 H_{\text{int}} + g\mu_B\mu_0 M_s \frac{k_\perp^2}{k^2}\right)},
$$
(7.59)

with $k_\perp = (k_x, k_y)$, spin wave stiffness constant $\mathcal{D} = g\mu_B\rho_s/M_s$ and the magnetic field applied along the z direction. Note, the prefactor convention is adapted here to the one chosen in Sec. 7.3.3. For very large wavenumbers, the resonance frequencies are mainly determined by the first term, which is induced by the DMI. Due to the linear dependence on k_z, a finite component in the z direction leads to a different resonance condition depending on the sign. This can be seen in the case of $k = Q$, where the minimum and maximum values are given at $\phi = 0°$ and $\phi = 180°$, respectively. In the limit of a small wavenumbers, it is evident that the additional term, but also the ones proportional to k^2 vanish and the angle-dependence is governed by the last term only, which is proportional to $\cos 2\phi$. If the cubic magnetocrystalline anisotropy takes on finite values ($K = 0.0002$), as it is shown in Fig. 7.43(b), its corresponding angle-dependence shapes the dispersion relation accordingly. In the case of perpendicular spin waves, the prior constant curve progression exhibits now a fourfold symmetry as a function of ϕ. For a finite in-plane wave vector, the additional contribution superimposes the one from the dipolar interactions, which results, in the small-k limit, in a two- and fourfold symmetry. Nevertheless, the effect originating from the dipolar interactions still dominates the overall appearance, even at low temperatures. Comparing now the calculated angle-dependencies with the measurement results, reveals a high level of resemblance. The overall appearance suggests that instead of the uniform mode, in-plane spin waves with small wave vectors are excited, which in turn causes the detected twofold

symmetry. Additionally the fact that the respective amplitude in the measurements scales with M_s agrees with the equation given above. Note, the small shift, which is observed in the measurements between both contributions, might arise from a slight misalignment of the sample edges with the coplanar waveguide. Since the surface normals are aligned with the crystallographic axes, this likewise leads to a distortion between the lattice and the driving field direction and therefore a phase shift, as resolved. Rotating the sample in a controlled manner with respect to the CPW in further experiments is expected to result in a continuous shift of this phase, which would support the arguments given above.
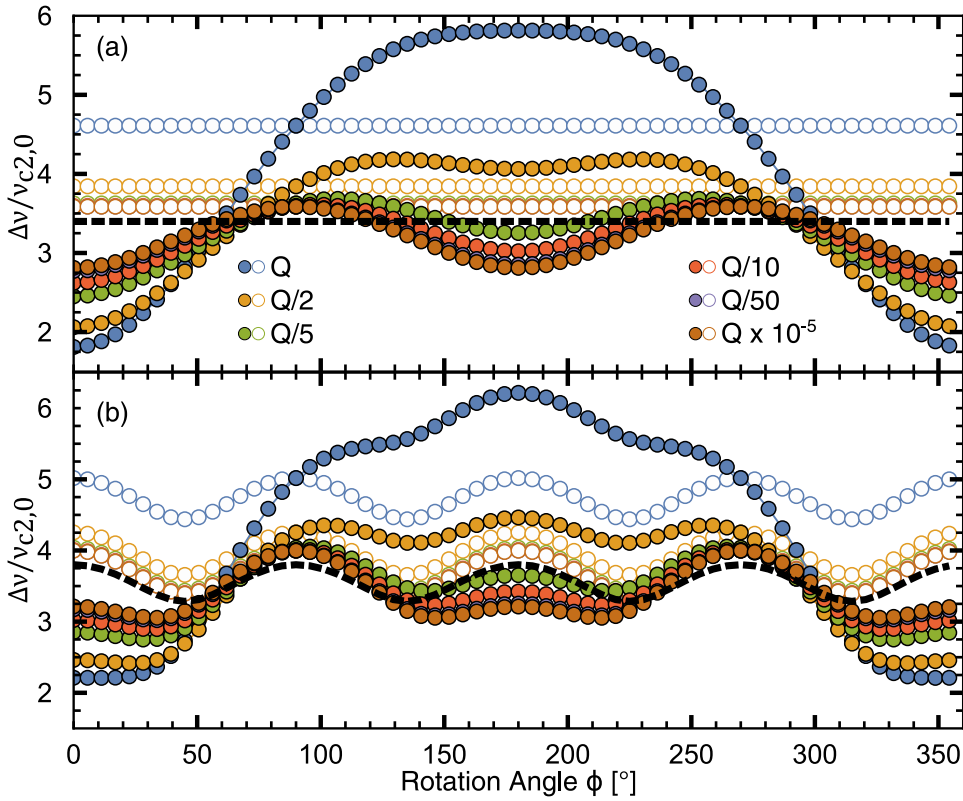
Figure 7.43: Angle-dependence of the resonance frequencies in the field-polarized phase for various wave vectors. The figure contrasts the results calculated for a cubic magnetocrystalline anisotropy constant of (a) $K = 0$ and (b) $K = 0.0002$. Here, the magnetic field is rotated in the x-y plane, while the spin waves are propagating either along the x or z direction, indicated by closed and open symbols, respectively. The uniform mode is illustrated by the dashed black line. The remaining parameters are set to $r_0 = -1000$, $B = 76$, $\tau = 0.88$ and $N_i = 1/3$.

Besides revealing the material characteristics, the analysis of the Kittel

mode and H_{c2} also allows in general to finally convert the cubic magnetocrystalline anisotropy strength from physical to dimensionless units. Since the twofold symmetry dominates the angle-dependence of the resonances in the field-polarized phase, the extracted conversion factor might be impaired. Therefore, in the following the discussion is limited to the critical transition field only. For moderate anisotropy strengths, the in-plane angle-dependence of the critical transition field in the Ginzburg-Landau model is given by Eq. 7.30 with its components Eq. 7.31. From this equation the relative oscillation amplitude, defined as

$$A(K) = \frac{B_{c2}(K, 45°) - B_{c2}(K, 0°)}{\frac{1}{2}\left(B_{c2}(K, 45°) + B_{c2}(K, 0°)\right)}, \qquad (7.60)$$

in the case of a disk or spherical sample shape, is extracted. Here, $B_{c2}(K, 45°)$ and $B_{c2}(K, 0°)$ correspond to the maximum and minimum values of H_{c2}, as illustrated in Fig. 7.33. This expression therefore represents the peak-to-peak value, which is normalized by the mean value of H_{c2}. The same procedure is established for the experimental side. By the fit routines, utilizing equation Eq. 7.58, first the different contributions are disentangled. Since for this analysis only the effect of the cubic magnetocrystalline anisotropy has to be considered, the angle-dependent term of the uniaxial anisotropy is neglected [3]. Finally, the maximum and minimum, but also the mean value of the critical transition field is extracted from the adapted fitting curves. The relative oscillation amplitudes, collected from the experimental and theoretical treatment, are visualized in Fig. 7.44(a). The results inferred from the measurements are indicated by the red symbols and given as a function of temperature. Based on its almost linear dependence on K, the curve progression of the amplitude A resembles the one of the anisotropy strength, presented in Fig. 7.42(c). The theoretically predicted amplitude, here visualized by the orange line, is plotted in dependence on the dimensionless anisotropy constant $\tilde{K}$. Note, in the interest of clarity, the tilde notation is reintroduced for the dimensionless variable. From this compilation it is evident that for anisotropy values up to approximately $K = 0.00022$ in the theoretical model, the whole temperature range is covered in the experiments. Furthermore, it reveals that the assumed strength of $K = 0.0002$ in the low-temperature limit in the previous chapter is justified. In previous publications [Cha18], an estimate of the conversion factor between physical and dimensionless units was derived by comparing the anisotropy strengths, which are required for stabilizing the low-temperature skyrmion phase in the experiments and the calculations, respectively. Since, for the stabilization of the LTS phase and consequently the detection of its signatures, a preceding cycling routine has to be performed, this comparison provides only

---

[3] It should be mentioned that for this analysis the amplitude of the fourfold symmetry contribution is assumed to originate only from the cubic magnetocrystalline anisotropy.

a rough estimate. The analysis of the critical transition field on the other hand, allows directly to calculate the dimensionless anisotropy constant $\tilde{K}$, by solving Eq. 7.60 numerically for the amplitude value, attributed to a certain strength K. The results obtained for the extracted anisotropy values are depicted in Fig. 7.44(b).
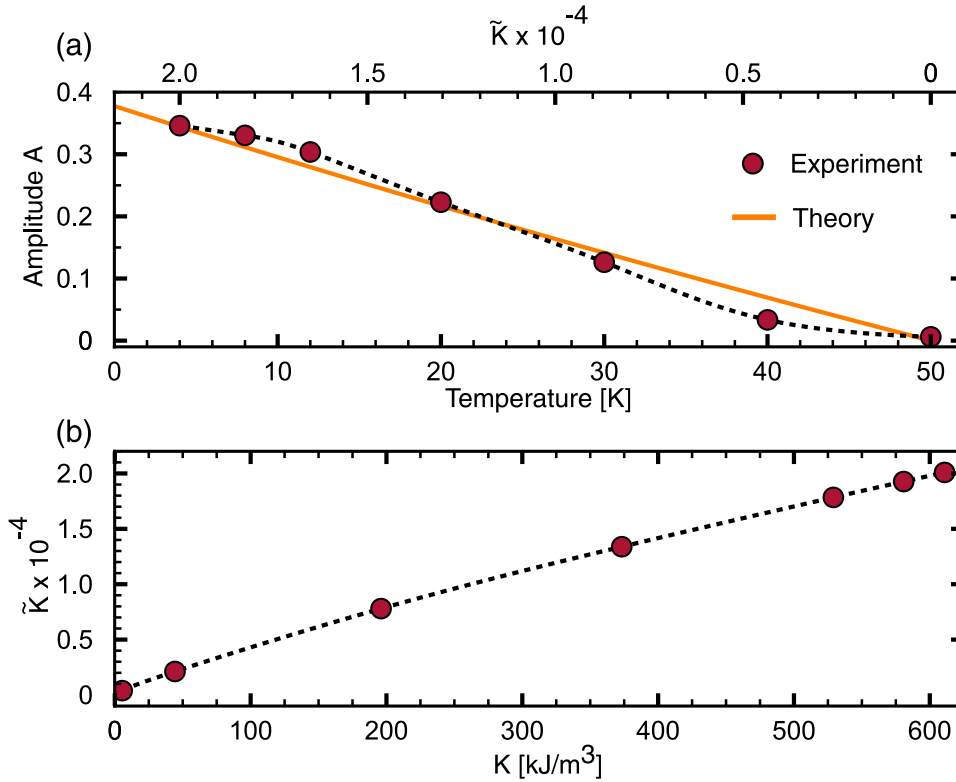
Figure 7.44: (a) Relative oscillation amplitude A of H_{c2}. The figure contrasts the results obtained from the experiments (red symbols) and the Ginzburg-Landau model (orange line). In the first case A is given as a function of temperature (bottom axis), while in the second case it is illustrated as a function of anisotropy strength $\tilde{K}$ (top axis). In the interest of clarity, the tilde notation is introduced for the dimensionless constant. (b) Calculated anisotropy strength $\tilde{K}$ for the extracted K values from the fitting procedures.

Spherical Sample

In order to verify that the resolved effect does not arise from the sample geometry, similar microwave spectroscopy experiments as presented above are performed now on a Cu_2OSeO_3 crystal of spherical shape. The sample with a diameter of approximately $2\,mm$ is placed on the same coplanar waveguide as utilized before for the cuboid sample. Since the coupling efficiency between the magnetization and the driving field depends on their orientation with respect to each other Sec. 3.1, the crystal is placed on the gap to guarantee a perpendicular alignment throughout the whole measurements. The magnetization is therefore subject to an in- and out-of-plane ac-field. Furthermore, the sample orientation is chosen such that one [001]-crystal direction is pointing out of plane and therefore parallel to the CPW surface normal, by using X-ray crystallography. This finally allows to rotate the external magnetic field in the plane spanned by the [100]- and [010]- directions. It should be mentioned that due to the small contact surface, a thick layer of glue was required to attach the sample to the coplanar waveguide. As a consequence the heat dissipation might be decreased so that during the measurements the sample temperature is slightly larger than the one of the cuboid sample, despite the same set heater temperature. In addition to that, the increased distance to the CPW leads to a lower ac-field strength at the sample position. It follows that the limited output power of the VNA on the one hand and its lower sensitivity on the other hand, is not sufficient enough to resolve the magnetization dynamics of the crystal in this configuration. For that reason microwave spectroscopy based on the lock-in technique, as described in Sec. 3.2, is employed. In the following, a similar experimental protocol as for the cuboid sample is established. For a fixed temperature and external field direction, an absorption trace is recorded. Since with this technique the measurements are performed in the field-domain, the excitation frequency of the rf-generator is set to be constant while the field is swept. The detected line-scan is then predicted to be given by the derivative of a Lorentzian profile, as it is shown in Eq. 3.4. The focus of this study is placed on the angle-dependence of the resonance modes in the field-polarized state. As for this a fine resolution in the frequency-domain is not required, the applied excitation frequencies are limited to 6, 8 and $12\,GHz$.

In Fig. 7.45(a) an absorption FMR trace as a function of the magnetic field strength is visualized. The measurement results, shown here by the blue line, are obtained at an excitation frequency of $6\,GHz$ and a temperature value of $55\,K$. Note, in the interest of simplicity, the signal is normalized with respect to its maximum absolute amplitude. In addition to the data, the fitting curve, drawn by the red line, is added to the figure. As already observed in the VNA based experiments, more than one resonance mode is resolved in the field-polarized phase. The fit equation is therefore a result of the sum of derivatives of two Lorentzian functions, which individual con-

tributions are visualized by the dashed black lines. In the low-temperature limit, the number of additional resonances increases significantly again, as can be seen in the bottom panel, Fig. 7.45(b). The shown field sweep is recorded also at an excitation frequency of 6 GHz, but the temperature is set to 6 K in this case. Due to its complexity, a comprehensive fitting routine to account for all resonance frequencies has proven to be too cumbersome. By focusing the analysis, however, on the low-field limit of each spectrum, adding several Lorentzian functions to the fit curve allows to reproduce the data in this field range. From these results, the resonance mode lowest in field can uniquely be extracted, and will be therefore employed for the analysis regarding its field direction and temperature dependence in the following. In addition to that, the amplitude-weighted resonance position in the field-domain is introduced, in analogy to the definition given in Eq. 7.54. For illustration purpose, the respective quantities are shown in Fig. 7.45(b) by a red color. This value will also be determined for each field-sweep and finally compared to the resonance field, which is extracted from the actual fitting routine.

For the analysis of the angle dependencies, first the absorption spectra recorded at the same frequencies and temperatures are collated. By way of illustration, two of these absorption spectra, which are measured at 6 GHz are given in Fig. 7.46. Here, the axis are given by the external field strength B and its respective direction ϕ. The signal amplitude is encoded in the background color, which indicates a positive amplitude by a red and a negative amplitude by blue. For the illustration, the individual line-scans are normalized with respect to their maximum absolute amplitude. Furthermore, the color gradient is rescaled, such that the maximum and minimum value of the whole spectrum set the boundaries of its range. The individual field-traces of each group are analyzed, regarding their resonance modes, as described above. Here, both methods applying Lorentzian fits to obtain the mode lowest in field and the weighted-amplitude protocol are employed. The extracted resonance positions are given by the symbols. The results inferred from the actual fitting procedure are given by the white symbols, while the ones obtained from the average method are indicated by the gray symbols. On the left hand side, Fig. 7.46(a), the absorption spectrum recorded at 55 K is visualized. As anticipated before, already at this temperature at least two resonance modes are observed. By means of this figure, the difference between the two approaches of extracting the resonance position is visible. Provided all modes would exhibit the same angle-dependence, the amplitude-weighted resonance field would only yield a higher value than the one lowest in field. Since, however, this is obviously not the case, the first method picks off the additionally emerging features, as can be seen by the corresponding gray symbols. The more interesting part is, however, the distinct angle-dependence of these. While the mode with the smaller resonance field in Fig. 7.46(a) varies only slightly with ϕ, the second one demonstrates
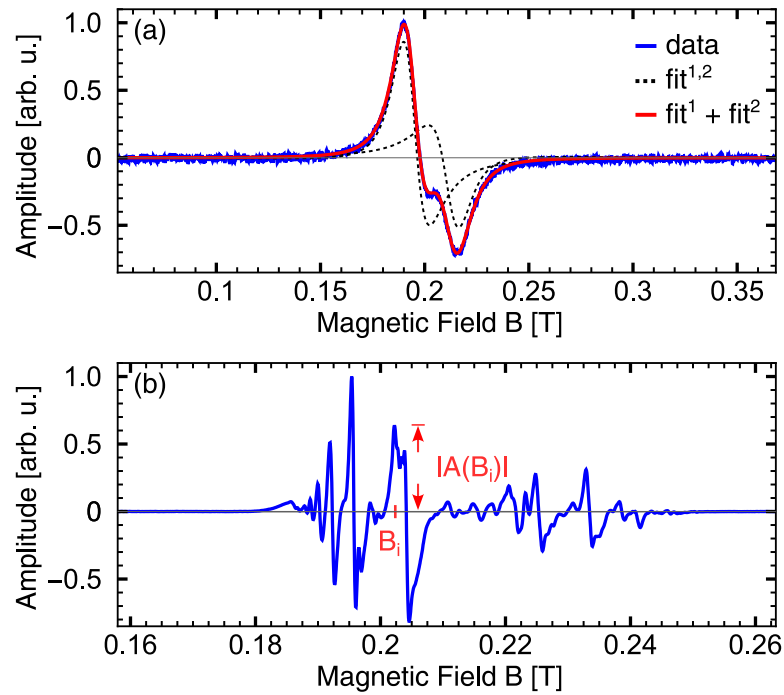
Figure 7.45: (a) Absorption A as a function of magnetic field strength B recorded at a temperature of $55\,\mathrm{K}$ and an excitation frequency of $6\,\mathrm{GHz}$. The figure comprises the raw data given by the blue line and the respective two-peak Lorentzian fit according to Sec. 3.2 illustrated by the red line. The individual Lorentzian functions are given by the dashed black lines. (b) Absorption A as a function of magnetic field strength B recorded at a temperature of $6\,\mathrm{K}$ and excitation frequency of $6\,\mathrm{GHz}$.

a clear angle-dependence, which appears to be of a twofold symmetry. Conversely, the two modes detected in the cuboid sample at this temperature, depicted in Fig. 7.38(a), show both the same curve progression. Comparing these findings to the numerical calculations in Fig. 7.43, might indicate that both in- and out-of-plane standing spin waves, attributed to the alternating and almost constant resonances, are simultaneously excited by the driving field. In the figure on the right hand side, Fig. 7.46(b), the absorption spectrum recorded at $20\,\mathrm{K}$ is depicted. Compared to the results discussed before in this temperature regime the cubic magnetocrystalline anisotropy strength is no longer zero but takes on finite values. As a consequence, its distinct spatial dependence dictates the one of the resonance fields. Interestingly, the division into two groups regarding the angle-dependence is also evident at this temperature. In the field-range of approximately $B = 160 - 200\,\mathrm{mT}$, the profile of the resonance modes are all following the one indicated by the fit results. For higher field values, a signal signature is mainly found at

field-angles, which correspond to the maxima of the second mode at 55 K. Based on this unequal distribution of the absorption signal, the trace of the amplitude-weighted resonance position deviates from the one extracted by the Lorentzian fits.
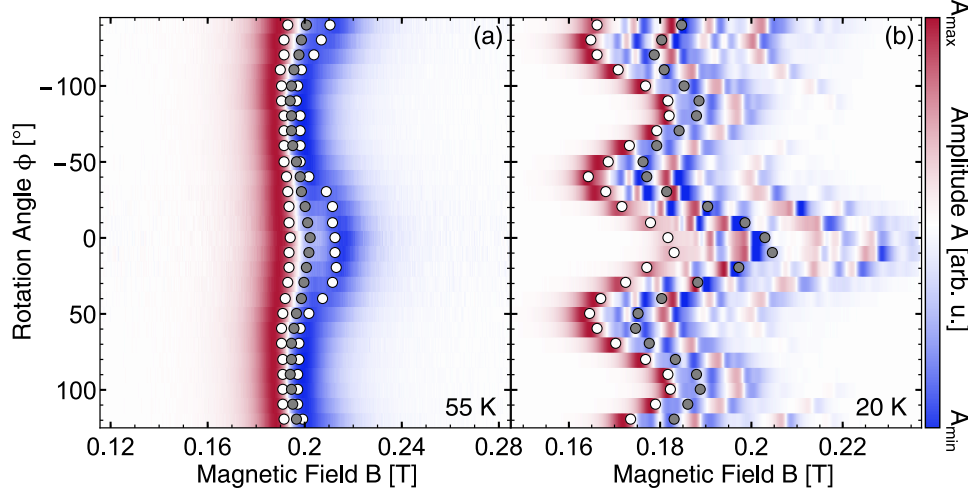
Figure 7.46: Angle-dependence of the normalized absorption spectra in the field-domain for a spherical sample. The figure illustrates the results obtained at (a) 55 K and (b) 20 K and an excitation frequency of 6 GHz. In addition to that the resonance frequencies extracted by Lorentzian fits and the amplitude-weighted resonance method are given by the white and gray symbols, respectively.

In the interest of completeness, again both models introduced before are employed for the fitting procedure of the angle-dependence of the resonance fields. In the first approach the energy functional is given by equation Eq. 7.5. Here, the spatial dependence originates from the shape and the cubic magnetocrystalline anisotropy. In the second model, the demagnetization factors are set to $N_i = 1/3$, which complies with the ones of a sphere. Consequently, this term does no longer contribute to the resonance condition and is hence substituted in the energy functional by the two uniaxial anisotropies, as shown in Eq. 7.55. Since the measurements on the spherical sample are performed in the field-domain, the previously derived resonance conditions have to be rearranged in order to calculate the resonance field in dependence of the excitation frequency. The resulting equation, which is obtained from the general resonance condition Eq. A.7, is presented in Eq. A.8 in the appendix. Depending on the model discussed, the respective parameters will be adapted accordingly. In the first fitting procedure, the demagnetization factors N_x, N_y, the respective orientation of the principal axes ϕ_D, the cubic magnetocrystalline anisotropy strength K and the angle offset ϕ_{off} enter the resonance condition as variables. The remaining

161

parameters are set to be constant. The gyromagnetic ratio is fixed to a value of $\gamma = 1.88 \times 10^{11}$ rad/sT [Sta17b], the excitation frequency ω is given by the rf-source and for the saturation magnetization M_s the results inferred from the SQUID measurements on the cuboid sample are taken. The uniaxial anisotropies are not considered in this model and consequently the respective constants U_1, U_2 are set to zero. One of the data sets to be analyzed is presented in Fig. 7.47. The figure illustrates the evolution of the resonance fields as a function of magnetic field direction for various temperatures. Here, the resonance positions, shown by the symbols, are obtained from the Lorentzian fits to the field sweeps measured at 6 GHz. In addition to that, the fitting curves according to the model discussed are drawn by the solid lines. The temperature values at which the experiments are conducted, are indicated by the color bar on the right hand side. While a low temperature is reflected by blue, a high temperature is given by red. Note, for the results extracted by the amplitude-weighted resonance method, we refer to Appendix F.
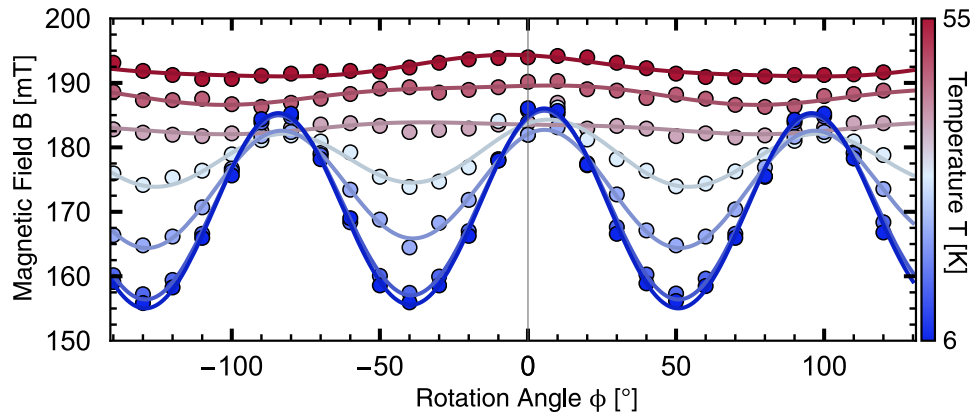
Figure 7.47: Angle-dependence of the resonance fields for various temperatures. The results, given by the symbols, represent the resonance positions inferred from Lorentzian fits to the data set at 6 GHz. The respective temperature value is indicated by the color gradient on the right hand side. The fitting curves according to Eq. A.8 in the appendix are drawn by the solid lines.

In the following discussion, the fit results of both data sets are analyzed. To differentiate between them, open symbols are chosen for the parameters assigned to the Lorentzian fit data set and closed symbols for the ones of the amplitude-weighted resonance method. In Fig. 7.48(a) the temperature evolution of the extracted parameters N_x and N_y is depicted. In the low-temperature limit, the demagnetization factors of the first data set are almost equal and amount to a value of approximately 0.2, which except for the absolute values agrees with the symmetry of the spherical sample.

By increasing the temperature, both values slightly increase, whereby the slope in the case of N_y is larger. As a consequence the discrepancy between them likewise increases. Provided that the small twofold symmetry in the angle-dependence indeed arises from the demagnetization energy contribution, this observation might indicate that the number of peaks in the fit routine for high temperatures is too small, which leads to a spurious shift of the obtained resonance position. From the fit results a value for N_z is obtained, which is almost three times as large as N_x and N_y. This observation would imply that the diameter of the sample in that direction is smaller by a factor of approximately 3 [Aha98], which does not match the actual sample dimensions. It follows that, either an additional energy term, which induces a shift of the spectrum along the field axes is missing, or the resonance mode lowest in frequency cannot be attributed to the FMR mode. In the case of the second data set, the demagnetization factors exhibit a significant difference over the whole temperature range, which also slightly increases under an increasing temperature. Compared to the previous results, a clear trend is nevertheless not observed. Since the weighted-amplitude method averages over all resonance modes, the obvious twofold symmetry, which is obtained for the ones at higher fields, is imprinted on the resulting angle-dependence. Consequently the fitting algorithm adapts the demagnetization factors which belong to the only energy term exhibiting such a spatial evolution. The large discrepancy between N_x and N_y is therefore expected. An important finding is that N_z in this case only slightly varies from $1/3$. The resonance field hence appears to be close to the one predicted for the uniform mode. Since in both data sets the difference between N_x and N_y does not vary strongly, the increase of the amplitude of the $\cos 2\phi$ term arises mainly from the increase of M_s under a decreasing temperature. The second quantity to be extracted from the fit routines is the anisotropy strength K. Its corresponding temperature evolution is illustrated in the bottom panel, Fig. 7.48(c). For both data sets, K demonstrates a continuous decrease in strength under increasing temperature, until reaching approximately $40\,\mathrm{K}$. For temperature values above this threshold, the anisotropy constant appears no longer to be finite. In the low-temperature limit, the fit results obtained for the average over all resonance modes are larger than the one of the other data set. This discrepancy originates mainly from the larger difference between the demagnetization factors, which on the other hand reduces the oscillation amplitude of the fourfold symmetry term, as can be seen from equation Eq. A.8. In order to compensate this reduction, the extracted K value is enhanced.

In the second fit routine, while the demagnetization factors are fixed to $N_i = 1/3$, the prefactors of the uniaxial anisotropy terms U_1 and U_2 are no longer set to zero. In addition to the orientation of the direction of the symmetry axis ϕ_{U_1}, they enter the fit equation as variables in the following. The extracted temperature evolution of the anisotropy strengths is visual-

ized in Fig. 7.48(b). From the fitting results of the first data set, no clear dependence of U_1 on the temperature is evident. The obtained values for this energy contribution only slightly deviate from zero, which agrees with the finding that the angle-dependence of the resonance mode lowest in field is mainly determined by a fourfold symmetry. The constant U_2 on the other hand, exhibits a clear increase in amplitude as a function of temperature. As
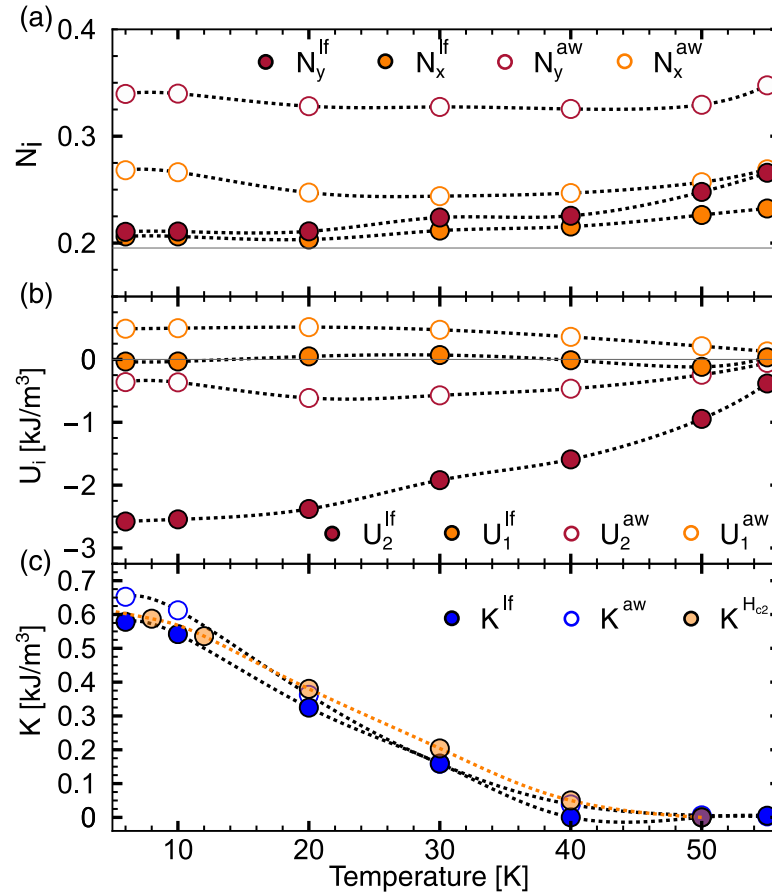
Figure 7.48: Visualization of the extracted fit parameters in the case of the spherical sample. (a) Temperature evolution of demagnetization factors N_x, N_y. (b) Uniaxial anisotropy strengths U_1 and U_2 as a function of temperature. (c) Temperature dependence of the cubic magnetocrystalline anisotropy constant K. The results corresponding to the amplitude-weighted resonance method (aw) are given by the closed symbols, while the ones obtained from the actual fitting procedure (lf) are illustrated by the open symbols. Note, the results of the anisotropy strength K are complemented by the ones, extracted from the critical transition field (Fig. 7.42). The data points, shown by the orange symbols, correspond to the mean value of both fit routines.

argued above, the out-of-plane uniaxial anisotropy is primary required to account for the offset between the obtained resonance position and the actual resonance field of the uniform mode. If further energy terms, which are not identified, are also contributing, cannot be determined from this analysis. Compared to the counterpart in the first fit model, the corresponding term does not scale with M_s, but demonstrates a different temperature evolution. For the results received by means of the amplitude-weighted resonances, a continuous decrease of anisotropy strength U_1 under an increasing temperature is observed. By a more detailed analysis it demonstrates to scale with M_s^2 and therefore contributes in a similar manner to the angle-dependence as the demagnetization term. In the case of the parameter U_2, no clear trend is evident. While for high and low temperatures it approaches nearly zero, for intermediate temperatures it takes on finite values. The curve progression agrees with the one already resolved for the demagnetization factors, and arises mainly by the field discrepancy to the uniform mode. Regarding the cubic magnetocrystalline anisotropy strength K, shown in Fig. 7.48(c), the exact same values as before are obtained from the fits. Since they are hidden by the previous results, a general notation of the respective labels is presented in the plot. A distinction is made only between the different data sets.

The comparison of the measurement results demonstrates a substantial difference between the two crystals, despite their similar shape according to the theoretical treatment of the demagnetization energy. In both samples an unexpected twofold symmetry in the angle-dependence of the resonance conditions is observed, whose amplitude scales linearly with M_s as a function of temperature. While in the case of the cuboid sample this contribution dominates the overall appearance of the angle-dependencies and is resolved for all modes, it is less pronounced in the spherical sample and does not affect all resonances. Contrasting the results obtained from the field-polarized phase and the critical transition field H_{c2} reveals that this effect is only resolved in the magnetization dynamics. It stands to reason that the theoretical treatment of only the uniform mode is not sufficient to reproduce the data, but requires the consideration of finite wave vectors and therefore spin waves. From the comparison with the numerical results, presented above, it follows that in the cuboid sample in-plane standing spin waves are excited, whereas in the spherical sample both in- and out-of-plane standing spin waves are formed. In order to account for this additional contribution to the angle-dependence, two different models are applied as a workaround to analyze the data and finally extract the cubic magnetocrystalline anisotropy strength K. Contrasting the results obtained from the resonances of the Kittel mode and its replica on the one hand and the ones from the critical transition field on the other hand demonstrates a clear discrepancy especially in the high-temperature limit, which might hint at additional anisotropy terms of a gradient like representation. Since the tem-

perature evolution of K extracted from the H_{c2} fitting procedure agrees well with the one obtained from the spherical sample, this difference might also just arise due to the prevailing contribution from the standing spin waves. In Fig. 7.48(c) the parameters extracted from the spherical sample are complemented by the temperature dependence of K, inferred from the critical transition field (orange symbols). Here, the shown data points are the average of both fitting procedures, given in Fig. 7.42. From this comparison it is evident that both data sets exhibit a very similar trend. The values obtained from the fitting routine of the Kittel mode are slightly lower though, which was already observed for the cuboid sample. The origin for the smaller strengths in the case of the spherical sample might be a slightly higher sample temperature, due to a thicker layer of glue, as mentioned before. A temperature discrepancy of approximately $5\,\mathrm{K}$, as suggested by the shown results, might be reasonable. Since, however, a clear ferromagnetic signal is resolved in the spherical sample at $55\,\mathrm{K}$ this discrepancy can not be greater than $3\,\mathrm{K}$, which corresponds to the maximum offset with respect to the critical temperature $T_\mathrm{c} = 58\,\mathrm{K}$. More important, the fact that the anisotropy strengths extracted from the resonances in the collinear state in both cases, cuboid and sphere, are smaller than the one resolved from the critical transition field, hints at a different origin. Another reason might be the presence of additional anisotropy terms, like the exchange anisotropy, which exhibit also a fourfold symmetry. Against the background of the excitation of spin waves instead of the uniform mode, both the resonances in the field-polarized phase and H_{c2} should be in principle subject to this additional angle-dependent contribution. Since however its respective term in the resonance conditions is scaling with k^2, the exchange anisotropy does not affect the magnetization dynamics in the small wave vector limit, but only its configuration. As a consequence, a finite difference in the amplitudes of the $\cos 4\phi$ term, which in the fitting procedures can only be assigned to the cubic magnetocrystalline anisotropy, should be resolved for both quantities. An assumption, which, in turn, agrees well with the experimental results, presented in Fig. 7.48(c). In order to get an estimate for the exchange anisotropy strength C, it is calculated from the induced amplitude difference of the fourfold symmetry term according to Eq. 7.48. In the interest of simplicity, the pitch vector length $Q = 2\pi/60\,\mathrm{nm}$ is set to be constant in these calculations. The obtained results are illustrated in Fig. 7.49 by the orange symbols. Note, due to the different set temperatures during the measurements, the data sets are interpolated in the low-temperature limit. The shown results do not demonstrate a clear dependence on the temperature. While under a decreasing temperature down to $20\,\mathrm{K}$ C increases, it suddenly decreases in amplitude at lower temperatures. The obtained values are of the same order of magnitude as reported for Zn-substituted $\mathrm{Cu_2OSeO_3}$ in [Moo21]. In contrast to these results, however, an opposite sign of constant C is observed. Finally, in order to translate these findings to the numerical

model a similar approach, as discussed in Eq. 7.60, is employed. By solving the amplitude difference,

$$B_{c2}(K, 0, 45°) - B_{c2}(K, 0, 0°) \overset{!}{=} B_{c2}(K', C, 45°) - B_{c2}(K', C, 0°) \quad (7.61)$$

C is determined numerically. Note, for this purpose Eq. 7.30 is extended by the exchange anisotropy term. The parameters are set to $r_0 = -1000$, $\tau = 0.88$, $N_i = 1/3$, $K = 0.0002$ and $K' = 1.14K$. Here, the factor of 1.14 is extracted from the anisotropy ratio $K^{H_{c2}}/K^{\text{sphere}}$, which is depicted in Fig. 7.49 as a function of temperature by the blue symbols. It reflects the average over the data points from 6 to 30 K. From this calculation it follows that a dimensionless exchange anisotropy strength of approximately $\tilde{C} = 0.15$ [4] is required to compensate the difference in the cubic magnetocrystalline anisotropy strengths.

The investigation of the angle-resolved FMR was motivated by the outstanding issues of the previous section Sec. 7.2. Including only the cubic magnetocrystalline anisotropy in the energy functional leads to a breathing-octupole mode hybridization gap, which is only half as large as the one extracted from the microwave experiments. In order to account for this discrepancy, the numerical model was complemented by the exchange anisotropy term. It could be shown in Fig. 7.30 that depending on the sign of the anisotropy strength either a value of approximately $\tilde{C} = 0.2$ or $\tilde{C} = -0.5$ is required. However, a concrete indication regarding the actual sign and amplitude of $\tilde{C}$ was up to that point not accessible. By performing the presented theoretical and experimental analysis, finally an estimate of the exchange anisotropy strength is provided, which agrees well with the one assumed in the previous section. This indeed suggests the additional exchange anisotropy energy to be the main origin of the increased hybridization gap size of the breathing-octupole mode interaction.

---

[4] Note, in the interest of clarity the tilde notation for dimensionless parameters is reintroduced.
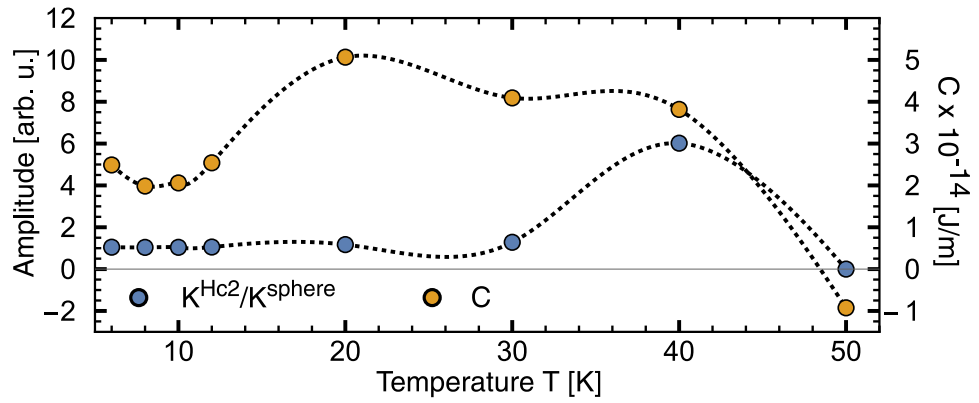
Figure 7.49: Temperature evolution of anisotropy ratio $K^{H_{c2}}/K^{\mathrm{sphere}}$ and exchange anisotropy constant C, given by blue and orange symbols, respectively. While the anisotropy ratio is extracted from the results shown in Fig. 7.48(c), C is calculated from the difference between $K^{H_{c2}}$ and K^{sphere} according to Eq. 7.48. More details are given in the main text.

Chapter 8

Summary

In the framework of this thesis we investigated the effect of anisotropies, arising from the underlying cubic lattice structure, on the collective spin excitations in the insulating helimagnet Cu_2OSeO_3. The focus on the additional energy terms is motivated by the identification of the cubic magnetocrystalline anisotropy as stabilization mechanism of the recently discovered second, independent skyrmion phase [Cha18] in the low-temperature regime. The results presented in this work are composed by the input from the theoretical and experimental side. The theoretical contribution, in turn, is divided into two parts. The first part comprises numerical calculations, which are performed by means of the *Wolfram Mathematica* code developed by Johannes Waizner during the course of his Phd thesis under the supervision of Professor Markus Garst. Previous results are published in [Sch15; Sta17b]. In order to take also anisotropies into account the code was extended by the cubic magnetocrystalline anisotropy and later on also by the exchange anisotropy in close collaboration with Professor Markus Garst. In the second part the angle-dependence of the resonance modes in the field-polarized phase and of the critical transition field H_{c2} is derived analytically, which is finally employed for the fitting procedure to extract the material parameters from the experimental data. These results in turn are recorded in terms of angle-resolved microwave spectroscopy experiments.

In the first chapter of this thesis the effect of the cubic magnetocrystalline anisotropy on the dynamic response of the magnetization dynamics is numerically investigated. The chapter is divided, regarding the dimensions of the momentum space of the magnetization configuration, into two parts. First, the results obtained for the topologically trivial states, which comprise the conical, tilted conical and field-polarized phase, are discussed. As observed already in [Cha18], for anisotropy strengths up to $K = 0.0003$ in the dimensionless unit notation, the pitch vector is aligned along the magnetic field direction. As a consequence, the microwave spectra resemble the one calculated in absence of K. For larger anisotropy values, the titled

conical phase forms, whose boundaries are marked by discontinuities in the field-dependence of the resonance frequencies. In addition to that, further discontinuities are observed within the field range attributed to the tilted conical phase, which arise from the occurrence of anti crossings with higher order modes in the low-frequency range. These additional modes are, due to their vanishing dynamic macroscopic dipole moment, usually not accessible in microwave experiments. In the second part of this chapter, the analysis is extended to the topologically non trivial state, the skyrmion lattice phase. Here, the focus is placed first on the results obtained for a hexagonal skyrmion lattice. For this magnetic texture three modes, which exhibit a finite spectral weight, are obtained. These modes are highly reminiscent of their counterparts in the isotropic case, regarding their spatial distribution of the dynamic magnetization, their field dependence and their sensitivity to the driving field direction. A peculiarity, which originates from the coupling to the underlying cubic lattice, is the occurrence of hybridizations with clockwise modes of higher order. From the respective spatial distribution of the magnetization dynamics, they are identified as sextupole, octupole and dectupole modes, which interact with the counterclockwise, breathing and clockwise modes. In the low-field limit, the hexagonal lattice gets distorted and metastable elongated skyrmions are formed. Also in this configuration, three dominant modes, akin to the ones discussed above are observed. Interestingly, the mode, which demonstrates a clockwise character, is linearly polarized and its polarization axis corresponds approximately to the long axis of the skyrmions. By detecting the spectral weight as a function of the driving-field direction, the orientation of the elongated skyrmions is therefore suggested to be determined experimentally. The numerical findings are complemented by microwave spectroscopy experiments provided from collaborators of our group. The recorded excitation spectra agree well with the numerically obtained results and furthermore hint at the existence of the metastable elongated skyrmion phase at low magnetic fields.

In the second part of this study, the hybridization of the resonance branches in the skyrmion lattice is elaborated in more detail. The numerical calculations are performed for two sample shapes, which comprise a sphere and platelet, in order to determine the effect of the demagnetization contribution. Although several resonance branches are crossing each other, not in every case a mode interaction is observed in the spectra. These findings are confirmed by examining the orthogonality between the eigenvectors. It follows that the cubic magnetocrystalline anisotropy imposes a selection rule. From the analysis of the eigenvectors it can be concluded that an interaction is only allowed if both modes exhibit either only an odd or even number of symmetry axes m or additionally a rotational symmetry and even m. In regard of the mode polarization, which is connected to the symmetry of the mode structure, a hybridization only occurs between modes which are polarized in the same plane. The quantity employed for the characteriza-

tion of the interaction strength is the gap size g, defined as the minimum frequency difference between the hybridizing resonance branches. It is extracted from the microwave spectra obtained from both sample geometries and for the three hybridizations of the uniform modes. It is observed that all three gap sizes scale linearly with K and that the contribution originating from the sample shape is negligible. These results are finally compared to microwave spectroscopy data, which are provided from collaborators from different groups. Despite the significantly different shapes of the investigated samples, the evolution of the gap size reveals a high level of resemblance. In contrast to the theoretical predicted values of g, however, the resolved data are larger by a factor of approximately 2-3. Against this background, the effect of the exchange anisotropy, which was already considered in previous studies [Bak80; Ban19], on the magnetization dynamics in the skyrmion lattice is investigated. From the numerical calculations it can be observed that, despite this additional energy term, the overall appearance of the microwave spectra remains the same. The hybridization gap of the breathing and octupole mode interaction, however, varies strongly as a function of exchange anisotropy strength C. While in the case of a positive C the gap size increases linearly, the competition between both anisotropies results first in a decrease and then in a subsequent increase of g, for negative C. In both cases, by exceeding a certain amplitude of C the gap size takes on values twice as large as the one obtained in absence of the exchange anisotropy, which finally corresponds to the ones obtained in the experiments. It should be mentioned that besides the breathing-octupole mode hybridization, also the counterclockwise-sextupole mode interaction is resolved in the lamella sample, as predicted by the numerical calculations.

In the last part the angle- and temperature-dependence of the resonance conditions is investigated. The aim of this study is to resolve the outstanding issues regarding the energy landscape arising from the underlying cubic lattice environment. For this purpose, microwave spectroscopy experiments on two Cu_2OSeO_3 crystals of a cuboid and spherical shape are performed and subsequently compared to the respective analytical and numerical calculations. In the first experiments on the cuboid sample, the quantities to be investigated are the resonances in the field-polarized phase and the critical transition field H_{c2}. By comparing the obtained results, it could be observed that besides the fourfold symmetry arising from the cubic magnetocrystalline anisotropy, the angle-dependence of the resonances in the collinear state is determined by a dominating twofold symmetry, which in turn is not found in the one of H_{c2}. It follows that only the dynamic response of the magnetization is affected and not its configuration. From the comparison with numerical calculations it can be concluded that the restriction of the theoretical model to the uniform mode is not sufficient to describe the measurement results. Instead, it stands to reason that the observed effect originates from the dipolar interactions which have to be

taken into account due to the formation of, in this case in-plane, standing spin waves. In the experiments on the spherical sample, which are limited to the resonance modes of the field-polarized phase, two different resonance groups, regarding their evolution as a function of angle are detected. Again, comparing these findings to the numerical calculations, suggests that in this case both in- and out-of-plane standing spin waves are excited. Finally, in order to extract the material parameters, despite the additional contribution to the angle-dependence, two different models are employed for the analysis of the resonance traces. It could be shown that the obtained temperature evolutions of the cubic magnetocrystalline anisotropy strength K in the case of the cuboid sample differ from each other, in particular in the high-temperature limit, which might be attributed to the dominant dipolar contribution. The trend of the temperature dependence resolved for the spherical sample, on the other hand, agrees well with the one obtained from the critical transition field. A finite difference in the absolute values is, however, evident. This suggests a gradient-like anisotropy term, which exhibits a fourfold symmetry, like the exchange anisotropy, to be present. The extracted exchange anisotropy values agree with the ones reported in [Moo21], the sign is however reversed. The resolved difference in K also allows to give an estimate for the dimensionless exchange anisotropy constant. The obtained value of $\tilde{C} = 0.15$ agrees well with the one which is required to reproduce the experimentally determined hybridization gap of the breathing-octupole mode anti-crossing in the previous section. This suggests that, indeed, both cubic magnetocrystalline anisotropy and exchange anisotropy are the main contributions to the hybridization mechanism. Finally, besides extracting the cubic magnetocrystalline anisotropy constants, the analysis of H_{c2} also allows to directly convert anisotropy strength K from physical to dimensionless units.

Part III

Appendix

Appendix A

Derivation of the angle-dependent FMR Condition (I)

The calculation of the resonance conditions follows the protocol elaborated in Chap. 2 and Sec. 7.3.1, which is based on solving the lossless Landau-Lifshitz equation of motion. The energy functional considered,

$$
\begin{aligned}
F = & \ \tau \boldsymbol{M} \mathcal{T}(\phi_{\mathrm{D}}, 0) \boldsymbol{N} \mathcal{T}^{-1}(\phi_{\mathrm{D}}, 0) \boldsymbol{M} - K \sum_i M_i^4 - \boldsymbol{B} \boldsymbol{M} \\
& - U_1 \left(\boldsymbol{M} \cdot \boldsymbol{k}_1 \right)^2 - U_2 \left(\boldsymbol{M} \cdot \boldsymbol{k}_2 \right)^2,
\end{aligned}
\tag{A.1}
$$

comprises the demagnetization contribution, the cubic magnetocrystalline anisotropy, the Zeeman energy and the two uniaxial anisotropies Here, the corresponding constants are the dipolar strength τ, demagnetization tensor $\boldsymbol{N}$, cubic magnetocrystalline anisotropy strength K, external field $\boldsymbol{B}$ and uniaxial anisotropy constants U_1 and U_2. For a finite angle between the principal axes of the sample and the crystal lattice, the demagnetization tensor is rotated via a rotation matrix $\mathcal{T}$ around the z axis by ϕ_D. The directions of the symmetry axes are denoted by $\boldsymbol{k}_1$ and $\boldsymbol{k}_1$ and are given by,

$$
\begin{aligned}
\boldsymbol{k}_1 &= (\cos \phi_{U_1}, \sin \phi_{U_1}, 0) \\
\boldsymbol{k}_2 &= (0, 0, 1).
\end{aligned}
\tag{A.2}
$$

Here the angle ϕ_{U_1} represents the deviation from the [100]-crystal lattice direction. In the first step the effective field is determined by $\boldsymbol{B}_{\mathrm{eff}} = -\frac{\delta F}{\delta \boldsymbol{M}}$. Then, in this expression the ansatz for the time-dependent magnetization vector, $\boldsymbol{M} = \boldsymbol{M}_{\mathrm{s}} + \delta \boldsymbol{M}$ is inserted and finally the equation is expanded up to linear order in the dynamic magnetization components $\delta \boldsymbol{M}$. This results

Appendix A. Derivation of the angle-dependent FMR Condition (I)

in the following effective fields,

$$
\boldsymbol{B}_{\text{eff}}^{0} = \begin{pmatrix} -B_x - 4KM_x^3 - 2U_1 \cos\phi_{U_1}(M_x \cos\phi_{U_1} + M_y \sin\phi_{U_1}) \\ -B_y - 4KM_y^3 - 2U_1 \sin\phi_{U_1}(M_x \cos\phi_{U_1} + M_y \sin\phi_{U_1}) \\ -B_z - 4KM_z^3 - 2U_2 M_z \end{pmatrix}
$$
$$
+ \begin{pmatrix} \tau(M_x(N^+ + N^- \cos 2\phi_{\text{D}}) + M_y N^- \sin 2\phi_{\text{D}}) \\ \tau(M_y(N^+ - N^- \cos 2\phi_{\text{D}}) + M_x N^- \sin 2\phi_{\text{D}}) \\ 2\tau M_z N_z \end{pmatrix},
$$
(A.3)

$$
\boldsymbol{B}_{\text{eff}}^{1} = \begin{pmatrix} -12KM_x^2 \delta M_x + \tau\left((N^+ + N^- \cos 2\phi_{\text{D}})\,\delta M_x + N^- \delta M_y \sin 2\phi_{\text{D}}\right) \\ -12KM_y^2 \delta M_y + \tau\left((N^+ - N^- \cos 2\phi_{\text{D}})\,\delta M_y + N^- \delta M_x \sin 2\phi_{\text{D}}\right) \\ -12KM_z^2 \delta M_z + 2\tau N_z \delta M_z \end{pmatrix}
$$
$$
+ \begin{pmatrix} \delta M_x(-2U_1 \cos^2\phi_{U_1}) - U_1 \delta M_y \sin 2\phi_{U_1} \\ \delta M_y(-2U_1 \sin^2\phi_{U_1}) - U_1 \delta M_x \sin 2\phi_{U_1} \\ -2\delta M_z U_2 \end{pmatrix}.
$$
(A.4)

Note, indices 0 and 1 indicate the order of the dynamic magnetization components. Additionally, the notations $N^+ = N_x + N_y$ and $N^- = N_x - N_y$ are introduced in the interest of clarity. In the next step, the effective fields are inserted into the reduced Landau-Lifshitz equation Eq. 2.7, which is denoted as a matrix $\mathcal{W}$. The resonance frequencies are then finally calculated by solving the equation $\text{Det}[\mathcal{W}'] = 0$, with $\mathcal{W}'_{ij} = \delta M_j \mathcal{W}_i$ introduced in Eq. 2.9. In order to obtain the resonance condition as a function of the field direction, the magnetization and field components are transformed into a spherical coordinate representation, reading

$$
\boldsymbol{M} = M_0 \left(\sin\theta_M \cos\phi_M, \sin\theta_M \sin\phi_M, \cos\theta_M\right)^{\text{T}} \tag{A.5}
$$

$$
\boldsymbol{B} = B_0 \left(\sin\theta_B \cos\phi_B, \sin\theta_B \sin\phi_B, \cos\theta_B\right)^{\text{T}}, \tag{A.6}
$$

with polar and azimuthal angles θ_M, θ_B and ϕ_M, ϕ_B. Assuming the external field to be applied in-plane, $\theta_B = \pi/2$, and the magnetization to be parallel to it, i.e. $\theta_M = \theta_B$ and $\phi_M = \phi_B$, leads to the following resonance condition,

$$\nu^2 = \gamma^2 \Bigg[B_0^2 + B_0 M_0 \Big(3KM_0^2 + U_1 - 2U_2 - \tau(N^+ - 2N_z) \Big) + 2M_0^2 \Big(2K^2 M_0^4$$

$$+ U_1^2 + \tau^2 (N^-)^2 \Big)$$

$$+ KM_0^3 \Big(5B_0 + 4M_0 \Big(3KM_0^2 + U_1 - 2U_2 - (N^+ - 2N_z)\tau \Big) \Big) \cos 4\phi_B$$

$$- M_0 \Big[\tau N^- \Big(3B_0 - 2M_0 \Big(-3KM_0^2 - U_1 + 2U_2 + \tau(N^+ - 2N_z) \Big) \Big)$$

$$\cdot \cos 2(\phi_B - \phi_D) + 6KM_0^3 N^- \tau \cos 2(\phi_B + \phi_D) \Big]$$

$$+ M_0 U_1 \Big[\Big(3B_0 + 2M_0 \Big(3KM_0^2 + U_1 - 2U_2 - \tau(N^+ - 2N_z) \Big) \Big)$$

$$\cdot \cos 2(\phi_B - \phi_{U_1}) \Big]$$

$$- M_0 U_1 \Big[4\tau M_0 N^- \cos 2(\phi_D - \phi_{U_1}) - 6KM_0^3 \cos 2(\phi + \phi_{U_1}) \Big] \Bigg].$$
(A.7)

In order to obtain the resonance field as a function of the excitation frequency ν, Eq. A.7 has to be solved for B_0. This results in the expression,

$$B_0 = -\frac{M_0}{2} \Bigg[3KM_0^2 + U_1 - 2U_2 - \tau(N^+ - 2N_z) + 5KM_0^2 \cos 4\phi_B$$

$$- 3\tau N^- \cos 2(\phi - \phi_D) + 3U_1 \cos 2(\phi_B - \phi_{U_1}) \Bigg]$$

$$+ \frac{1}{2\gamma^2} \Bigg[M_0^2 \gamma^4 \Big(3KM_0^2 + U_1 - 2U_2 - \tau(N^+ - 2N_z) + 5KM_0^2 \cos 4\phi_B$$

$$- 3\tau N^- \cos 2(\phi_B - \phi_D) + 3U_1 \cos 2(\phi_B - \phi_{U_1}) \Big)^2$$

$$- 4\gamma^2 \Big[- \nu + 2M_0^2 \gamma^2 \Big(2K^2 M_0^4 + U_1^2 + \tau^2 (N^-)^2 \Big) + 4KM_0^4 \gamma^2 \Big(3KM_0^2$$

$$+ U_1 - 2U_2 - \tau(N^+ - 2N_z) \Big) \cos 4\phi_B$$

$$+ 2M_0^2 N^- \gamma^2 \tau \Big(- 3KM_0^2 - U_1 + 2U_2 + \tau(N^+ - 2N_z) \Big) \cos 2(\phi - \phi_D)$$

$$- 2M_0^2 \gamma^2 \Big(3KM_0^2 \tau N^- \cos 2(\phi_B + \phi_D) \Big)$$

$$+ 2M_0^2 \gamma^2 U_1 \Big(\Big(3KM_0^2 + U_1 - 2U_2 - \tau(N^+ - 2N_z) \Big) \cos 2(\phi_B - \phi_{U_1})$$

$$- 2\tau N^- \cos 2(\phi_D - \phi_{U_1}) + 3KM_0^2 \cos 2(\phi_B + \phi_{U_1}) \Big) \Bigg] \Bigg]^{1/2}.$$
(A.8)

Appendix A. Derivation of the angle-dependent FMR Condition (I)

Finally, for the conversion from dimensionless to physical units we refer to the notation introduced in Chap. 6,

$$
\begin{aligned}
B_0 &\to \mu_0 H_0 & M_0 &\to M_{\mathrm{s}} \\
\tau &\to 1/2\mu_0 & K &\to K/M_{\mathrm{s}}^4 \\
U_1 &\to U_1/M_{\mathrm{s}}^2 & U_2 &\to U_2/M_{\mathrm{s}}^2
\end{aligned}
\tag{A.9}
$$

Appendix B

Derivation of the angle-dependent FMR Condition (II)

In this section the origin of the discrepancy between the numerical data and the analytical model in regard of the resonance frequencies will be elaborated. As anticipated before, the implementation of anisotropic energy terms into the energy functional leads to a canting of the magnetization with respect to the external field, in the case it is not applied along one of the easy axes of the system. As a consequence, the direction of the effective field around, which the magnetization precesses, changes slightly and results likewise in a shift in frequency. The following derivation is divided into two parts. First, the actual equilibrium configuration of the magnetization for certain magnetic field directions will be determined. Finally, with these results, the adapted excitation frequencies will be calculated and compared to the numerical results, presented in Fig. 7.32.

The energy density to be considered,

$$F = \tau \boldsymbol{M} \boldsymbol{N} \boldsymbol{M} - K \sum_i M_i^4 - \boldsymbol{B} \boldsymbol{M}, \qquad \text{(B.1)}$$

comprises the demagnetization energy, the cubic magneotcrystalline anisotropy and the Zeeman interaction, represented by the respective demagnetization tensor $\boldsymbol{N}$, anisotropy strength K and external magnetic field $\boldsymbol{B}$. Here, for simplicity, the principal axes of the sample and the crystal lattice are assumed to coincide with the laboratory coordinate system. Inserting the spherical coordinates representation of the magnetization, Eq. A.5, and

Appendix B. Derivation of the angle-dependent FMR Condition (II)

the external field, Eq. A.6, into the energy functional leads to,

$$
\begin{aligned}
F[\phi, \theta] = - &B_0 M_0 \Big(\sin \theta_M \sin \theta_B \cos(\phi_M - \phi_B) + \cos \theta_M \cos \theta_B \Big) \\
&+ \tau M_0^2 \Big(\sin^2 \theta_M \left(N_x \cos^2 \phi_M + N_y \sin^2 \phi_M \right) + N_z \cos^2 \theta_M \Big) \\
&- K M_0^4 \left(\frac{1}{4} \sin^4 \theta_M (3 + \cos 4\phi_M) + \cos^4 \theta_M \right).
\end{aligned}
$$

(B.2)

For the determination of the equilibrium configuration of M, the energy functional is minimized with respect to the free parameters, which requires solving the equations,

$$
\frac{\mathrm{d}F[\phi_M, \theta_M]}{\mathrm{d}\phi_M} = 0, \qquad \frac{\mathrm{d}F[\phi_M, \theta_M]}{\mathrm{d}\theta_M} = 0.
$$

(B.3)

In the following, the discussion will be limited to an in-plane rotation of the external field, i.e. $\theta_B = \frac{\pi}{2}$. The minimization routine for the polar angle leads to the equation,

$$
\begin{aligned}
\frac{\mathrm{d}F[\phi_M, \theta_M]}{\mathrm{d}\theta_M} = - &\cos \theta_M \ \Big(B_0 M_0 \cos(\phi_M - \phi_B) \\
&- 2\tau M_0^2 \sin \theta_M \left(N_x \cos^2 \phi_M + N_y \sin^2 \phi_M - N_z \right) \\
&- K M_0^4 \left(4 \cos^2 \theta_M \sin \theta_M - \sin^3 \theta_M (3 + \cos 4\phi_M) \right) \Big) \\
\overset{!}{=} \ &0
\end{aligned}
$$

(B.4)

which is fulfilled for $\theta_M = \frac{\pi}{2}$. With both θ_B and θ_M set to 90 degrees, the energy functional hence reduces to,

$$
\begin{aligned}
F[\phi_M] = - &B_0 M_0 \cos(\phi_M - \phi_B) + \tau M_0^2 (N_x \cos^2 \phi_M + N_y \sin^2 \phi_M) \\
&- \frac{1}{4} M_0^4 (3 + \cos 4\phi_M).
\end{aligned}
$$

(B.5)

Despite this simplified form, the search for the azimuthal angle, minimizing the energy, remains challenging and highly nontrivial. It is therefore performed numerically during the further discussion. In order to compare the numerical and semi-analytical model, the respective angle mismatch $\Delta\phi = \phi_M - \phi_B$ as a function of magnetic field orientation is illustrated in Fig. B.1(a). Given by the symbols are the numerical data, which correspond to the results previously discussed in Sec. 7.3.1. Here, the dipolar strength, Ginzburg-Landau parameter, demagnetization factors and field strength are set to $\tau = 0.88$, $r_0 = -1000$, $N_x = 0.25$, $N_y = 0.35$, $N_z = 0.4$ and $B_0 = 76$, while the anisotropy value ranges between $K = 0 - 0.0004$. Note that the chosen field strength complies with twice the transition field of a spherical sample. The resulting $\Delta\phi$, obtained by minimizing Eq. B.5, is depicted

by the dashed black lines. The excellent agreement between both models, confirms the competition between the external field on one side and the anisotropic energy terms on the other side to be the origin of the orientation discrepancy.

For the determination of the resonance frequencies in the case of a different field and magnetization orientation, a similar procedure of solving the Landau-Lifshitz equation of motion as presented in Appendix A is applied. In order to account for the angle mismatch between these quantities, however, two sets of polar and azimuthal angles (θ_M, ϕ_M and θ_B, ϕ_B) enter the calculations. Utilizing the results from the minimization routine described above, the respective resonance condition reads,

$$
\begin{aligned}
\nu^2 =& B_0^2 + 4\left(KM_0^3\right)^2 + 2M_0^2\left(N^-\right)^2\tau^2 + B_0 M_0 \cos(\phi_B - \phi_M)\big(3KM_0^2 \\
& - (N^+ - 2N_z)\tau\big) \\
& + 2M_0^2 N^- \tau\big(6KM_0^2 - (N^+ - 2N_z)\tau\big)\cos 2\phi_M \\
& + 4KM_0^4\Big(3KM_0^2 - (N^+ - 2N_z)\tau\Big)\cos 4\phi_M \\
& + 3B_0 M_0 N^- \tau \cos(\phi_B + \phi_M) + 5B_0 KM_0^3 \cos(\phi_B + 3\phi_M).
\end{aligned}
$$
(B.6)

In the limit of $\phi_M = \phi_B$, this equation recovers the results given in Eq. 7.15. Finally, in Fig. B.1(b) both models are contrasted again. While the numerical data are given by the symbols, equation Eq. B.6 is visualized by the dashed black lines. From the likewise excellent agreement, it is evident that the deviations in Fig. 7.32 arise from the assumption made that the magnetization is collinear with the external field. Since the discrepancy in frequency is rather small this assumption is justified and allows therefore to apply the model directly to the experimental data.
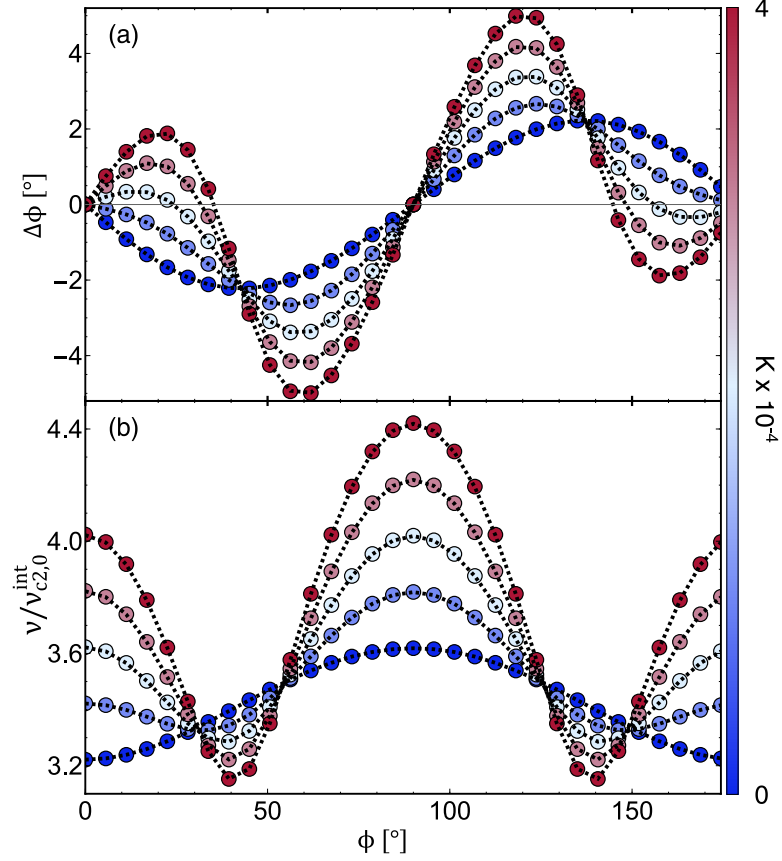
Figure B.1: (a) Angle mismatch $\Delta\phi$ as a function of the magnetic field orientation ϕ, for different anisotropy strengths. The numerically determined magnetization configuration is given by the symbols, while the semi-analytical results, according to Eq. B.5, are shown by the dashed black lines. (b) Angle-dependence of the resonance frequencies for various K values. The numerically determined excitation frequencies are given by the symbols, while the semi-analytical results, according to Eq. B.5 and Eq. B.6, are shown by the dashed black lines. Note, the anisotropy strength is indicated by the color gradient, which reflects small and large values by blue and red colors. The remaining parameters are set to $r_0 = -1000$, $\tau = 0.88$, $N_x = 0.25$, $N_y = 0.35$, $N_z = 0.4$ and $B = 76$.

Appendix C

Small K Approximation

In order to demonstrate that the term linear in K of the resonance condition given in Eq. 7.23,

$$\nu = \gamma \left(\sqrt{(B_0 + 2\tau M_0(N_x - N_y))(B_0 + 2\tau M_0(N_z - N_y))} \right.$$
$$\left. + 4KM_0^3 \frac{(B_0 + \tau M_0(N_x + N_z - 2N_y))}{\sqrt{(B_0 + 2\tau M_0(N_x - N_y))(B_0 + 2\tau M_0(N_z - N_y))}} \right), \quad \text{(C.1)}$$

indeed scales with a factor of $4M_0^3$, it will be shown in the following that despite maximizing

$$\zeta \equiv \frac{(B_0 + \tau M_0(N_x + N_z - 2N_y))}{\sqrt{(B_0 + 2\tau M_0(N_x - N_y))(B_0 + 2\tau M_0(N_z - N_y))}}, \quad \text{(C.2)}$$

$\zeta - 1$ converges to zero. In the density plot Fig. C.1(a) $\zeta - 1$ is given as a function of demagnetization factors N_x and N_y. Based on the identity $N_x + N_y + N_z = 1$, N_z is substituted in the calculations accordingly. The parameters remaining are set to $\tau = 0.88$, $r_0 = -1000$ and $B_0 = 2B_{c2} = 76$. Note that the value of the transition field corresponds to the one extracted for a spherical sample. It is evident that ζ reaches its maximum in the case of a thin film sample, with the surface normal orientated either along the y or z direction. Since a maximum deviation of around 2% is still rather small, $\zeta = 1$ is a reasonable approximation. On the contrary, if the surface normal of the thin film is aligned along the x axis or the sample shape is given by a sphere, $\zeta - 1$ reaches its minimum value, which exactly equates to zero. Besides the demagnetization factors, also the external field enters the calculations as a tunable parameter. On that account, in Fig. C.1(b), $\zeta - 1$ is illustrated as a function of field for a thin film ($N_y = 1$, $N_{x,z} = 0$, red) and cuboid ($N_x = 0.25$, $N_y = 0.35$, $N_z = 0.4$, blue) sample. It can be shown that, by increasing the magnetic field strength, its contribution to ζ gets more and more dominant and with this ζ-1 starts to decrease.

Figure C.1: (a) Prefactor $\zeta-1$ as a function of demagnetization factors N_x and N_y, with the external field set to $B_0 = 76$. The amplitude of $\zeta-1$ is given by the background color, which indicates small and large values by blue and red colors, respectively. (b) Prefactor $\zeta-1$ as a function of magnetic field for a thin film ($N_x = 0$, $N_y = 1$, $N_z = 0$) and cuboid ($N_x = 0.25$, $N_y = 0.35$, $N_z = 0.4$) sample. The remaining parameters are set to $r_0 = -1000$ and $\tau = 0.88$

Appendix D

Derivation of B_{c2}

For the calculation of the critical transition field between the conical and the field-polarized phase in presence of the two additional uniaxial anisotropies, the same derivations as presented in Sec. 7.3.3 are executed. The energy functional to be considered reads,

$$
\begin{aligned}
\mathcal{F} = \ & \frac{\rho_\mathrm{s}}{2}\left[(\nabla_i\hat{n}_j)^2 + 2Q\hat{\boldsymbol{n}}(\nabla\times\hat{n})\right] + \frac{\mu_0}{2}M_\mathrm{s}^2\hat{\boldsymbol{n}}\mathcal{T}(\phi_\mathrm{D},0)\boldsymbol{N}\mathcal{T}^{-1}(\phi_\mathrm{D},0)\hat{\boldsymbol{n}} \\
& - \mu_0 M_\mathrm{s}\hat{\boldsymbol{n}}\hat{\boldsymbol{H}}_0^\mathrm{ext} - K\sum_i\hat{n}_i^4 + CM_\mathrm{s}^2\sum_i(\partial_i\hat{n}_i)^2 \\
& - \frac{U_1}{M_s^2}\left(\boldsymbol{M}\cdot\boldsymbol{k}_1\right)^2 - \frac{U_2}{M_s^2}\left(\boldsymbol{M}\cdot\boldsymbol{k}_2\right)^2.
\end{aligned}
$$

(D.1)

Here, $\rho_\mathrm{s} = 2JM_\mathrm{s}^2$ is denoted as the exchange stiffness constant and the pitch vector length is given by $Q = D/J$. In this approach the magnetization amplitude is assumed to be constant, which reduces its configuration to $\boldsymbol{M}(\boldsymbol{r}) = M_\mathrm{s}\hat{\boldsymbol{n}}(\boldsymbol{r})$. The energy functional is therefore determined only by the orientation of $\boldsymbol{M}$, which is given by the unit vector $\hat{\boldsymbol{n}}(\boldsymbol{r})$. For the magnetization configuration, a helix representation, defined as

$$
\hat{\boldsymbol{n}} = \cos(\theta_\mathrm{c})\hat{\boldsymbol{e}}_3 + \sin(\theta_\mathrm{c})\cos(\boldsymbol{Q}\cdot\boldsymbol{r})\hat{\boldsymbol{e}}_1 + \sin(\theta_\mathrm{c})\sin(\boldsymbol{Q}\cdot\boldsymbol{r})\hat{\boldsymbol{e}}_2,
\qquad(\text{D.2})
$$

is assumed. Here, the canting of the spins is characterized by the cone angle θ_c. Furthermore, for an analytical treatment, the uniform magnetization and the pitch vector $\boldsymbol{Q}$ are assumed to be aligned parallel to the external field direction and a distortion of the helical texture to be negligible. In the first step the helix ansatz is inserted into the energy functional presented above. Note, in case of the spatially dependent energy contributions, additionally the integration along the pitch direction and over one helix period

Appendix D. Derivation of B_{c2}

is performed. The energy functional is therefore given by,

$$
\mathcal{F} =
$$

$$
\begin{aligned}
& -\mu_0 M_{\mathrm{s}} H_0 \cos\theta_c - \frac{1}{2} Q^2 \rho_{\mathrm{s}} \sin^2\theta_c \\
& + \frac{\mu_0 M_{\mathrm{s}}^2}{4} \cos^2\theta_c \left(2N_z \cos^2\theta + (N_x + N_y + (N_x - N_y)\cos 2(\phi_D - \phi))\sin^2\theta \right) \\
& - \frac{1}{32} K \Big(\cos^4\theta_c (21 + 4\cos 2\theta + 7\cos 4\theta + 8\cos 4\phi \sin^4\theta) \\
& + \frac{3}{8}\sin^4\theta_c \left(53 + 4\cos 2\theta + 7\cos 4\theta + 8\cos 4\phi \sin^4\theta \right) \\
& + 12\sin^2\theta \cos^2\theta_c \sin^2\theta_c \left(9 + 7\cos 2\theta - 2\cos 4\phi \sin^2\theta \right) \Big) \\
& + \frac{1}{32} C M_{\mathrm{s}}^2 Q^2 \Big(18 + 14\cos 2\theta + \cos 2(\theta - 2\phi) \\
& - 2\cos 4\phi + \cos 2(\theta + 2\phi) \Big) \sin^2\theta_c \sin^2\theta \\
& + \frac{1}{16} U_1 \Big(-5 + \cos 2\theta_c + \cos 2\theta + 3\cos 2\theta_c \cos 2\theta - 2(1 + 3\cos 2\theta_c) \\
& \times \cos 2(\phi - \phi_{U_1})\sin\theta^2 \Big) \\
& - \frac{1}{8} U_2 \Big(3 + \cos 2\theta + \cos 2\theta_c (1 + 3\cos 2\theta) \Big),
\end{aligned}
$$

(D.3)

with polar and azimuthal angles of the external field indicated by θ and ϕ, respectively. Minimizing this equation with respect to the cone angle and subsequently solving the resulting equation for H_0, allows to derive an expression for the external field. Setting θ_c to zero, which marks the onset of the field-polarized phase, leads to the general equation for the critical transition field H_{c2} given by,

$$
\begin{aligned}
H_{c2} = & \frac{1}{2} M_{\mathrm{s}} (\sin^2\theta(N_x + N_y + (N_x - N_y)\cos 2(\phi_D - \phi)) + 2N_z \cos^2\theta) \\
& + \frac{Q^2 \rho_{\mathrm{s}}}{\mu_0 M_{\mathrm{s}}} - \frac{K}{16\mu_0 M_{\mathrm{s}}}(9 + 20\cos 2\theta + 35\cos 4\theta + 40\cos 4\phi \sin^4\theta) \\
& - \frac{C M_{\mathrm{s}}^2 Q^2}{32\mu_0 M_{\mathrm{s}}}(11 - 4\cos 2\theta - 7\cos 4\theta - 8\cos 4\phi \sin^4\theta) \\
& + \frac{U_1}{4\mu_0 M_{\mathrm{s}}}\left(1 + 3\cos 2\theta - 6\cos 2(\phi - \phi_{U_1})\sin^2\theta\right) \\
& - \frac{U_2}{2\mu_0 M_{\mathrm{s}}}(1 + 3\cos 2\theta).
\end{aligned}
$$

(D.4)

If the external magnetic field is applied in plane, $\theta = \pi/2$, as it is the case for the microwave experiments presented above, this expression reduces to,

$$
\begin{aligned}
H_{c2} ={} & \frac{1}{2} M_{\mathrm{s}} \left((N_x + N_y) + (N_x - N_y) \cos(2(\phi_{\mathrm{D}} - \phi)) \right) + \frac{\rho_{\mathrm{s}} Q^2}{\mu_0 M_{\mathrm{s}}} \\
& - \frac{K}{2\mu_0 M_{\mathrm{s}}} (3 + 5\cos(4\phi)) - \frac{2C M_{\mathrm{s}}^2 Q^2}{\mu_0 M_{\mathrm{s}}} \cos^2 \phi \sin^2 \phi \\
& - \frac{U_1 (1 + 3\cos 2(\phi - \phi_{U_1}))}{2\mu_0 M_{\mathrm{s}}} + \frac{U_2}{\mu_0 M_{\mathrm{s}}}.
\end{aligned}
\tag{D.5}
$$

From this equation it is evident that the spatial dependence of the critical transition field is given by the demagnetization energy, the cubic magnetocrystalline anisotropy, the exchange anisotropy and the in-plane uniaxial anisotropy. The out-of-plane uniaxial anisotropy as well as the exchange stiffness term contribute only to a constant shift to H_{c2}.

Appendix E

SQUID Measurements

In order to reduce the number of free parameters in the fit equations of the angle-resolved resonance condition and critical transition field, the saturation magnetization of the cuboid-shaped crystal is measured, employing a commercial superconducting quantum interference device (SQUID) magnetometer. In Fig. E.1 the extracted evolution of the saturation magnetization as a function of temperature is illustrated. The measurements are performed following the field-cooled protocol, i.e. the magnetic field is applied during the cooling process. For the experiments a field strength of $B = 100\,\text{mT}$ is chosen. It should be mentioned that the orientation of the crystal lattice with respect to the external field is not determined in the experiments. In addition to the data, the fitting curve (red line), which is given by [Živ12],

$$\mu(T) = \mu(0) \left(1 - \left(\frac{T}{T_c} \right)^\alpha \right)^\beta \tag{E.1}$$

is added to the figure. Assuming $\alpha = 2$ [Mai11; Živ12] in the fitting procedure, gives $\mu(0) = 0.434$, $T_\text{c} = 58.236$ and $\beta = 0.3234$. By measuring the mass, $m = 0.021\,\text{g}$, and the sample dimensions, $1.65 \times 1.65 \times 1.8\,\text{mm}^3$ (density: $\rho = 4.29\frac{\text{g}}{\text{cm}^3}$), the saturation magnetization is finally converted into units of Tesla.

Figure E.1: Saturation magnetization of the cuboid-shaped crystal as a function of temperature with the external field strength set to $B = 100\,\text{mT}$. The fitting curve according to Eq. E.1 is drawn by the red line.

Appendix F

Supplementary Fit Results

For the analysis of the angle-dependence of the resonance modes in the spherically shaped crystal, the respective resonance fields are first required to be extracted from the individual line scans. As described above, two methods, which are the application of Lorentzian fits on the one hand and the amplitude-weighted resonance condition on the other hand, are employed. Since the results of the fitting procedure are already presented in the main text (Fig. 7.47), the ones of the averaging routine are now discussed here in the interest of completeness. In Fig. F.1 the evolution of the resonance fields as a function of the field direction is illustrated for various temperatures. The figure comprises the results (symbols) obtained at an excitation frequency of 6, 8 and 12 GHz, which are labeled accordingly. The set temperature is indicated by the color bar on the right hand side, reflecting low and high values by blue and red colors, respectively. As it was observed in the spectrum measured at 55 K in Fig. 7.46, two modes, exhibiting a different angle-dependence are excited. While the one lowest in field is almost constant, the second mode demonstrates a twofold symmetry as a function of the angle. Based on the comparison with the numerical calculations, these are attributed to out-of-plane and in-plane standing spin waves. Since the amplitude-weighted resonance condition represents an average over all modes, this results in a combination of both signatures, as it is resolved in the visualized data sets.

In order to determine the strengths and constants of the energy terms the two fit models introduced in Sec. 7.3.4 are applied. In the first approach, demagnetization factors N_x and N_y, the orientation of the principal axes of the sample with respect to the crystal lattice and the cubic magnetocrystalline anisotropy strength K enter the fit equation as variables. In the second model, the demagnetization factors are fixed to $N_i = 1/3$ and the fit parameters are extended by the uniaxial anisotropy constants U_1, U_2 and the direction of the symmetry axis ϕ_{U_1}. The remaining quantities, which are the excitation frequency, gyromagnetic ratio γ and saturation magnetization
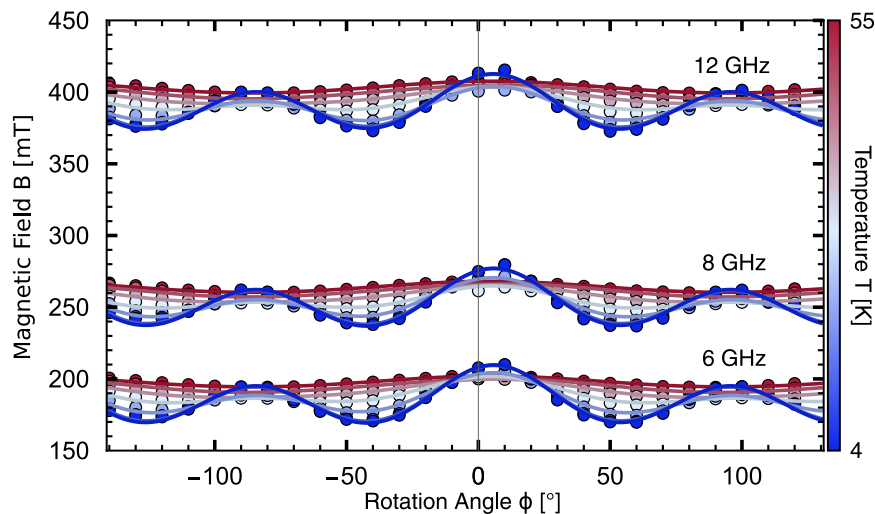
Figure F.1: Angle-dependence of the resonance fields at 6, 8 and 12 GHz and for various temperatures. The results, given by the symbols, represent the resonance positions inferred by the amplitude-weighted resonance method. The respective temperature value is indicated by the color gradient on the right hand side. The fitting curves according to Eq. A.8 are drawn by the solid lines.

M_{s}, are set to be constant, as described in the main text. The fitting curves obtained, according to Eq. A.8, are drawn in Fig. F.1 by solid lines. The extracted temperature evolution of the fit results is depicted in Fig. F.2. Here, orange, red and blue symbols are assigned to the results obtained for the driving frequency set to 6, 8 and 12 GHz. In the top panel Fig. F.2(a), the curve progressions of the demagnetization factors N_x and N_y are presented. It can be seen that for all three cases a similar behavior is resolved: both N_x and N_y first decrease and subsequently increase again under an increasing temperature. A clear dependence on the temperature is therefore not observed. The significant difference between the demagnetization factors of the individual data sets, which contradicts the actual sample shape, is a result of the twofold symmetry of the high-field modes. Since the demagnetization term is the only one complying to this symmetry and the amplitude of its spatial contribution is proportional to $N_x - N_y$, the parameters are adapted accordingly. Interestingly, the discrepancy between the parameters varies only slightly. This implies that the amplitude of the $\cos 2\phi$ contribution obviously scales with the saturation magnetization, as it is the case for the dipolar interactions, shown in Eq. 7.59. Against the background that these findings cannot be explained in terms of the demagnetization energy, this supports the assumption that the resolved modes are more likely to be attributed to spin waves. The visualized trend of N_x and N_y arises from the

fact that the extracted resonance fields do not correspond to the one of the uniform mode, but are shifted by a constant offset. In order to compensate for this effect in the fitting algorithm, the remaining demagnetization factor N_z, which is determined by the sum of N_x and N_y and mainly induces a likewise shift of the resonance field, is increased or decreased. In the bottom panel Fig. F.2(b), the uniaxial anisotropy strengths U_1 and U_2 are plotted as a function of temperature. Apart from minor deviations, a similar continuous decrease of U_1 under an increasing temperature is evident for all three data sets. In a more detailed analysis this trend reveals to scale with M_s^2. The resulting contribution to the angle-dependence of the resonance fields is therefore linear in M_s, as discussed above. The second anisotropy strength U_2 exhibits a similar temperature dependence as the demagnetization factors. These findings originate from the fact that the out-of-plane unaxial anisotropy mainly induces a shift of the resonance conditions. It therefore compensates the field offset due to the applied weighted-amplitude method, in the same manner as the demagnetization energy term.
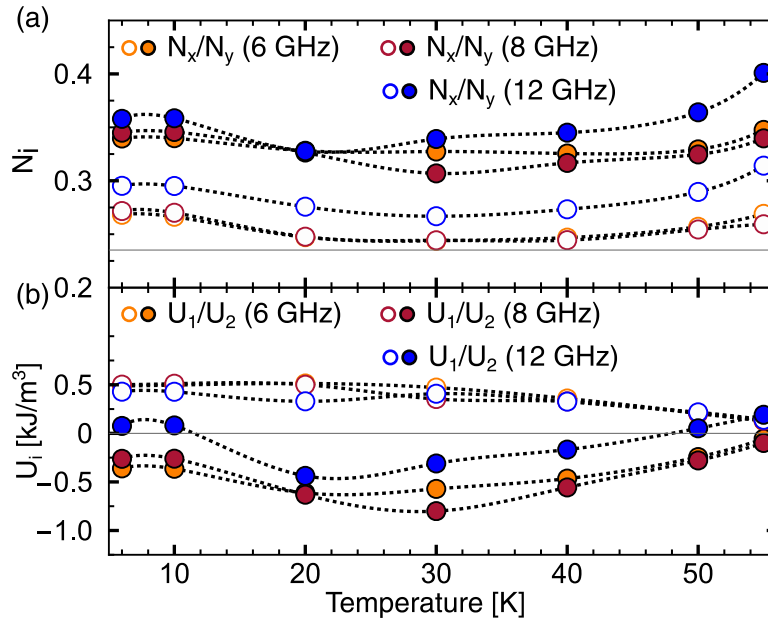
Figure F.2: Visualization of the extracted fit parameters in the case of the spherical sample. (a) Temperature evolution of demagnetization factors N_x, N_y. (b) Uniaxial anisotropy strengths U_1 and U_2 as a function of temperature. The results are obtained from the measurements at 6, 8 and 12 GHz, which are reflected by orange, red and blue colors.

Bibliography

[A G96]   G. A. Melkov A. G. Gurevich. *Magnetization Oscillations and Waves.* CRC Press, 1996.

[A H09]   R. Schäfer A. Hubert. *Magnetic Domains - The analysis of Magnetic Microstructures.* Springer-Verlag Berlin Heidelberg, 2009.

[Abd19]   L. V. Abdurakhimov et al. "Magnon-photon coupling in the noncollinear magnetic insulator Cu_2OSeO_3". In: *Phys. Rev. B* 99 (14 Apr. 2019), p. 140401. DOI: 10.1103/PhysRevB.99.140401.

[Ada12]   T. Adams et al. "Long-Wavelength Helimagnetic Order and Skyrmion Lattice Phase in Cu_2OSeO_3". In: *Phys. Rev. Lett.* 108 (23 June 2012), p. 237204. DOI: 10.1103/PhysRevLett.108.237204.

[Aha01]   A. Aharoni. *Introduction to the Theory of Ferromagnetism.* Oxford University Press, 2001.

[Aha98]   A. Aharoni. "Demagnetizing factors for rectangular ferromagnetic prisms". In: *J. Appl. Phys.* 83.6 (1998), pp. 3432–3434. DOI: 10.1063/1.367113.

[Aqe21]   A. Aqeel et al. "Microwave Spectroscopy of the Low-Temperature Skyrmion State in Cu_2OSeO_3". In: *Phys. Rev. Lett.* 126 (1 Jan. 2021), p. 017202. DOI: 10.1103/PhysRevLett.126.017202.

[Ars18]   A.Z. Arsad and N.B. Ibrahim. "Temperature-dependent magnetic properties of YIG thin films with grain size less 12 nm prepared by a sol-gel method". In: *J. Magn. Magn. Mater.* 462 (2018), pp. 70–77. ISSN: 0304-8853. DOI: https://doi.org/10. 1016/j.jmmm.2018.05.003.

[Bac20]   C. Back et al. "The 2020 skyrmionics roadmap". In: *J. Phys. D. Appl. Physi.* 53.36 (June 2020), p. 363001. DOI: 10.1088/1361-6463/ab8418.

[Bai03]   M. Bailleul, D. Olligs, and C. Fermon. "Propagating spin wave spectroscopy in a permalloy film: A quantitative analysis". In: *Appl. Phys. Lett.* 83.5 (2003), pp. 972–974. DOI: 10.1063/1. 1597745.

Bibliography

[Bak80]   P. Bak and M. H. Jensen. "Theory of helical magnetic structures and phase transitions in MnSi and FeGe". In: *J. Phys. C Solid State Phys.* 13.31 (Nov. 1980), p. L881. DOI: 10.1088/0022-3719/13/31/002.

[Ban19]   L. J. Bannenberg et al. "Multiple low-temperature skyrmionic states in a bulk chiral magnet". In: *npj Quantum Mater.* 4.1 (2019), p. 11. ISSN: 2397-4648. DOI: 10.1038/s41535-019-0150-7.

[Bar21]   A. Barman et al. "The 2021 Magnonics Roadmap". In: *J. Phys. Condens. Matter* 33.41 (Aug. 2021), p. 413001. DOI: 10.1088/1361-648X/abec1a.

[Bau10]   A. Bauer et al. "Quantum phase transitions in single-crystal $Mn_{1-x}Fe_xSi$ and $Mn_{1-x}Co_xSi$: Crystal growth, magnetization, ac susceptibility, and specific heat". In: *Phys. Rev. B* 82 (6 Aug. 2010), p. 064404. DOI: 10.1103/PhysRevB.82.064404.

[Bau14]   H. G. Bauer et al. "Coupling of spinwave modes in wire structures". In: *Appl. Phys. Lett.* 104.10 (2014), p. 102404. DOI: 10.1063/1.4868250.

[Bau15]   H. G. Bauer et al. "Nonlinear spin-wave excitations at low magnetic bias fields". In: *Nat. Commun.* 6.1 (2015), p. 8274. ISSN: 2041-1723. DOI: 10.1038/ncomms9274.

[Bau16]   A. Bauer and C. Pfleiderer. "Generic Aspects of Skyrmion Lattices in Chiral Magnets". In: *Topological Structures in Ferroic Materials: Domain Walls, Vortices and Skyrmions*. Ed. by Jan Seidel. Cham: Springer International Publishing, 2016, pp. 1–28. DOI: 10.1007/978-3-319-25301-5_1.

[Bel10]   M. Belesi et al. "Ferrimagnetism of the magnetoelectric compound Cu_2OSeO_3 probed by ^{77}Se NMR". In: *Phys. Rev. B* 82 (9 Sept. 2010), p. 094422. DOI: 10.1103/PhysRevB.82.094422.

[Ber20]   I. Bertelli et al. "Magnetic resonance imaging of spin-wave transport and interference in a magnetic insulator". In: *Sci. Adv.* 6.46 (2020), eabd3556. DOI: 10.1126/sciadv.abd3556.

[Bil07a] C. Bilzer. "Microwave susceptibility of thin ferromagnetic films: metrology and insight into magnetization dynamics". PhD thesis. Université Paris Sud, 2007.

[Bil07b] C. Bilzer et al. "Vector network analyzer ferromagnetic resonance of thin films on coplanar waveguides: Comparison of different evaluation methods". In: *J. Appl. Phys.* 101.7 (2007), p. 074505. DOI: 10.1063/1.2716995.

[Bir09]   D. R. Birt et al. "Diffraction of spin waves from a submicrometer-size defect in a microwaveguide". In: *Appl. Phys. Lett.* 95.12 (Sept. 2009), p. 122510. ISSN: 0003-6951. DOI: 10.1063/1.3237168.

[Blu01]   S. Blundell. *Magnetism in Condensed Matter.* Oxford University Press, 2001.

[Bos08]   J. W. G. Bos, C. V. Colin, and T. T. M. Palstra. "Magnetoelectric coupling in the cubic ferrimagnet Cu_2OSeO_3". In: *Phys. Rev. B* 78 (9 Sept. 2008), p. 094416. DOI: 10.1103/PhysRevB.78.094416.

[Bou16]   Olivier Boulle et al. "Room-temperature chiral magnetic skyrmions in ultrathin magnetic nanostructures". In: *Nat. Nanotechnol.* 11.5 (2016), pp. 449–454. ISSN: 1748-3395. DOI: 10.1038/nnano.2015.315.

[Bra19]   J. Brandao et al. "Observation of magnetic skyrmions in un-patterned symmetric multilayers at room temperature and zero magnetic field". In: *Sci. Rep.* 9.1 (2019), p. 4144. ISSN: 2045-2322. DOI: 10.1038/s41598-019-40705-4.

[Bro78]   W. F. Brown. *Micromagnetics.* Krieger, New York, 1978.

[Büt17]   F. Büttner et al. "Field-free deterministic ultrafast creation of magnetic skyrmions by spin-orbit torques". In: *Nat. Nanotechnol.* 12.11 (2017), pp. 1040–1044. ISSN: 1748-3395. DOI: 10.1038/nnano.2017.178.

[Cel97]   Z. Celinski, K.B. Urquhart, and B. Heinrich. "Using ferromagnetic resonance to measure the magnetic moments of ultrathin films". In: *J. Magn. Magn. Mater.* 166.1 (1997), pp. 6–26. ISSN: 0304-8853. DOI: https://doi.org/10.1016/S0304-8853(96)00428-3.

[Cha14]   J. Y. Chauleau et al. "Self-consistent determination of the key spin-transfer torque parameters from spin-wave Doppler experiments". In: *Phys. Rev. B* 89 (2 Jan. 2014), p. 020403. DOI: 10.1103/PhysRevB.89.020403.

[Cha15]   A. Chacon et al. "Uniaxial Pressure Dependence of Magnetic Order in MnSi". In: *Phys. Rev. Lett.* 115 (26 Dec. 2015), p. 267202. DOI: 10.1103/PhysRevLett.115.267202.

[Cha18]   A. Chacon et al. "Observation of two independent skyrmion phases in a chiral magnetic material". In: *Nat. Phys.* 14.9 (2018), pp. 936–941. ISSN: 1745-2481. DOI: 10.1038/s41567-018-0184-y.

Bibliography

[Che19a] A. M. Cheghabouri and M. C. Onbasli. "Direct current-tunable MHz to multi-GHz skyrmion generation and control". In: *Sci. Rep.* 9.1 (2019), p. 9496. ISSN: 2045-2322. DOI: 10.1038/s41598-019-45972-9.

[Che19b] J. Chen et al. "Evidence for Magnetic Skyrmions at the Interface of Ferromagnet/Topological-Insulator Heterostructures". In: *Nano Lett.* 19.9 (Sept. 2019), pp. 6144–6151. ISSN: 1530-6984. DOI: 10.1021/acs.nanolett.9b02191.

[Che21] P. Che et al. "Confined dipole and exchange spin waves in a bulk chiral magnet with Dzyaloshinskii-Moriya interaction". In: *Phys. Rev. Res.* 3 (3 July 2021), p. 033104. DOI: 10.1103/PhysRevResearch.3.033104.

[Cho06] S. Choi, K. S. Lee, and S. K. Kim. "Spin-wave interference". In: *Appl. Phys. Lett.* 89.6 (Aug. 2006), p. 062501. ISSN: 0003-6951. DOI: 10.1063/1.2259813.

[Chu14] A. V. Chumak, A. A. Serga, and B. Hillebrands. "Magnon transistor for all-magnon data processing". In: *Nat. Commun.* 5.1 (2014), p. 4700. ISSN: 2041-1723. DOI: 10.1038/ncomms5700.

[Chu15] A. V. Chumak et al. "Magnon spintronics". In: *Nat. Phys.* 11.6 (2015), pp. 453–461. ISSN: 1745-2481. DOI: 10.1038/nphys3347.

[Chu17] A. V. Chumak, A. A. Serga, and B. Hillebrands. "Magnonic crystals for data processing". In: *J. Phys. D. Appl. Physi.* 50.24 (May 2017), p. 244001. DOI: 10.1088/1361-6463/aa6a65.

[Coe10] J. M. D. Coey. *Magnetism and Magnetic Materials*. Cambridge University Press, 2010.

[Dec18] M. M. Decker. "Spin Current Induced Control of Magnetization Dynamics". PhD thesis. Universität Regensburg, 2018.

[Dem11] V. E. Demidov et al. "Excitation of short-wavelength spin waves in magnonic waveguides". In: *Appl. Phys. Lett.* 99.8 (2011), p. 082507. DOI: 10.1063/1.3631756.

[Den20] L. Deng et al. "Room-temperature skyrmion phase in bulk Cu2OSeO3 under high pressures". In: *Proc. Natl. Acad. Sci. U.S.A.* 117.16 (2020), pp. 8783–8787. ISSN: 0027-8424. DOI: 10.1073/pnas.1922108117.

[Dev13] T. Devolder et al. "Damping of CoxFe80-xB20 ultrathin films with perpendicular magnetic anisotropy". In: *Appl. Phys. Lett.* 102.2 (2013), p. 022407. DOI: 10.1063/1.4775684.

[Din15] J. Ding, X. Yang, and T. Zhu. "The Motion of Magnetic Skyrmions Driven by Propagating Spin Waves". In: *IEEE Trans. Magn.* 51.11 (2015), pp. 1–4. DOI: 10.1109/TMAG.2015.2446516.

[Div22]   S. Divic et al. "Magnetic skyrmion crystal at a topological insulator surface". In: *Phys. Rev. B* 105 (3 Jan. 2022), p. 035156. DOI: 10.1103/PhysRevB.105.035156.

[Doh19]   T. Dohi et al. "Formation and current-induced motion of synthetic antiferromagnetic skyrmion bubbles". In: *Nat. Commun.* 10.1 (2019), p. 5153. ISSN: 2041-1723. DOI: 10.1038/s41467-019-13182-6.

[Don17]   C. Donnelly et al. "Three-dimensional magnetization structures revealed with X-ray vector nanotomography". In: *Nature* 547.7663 (2017), pp. 328–331. ISSN: 1476-4687. DOI: 10.1038/nature23006.

[Dzy58]   I. Dzyaloshinsky. "A thermodynamic theory of weak ferromagnetism of antiferromagnetics". In: *J. Phys. Chem. Solids* 4.4 (1958), pp. 241–255. ISSN: 0022-3697. DOI: https://doi.org/10.1016/0022-3697(58)90076-3.

[Ehl16]   D. Ehlers et al. "Skyrmion dynamics under uniaxial anisotropy". In: *Phys. Rev. B* 94 (1 July 2016), p. 014406. DOI: 10.1103/PhysRevB.94.014406.

[Eve12]   K. Everschor. "Current-Induced Dynamics of Chiral Magnetic Structures". PhD thesis. Universtität Köln, 2012.

[Eve18]   K. Everschor-Sitte et al. "Perspective: Magnetic skyrmions-Overview of recent progress in an active research field". In: *J. App. Phys.* 124.24 (2018), p. 240901. DOI: 10.1063/1.5048972.

[Far98]   M. Farle. "Ferromagnetic resonance of ultrathin metallic layers". In: *Rep. Prog. Phys.* 61.7 (July 1998), pp. 755–826. DOI: 10.1088/0034-4885/61/7/001.

[Fen18]   Q. Fengjiao et al. "New magnetic phase of the chiral skyrmion material Cu2OSeO3". In: *Sci. Adv.* 4.9 (Oct. 2018), eaat7323. DOI: 10.1126/sciadv.aat7323.

[Fer13]   A. Fert, V. Cros, and J. Sampaio. "Skyrmions on the track". In: *Nat. Nanotechnol.* 8.3 (2013), pp. 152–156. ISSN: 1748-3395. DOI: 10.1038/nnano.2013.29.

[Gar17]   M. Garst, J. Waizner, and D. Grundler. "Collective spin excitations of helices and magnetic skyrmions: review and perspectives of magnonics in non-centrosymmetric magnets". In: *J. Phys. D Appl. Phys* 50.29 (June 2017), p. 293002. DOI: 10.1088/1361-6463/aa7573.

[Gie13]   R. Gieniusz et al. "Single antidot as a passive way to create caustic spin-wave beams in yttrium iron garnet films". In: *Appl. Phys. Lett.* 102.10 (2013), p. 102409. DOI: 10.1063/1.4795293.

Bibliography

[Gie14]   R. Gieniusz et al. "An antidot array as an edge for total non-reflection of spin waves in yttrium iron garnet films". In: *Appl. Phys. Lett.* 104.8 (2014), p. 082412. DOI: 10.1063/1.4867026.

[Gil55]   T. L. Gilbert. "A Lagrangian Formulation of the Gyromagnetic Equation of the Magnetization Field". In: *Phys. Rev. D* 100 (1955), p. 1243.

[Grä20]   J. Gräfe et al. "Direct observation of spin-wave focusing by a Fresnel lens". In: *Phys. Rev. B* 102 (2 July 2020), p. 024420. DOI: 10.1103/PhysRevB.102.024420.

[Gru16]   P. Gruszecki et al. "Microwave excitation of spin wave beams in thin ferromagnetic films". In: *Sci. Rep.* 6.1 (2016), p. 22367. ISSN: 2045-2322. DOI: 10.1038/srep22367.

[Gul01]   Y. V. Gulyaev and A. A. Nikitov. "Magnonic crystals and spin waves in periodic structures". In: *Dokl. Phys.* 46.10 (2001), pp. 687–689. ISSN: 1562-6903. DOI: 10.1134/1.1415579.

[Hal18]   M. Halder et al. "Thermodynamic evidence of a second skyrmion lattice phase and tilted conical phase in Cu_2OSeO_3". In: *Phys. Rev. B* 98 (14 Oct. 2018), p. 144429. DOI: 10.1103/PhysRevB.98.144429.

[Här16]   M. O. Härtinger. "Untersuchung magnetischer Materialien mit Methoden der Ferromagnetischen Resonanz". PhD thesis. Universität Regensburg, 2016.

[Hei11]   S. Heinze et al. "Spontaneous atomic-scale magnetic skyrmion lattice in two dimensions". In: *Nat. Phys.* 7.9 (2011), pp. 713–718. ISSN: 1745-2481. DOI: 10.1038/nphys2045.

[Hio20]   T. Hioki, Y. Hashimoto, and E. Saitoh. "Bi-reflection of spin waves". In: *Commun. Phys.* 3.1 (2020), p. 188. ISSN: 2399-3650. DOI: 10.1038/s42005-020-00455-6.

[Hof10]   F. Hoffmann. "Magnetic anisotropies of (Ga,Mn)As films and nanostructures". PhD thesis. Universität Regensburg, 2010.

[Hra17]   A. Hrabec et al. "Current-induced skyrmion generation and dynamics in symmetric bilayers". In: *Nat. Commun.* 8.1 (2017), p. 15765. ISSN: 2041-1723. DOI: 10.1038/ncomms15765.

[Iwa13]   J. Iwasaki, M. Mochizuki, and N. Nagaosa. "Current-induced skyrmion dynamics in constricted geometries". In: *Nat. Nanotechnol.* 8.10 (2013), pp. 742–747. ISSN: 1748-3395. DOI: 10.1038/nnano.2013.176.

[Iwa14]   J. Iwasaki, A. J. Beekman, and N. Nagaosa. "Theory of magnon-skyrmion scattering in chiral magnets". In: *Phys. Rev. B* 89 (6 Feb. 2014), p. 064412. DOI: 10.1103/PhysRevB.89.064412.

[Jam13]   M. Jamali et al. "Spin wave nonreciprocity for logic device applications". In: *Sci. Rep.* 3.1 (2013), p. 3160. ISSN: 2045-2322. DOI: 10.1038/srep03160.

[Jan14]   O. Janson et al. "The quantum nature of skyrmions and half-skyrmions in Cu2OSeO3". In: *Nat. Commun.* 5.1 (2014), p. 5376. ISSN: 2041-1723. DOI: 10.1038/ncomms6376.

[Jia15]   W. Jiang et al. "Blowing magnetic skyrmion bubbles". In: *Science* 349.6245 (July 2015), pp. 283–286. DOI: 10.1126/science.aaa1442.

[Jos04]   J. P. Joshi and S.V. Bhat. "On the analysis of broad Dysonian electron paramagnetic resonance spectra". In: *J. Magn. Reson.* 168.2 (2004), pp. 284–287. ISSN: 1090-7807. DOI: https://doi.org/10.1016/j.jmr.2004.03.018.

[Kal06]   S. S. Kalarickal et al. "Ferromagnetic resonance linewidth in metallic thin films: Comparison of measurement methods". In: *J. Appl. Phys.* 99.9 (2006), p. 093909. DOI: 10.1063/1.2197087.

[Kar16]   K. Karube et al. "Robust metastable skyrmions and their triangular-square lattice structural transition in a high-temperature chiral magnet". In: *Nat. Mater.* 15.12 (2016), pp. 1237–1242. ISSN: 1476-4660. DOI: 10.1038/nmat4752.

[Kat87]   M. Kataoka. "Spin Waves in Systems with Long Period Helical Spin Density Waves Due to the Antisymmetric and Symmetric Exchange Interactions". In: *J. Phys. Soc. Jpn.* 56.10 (Oct. 1987), pp. 3635–3647. ISSN: 0031-9015. DOI: 10.1143/JPSJ.56.3635.

[Kéz15]   I. Kézsmárki et al. "Néel-type skyrmion lattice with confined orientation in the polar magnetic semiconductor GaV_4S_8". In: *Nat. Mater.* 14.11 (2015), pp. 1116–1122. ISSN: 1476-4660. DOI: 10.1038/nmat4402.

[Kha21]   S. Khan et al. "Coupling microwave photons to topological spin textures in Cu_2OSeO_3". In: *Phys. Rev. B* 104 (10 Sept. 2021), p. L100402. DOI: 10.1103/PhysRevB.104.L100402.

[Kit48]   C. Kittel. "On the Theory of Ferromagnetic Resonance Absorption". In: *Phys. Rev.* 73 (2 Jan. 1948), pp. 155–161. DOI: 10.1103/PhysRev.73.155.

[Kli17]   S. Klingler et al. "Gilbert damping of magnetostatic modes in a yttrium iron garnet sphere". In: *Appl. Phys. Lett.* 110.9 (2017), p. 092409. DOI: 10.1063/1.4977423.

[Kör17]   H. S. Körner, J. Stigloher, and C. H. Back. "Excitation and tailoring of diffractive spin-wave beams in NiFe using nonuniform microwave antennas". In: *Phys. Rev. B* 96 (10 Sept. 2017), p. 100401. DOI: 10.1103/PhysRevB.96.100401.

Bibliography

[Kov14]   A. A. Kovalev. "Skyrmionic spin Seebeck effect via dissipative thermomagnonic torques". In: *Phys. Rev. B* 89 (24 June 2014), p. 241101. DOI: 10.1103/PhysRevB.89.241101.

[Kra14]   M. Krawczyk and D. Grundler. "Review and prospects of magnonic crystalsÂ and devices with reprogrammable band structure". In: *J. Phys. Condens. Matter* 26.12 (Mar. 2014), p. 123202. DOI: 10.1088/0953-8984/26/12/123202.

[Kru10]   V. V. Kruglyak, S. O. Demokritov, and D. Grundler. "Magnonics". In: *J. Phys. D. Appl. Physi.* 43.26 (June 2010), p. 264001. DOI: 10.1088/0022-3727/43/26/264001.

[Lan35]   L. Landau and E. Lifshitz. "On the theory of the dispersion of magnetic permeability in ferromagnetic bodies". In: *Phys. Z. Sowjet. 8, 153* (1935). Ed. by L.P. PITAEVSKI, pp. 51–65. DOI: https://doi.org/10.1016/B978-0-08-036364-6.50008-9.

[Lee21]   O. Lee et al. "Tunable gigahertz dynamics of low-temperature skyrmion lattice in a chiral magnet". In: *J. Phys. Condens. Matter* (2021). ISSN: 0953-8984.

[Len11]   B. Lenk et al. "The building blocks of magnonics". In: *Phys. Rep.* 507.4 (2011), pp. 107–136. ISSN: 0370-1573. DOI: https://doi.org/10.1016/j.physrep.2011.06.003.

[Lin14]   S. Z. Lin et al. "ac Current Generation in Chiral Magnetic Insulators and Skyrmion Motion induced by the Spin Seebeck Effect". In: *Phys. Rev. Lett.* 112 (18 May 2014), p. 187203. DOI: 10.1103/PhysRevLett.112.187203.

[Liu06]   X. Liu and J. K. Furdyna. "Ferromagnetic resonance in $Ga_{1-x}Mn_xAs$ dilute magnetic semiconductors". In: *J. Phys. Condens. Matter* 18.13 (Mar. 2006), R245–R279. DOI: 10.1088/0953-8984/18/13/r02.

[Liu13]   Y. H. Liu, Y. Q. Li, and J. H. Han. "Skyrmion dynamics in multiferroic insulators". In: *Phys. Rev. B* 87 (10 Mar. 2013), p. 100402. DOI: 10.1103/PhysRevB.87.100402.

[Mac18]   D. Maccariello et al. "Electrical detection of single magnetic skyrmions in metallic multilayers at room temperature". In: *Nat. Nanotechnol.* 13.3 (2018), pp. 233–237. ISSN: 1748-3395. DOI: 10.1038/s41565-017-0044-4.

[Mah20]   A. Mahmoud et al. "Introduction to spin wave computing". In: *J. Appl. Phys.* 128.16 (2020), p. 161101. DOI: 10.1063/5.0019328.

[Mai11]   A. Maisuradze et al. "μSR investigation of magnetism and magnetoelectric coupling in Cu2OSeO3". In: *Phys. Rev. B* 84 (6 Aug. 2011), p. 064433. DOI: 10.1103/PhysRevB.84.064433.

[Mai18]   H. Maier-Flaig et al. "Note: Derivative divide, a method for the analysis of broadband ferromagnetic resonance in the frequency domain". In: *Rev. Sci. Instrum.* 89.7 (2018), p. 076101. DOI: 10.1063/1.5045135.

[Man12]   S. Mansfeld et al. "Spin Wave Diffraction and Perfect Imaging of a Grating". In: *Phys. Rev. Lett.* 108 (4 Jan. 2012), p. 047204. DOI: 10.1103/PhysRevLett.108.047204.

[Man20]   A.O. Mandru et al. "Coexistence of distinct skyrmion phases observed in hybrid ferromagnetic/ferrimagnetic multilayers". In: *Nat. Commun.* 11.1 (2020), p. 6365. ISSN: 2041-1723. DOI: 10.1038/s41467-020-20025-2.

[Mey14]   S. A. Meynell et al. "Surface twist instabilities and skyrmion states in chiral ferromagnets". In: *Phys. Rev. B* 90 (1 July 2014), p. 014406. DOI: 10.1103/PhysRevB.90.014406.

[Mey19]   S. Meyer et al. "Isolated zero field sub-10 nm skyrmions in ultrathin Co films". In: *Nat. Commun.* 10.1 (2019), p. 3823. ISSN: 2041-1723. DOI: 10.1038/s41467-019-11831-4.

[Mil13]   P. Milde et al. "Unwinding of a Skyrmion Lattice by Magnetic Monopoles". In: *Science* 340.6136 (May 2013), pp. 1076–1080. DOI: 10.1126/science.1234657.

[Moc12]   M. Mochizuki. "Spin-Wave Modes and Their Intense Excitation Effects in Skyrmion Crystals". In: *Phys. Rev. Lett.* 108 (1 Jan. 2012), p. 017601. DOI: 10.1103/PhysRevLett.108.017601.

[Moc14]   M. Mochizuki et al. "Thermally driven ratchet motion of a skyrmion microcrystal and topological magnon Hall effect". In: *Nat. Mater.* 13.3 (2014), pp. 241–246. ISSN: 1476-4660. DOI: 10.1038/nmat3862.

[Moo21]   S. H. Moody et al. "Experimental evidence of a change of exchange anisotropy sign with temperature in Zn-substituted Cu_2OSeO_3". In: *Phys. Rev. Res.* 3 (4 Dec. 2021), p. 043149. DOI: 10.1103/PhysRevResearch.3.043149.

[Mor60]   T. Moriya. "New Mechanism of Anisotropic Superexchange Interaction". In: *Phys. Rev. Lett.* 4 (5 Mar. 1960), pp. 228–230. DOI: 10.1103/PhysRevLett.4.228.

[Müh09]   S. Mühlbauer et al. "Skyrmion Lattice in a Chiral Magnet". In: *Science* 323.5916 (Feb. 2009), pp. 915–919. DOI: 10.1126/science.1166767.

[Mül17]   J. Müller. "Magnetic skyrmions on a two-lane racetrack". In: *New J. Phys.* 19.2 (2017), p. 025002. ISSN: 1367-2630. DOI: 10.1088/1367-2630/aa5b55.

Bibliography

[Mün10]   W. Münzer et al. "Skyrmion lattice in the doped semiconductor $Fe_{1-x}Co_xSi$". In: *Phys. Rev. B* 81 (4 Jan. 2010), p. 041203. DOI: 10.1103/PhysRevB.81.041203.

[Nag13]   N. Nagaosa and Y. Tokura. "Topological properties and dynamics of magnetic skyrmions". In: *Nat. Nanotechnol.* 8.12 (2013), pp. 899–911. ISSN: 1748-3395. DOI: 10.1038/nnano.2013.243.

[Nak17]   T. Nakajima et al. "Skyrmion lattice structural transition in MnSi". In: *Sci. Adv.* 3.6 (June 2017), e1602562. DOI: 10.1126/sciadv.1602562.

[Nak80]   O. Nakanishi et al. "The origin of the helical spin density wave in MnSi". In: *Solid State Commun.* 35.12 (1980), pp. 995–998. ISSN: 0038-1098. DOI: https://doi.org/10.1016/0038-1098(80)91004-2.

[Nay17]   A. K. Nayak et al. "Magnetic antiskyrmions above room temperature in tetragonal Heusler materials". In: *Nature* 548.7669 (2017), pp. 561–566. ISSN: 1476-4687. DOI: 10.1038/nature23466.

[Neu06]   I. Neudecker. "Magnetization Dynamics of Confined Ferromagnetic Systems". PhD thesis. Universität Regensburg, 2006.

[Neu09]   S. Neusser and D. Grundler. "Magnonics: Spin Waves on the Nanoscale". In: *Adv. Mater.* 21.28 (2009), pp. 2927–2932. DOI: https://doi.org/10.1002/adma.200900809.

[Nii15]   Y. Nii et al. "Uniaxial stress control of skyrmion phase". In: *Nat. Commun.* 6.1 (2015), p. 8539. ISSN: 2041-1723. DOI: 10.1038/ncomms9539.

[Nik15]   S. A. Nikitov et al. "Magnonics: a new research area in spintronics and spin wave electronics". In: *Phys.-Uspekhi* 58.10 (Oct. 2015), p. 1002. DOI: 10.3367/UFNe.0185.201510m.1099.

[Obs15]   M. Obstbaum. "Inverse spin Hall effect in metallic heterostructures". PhD thesis. Universität Regensburg, 2015.

[Oga21]   N. Ogawa et al. "Nonreciprocity of spin waves in the conical helix state". In: *Proc. Natl. Acad. Sci. U.S.A.* 118.8 (2021). ISSN: 0027-8424. DOI: 10.1073/pnas.2022927118.

[Oik16]   H. Oike et al. "Interplay between topological and thermodynamic stability in a metastable magnetic skyrmion lattice". In: *Nat. Phys.* 12.1 (2016), pp. 62–66. ISSN: 1745-2481. DOI: 10.1038/nphys3506.

[Onb14]   M. C. Onbasli et al. "Pulsed laser deposition of epitaxial yttrium iron garnet films with low Gilbert damping and bulk-like magnetization". In: *APL Materials* 2.10 (2014), p. 106102. DOI: 10.1063/1.4896936.

[Ono12]   Y. Onose et al. "Observation of Magnetic Excitations of Skyrmion Crystal in a Helimagnetic Insulator Cu_2OSeO_3". In: *Phys. Rev. Lett.* 109 (3 July 2012), p. 037603. DOI: 10.1103/PhysRevLett.109.037603.

[Pap21]   Á. Papp et al. "Experimental demonstration of a concave grating for spin waves in the Rowland arrangement". In: *Sci. Rep.* 11.1 (2021), p. 14239. ISSN: 2045-2322. DOI: 10.1038/s41598-021-93700-z.

[Pen21]   L. Peng et al. "Dynamic transition of current-driven single-skyrmion motion in a room-temperature chiral-lattice magnet". In: *Nat. Commun.* 12.1 (2021), p. 6797. ISSN: 2041-1723. DOI: 10.1038/s41467-021-27073-2.

[Per08]   K. Perzlmaier, G. Woltersdorf, and C. H. Back. "Observation of the propagation and interference of spin waves in ferromagnetic thin films". In: *Phys. Rev. B* 77 (5 Feb. 2008), p. 054425. DOI: 10.1103/PhysRevB.77.054425.

[Pfl10]   C. Pfleiderer et al. "Skyrmion lattices in metallic and semiconducting B20 transition metal compounds". In: *J. Phys. Condens. Matter* 22.16 (Mar. 2010), p. 164207. DOI: 10.1088/0953-8984/22/16/164207.

[Pir11]   P. Pirro et al. "Interference of coherent spin waves in micronsized ferromagnetic waveguides". In: *Phys. Status Solidi B* 248.10 (2011), pp. 2404–2408. DOI: https://doi.org/10.1002/pssb.201147093.

[Ran21]   K. Ran et al. "Creation of a Chiral Bobber Lattice in Helimagnet-Multilayer Heterostructures". In: *Phys. Rev. Lett.* 126 (1 Jan. 2021), p. 017204. DOI: 10.1103/PhysRevLett.126.017204.

[Rom13]   N. Romming et al. "Writing and Deleting Single Magnetic Skyrmions". In: *Science* 341.6146 (Aug. 2013), pp. 636–639. DOI: 10.1126/science.1240573.

[Ruf15]   E. Ruff et al. "Magnetoelectric effects in the skyrmion host material Cu2OSeO3". In: *Sci. Rep.* 5.1 (2015), p. 15025. ISSN: 2045-2322. DOI: 10.1038/srep15025.

[Ryb15]   F. N. Rybakov et al. "New Type of Stable Particlelike States in Chiral Magnets". In: *Phys. Rev. Lett.* 115 (11 Sept. 2015), p. 117201. DOI: 10.1103/PhysRevLett.115.117201.

[Sam13]   J. Sampaio et al. "Nucleation, stability and current-induced motion of isolated magnetic skyrmions in nanostructures". In: *Nat. Nanotechnol.* 8.11 (2013), pp. 839–844. ISSN: 1748-3395. DOI: 10.1038/nnano.2013.210.

Bibliography

[Sch10]   T. Schneider et al. "Nondiffractive Subwavelength Wave Beams in a Medium with Externally Controlled Anisotropy". In: *Phys. Rev. Lett.* 104 (19 May 2010), p. 197203. DOI: 10.1103/PhysRevLett.104.197203.

[Sch12]   T. Schulz et al. "Emergent electrodynamics of skyrmions in a chiral magnet". In: *Nat. Phys.* 8.4 (2012), pp. 301–304. ISSN: 1745-2481. DOI: 10.1038/nphys2231.

[Sch13]   T. Schwarze. "Spin Waves in 2D and 3D Magnonic Crystals: From Nanostructured Ferromagnetic Materials to ChiralHelimagnets". PhD thesis. Technische Universität München, 2013.

[Sch14]   C. Schütte and M. Garst. "Magnon-skyrmion scattering in chiral magnets". In: *Phys. Rev. B* 90 (9 Sept. 2014), p. 094423. DOI: 10.1103/PhysRevB.90.094423.

[Sch15]   T. Schwarze et al. "Universal helimagnon and skyrmion excitations in metallic, semiconducting and insulating chiral magnets". In: *Nat. Mater.* 14.5 (2015), pp. 478–483. ISSN: 1476-4660. DOI: 10.1038/nmat4223.

[Sek12a]   S. Seki, S. Ishiwata, and Y. Tokura. "Magnetoelectric nature of skyrmions in a chiral magnetic insulator Cu2OSeO3". In: *Phys. Rev. B* 86 (6 Aug. 2012), p. 060403. DOI: 10.1103/PhysRevB.86.060403.

[Sek12b]   S. Seki et al. "Formation and rotation of skyrmion crystal in the chiral-lattice insulator Cu_2OSeO_3". In: *Phys. Rev. B* 85 (22 June 2012), p. 220406. DOI: 10.1103/PhysRevB.85.220406.

[Sek12c]   S. Seki et al. "Observation of Skyrmions in a Multiferroic Material". In: *Science* 336.6078 (Apr. 2012), pp. 198–201. DOI: 10.1126/science.1214143.

[Sek16]   S. Seki et al. "Magnetochiral nonreciprocity of volume spin wave propagation in chiral-lattice ferromagnets". In: *Phys. Rev. B* 93 (23 June 2016), p. 235131. DOI: 10.1103/PhysRevB.93.235131.

[Sek17]   S. Seki et al. "Stabilization of magnetic skyrmions by uniaxial tensile strain". In: *Phys. Rev. B* 96 (22 Dec. 2017), p. 220404. DOI: 10.1103/PhysRevB.96.220404.

[Sek20]   S. Seki et al. "Propagation dynamics of spin excitations along skyrmion strings". In: *Nat. Commun.* 11.1 (2020), p. 256. ISSN: 2041-1723. DOI: 10.1038/s41467-019-14095-0.

[Sek21]   S. Seki et al. "Direct visualization of the three-dimensional shape of skyrmion strings in a noncentrosymmetric magnet". In: *Nat. Mater.* (2021). ISSN: 1476-4660. DOI: 10.1038/s41563-021-01141-w.

[Ser10]   A. A. Serga, A. V. Chumak, and B. Hillebrands. "YIG magnonics". In: *J. Phys. D. Appl. Physi.* 43.26 (June 2010), p. 264002. DOI: 10.1088/0022-3727/43/26/264002.

[Shi13]   K. Shibata et al. "Towards control of the size and helicity of skyrmions in helimagnetic alloys by spin-orbit coupling". In: *Nat. Nanotechnol.* 8.10 (2013), pp. 723–728. ISSN: 1748-3395. DOI: 10.1038/nnano.2013.174.

[Sko05]   R. Skomski et al. "Anisotropic exchange". In: *J. Appl. Phys.* 97.10 (2005), 10B302. DOI: 10.1063/1.1850401.

[Sou16]   A. Soumyanarayanan et al. "Emergent phenomena induced by spin-orbit coupling at surfaces and interfaces". In: *Nature* 539.7630 (2016), pp. 509–517. ISSN: 1476-4687. DOI: 10.1038/nature19820.

[Sta16]   I. Stasinopoulos. "Low damping and linearly polarized GHz magnetization dynamics in the chiral magnet Cu2OSeO3 hosting spin helices and skyrmions". PhD thesis. Technische Universität München, 2016.

[Sta17a]   I. Stasinopoulos et al. "Linearly polarized GHz magnetization dynamics of spin helix modes in the ferrimagnetic insulator Cu2OSeO3". In: *Sci. Rep.* 7.1 (2017), p. 7037. ISSN: 2045-2322. DOI: 10.1038/s41598-017-07020-2.

[Sta17b]   I. Stasinopoulos et al. "Low spin wave damping in the insulating chiral magnet Cu2OSeO3". In: *Appl. Phys. Lett.* 111.3 (July 2017), p. 032408. ISSN: 0003-6951. DOI: 10.1063/1.4995240.

[Sti16]   J. Stigloher et al. "Snell's Law for Spin Waves". In: *Phys. Rev. Lett.* 117 (3 July 2016), p. 037204. DOI: 10.1103/PhysRevLett.117.037204.

[Suz18]   M. Suzuki et al. "Three-dimensional visualization of magnetic domain structure with strong uniaxial anisotropy via scanning hard X-ray microtomography". In: *Appl. Phys. Express* 11.3 (Jan. 2018), p. 036601. DOI: 10.7567/apex.11.036601.

[Tac12]   S. Tacchi et al. "Mode conversion from quantized to propagating spin waves in a rhombic antidot lattice supporting spin wave nanochannels". In: *Phys. Rev. B* 86 (1 July 2012), p. 014417. DOI: 10.1103/PhysRevB.86.014417.

[Tak21]   R. Takagi et al. "Hybridized magnon modes in the quenched skyrmion crystal". In: *Phys. Rev. B* 104 (14 Nov. 2021), p. 144410. DOI: 10.1103/PhysRevB.104.144410.

[Udv03]   L. Udvardi et al. "First-principles relativistic study of spin waves in thin magnetic films". In: *Phys. Rev. B* 68 (10 Sept. 2003), p. 104436. DOI: 10.1103/PhysRevB.68.104436.

Bibliography

[Vad18]   V. L. Vadimov, M. V. Sapozhnikov, and A. S. Mel'nikov. "Magnetic skyrmions in ferromagnet-superconductor (F/S) heterostructures". In: *Appl. Phys. Lett.* 113.3 (2018), p. 032402. DOI: 10.1063/1.5037934.

[Ver16]   R. B. Versteeg et al. "Optically probed symmetry breaking in the chiral magnet Cu_2OSeO_3". In: *Phys. Rev. B* 94 (9 Sept. 2016), p. 094409. DOI: 10.1103/PhysRevB.94.094409.

[Ver19]   R. B. Versteeg. "Optically probed order and dynamics in the chiral cluster magnet Cu_2OSeO_3". PhD thesis. Universität Köln, 2019.

[Vla08]   V. Vlaminck and M. Bailleul. "Current-Induced Spin-Wave Doppler Shift". In: *Science* 322.5900 (2008), pp. 410–413. DOI: 10.1126/science.1162843.

[Vog18]   M. Vogel et al. "Control of Spin-Wave Propagation using Magnetisation Gradients". In: *Sci. Rep.* 8.1 (2018), p. 11099. ISSN: 2045-2322. DOI: 10.1038/s41598-018-29191-2.

[Wai13]   J. Waizner. "Dynamics in chiral magnets". MA thesis. Universität Köln, 2013.

[Wai17]   J. Waizner. "Spin wave excitations in magnetic helices and skyrmion lattices". PhD thesis. Universität zu Köln, 2017.

[Wan19]   S. Wang et al. "Electrical Detection of Magnetic Skyrmions". In: *J. Low Temp. Phys.* 197.3 (2019), pp. 321–336. ISSN: 1573-7357. DOI: 10.1007/s10909-019-02202-w.

[Wei17]   M. Weiler et al. "Helimagnon Resonances in an Intrinsic Chiral Magnonic Crystal". In: *Phys. Rev. Lett.* 119 (23 Dec. 2017), p. 237204. DOI: 10.1103/PhysRevLett.119.237204.

[Wol04]   G. Woltersdorf. "Spin-Pumping and Two-Magnon Scattering in Magnetic Multilayers". PhD thesis. Simon Fraser University, 2004.

[Woo16]   S. Woo et al. "Observation of room-temperature magnetic skyrmions and their current-driven dynamics in ultrathin metallic ferromagnets". In: *Nat. Mater.* 15.5 (2016), pp. 501–506. ISSN: 1476-4660. DOI: 10.1038/nmat4593.

[Yu10]   X. Z. Yu et al. "Real-space observation of a two-dimensional skyrmion crystal". In: *Nature* 465.7300 (2010), pp. 901–904. ISSN: 1476-4687. DOI: 10.1038/nature09124.

[Yu11]   X. Z. Yu et al. "Near room-temperature formation of a skyrmion crystal in thin-films of the helimagnet FeGe". In: *Nat. Mater.* 10.2 (2011), pp. 106–109. ISSN: 1476-4660. DOI: 10.1038/nmat2916.

[Yu12]   X. Z. Yu et al. "Skyrmion flow near room temperature in an ultralow current density". In: *Nat. Commun.* 3.1 (2012), p. 988. ISSN: 2041-1723. DOI: 10.1038/ncomms1990.

[Yu16]   H. Yu et al. "Approaching soft X-ray wavelengths in nanomagnet-based microwave technology". In: *Nat. Commun.* 7.1 (2016), p. 11255. ISSN: 2041-1723. DOI: 10.1038/ncomms11255.

[Yu20]   X. Z. Yu et al. "Motion tracking of 80-nm-size skyrmions upon directional current injections". In: *Sci. Adv.* 6.25 (2020), eaaz9744. DOI: 10.1126/sciadv.aaz9744.

[Zha15a]   S. Zhang et al. "Current-induced magnetic skyrmions oscillator". In: *New J. Phys.* 17.2 (Feb. 2015), p. 023061. DOI: 10.1088/1367-2630/17/2/023061.

[Zha15b]   X. Zhang et al. "All-magnetic control of skyrmions in nanowires by a spin wave". In: *Nanotechnology* 26.22 (2015), p. 225701. ISSN: 1361-6528. DOI: 10.1088/0957-4484/26/22/225701.

[Zha17]   X. Zhang et al. "Motion of skyrmions in nanowires driven by magnonic momentum-transfer forces". In: *New J. Phys.* 19.6 (June 2017), p. 065001. DOI: 10.1088/1367-2630/aa6b70.

[Zha19]   Z. Zhang et al. "Controlled interconversion of quantized spin wave modes via local magnetic fields". In: *Phys. Rev. B* 100 (1 July 2019), p. 014429. DOI: 10.1103/PhysRevB.100.014429.

[Zhe18]   F. Zheng et al. "Experimental observation of chiral magnetic bobbers in B20-type FeGe". In: *Nat. Nanotechnol.* 13.6 (2018), pp. 451–455. ISSN: 1748-3395. DOI: 10.1038/s41565-018-0093-3.

[Zhe21]   F. Zheng et al. "Magnetic skyrmion braids". In: *Nat. Commun.* 12.1 (2021), p. 5316. ISSN: 2041-1723. DOI: 10.1038/s41467-021-25389-7.

[Živ12]   I. Živković et al. "Two-step transition in a magnetoelectric ferrimagnet Cu2OSeO3". In: *Phys. Rev. B* 85 (22 June 2012), p. 224402. DOI: 10.1103/PhysRevB.85.224402.

List of Publications

Covered in this thesis:

A. Aqeel, **J. Sahliger**, T. Taniguchi, S. Mändl, D. Mettus, H. Berger, A. Bauer, M. Garst, C. Pfleiderer, and C. H. Back. *Microwave Spectroscopy of the Low-Temperature Skyrmion State in Cu_2OSeO_3* Phys. Rev. Lett. 126, 017202 - Published 6 January 2021

R. Takagi, M. Garst, **J. Sahliger**, C. H. Back, Y. Tokura, and S. Seki. *Hybridized magnon modes in the quenched skyrmion crystal* Phys. Rev. B 104, 144410 - Published 12 October 2021

O. Lee, **J. Sahliger**, A. Aqeel, S. Khan, S. Seki, H. Kurebayashi and C. H Back. *Tunable gigahertz dynamics of low-temperature skyrmion lattice in a chiral magnet* J. Phys. Condens. Matter 34 095801 - Published 13 December 2021

Other contributions:

A. Aqeel, M. Azhar, N. Vlietstra, A. Pozzi, **J. Sahliger**, H. Huebl, T. T. M. Palstra, C. H. Back, and M. Mostovoy. *All-electrical detection of skyrmion lattice state and chiral surface twists* Phys. Rev. B 103, L100410 - Published 19 March 2021

A. Aqeel, **J. Sahliger**, G. Li, J. Baas, G. R. Blake, T.. T. M. Palstra, C. H. Back. *Growth and Helicity of Noncentrosymmetric Cu_2OSeO_3 Crystals* Phys. Status Solidi B 2100152 - Published 07 September 21

Y. Wang, T. Taniguchi, P. H. Lin, D. Zicchino, A. Nickl, **J. Sahliger**, C. H. Lai, C. Song, H. Wu, Q. Dai, C. Back, *Time-Resolved Detection of Multilevel Switching of the Magnetization and Exchange Bias Driven by Spin-Orbit Torques* Nat. Electron. issn: 2520-1131 - Published 28 November 2022

Acknowledgement

Bibliography

collaboration concerning the spin wave experiments, all the discussions we had and the shared night shifts.

Laura Pietanesi for the discussions concerning the FMR setup, also for the joint night shifts and for her constant support.

Franz Vilsmeier and Christian Riedel for the great time in the TRMOKE lab.

Dr. Thomas Meier for answering various questions concerning physical and technical issues and for the thoroughly proofreading of this thesis.

Stephan Lichtenauer and Thomas Rapp for their technical support and Getrud Weiss for her organizational support

All other former and current members of the group for the great and helpful atmosphere and the joint activities within and outside the institute.

Finally, i want to thank my friends and family for their support over all this years.